Encyclopedic Handbook of
Emulsion Technology

edited by

Johan Sjöblom

Statoil A/S
Trondheim, Norway

MARCEL DEKKER, INC. NEW YORK • BASEL

ISBN: 0-8247-0454-1

This book is printed on acid-free paper.

Headquarters
Marcel Dekker, Inc.
270 Madison Avenue, New York, NY 10016
tel: 212-696-9000; fax: 212-685-4540

Eastern Hemisphere Distribution
Marcel Dekker AG
Hutgasse 4, Postfach 812, CH-4001 Basel, Switzerland
tel: 41-61-261-8482; fax: 41-61-261-8896

World Wide Web
http://www.dekker.com

The publisher offers discounts on this book when ordered in bulk quantities. For more information, write to Special Sales/ Professional Marketing at the headquarters address above.

Current printing (last digit):
10 9 8 7 6 5 4 3 2 1

PRINTED IN THE UNITED STATES OF AMERICA

Cover illustration: Courtesy of Statoil A/S, Trondheim, Norway.

Preface

In our everyday life we are confronted with different aspects of emulsions—either water- or oil-continuous—with varying amounts of oil, fat, and water. Margarine, butter, milk, and dressings all represent central food emulsions. In specific cases involving food emulsions, it is beneficial for the customer to control the stability of the product, particularly with regard to flocculation, sedimentation/creaming, and coalescence. In other branches of industry, emulsion stability may cause severe problems for the entire process. The most well-known examples are crude-oil–based emulsions, wastewater emulsions, etc. The multiplicity of industrial applications of emulsions has catalyzed a better fundamental understanding of these dispersed systems. The academic research has been successfully interfaced to practical concerns in order to facilitate the solutions to emulsion problems.

The first chapter in this book deals with the fundamental properties and characterization of the water/oil interface. This outstanding contribution by Miller and coworkers is very central in understanding the basics of emulsions from a thermodynamic point of view. The chapter summarizes the newest findings with regard to interfacial processes, theory, and experimental facilities.

In the second chapter, Professor Friberg reviews the use of phase diagrams within emulsion science and technology. Special emphasis is given to emulsion stability, preparation of emulsions, and prediction of structural changes during evaporation. The author has refined to completion the use of phase equilibria (equilibrium conditions for the components) to understand the nature of the processes taking place and the final conditions obtained within the emulsified systems.

The third chapter, by Wasan and Nikolov, discusses fundamental processes in emulsions, i.e., creaming/sedimentation, flocculation, coalescence, and final phase separation. A number of novel experimental facilities for characterization of emulsions and the above-mentioned processes are presented. This chapter highlights recent techniques such as film rheometry for dynamic film properties, capillary force balance in conjunction with differential microinterferometry for drainage of curved emulsion films, Kossel diffraction, imaging of interdroplet interactions, and piezo imaging spectroscopy for drop-homophase coalescence rate processes.

Next, Professor Dukhin et al. contribute a chapter dealing with fundamental processes in dilute O/W emulsions. A basic problem is to couple the processes of coalescence and flocculation by introducing a reversible flocculation, i.e., a process whereby the floc is disintegrated into individual droplets. The authors have utilized video-enhanced microscopy (VEM) to study the emulsified systems and to determine critical time constants for a stepwise flocculation/deflocculation and coalescence.

The Lund group, represented by Professors Wennerström, Söderman, Olsson, and Lindman, addresses the emulsion concept from the perspective of microemulsions. The vast number of studies of microemulsions has contributed to a better under-

standing of the properties of surfactant films. In this chapter, the contributors discuss the role of surfactant phase behavior (under equilibrium conditions), diffusion properties of both microemulsions and macroemulsions, the implications of the flexible surface model for emulsion stability, and the Ostwald ripening process in a potentially metastable emulsion system.

Dielectric spectroscopy has proved to be an important tool to describe emulsion and microemulsion systems. Professor Yuri Feldman and his Norwegian colleagues review in Chapter 6 the fundamentals of this technique and its plausible applications. The span of applications is very wide and includes flocculation processes in emulsions, diffusion processes and porosity measurements in solid materials, characterization of particulate biosuspensions, and percolation phenomena in microemulsions.

Electroacoustics provide a unique opportunity to estimate both the size of emulsion droplets and the state of the surface (kinetic) charge in a single measurement. The next two chapters, by Hunter and by A. Dukhin, Wines, Goetz and Somasundaran describe in detail the advantages of these techniques and their current development. The latter chapter also describes the application of acoustic techniques to microemulsion systems, revealing interesting structural details.

Professor Dalgleish's chapter contains a comprehensive and detailed review of the important emulsified food systems. The chapter covers the chemistry of the stabilizers (low-molecular-weight and high-molecular-weight stabilizers), the formation of the emulsion during the preparation stage, and the characterization of the formed droplets with respect to particle sizes and size distributions. The author describes the structure of the formed droplets, with details about the stabilizing interfacial layer. Macroscopic stability and destabilization of the systems are also discussed, together with kinetic aspects and the topic of partial coalescence. The author also reviews the concept of multiple emulsions.

Coupland and McClements further elaborate food emulsions in Chapter 10, reviewing the basic theory behind the propagation of ultrasound in emulsified systems and the mechanisms behind the thermal and visco-inertial losses. The pros and cons of different experimental techniques are also reviewed. Crystallization (formation and melting of crystals) and influence of droplet concentration (individual droplets and flocs), as well as droplet size and droplet charge, are all parameters discussed by the authors.

Chapters 11–16 discuss various aspects of measurement techniques as applied to different kinds of emulsifed systems. The chapters review rheology and concentrated emulsions (Princen), the NMR perspective (Balinov and Söderman), surface forces (Claesson, Blomberg, and Poptotshev), microcalorimetry (Dalmazzone and Clausse), video-enhanced microscopy (Sæther), and conductivity (Gundersen and Sjöblom). Some of these experimental techniques represent traditional approaches, while others give new avenues to a physicochemical in-depth interpretation of ongoing processes in emulsions, in both water- and oil-continuous systems.

Professors Nissim Garti and Axel Benichou review formation and preparation of intricate multiple emulsions, of both the water-in-oil-in-water and oil-in-water-in-oil types. Emulsions of this type occur especially when mixtures of both hydrophobic and hydrophilic stabilizers are used. These mixtures can be either commercial or naturally occurring. This chapter is an important complement to the traditional view of "simple emulsions" with only one dispersed phase.

Chapters 18–25 are related in that they discuss aspects of crude oil-based emulsions. The topic of environmental emulsions is covered by Fingas, Fieldhouse, and Mullin. They analyze in depth the emulsification and stabilization processes in oil spills. These processes are crucial because they complicate the removal and treatment of these so-called "mousses" or "chocolate mousses." Natural forces in the form of wind and waves are important mechanisms for the formation of the oil-spill emulsions. Most likely, the stabilization of the formed dispersions is due to naturally occurring components such as asphaltenes and resins. The authors give a comprehensive analysis of different kinds of oil spills with regard to stability and rheological properties.

The next chapter, by Kvamme and Kuznetsova, presents a theoretical approach to molecular-level processes taking place at the W/O interface. The chapter comprises state-of-the-art concepts, experimental results, and atomic-level computer simulations of processes determing the stability of the dispersions. Parallels are drawn to lipid bilayers. A strategy suitable for molecular dynamics simulation of water-in-crude-oil emulsions is presented, with most of its constituents' elements proved by computer simulations of less complex systems.

The processing of extraheavy crude oils/bitumens is extremely important because world reserves amount to 450 billion tons. To date, the mammoth Athabasca deposit in Alberta, Canada, and the Orinoco Oil Belt in western Venezuela are the largest. Together, Canada

and Venezuela hold over 40% of the total extraheavy hydrocarbon reserves. The next two chapters by Professors Salager, Briceño, and Bracho from Merida, Venezuela, and Professor Czarnecki from Edmonton, Canada, review the role of emulsions in the processing of these crude oils.

In Venezuela, the Orimulsion concept has been a success in the transportation of extraheavy crudes. These oil-in-water emulsions normally contain about 30% water and about 65% bitumen. Venezuela exports the Orimulsion to countries such as Canada, Japan, China, Denmark, Italy, and Lithuania. In 1998, 4 million tons were exported. The recovery of hydrocarbons from the oil sands is surveyed in detail by Czarnecki, who describes the problems with water-in-oil emulsions during the process steps. A major problem is created by downstream complications due to high amounts of water and high salinity.

The film properties of some selected Chinese and North Sea crude oils are the topics of the next two chapters, by Li, Peng, Zheng, and Wu and by Yang, Lu, Ese, and Sjöblom. Different aspects of interfacial rheology (interfacial shear viscosity) and Langmuir films are explored in depth for the crude oils as such or, alternatively, for selected crude oil components. Correlations between these findings and the macroscopic emulsion stability are pointed out.

Chemical destabilization is the mutual topic for the chapters by Angle and by Sjöblom, Johnsen, Westvik, Ese, Djuve, Auflem, and Kallevik ("Demulsifiers in the Oil Industry"). These contributions present a comprehensive treatise on chemicals used to promote coalescence, as well as their interaction patterns with different indigenous film-forming components in the crude oils. The competition between categories of demulsifiers in the bulk and at the W/O interfaces is central in these chapters. The question of chemical administration to enhance the efficiency of the chemical agents is also raised. The upscaling of the use of the chemicals in actual recovery operations onshore as well as offshore is also reviewed.

Chapters 26–29 all discuss hydrodynamic aspects of emulsified systems. The contribution by Danov, Kralchevsky, and Ivanov presents a very fundamental and thorough survey of different phenomena in emulsions related to dynamic and hydrodynamic motions, such as the dynamics of surfactant adsorption monolayers, which include the Gibbs surface elasticity, and characteristic time of adsorption, mechanisms of droplet–droplet coalescence, hydrodynamic interactions and drop coalescence, interpretation of the Bancroft rule with regard to droplet symmetry, and, finally, kinetics of coagulation in emulsions covering both reversible and irreversible coagulation and the kinetics of simultaneous flocculation and coalescence.

Arntzen and Andresen in their chapter cover the emulsification conditions under different flow conditions in true horizontal gravity separators. The theoretical section includes formation of droplets in turbulent regimes, turbulence-induced coalescence, settling laws in gravity separators, plug velocities and retention times, binary coalescence and hindered settling, and the dispersion layer theory. The authors then describe the choice of internals in order to accelerate the separation of water, oil, and gas, such as foam and mist handling devices, flow distributing devices, and settling enhancing devices. Current models for flow patterns in gravity separators and the impact of various models and internals on the flow of the different phases, including the dispersed phase, are also discussed. The final section in this chapter is devoted to emerging technologies.

The chapter by Urdahl, Wayth, Førdedal, Williams, and Bailey begins by discussing droplet break-up processes under both laminar and turbulent flow conditions and in electrostatic fields. The authors then discuss the droplet coalescence process under normal Brownian motion, under gravity sedimentation, and in laminar shear, including turbulent collisions as well as collisions due to electrostatic forces. The remainder of the chapter is devoted to electrostatic-induced separation of the water-in-oil emulsions and emerging technologies.

Gas hydrate formation is a well-known obstacle in the transport of gas, oil, and water. The formation of such chlatrates and their agglomeration will eventually plug pipes and prevent transport. One way to overcome this problem is to form the gas hydrates in a water-in-oil emulsion. The chapter by Tore Skodvin summarizes some current research at the University of Bergen in this field. It is stated that dielectric spectroscopy is a convenient technique to follow the formation of gas hydrates inside the water droplets, and because of this formation the dielectric properties of water change remarkably. It is also shown that when the gas hydrate particles are emulsified in a water-in-oil matrix one can transport up to about 30 weight% of water without any inhibitors present.

In the final chapter on asphaltene-stabilized crude oil emulsions, Kilpatrick and Spiecker present an extensive survey of naturally occurring crude oil surfactants and their role in the stabilization of the crude oil-based emulsions, based on a large matrix of various crude oils from different parts of the world. The

authors also explain the destabilization process by means of a variety of experimental techniques, such as high voltage break-throughs and rheology.

When I began the process of compiling the text in the next 30 chapters and contacted my colleagues all over the world, I was overwhelmed by the extremely positive attitude they all had. This was very important to me, because in editing a volume such as the *Encyclopedic Handbook of Emulsion Technology* it is necessary to ask one's colleagues to give priority — in both time and science — to the project by completing their contributions within the timeframe available. The chapter authors have been very conscientious in this respect. Therefore, I express my most sincere gratitude to all the renowned contributors for their time and effort. I hope that the international community in surface and colloid science/emulsions science and technology will appreciate this volume. I am sure that I speak on behalf of all the authors when I say that all the scientists involved in this project have contributed to a better and deeper understanding of the very complex and intricate emulsified systems.

Finally, I would also like to express my gratitude to my employer Statoil R&D Centre in Trondheim, Norway, for giving me the opportunity to complete this extensive handbook.

Johan Sjöblom

Contents

Contributors

Per Arild K. Andresen, Ph.D. Provida ASA, Oslo, Norway

Chandra W. Angle, M.Sc. Natural Resources Canada, Devon, Alberta, Canada

Richard Arntzen Kværner Process Systems a.s., Lysaker, Norway

Inge H. Auflem, M.Sc. Norwegian University of Science and Technology, Trondheim, Norway

Adrian G. Bailey, Ph.D., M.I.E.E., F.Inst.P. University of Southampton, Southampton, Hampshire, England

Balin Balinov, Ph.D. Nycomed Imaging AS, Oslo, Norway

Axel Benichou Casali Institute of Applied Chemistry, The Hebrew University of Jerusalem, Jerusalem, Israel

Eva Blomberg, Ph.D. Royal Institute of Technology and Institute for Surface Chemistry, Stockholm, Sweden

Carlos Luis Bracho Universidad de Los Andes, Mérida, Venezuela

María Isabel Briceño* Universidad de Los Andes, Mérida, Venezuela

Per M. Claesson, Ph.D. Royal Institute of Technology and Institute for Surface Chemistry, Stockholm, Sweden

Danièle Clausse Université de Technologie de Compiègne, Compiègne, France

John N. Coupland, Ph.D. Pennsylvania State University, University Park, Pennsylvania

Jan Czarnecki, Ph.D., D.Sc. Edmonton Research Centre, Syncrude Canada Ltd., Edmonton, Alberta, Canada

**Previous affiliation*: INTEVEP, Los Teques, Venezuela.

Douglas G. Dalgleish, Ph.D. Danone Vitapole, Le Plessis-Robinson, France

Christine S. H. Dalmazzone, Ph.D. Institut Français du Pétrole, Rueil-Malmaison, France

Krassimir D. Danov, Ph.D. University of Sofia, Sofia, Bulgaria

Jostein Djuve, M.Sc. University of Bergen, Bergen, Norway

Andrei S. Dukhin, Ph.D. Dispersion Technology Inc., Mount Kisco, New York

Stanislav Dukhin, Ph.D., Dr.Sc. New Jersey Institute of Technology, Newark, New Jersey

Marit-Helen Ese, Ph.D. University of Bergen, Bergen, Norway

V. B. Fainerman Institute of Technical Ecology, Donetsk, Ukraine

Yuri Feldman, Ph.D. The Hebrew University of Jerusalem, Jerusalem, Israel

Benjamin G. Fieldhouse, B.Sc. Environment Canada, Ottawa, Ontario, Canada

Merv Fingas, Ph.D. Environment Canada, Ottawa, Ontario, Canada

Harald Førdedal, Ph.D. Statoil A/S, Trondheim, Norway

Stig E. Friberg, Ph.D. Clarkson University, Potsdam, New York

Nissim Garti, Ph.D. Casali Institute of Applied Chemistry, The Hebrew University of Jerusalem, Jerusalem, Israel

P. J. Goetz Dispersion Technology Inc., Mount Kisco, New York

D. O. Grigoriev, Ph.D. Max-Planck Institute, Berlin, Germany, and St. Petersburg State University, St. Petersburg, Russia

Stig Are Gundersen, Ph.D. University of Bergen, Bergen, Norway

Robert J. Hunter, Ph.D. University of Sydney, Sydney, New South Wales, Australia

Ivan B. Ivanov, Ph.D., Dr.Sc. University of Sofia, Sofia, Bulgaria

Einar Eng Johnsen, Ph.D. Statoil A/S, Trondheim, Norway

Harald Kallevik Norwegian University of Science and Technology, Trondheim, Norway

Peter K. Kilpatrick, Ph.D. North Carolina State University, Raleigh, North Carolina

J. Krägel Max-Planck-Institut, Berlin, Germany

Peter A. Kralchevsky, Ph.D. University of Sofia, Sofia, Bulgaria

Tatyana Kuznetsova, Ph.D.* University of Bergen, Bergen, Norway

Bjørn Kvamme, Ph.D. University of Bergen, Bergen, Norway

D. Y. Kwok Massachusetts Institute of Technology, Cambridge, Massachusetts

Mingyuan Li, Ph.D. University of Petroleum, Changping, Beijing, China

L. Liggieri, Ph.D. Istituto di Chimica Fisica Applicata dei Materiali–CNR, Genoa, Italy

Björn Lindman, Ph.D. University of Lund, Lund, Sweden

Wanzhen Lu, Ph.D. Research Institute of Petroleum Processing, Beijing, China

A. V. Makievski, Ph.D. Max-Planck-Institut, Berlin, Germany, and Institute of Technical Ecology, Donetsk, Ukraine

D. Julian McClements, Ph.D. University of Massachusetts, Amherst, Massachusetts

R. Miller, Ph.D. Max-Planck-Institut, Berlin, Germany

Joseph V. Mullin, B.O.T. U.S. Minerals Management Service, Department of the Interior, Herndon, Virginia

A. W. Neumann, Ph.D. University of Toronto, Toronto, Ontario, Canada

Alex D. Nikolov, Ph.D. Illinois Institute of Technology, Chicago, Illinois

Ulf Olsson, Ph.D. University of Lund, Lund, Sweden

Bo Peng, Ph.D. University of Petroleum, Changping, Beijing, China

Evgeni Poptoshev, M.Sc. Royal Institute of Technology and Institute for Surface Chemistry, Stockholm, Sweden

H. M. Princen, Ph.D.‡ Mobil Technology Company, Paulsboro, New Jersey

F. Ravera, Ph.D. Istituto di Chimica Fisica Applicata dei Materiali–CNR, Genoa, Italy

Øystein Sæther, Ph.D. Norwegian University of Science and Technology, Trondheim, Norway

Jean-Louis Salager Universidad de Los Andes, Mérida, Venezuela

Johan Sjöblom, Ph.D. Statoil A/S, Trondheim, Norway

Tore Skodvin, Dr. Sc. University of Bergen, Bergen, Norway

Olle Söderman, Ph.D. University of Lund, Lund, Sweden

P. Somasundaran, Ph.D. Columbia University, New York, New York

*On leave from Institute of Physics, St. Petersburg University, St. Petersburg, Russia.
‡*Current affiliation*: Consultant, Flemington, New Jersey.

P. Matthew Spiecker, Ph.D. North Carolina State University, Raleigh, North Carolina

Olav Urdahl, Ph.D. Veslefrikk Operations, Statoil, Sandsli, Norway

Darsh T. Wasan, Ph.D. Illinois Institute of Technology, Chicago, Illinois

Nicholas J. Wayth, Ph.D. BP Amoco Exploration, Greenford, Scotland

Håkan Wennerström, Ph.D. University of Lund, Lund, Sweden

Arild Westvik Statoil A/S, Trondheim, Norway

Trevor J. Williams, Ph.D. University of Southampton, Southampton, Hampshire, England

T. H. Wines Columbia University, New York, New York

Zhaoliang Wu University of Petroleum, Changping, Beijing, China

Xiaoli Yang Research Institute of Petroleum Processing, Beijing, China

Xiaoyu Zheng, Ph.D. University of Petroleum, Changping, Beijing, China

6

Dielectric Spectroscopy on Emulsion and Related Colloidal Systems—A Review

Yuri Feldman
The Hebrew University of Jerusalem, Jerusalem, Israel

Tore Skodvin
University of Bergen, Bergen, Norway

Johan Sjöblom
Statoil A/S, Trondheim, Norway

I. INTRODUCTION

In general, there seems to be a shortage in modern process industry of elegant and nonintrusive techniques to describe accurately the process with regard to yield, competing reactions, external parameters, contaminations, and formation of disturbing colloidal states. It goes without saying that the development of such techniques will highly secure the success of many uncertain processes in operation today. In reviewing possible techniques one can point out dielectric (or capacitance), ultrasound, and analytical techniques, together with spectroscopic alternatives.

In this review we have chosen to highlight the pros and cons of dielectric spectroscopy applied to emulsified and related systems. The reason for the choice of these systems is that they represent multiphase systems containing phase boundaries or interfaces. It is shown that dielectric spectroscopy scanning over large frequency intervals (from some kilohertz up to several gigahertz) is extremely sensitive towards interfacial phenomena and interfacial polarization. Hence, there exist many possibilities for this technique to map processes taking place in the bulk phases as well as at the phase boundaries. This is one of several reasons why the technique is so powerful and frequently used in the study of heterogeneous systems.

In a large number of processes, one factor determining failure or success may be the state of colloids present in the system at some stage in the process. This is true whether the process is the manufacture of pharmaceuticals, application of paint, separation of water from crude oil, blood flow, preparation of carrier matrices for catalysts, preparation of novel materials, food production, etc. (the list could be expanded several times without becoming complete). Even though the science of colloids has reached a high level of sophistication, new or improved techniques that can shed light on the complex and highly dynamic interactions taking place in colloidal systems are still needed.

In the following we combine dielectric spectroscopy and colloidal systems. We believe this to be a fruitful combination of two highly important and current topics. Dielectric measurements have roots from over a hundred years ago; in the beginning of course only simple capacitance measurements were made.

However, the findings made especially on more complex systems encouraged scientists to analyze the physics and chemistry of what we call heterogeneous systems. A prediction of the dielectric properties of such systems was a main concern of scientists such as Maxwell, Wagner, Debye, and Sillars. Historically, we find a genuine interest in understanding dielectric properties of chemically very intricate systems. Depending on the problem, either the theory or the experiments have been in the lead.

Today, both dielectric measurements and colloidal systems (as a representative of heterogeneous systems) are of great interest both with regard to basic as well as applied science.

Dielectric measurements have developed from cumbersome Wheatstone-bridge measurements to an efficient, precise, and rapid spectroscopic technique. The new technique dielectric spectroscopy soon found interesting applications within the field of colloid chemistry. The technique can be applied as a precision method in a thorough mapping of the static and dynamic properties of colloidal systems. Industrially, dielectric measurements can be utilized in the on-line characterization of such complex systems.

First, we give an introduction to the basic concepts underlying the measuring technique, before the technique itself is reviewed. Finally, experimental work is presented. The experimental part has three main sections, i.e., one section covers equilibrium systems, in the second non-equilibrium systems are regarded and the last one is on the application of dielectric spectroscopy to biological systems.

In the writing of this review we have not sought to cover every aspect of the dielectric properties of colloidal systems. Our aim has rather been to demonstrate the usefulness of dielectric spectroscopy for such systems, using the application to selected systems as illustrations.

II. DIELECTRIC POLARIZATION — BASIC PRINCIPLES

Recently a new field, mesoscopic physics, has emerged. It is interesting to understand the physical properties of systems that are not as small as a single atom, but small enough that the properties can be dramatically different from those in a larger assembly. All these new mesoscopic phenomena can easily be observed in the dielectric properties of colloid systems. Their properties strictly depend on the dimensional scale and the time scale of observation. Self-assembling systems such as micellar surfactant solutions, microemulsions, emu sions, aqueous solutions of biopolymers, and cell a liposome suspensions all together represent t population of complex liquids that have their almo unique dynamic and structural properties emphasiz on the mesoscale.

Consequently, let us consider different types polarization that can take place in such structur There can be two considerations in this case. O from a phenomenological point of view, in terms the macroscopic polarization vector, another fro the molecular point of view, taking into account possible contributions to the macroscopic polarizati vector of unit sample volume.

A. Dielectric Polarization in Static Electric Fields

Being placed in an external electric field, a dielectr sample acquires a nonzero *macroscopic dipole momen* This means that the dielectric is polarized under t influence of the field. The polarization $\boldsymbol{P}$ of the sampl or dipole density, can be presented in a very simp way:

$$\boldsymbol{P} = \frac{\boldsymbol{M}}{V} \quad ($$

where $\boldsymbol{M}$ is the macroscopic dipole moment per un volume, and V is the volume of the sample. In a line approximation the polarization of the dielectric samp is proportional to the strength of the applied extern electric field $\boldsymbol{E}(1)$:

$$\boldsymbol{P} = \chi \boldsymbol{E} \quad ($$

where χ is the *dielectric susceptibility* of the material. the dielectric is isotropic, χ is scalar, whereas for anisotropic system χ is a tensor.

In the Maxwell approach, in which matter is treat as a continuum, we must in many cases ascribe a dipo density to matter. Let us compare the vector fields and $\boldsymbol{E}$ for the case in which only a dipole density present. Differences between the values of the fie vectors arise from differences in their sources. Bo the external charges and the dipole density of the sa ple act as sources of these vectors. The external charg contribute to $\boldsymbol{D}$ and $\boldsymbol{E}$ in the same manner (2). T electric displacement (electric induction) vector $\boldsymbol{D}$ defined as

$$\boldsymbol{D} = \boldsymbol{E} + 4\pi \boldsymbol{P} \quad ($$

For a uniform isotropic dielectric medium, the vectors $\boldsymbol{D}, \boldsymbol{E}, \boldsymbol{P}$ have the same direction, and the susceptibility is coordinate independent, therefore

$$\boldsymbol{D} = \boldsymbol{E}(1 + 4\pi\chi)\boldsymbol{P} = \varepsilon\boldsymbol{E} \tag{4}$$

where ε is *the dielectric permittivity*. It is also called the dielectric constant, because it is independent of the field strength. It is, however, dependent on the frequency of the applied field, the temperature, the density (or the pressure), and the chemical composition of the system.

1. Types of Polarization

For isotropic systems and static linear electric fields, we have

$$\boldsymbol{P} = \frac{\varepsilon - 1}{4\pi}\boldsymbol{E} \tag{5}$$

The applied electric field gives rise to a dipole density through the following mechanisms:

Deformation polarization — This can be further divided into two independent types:

Electron polarization — the displacement of nuclei and electrons in the atom under the influence of the external electric field. As electrons are very light they have a rapid response to the field changes; they may even follow the field at optical frequencies.

Atomic polarization — the displacement of atoms or groups of atoms in the molecule under the influence of the external electric field.

Orientation polarization — The electric field tends to direct the permanent dipoles. The rotation is counteracted by the thermal motion of the molecules. Therefore, the orientation polarization is strongly dependent on the temperature and the frequency of the applied electric field.

Ionic polarization — In an ionic lattice, the positive ions are displaced in the direction of an applied field while the negative ions are displaced in the opposite direction, giving a resultant dipole moment to the whole body. The mobility of ions also strongly depends on the temperature, but contrary to the orientation polarization the ionic polarization demonstrates only a weak temperature dependence and is determined mostly by the nature of the interface where the ions can accumulate. Most of the cooperative processes in heterogeneous systems are connected with ionic polarization.

To investigate the dependence of the polarization on molecular quantities it is convenient to assume the polarization $\boldsymbol{P}$ to be divided into two parts: the induced polarization $\boldsymbol{P}_\alpha$, caused by translation effects, and the dipole polarization $\boldsymbol{P}_\mu$, caused by orientation of the permanent dipoles.

$$\frac{\varepsilon - 1}{4\pi}\boldsymbol{E} = \boldsymbol{P}_\alpha + \boldsymbol{P}_\mu \tag{6}$$

We can now define two major groups of dielectrics: polar and nonpolar. A *polar dielectric* is one in which the individual molecules possess a dipole moment even in the absence of any applied field, i.e., the center of positive charge is displaced from the center of negative charge. A *nonpolar dielectric* is one where the molecules possess no dipole moment, unless they are subjected to an electric field. The mixture of these two types if dielectrics is common in the case of complex liquids and the most interesting dielectric processes are going on at their phase borders or at liquid–liquid interfaces.

Owing to the long range of the dipolar forces an accurate calculation of the interaction of a particular dipole with all other dipoles of a specimen would be very complicated. However, a good approximation can be made by considering that the dipoles beyond a certain distance, say some radius a, can be replaced by a continuous medium having the macroscopic dielectric properties of the specimen. Thus, the dipole whose interaction with the rest of the specimen is calculated may be considered as surrounded by a sphere of radius a containing a discrete number of dipoles, beyond which there is a continuous medium. To make this a good approximation the dielectric properties of the whole region within the sphere should be equal to those of a macroscopic specimen, i.e., it should contain a sufficient number of molecules to make fluctuations very small (3, 4). This approach can be successfully used for the calculation of dielectric properties of ionic self-assembled liquids. In this case the system can be considered to be a monodispersed system consisting of spherical water droplets dispersed in the nonpolar medium (5).

Inside the sphere where the interactions take place, the use of statistical mechanics is required. This is a second method for calculating the polarization from molecular parameters that allows us to take into account the short range of dipole–dipole interaction (1, 2). Here, we may write for the dipole density $\boldsymbol{P}$ of a homogeneous system:

$$\boldsymbol{P}V = \langle \boldsymbol{M} \rangle \tag{7}$$

where V is the volume of the dielectric under consideration and $\langle \boldsymbol{M} \rangle$ is its average total dipole moment and $\langle\,\rangle$ denote a statistical mechanical average. For an isotropic system, using Eq. (4), we find:

$$(\varepsilon - 1)\boldsymbol{E} = \frac{4\pi}{V}\langle \boldsymbol{M} \rangle \tag{8}$$

Further calculations, using all necessary statistical mechanical approaches for the appropriate border conditions, allow us to obtain the well-known Kirkwood–Frölich relationship for static dielectric permittivity:

$$g\mu = \frac{9kT}{4\pi}\frac{(\varepsilon - \varepsilon_\infty)(2\varepsilon + \varepsilon_\infty)}{\varepsilon(\varepsilon_\infty + 2)^2} \tag{9}$$

where μ is the dipole moment of the molecule in the gas phase, k is the Boltzmann constant, T is the absolute temperature, ε_∞ is the high-frequency limit of complex dielectric permittivity, and g is a correlation factor. Kirkwood introduced the correlation factor in his theory in order to take into account the short-range order interactions in associated polar liquids.

An approximate expression for the Kirkwood correlation factor can be derived by taking into account only the nearest-neighbors' interactions. In this case the sphere is reduced to contain only the jth molecule and its z nearest neighbors. For this definition it is possible to derive the following relationship for the parameter g:

$$g = 1 + z\langle \cos\theta_{ij} \rangle \tag{10}$$

where $\langle \cos\theta_{ij} \rangle$ gives the average angle of orientations between the ith and jth dipoles in the sphere of short-range interactions. From Eq. (10) it is obvious that when $\langle \cos\theta_{ij} \rangle \neq 0$, g will be different from 1. It means that the neighboring dipoles are correlated between themselves. The parallel orientation of dipoles leads to a positive value of the average cosines and g larger than 1. When the antiparallel orientation of dipoles can be observed, g will be smaller than 1. Both cases are observed experimentally (1, 2, 4). This parameter will be extremely useful in the understanding of the short-range molecular mobility and interaction in self-assembled systems.

B. Dielectric Polarization in Time-dependent Electric Fields

When an external field is applied the dielectric polarization reaches its equilibrium value, not instantly, but over a period of time. By analogy, when the field is removed suddenly, the polarization decay caused by thermal motion follows the same law as the relaxation or decay function:

$$\alpha(t) = \frac{\boldsymbol{P}(t)}{\boldsymbol{P}(0)} \tag{11}$$

The relationship, Eq. (4), for the displacement vector in the case of time-dependent fields may be written as follows (1, 3):

$$\boldsymbol{D}(t) = \varepsilon_\infty \boldsymbol{E}(t) + \int_{-\infty}^{t} \boldsymbol{E}(t')\dot{\Phi}(t - t')\mathrm{d}t' \tag{12}$$

where $\boldsymbol{D}(t) = \boldsymbol{E}(t) + 4\pi\boldsymbol{P}(t)$, ε_∞ is the high-frequency limit of the complex dielectric permittivity $\varepsilon^*(\omega)$, and $\Phi(t)$ is the dielectric response function ($\dot{\Phi}(t) = (\varepsilon_s - \varepsilon_\infty)[1 - \alpha(t)]$ where $\alpha(t)$ is the relaxation function or the decay function of dielectric polarization). (ε_s is the low-frequency limit of the permittivity, commonly denoted the static permittivity.) The point denotes the time derivative in Eq. (12). The complex dielectric permittivity $\varepsilon^*(\omega)$ is connected with the relaxation function by a very simple relationship:

$$\frac{\varepsilon^*(\omega) - \varepsilon_\infty}{\varepsilon_s - \varepsilon_\infty} = L\{-\dot{\alpha}(t)\} \tag{13}$$

where L is the operator of the Laplace transform, which is defined for the arbitrary time-dependent function $f(t)$ as:

$$L\{f(t)\} \equiv F(\omega) = \int_0^\infty \mathrm{e}^{-st} f(t)\mathrm{d}t, \qquad s = i\omega + x, \text{ where } x \to 0 \tag{14}$$

If

$$\alpha(t) \sim \exp(-t/\tau_m) \tag{15}$$

where τ_m represents the dielectric relaxation time, then the relation first obtained by Debye, is true for the frequency domain (1, 3, 4):

$$\frac{\varepsilon^*(\omega) - \varepsilon_\infty}{\varepsilon_s - \varepsilon_\infty} = \frac{1}{1 + i\omega\tau_m} \tag{16}$$

For most of the systems being studied such a relation does not sufficiently describe the experimental results. This makes it necessary to use empirical relations which formally take into account the distribution of relaxation times with the help of various parameters (α, β) (3). In the most general way such nonDebye dielectric behavior can be described by the so called Havriliak–Negami relationship (3, 4, 6):

$$\varepsilon(\omega) = \varepsilon_\infty + \frac{\varepsilon_s - \varepsilon_\infty}{[1 + (i\omega\tau)^\alpha]^\beta}, \qquad \alpha, \beta > 0 \tag{17}$$

The specific case $\alpha = 1, \beta = 1$ gives the Debye relaxation law, $\beta = 1$, $\alpha \neq 1$ corresponds to the so-called Cole–Cole equation, whereas the case $\alpha = 1$, $\beta \neq 1$ corresponds to the Cole–Davidson formula. Recently, some progress in the understanding of the physical meaning of the empirical parameters (α, β) has been made (7, 8). Using the conception of a self-similar relaxation process it is possible to understand thenature of a nonexponential relaxation of the Cole–Cole, Cole–Davidson, or Havriliak–Negami type.

An alternative approach is to obtain information on the dynamic molecular properties of a substance directly in the time domain. Relation Eq. (13) shows that the equivalent information on the dielectric relaxation properties of a sample being tested can be obtained both in the frequency and the time domains. Indeed, the polarization fluctuations caused by thermal motion in the linear response case are the same as for the macroscopic reconstruction induced by the electric field (9, 10). This means that one can equate the relaxation function $\alpha(t)$ and the macroscopic dipole correlation function $\Gamma(t)$:

$$\alpha(t) \cong \Gamma(t) = \frac{\langle \boldsymbol{M}(0)\boldsymbol{M}(t)\rangle}{\langle \boldsymbol{M}(0)\boldsymbol{M}(0)\rangle} \tag{18}$$

where $\boldsymbol{M}(t)$ is the macroscopic fluctuating dipole moment of the sample volume unit which is equal to the vector sum of all the molecular dipoles. The rate and laws govering the decay function $\Gamma(t)$ are directly related to the structural and kinetic properties of the sample and characterize the macroscopic properties of the system studied. Thus, the experimental function $\Phi(t)$ and hence $\alpha(t)$ or $\Gamma(t)$ can be used to obtain information on the dynamic properties of a dielectric in terms of the dipole correlation function.

C. Dielectric Polarization in Heterogeneous Systems

Complex fluids composed of several pseudophases with a liquid–liquid interface (emulsions, macroemulsions, cells, liposomes) or liquid–solid interface (suspensions of silica, carbon black, latex, etc.) can, from a dielectric point of view, be considered as classical heterogeneous systems. Several basic theoretical approaches have been developed in order to describe the dielectric behavior of such systems. Depending on the concentration, the shape of the dispersed phase, and the conductivity of both the media and disperse phase, different mixture formulas can be applied to describe the electric property of the complex liquids (11–15).

Two general theoretical approaches have been applied in the analysis of heterogeneous materials. The macroscopic approach, in terms of classical electrodynamics, and the statistical mechanics approach, in terms of charge-density calculations. The first is based on the application of the Laplace equation to calculate the electric potential inside and outside a dispersed spherical particle (11, 12). The same result can be obtained by considering the relationship between the electric displacement $\boldsymbol{D}$ and the macroscopic electric field $\boldsymbol{E}$ in a disperse system (12, 13). The second approach takes into account the coordinate-dependent concentration of counterions in the diffuse double layer, regarding the self-consistent electrostatic potential of counterions via Poisson's equation (5, 16, 17). Let us consider these approaches briefly.

The first original derivation of mixture formula for spherical particles was performed by Maxwell (18) and was later extended by Wagner (19). This Maxwell–Wagner (MW) theory of interfacial polarization usually can be successfully applied only for dilute dispersions of spherical particles. The dielectric permittivity of such a mixture can be expressed by the well-known relationship:

$$\varepsilon = \varepsilon_1 \frac{(2\varepsilon_1 + \varepsilon_2) - 2\phi(\varepsilon_1 - \varepsilon_2)}{(2\varepsilon_1 + \varepsilon_2) + \phi(\varepsilon_1 - \varepsilon_2)}, (\phi \ll 1) \tag{19}$$

Here, ε_1 and ε_2 are the dielectric permittivities of the continuous phase and inclusions, respectively, and ϕ is the volume fraction of inclusions.

Fricke and Curtis (20) and then Sillars (21) generalized the MW theory for the case of ellipsoidal particles. Bruggemann (22) and Hanai (23) in his series of papers extended the theory also for the case of concentrated disperse systems. For a system containing homogeneously distributed spherical particles Hanai found that the complex permittivity of the system is given by

$$\left(\frac{\varepsilon_2^* - \varepsilon^*}{\varepsilon_2^* - \varepsilon_1^*}\right)\left(\frac{\varepsilon_1^*}{\varepsilon^*}\right)^{1/3} = 1 - \phi \tag{20}$$

Boned and Peyrelasse (24) and Boyle (25) made extensions of the MW theory to include nonspherical droplets and concentrated emulsions. In the case of disperse systems containing spheroidal particles aligned in parallel, the total permittivity according to Boyle may be found from (25):

$$\left(\frac{\varepsilon_2^* - \varepsilon^*}{\varepsilon_2^* - \varepsilon_1^*}\right)\left(\frac{\varepsilon_1^*}{\varepsilon^*}\right)^{A_a} = 1 - \phi \tag{21}$$

where A_a is a depolarization factor dependent on the axial ratio a/b describing the spheroids. When $A_a = 1/3$, Eq. (21) is reduced to Eq. (20).

In the cases where spheroidal particles are randomly oriented, the Boned–Peyrelasse equation may be applied (24):

$$\left(\frac{\varepsilon_1^*}{\varepsilon^*}\right)^{3d}\left(\frac{\varepsilon_2^*-\varepsilon^*}{\varepsilon_2^*-\varepsilon_1^*}\right)\left(\frac{\varepsilon_1^*(1+3A)+\varepsilon_2^*(2-3A)}{\varepsilon^*(1+3A)+\varepsilon_2^*(2-3A)}\right)^{3K} = 1-\phi \tag{22}$$

Here, $A = (1 - A_a)/2$ is the depolarization factor while d and K are functions of A. Also in this case, when all three axis are equal, i.e., the particles are spherical, $A = 1/3$ and Eq. (22) simplifies to Eq. (20).

The main assumption in all these approaches is that the characteristic sizes of the single-phase regions are much larger than the Debye screening length (26). Provided that the dielectric permittivity and electric conductivity of the individual phases are known, the MW models enable us to calculate the total frequency-dependent permittivity of the system.

An essential feature of the MW polarization effect in complex liquids with liquid–liquid interfaces is the appearance of an accumulated charge at the boundaries between differing dielectric media as a result of ionic migration processes (12, 13). It is further assumed in the MW theory that the conductivities of each phase are uniform and constant. However, the presence of spatial charges in the suspending medium alters the potential gradient near the interface. Thermal motions and ion concentration effects result in this surface-charge layer. In emulsion systems, where the water droplet also contains counterions, a considerable part of the dielectric response to an applied field originates from the redistribution of counterions (27). It is known (12, 28–31) that counterions near the charged surface can be distributed into two regions: the Stern layer and the Gouy–Chapman diffuse double layer. Counterions in the Stern layer are considered fixed on the inner surface of the droplet and are unable to exchange position with the ion in the bulk. The distribution of counterions in the diffuse double layer is given by the Boltzmann distribution in terms of the electrostatic potential. This potential is given, self-consistently, in terms of these counterion charges by Poisson's equation instead of Laplace's equation just as it was performed in the models of interfacial polarization.

The distribution of counterions is essentially determined by their concentration and the geometry of the water core. Thus, in the case of large droplets, the assumption can be made that the droplet radius is much larger than the length of the diffuse double layer as measured by the Debye screening length. In such an approximation, the counterions can be considered to form a thin layer near the inner surface of the droplet. The difference between the Stern layer and the diffuse double layer peters out and the polarization can be described by the Schwarz model (32). In the Schwarz model the mechanism controlling the relaxation is the diffusion of the counterions along the surface. This model is more relevant to the dielectric behavior of macroemulsions than to microemulsions, for example. The above approach (unlike the "classical" MW) institutes the dependence of the dielectric properties on the characteristic size of mesoscale structures (e.g., on the radius of dispersed particle), and the ionic strength or dissociation ability of substances.

III. BASIC PRINCIPLES OF DIELECTRIC SPECTROSCOPY

The dielectric spectroscopy (DS) method occupies a special place among the numerous modern methods used for physical and chemical analysis of material, because it allows investigation of dielectric relaxation processes in an extremely wide range of characteristic times (10^4–10^{-12} s). Although the method does not possess the selectivity of NMR or ESR it offers important and sometimes unique information on the dynamic and structural properties of substances. DS is especially sensitive to intermolecular interactions, and cooperative processes may be monitored. It provides a link between the properties of the individual constituents of a complex material and the characterization of its bulk properties (see Fig. 1).

However, despite its long history of development this method is not widespread for comprehensive use because the wide frequency range (10^{-5}–10^{12} Hz) overlapped by discrete frequency domain methods have required a great deal of complex and expensive equipment. Also, for different reasons, not all the ranges have been equally available for measurement. Investigations of samples with variable properties over time (e.g., nonstable emulsions or biological systems) have thus been difficult to conduct. The low-frequency measurements of conductive systems had a strong limitation due to electrode polarization. All the above mentioned reasons led to the fact that information on dielectric characteristics of a substance could only be obtained over limited frequency ranges. As a result the investigator had only part of the dielectric spec

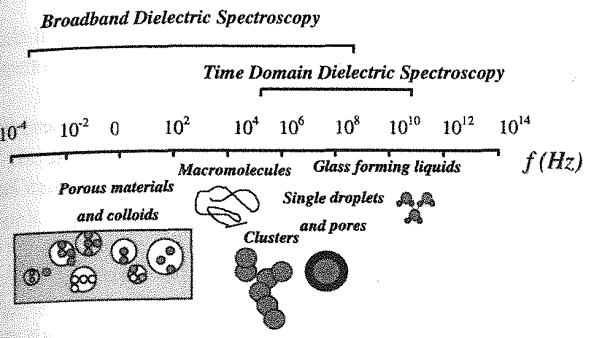

Figure 1 Electromagnetic wave scale of DS applicability for complex materals.

trum at his/her disposal to determine the relaxation parameters.

The successful development of the time-domain dielectric spectroscopy method (generally called time-domain spectroscopy – TDS) (33–38) and of broadband dielectric spectroscopy (BDS) (39–41) have radically changed attitudes toward DS, making it an effective tool for the investigation of solids and liquids, on the macroscopic, microscopic, and mesoscopic levels.

The basic approaches, the principles of experimental realization, sample holders for different applications, data treatment and presentation, and different TDS methods, which enable one to obtain the complete spectrum of $\varepsilon^*(\omega)$ in the frequency range 10^5–10^{10} Hz, are given below.

A. Basic Principles of the TDS Method

TDS is based on transmission-line theory in the time domain that aids in the study of heterogeneities in coaxial lines according to the change in shape of a test signal (33–38). As long as the line is homogeneous the shape of this pulse will not change. However, in the case of a heterogeneity in the line (the inserted dielectric, for example) the signal is partly reflected from the air-dielectric interface and partly passes through it. Dielectric measurements are made along a coaxial transmission line with the sample mounted in a cell that terminates the line. A simplified block diagram of the set-up common for most TDS methods (except transmission techniques) is presented in Fig. 2. Differences mainly include the construction of the measuring cell and its position in the coaxial line. These lead to different kinds of expressions for the values that are registered during the measurement and for the dielectric characteristics of the objects under study.

A rapidly increasing voltage step $V_0(t)$ is applied to the line and recorded, along with the reflected voltage $R(t)$ returned from the sample and delayed by the cable propagation time (Fig. 2). Any cable or instrument artifacts are separated from the sample response as a result of the propagation delay, thus making them easy to identify and control. The entire frequency spectrum is captured at once, thus eliminating drift and distortion between frequencies.

The complex permittivity is obtained as follows: for nondisperse materials (frequency-independent permittivity), the reflected signal follows the RC exponential response of the line–cell arrangement; for disperse materials, the signal follows a convolution of the line–cell response with the frequency response of the sample. The actual sample response is found by writing the total voltage across the sample:

$$V(t) = V_0(t) + R(t) \tag{23}$$

and the total current through the sample (38, 42, 44):

$$I(t) = \frac{1}{Z_0}[V_0(t) - R(t)] \tag{24}$$

where the sign change indicates direction and Z_0 is the characteristic line impedance. The total current through a conducting dielectric is composed of the displacement current $I_D(t)$, and the low-frequency current between the capacitor electrodes $I_R(t)$. Since the active resistance at zero frequency of the sample-containing cell is (38) (see Fig. 3):

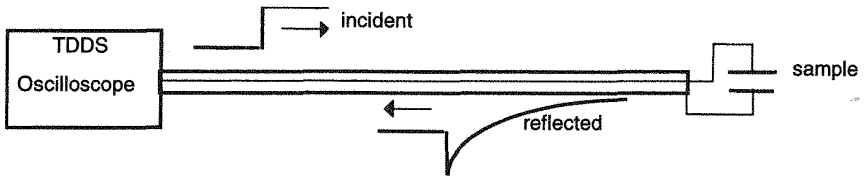

Figure 2 Basic TDS set-up.

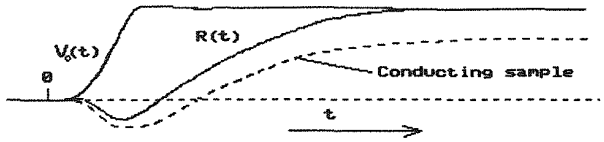

Figure 3 Characteristic shape of the signal recorded during a TDS experiment; $V_0(t)$: incident pulse, $R(t)$: reflected signal.

$$r = \lim_{t\to\infty} \frac{V(t)}{I(t)} = Z_0 \lim_{t\to\infty} \frac{V_0(t) + R(t)}{V_0(t) - R(t)} \tag{25}$$

the low-frequency current can be expressed as:

$$I_R(t) = \frac{V(t)}{r} = \frac{V_0(t) + R(t)}{Z_0} \lim_{t\to\infty} \frac{V_0(t) - R(t)}{V_0(t) + R(t)} \tag{26}$$

Thus, Eq. 24 can be written as:

$$I_D(t) = \frac{1}{Z_0}\left\{[V_0(t) = R(t)] - [V_0(t) + R(t)] \lim_{t\to\infty} \frac{V_0(t) - R(t)}{V_0(t) + R(t)}\right\} \tag{27}$$

Relations (23) and (27) represent the basic equations that relate $I(t)$ and $V(t)$ to the signals recorded during the experiment. In addition, Eq. (27) shows that TDS permits one to determine the low-frequency conductivity σ of the sample directly in the time domain (36–38):

$$\sigma = \frac{\varepsilon_0}{Z_0 C_0} \lim_{t\to\infty} \frac{V_0(t) - R(t)}{V_0(t) + R(t)} \tag{28}$$

where $\varepsilon_0 = 8.85 \times 10^{-12}$ F/m, and C_0 is the electric capacity of the coaxial sample cell terminated to the coaxial line. Using $I(t)$ and $V(t)$ or their complex Laplace transforms $i(\omega)$ and $v(\omega)$ one can deduce the relations that will describe the dielectric characteristics of a sample being tested either in frequency or time domain. The final form of these relations depends on the geometric configuration of the sample cell and its equivalent presentation (33–38).

The sample admittance for the sample cell terminated to the coaxial line is then given by

$$Y(\omega) = \frac{i(\omega)}{v(\omega)} \tag{29}$$

and the sample permittivity can be presented as follows:

$$\varepsilon(\omega) = \frac{Y(\omega)}{i\omega C_0} \tag{30}$$

where C_0 is the geometric capacitance of the empty sample cell. To minimize line artifacts and establish a common time reference, Eq. (29) is usually rewritten in differential form, to compare reflected signals from the sample and a calibrated reference standard and thus eliminate $V_0(t)$ (33–38).

If one takes into account the definite physical length of the sample and multiple reflections from the air–dielectric or dielectric-air interfaces, Eq. (30) must be written in the following form (33–36, 44):

$$\varepsilon^*(\omega) = \frac{c}{i\omega(\gamma d)} Y(\omega) X \cot X \tag{31}$$

where $X = (\omega d/c)\sqrt{\varepsilon^*(\omega)}$, d is the effective length of the inner conductor, c is the velocity of light, and γ is the ratio between the capacitance per unit length of the cell and that of the matched coaxial cable. Equation (31), in contrast to Eq. (30), is a transcendental one, and its exact solution can be only obtained numerically (33–37, 42). The essential advantage of TDS methods in comparison with frequency methods is the ability to obtain the relaxation characteristics of a sample directly in the time domain. Solving the integral equation one can evaluate the results in terms of the dielectric response function $\Phi(t)$ (38, 43, 44). It is then possible to associate $\varphi(t) = \Phi(t) + \varepsilon_\infty$ with the macroscopic dipole correlation function $\Gamma(t)$ (9, 46) in the framework of linear-response theory.

B. Experimental Tools

1. Hardware

The standard time-domain reflectometers used to measure the inhomogeneities of coaxial lines (38, 42, 47, 48) are the basis of the majority of modern TDS set-ups. The reflectometer consists of a high-speed voltage step generator and a wide-band registering system with a single- or double-channel sampling head. In order to meet the high requirements of TDS measurements such commercial equipment must be considerably improved. The main problem is due to the fact that the registration of incident $V(t)$ and reflected $R(t)$ signals is accomplished by several measurements. In order to enhance the signal-to-noise ratio one must accumulate all the registered signals. The high level of drift and instabilities during generation of the signal and its detection in the sampler are usually inherent to serial reflectometry equipment.

The new generation of digital sampling oscilloscopes (36, 45) and specially designed time-domain measuring set-ups (TDMS) (38) offer comprehensive, high precision, and automatic measuring systems for TDS hardware support. They usually have a small jitter factor (< 1.5 ps), important for rise time, a small flatness of incident pulse ($< 0.5\%$ for all amplitudes),

and in some systems a unique option for parallel-time nonuniform sampling of the signal (38).

The typical TDS set-up consists of a signal recorder, a two-channel sampler, and a built-in pulse generator. The generator produces 200-mV pulses of 10 μs duration and short rise time (~ 30 ps). Two sampler channels are characterized by an 18 GHz bandwidth and 1.5 mV noise (RMS). Both channels are triggered by one common sampling generator that provides their time correspondence during operation. The form of the voltage pulse thus measured is digitized and averaged by the digitizing block of TDMS. The time base is responsible for major metrology TDMS parameters. The block diagram of the described TDS set-up is presented in Fig. 4 (38).

a. Nonuniform Sampling

In highly disperse materials, as described in this review, the reflected signal $R(t)$ extends over wide ranges in time and cannot be captured on a single time scale with adequate resolution and sampling time. In an important modification of regular TDS systems, a nonuniform sampling technique (parallel or series) has been developed (38, 49).

In the series realization, consecutive segments of the reflected signal on an increasing time scale are registered and linked into a combined time scale. The combined response is then transformed using a running Laplace transform to produce the broad frequency spectra (49).

In the parallel realization, a multiwindow time scale of sampling is created (38). The implemented time scale is the piecewise approximation of the logarithmic scale. It includes $nw \leq 16$ sites with the uniform discretization step determined by the following formula:

$$\delta_{nw} = \delta_1 \times 2^{nw} \tag{32}$$

where $\delta_1 = 5$ ps is the discretization step at the first site, with the number of points in each step except for the first one being equal to $npw = 32$. At the first site, the number of points $npw_1 = 2npw$. The doubling of the number of points at the first site is necessary in order to have the formal zero-time position, which is impossible in the case of the strictly logarithmic structure of the scale. In addition, a certain number of points located in front of the zero-time position is added. They serve exclusively for the visual estimation of the stability of the time position of a signal and are not used for the data processing.

The structure of the time scale described allows the overlapping of the time range from 5 ps to 10 μs during one measurement, which results in a limited number of registered readings. The overlapped range can be shortened, resulting in a decreasing number of registered points and thus reducing the time required for data recording and processing.

The major advantage of the multiwindow time scale is the ability to obtain more comprehensive information. The signals received by using such a scale contain information within a very wide time range and the user merely decides which portion of this information to use for further data processing. Also, this scale provides for the filtration of registered signals close to the optimal one already at the stage of recording.

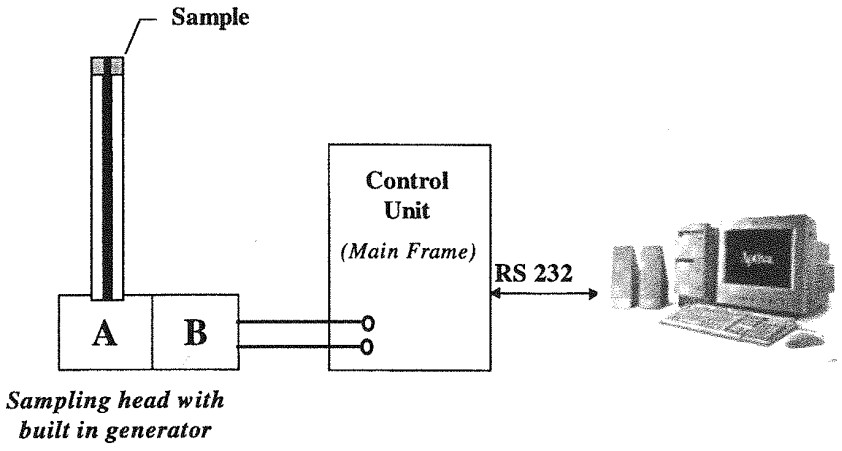

Figure 4 Circuit diagram of a TDS set-up.

b. Sample Holders

A universal sample holder that can be used for both liquid and solid samples in both the low- and high-frequency regions of the TDS method is unfortunately not yet available. The choice of its configuration depends on the measurement method and data-treatment procedure. In the framework of the lumped capacitor approximation one can consider three general types of sample holders (38, 44) (Fig. 5a): a cylindrical capacitor filled with sample. This cell (a cut-off cell) can also be regarded as a coaxial line segment with the sample having an effective γd length characterized in this case by the corresponding spread parameters. This makes it possible to use practically identical cells for various TDS and BDS method modification (50). For the total-reflection method the cut-off cell is the most frequent configuration (33–37, 42). The theoretical analysis of the cut-off sample cell (Fig. 5a) showed that a lumped-element representation enables the sample-cell properties to be accurately determined over a wide frequency range (50). Another type of sample holder that is frequently used is a plate capacitor terminated to the central electrode on the end of the coaxial line (Fig. 5b) (38, 44, 51, 52). The most popular now for different applications is an open-ended coaxial line sensor (Fig. 5c) (53–59). In lumped-capacitance approximation the configurations in Fig. 5a,b have high-frequency limitations, and for highly polar systems one must take into account the finite propagation velocity of the incident pulse or, in other words, the spread parameters of the cell (34–38). The choice of cell shape is determined to a great extent by the aggregate condition of the system studied. While cell (a) is convenient for measuring liquids (see Fig. 6a), configuration (b) is more suitable for the study of solid disks and films (Fig. 6b). Both cell types can be used to measure powder samples. While studying anisotropic systems (liquid crystals, for instance) the user may replace a coaxial line by a strip line or construct a cell with the configuration providing the measurements under various directions of the applied electric field (35, 36). The (c) type cell (see Fig. 5c) is used only when it is impossible to place the sample in the (a) or (b) type cells (38, 54–61). The fringing capacity of the coaxial-line end is the working capacity for such a cell. This kind of cell is widely used now for investigating the dielectric properties of biological materials and tissues (56–58), petroleum products (58), constructive materials (45), soil (60), and numerous other nondestructive

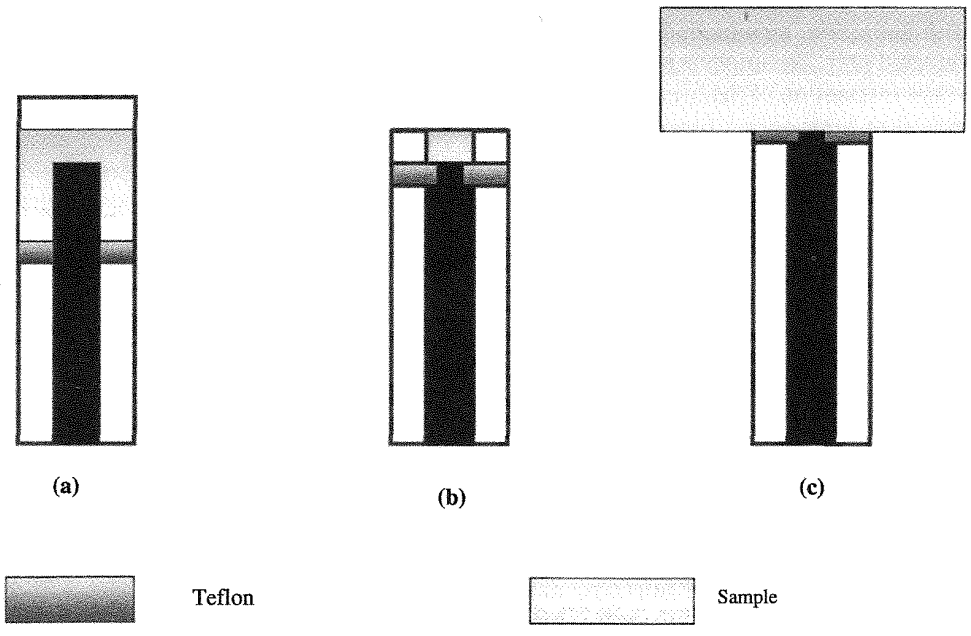

Figure 5 Simplified drawings of sample cells: (a) open coaxial line cell; (b) lumped capacitance cell; (c) end capacitance cell.

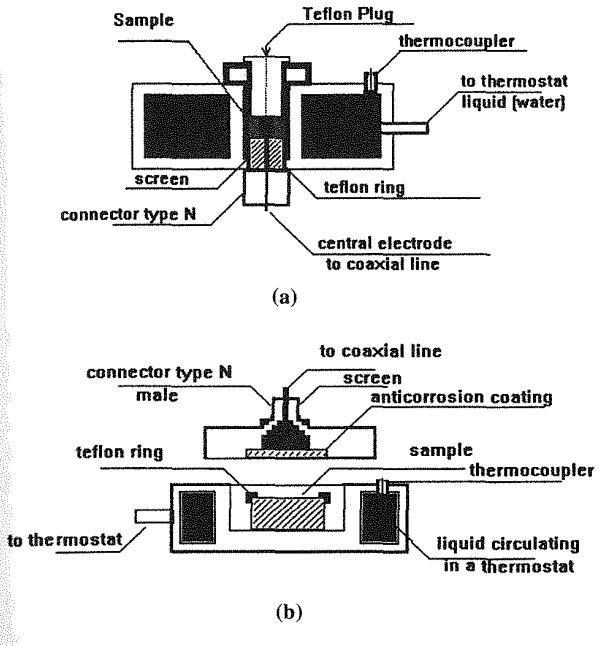

Figure 6 (a) Sample cell for high-frequency measurements of liquids; (b) sample cell for low-frequency measurements of liquids, solids, and powders. (From Ref. 38. With permission from American Institute of Physics.)

permittivity and permeability measurements. The theory and calibration procedures for such open-coaxial probes are well developed (61, 62) and the results are meeting the high standards of modern measuring systems.

2. Software

Measurement procedures, registration, storage, time referencing, and data analyses are carried out automatically in modern TDS systems. The process of operation is performed in on-line mode and the results can be presented both in frequency and time domains (34, 36, 38, 45, 49). There are several features of the modern software that control the process of measurement and calibration. One can define the time windows of interest that may be overlapped by one measurement. During the calibration procedure precise determination of the front-edge position is carried out and the setting of the internal autocenter on this position applies to all the following measurements. The precise determination and settings of horizontal and vertical positions of calibration signals are also carried out. All parameters may be saved in a configuration file, allowing for a complete set of measurements, using the same parameters and without additional calibration.

A typical flow chart of the data-processing software is presented in Fig. 7. It includes the options of signal corrections, correction of electrode polarization and d.c. conductivity, and different fitting procedures both in time and frequency domains.

C. Electrode Polarization Corrections

Many dielectric materials are conductive. This complicates the TDS study of conductive samples, and the effect of low-frequency conductivity needs to be corrected for. Usually, for a low-conductivity system the value of the d.c. conductivity can be evaluated as described in Sec. III.A.

One of the greatest obstacles in TDS measurements of conductive systems is the parasitic effect of electrode polarization. This accumulation of charge on electrode surfaces results in the formation of electric double layers (63–67). The associated capacitance and complex impedance due to this polarization is so large that the correction for it is one of the major requisites in obtaining meaningful measurements on conductive samples, especially in aqueous biological and colloidal systems (65–71). The details of electrode polarization depend microscopically upon the electrode surface topography and surface area, as well as upon the surface chemistry (reactive surface groups or atoms) and the interactions with the dielectric material or sample being examined. In the case of complex conductive liquids, the principal motivation of this work, surface ionization and ion-exchange processes in the electric double layer, can depend critically upon the chemical nature of the sample being investigated as well as upon the chemical and physical nature of the electrodes used. Because these many effects can be so diverse, no simple correction technique has been widely accepted. Several equivalent circuits have been proposed for describing the essential elements of a sample cell containing electrolyte solution (15, 65, 68), and the most generally accepted approach is shown in Fig. 8. Under the assumption that the electrodes are blocking with respect to Faradaic electron transfer, the polarization impedance of the electrodes Z, may be expressed as

$$Z_p = R_p + \frac{1}{i\omega C_p} \tag{33}$$

where $i = \sqrt{-1}$. Both C_p and R_p vary with frequency and Z_p is often considered negligible at sufficiently high frequencies. This high-frequency limit for electrode polarization has been estimated in different

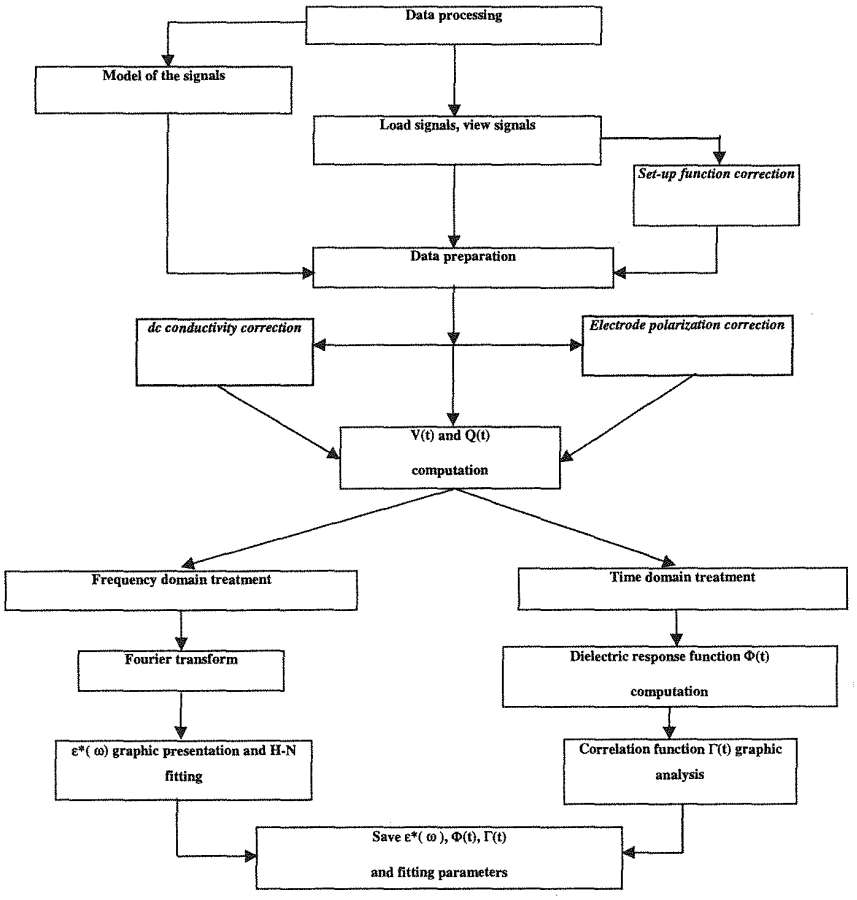

Figure 7 Flow chart of data-treatment software. (From Ref. 38. With permission from American Institute of Physics.)

ways, depending on the particular type of electrode assembly and DS experiment, but has generally fallen in the interval 100–500 kHz. Owing to the diverse nature of the processes that can contribute to electrode polarization, such as sample-dependent chemical processes alluded to above, it is difficult to estimate an upper bound for this frequency limit.

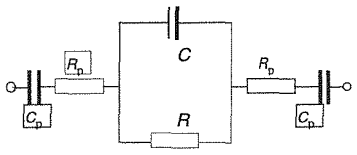

Figure 8 Equivalent circuits for a conductive dielectric sample with electrode polarization impedance described by C_p and R_p.

Two different approaches (71, 72) have been developed to correct for this phenomenon in TDS measurements directly in the time domain. One of them is applicable to weak electrolytes with a small level of low-frequency conductivity and hence a comparatively small effect of electrode polarization (72). In the other approach, applied to very conductive systems, the fractal nature of electrode polarization is considered (71). Let us consider these approaches.

In the case of TDS we can present a double layer with a capacitance C_p that is connected in series to the sample cell filled with the conductive material (Fig. 9). The characteristic charge time of C_p is much larger than the relaxation time of the measured sample. This allows us to estimate the parameters of parasitic capacitance in the long-time window where only the parasitic electrode polarization takes place. Considering the relationship for the current $i(s)$

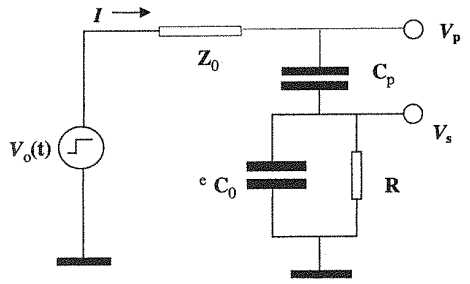

Figure 9 Equivalent circuit accounting for the electrode-polarization effect. $V_0(t)$ is a rapidly increasing voltage step; $I(t)$ is a current; Z_0 is the coaxial line impedance; C_p is the capacitance of electrode polarization; C_0 is an empty cell capacitance filled with a dielectric sample of permittivity ε and conductivity $1/R$; $V_p(t)$ and $V_s(t)$ are the voltages at the appropriate parts of the circuit. (From Ref. 72. With permission from Elsevier Science B.V.)

($s = \gamma + i\omega$, $\gamma \to 0$ is a generalized frequency in the Laplace transform) and voltage $v_p(s)$ in the frequency domain (Fig. 9) and making an inverse Laplace transform in the limit $t \to \infty$, one can obtain the analytical expression for the electrode polarization correction function $V_{ec}(t)$ as follows (72):

$$V_{ec}(t) = \frac{2\tau_p}{\tau_R + \tau_p}(1 - e^{-t/\tau_2}) \tag{34}$$

where $\tau_p = Z_0 C_p$, $\tau_R = RC_R$, and $\tau_0 = C_0 R = C_0/\sigma$. The parameter τ_2 may be obtained from the tail of the signal where only the electrode polarization effect takes place:

$$\tau_2 = \lim_{t\to\infty} \frac{2 - V_p(t)}{V_p(t)} \tag{35}$$

In order to eliminate the influence of the polarization capacitance it is necessary to subtract the exponential function with the appropriate parameters from the raw signal of the conductive sample. The exponential function $V_{ec}(t)$ of electrode polarization correction can easily be fitted to the real signal (see Fig. 10).

The TDS measurements on aqueous solutions of proteins and cell suspensions at up to several gigahertz (70–73) have shown that electrode polarization has to be taken into account even at frequencies as high as several hundred megahertz. Schwan noted the porous nature of electrode polarization phenomena (67). We nowadays often attribute such porosity to fractality and characterize porous tortuosity in terms of fractal dimension. Schwan also mentioned the increasing magnitude of this effect with increasing frequency.

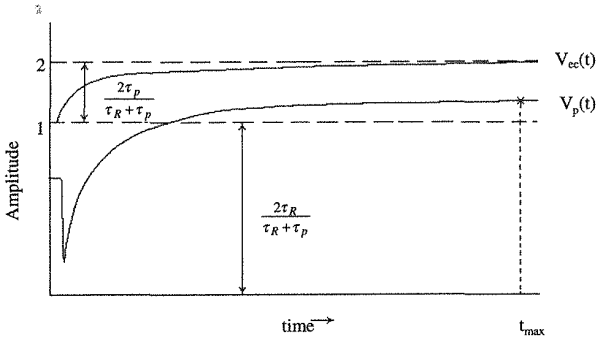

Figure 10 Schematic presentation of signal from a sample with conductivity [signal $V_p(t)$] and the correction exponential function described by the electrode polarization curve $Vec(t)$. (From Ref. 72. With permission from Elsevier Science B.V.)

While the fractal nature of *electrode surfaces* is now well appreciated (74–79), no applications for making polarization corrections, capitalizing upon the fractal nature of *electrode polarization*, appear to have been developed previously.

A general form for depicting the fractal nature of an electrode double-layer impedance is given by

$$Z_v(j\omega) = A(v)(j\omega)^{-v} \tag{36}$$

where $0 < v < 1$, $A(v)$ is an adjustable paramter, and the frequency ω is located in a certain range $\omega_{min} \leq \omega \leq \omega_{max}$ due to the self-similar electrode-polarization properties of the electrode surface (74–78). At sufficiently high and low frequencies the self-similarity of the electrode polarization disappears.

The exponent v has often been connected with the fractal dimension of the electrode surface, but this connection is not necessary. Pajkossy and coworkers (76, 77) have shown, however, that specific adsorption effects in the double layer necessarily do appear for such a dispersion. We can connect the exponent to the fractality of the dynamical polarization and show that the polarization is self-similar in time, in contrast to the self-similar geometrical structure.

The specific frequency dependence in Eq. (36) is known as the *constant phase angle* (CPA) dependence (78–80). This impedance behavior occurs for a wide class of electrodes (75–77) and suggests the introduction of a new equivalent circuit element with impedance characteristics similar to those of Eq. (36). We call this element a *recap* element (derived from *re*sistance and *cap*acitance). The electric and fractal properties for this recap complex impedance $C_v(s)$ are given by:

$$C_v(s) = R(RC)^{-v}s^{-v} \qquad 0 < v < 1 \tag{37}$$

This circuit element occupies an intermediate position between $R_p(v=0)$ and $C_p(v=1)$ and expresses its impedance in the finite range of frequencies articulated above. Using the definition of Eq. (37) we can rearrange the equivalent circuit of the measuring sample cell filled with electrolyte solution, as shown in Fig. 11.

The impedance of the sample cell (electrodes) containing an electrolyte solution can then be derived using one of these recap elements for the impedance at each electrode. Since the electrodes in general are not perfectly identical, each can be defined according to Eq. (37) to give

$$C_{v_i}(s) \equiv C_{v_i} \cdot s^{-v_i} = R_i(R_iC_i)^{-v_i}s^{-v_i} \tag{38}$$

with $i = 1$ and 2. In this fractal representation the measuring cell is defined in terms of the fractal impedance of the electrode polarization.

In order to derive the current–voltage relationship obtained for the equivalent circuit of Fig. 10, it is convenient to note the following identity (81):

$$s^{-v}i(s) = \frac{1}{\Gamma(v)}\int_0^t (t-t')^{v-1}I(t')\mathrm{d}t' \tag{39}$$

where $I(t)$ is a time-dependent current, $\Gamma(v)$ is the gamma function, s is a complex frequqency, and $i(s)$ is the Laplace transformation of $I(t)$. This resulting current–voltage relationship:

$$\begin{aligned} V(t) = &\frac{C_{v_1}}{\Gamma(v_1)}\int_0^t (t-t')^{v_1-1}I(t')\mathrm{d}t' \\ &+ \frac{C_{v_2}}{\Gamma(v_2)}\int_0^t (t-t')^{v_2-1}I(t')\mathrm{d}t' \\ &+ \frac{1}{C}\int_0^t \exp[-(t-t')/\tau_c]I(t')\mathrm{d}t' \end{aligned} \tag{40}$$

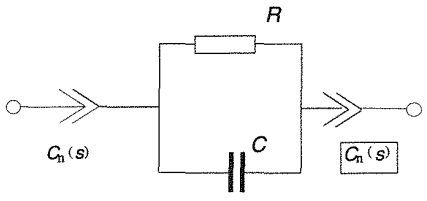

Figure 11 Equivalent circuits for a conductive dielectric sample with electrode-polarization impedance described by recap $C_V(s)$. (From Ref. 71. With permission from American Physical Society.)

has two terms describing the polarization of the respective electrodes and a third term describing the contribution from the bulk sample, where $\tau_c = RC$. Equation (40) shows how $V(t)$ and $I(t)$ are related for different kinds of measuring cells (i.e., different C_{v_i}, v_i) containing conductive solutions that polarize electrodes in conformity with the equivalent circuit illustrated in Fig. 11.

When $I(t)$ is constant, as will be the case at long times after all the transients associated with sample relaxation have died out, Eq. (40) reduces to

$$V(t) \propto \frac{C_{v_1}}{v_1\Gamma(v_1)}t^{v_1} + \frac{Cv_2}{v_2\Gamma(v_2)}t^{v_2} + R[1-\exp(-t/\tau_c)] \tag{41}$$

where τ_c defines the time scale wherein the recap elements (the electrode polarization) affect the $V(t)$ measured for the sample cell containing a conductive solution. If we make the simplifying assumptions that (1) both electrodes of the sample cell have the same (or equivalent) fractal polarization ($v_1 = v_2$; $C_{v_1} = C_{v_2}$); and (2) that there is no dispersion of the conductive solution (sample) in the time window defined by $\tau_c (> t_{\min} = 1/\omega_{\max})$, Eq. (41) can be rewritten in the following way:

$$V(t) = Bt^v + Rt/\tau_c \qquad \text{for } t/\tau_c \ll 1 \tag{42}$$

and

$$V(t) = Bt^v + R \qquad \text{for } t/\tau_c \gg 1 \tag{43}$$

Equations (41) and (42) are particularly useful in illustrating how the contribution of electrode polarization Bt^v should be substracted from $V(t)$.

The voltage $V(t)$ and the current $I(t)$ observed at the sample cell [plate or cylindrical capacity (72, 73)] at the end of a coaxial line are presented by Eqs (23) and (24), respectively. In the case of conductive solutions, Eqs. (23) and (24) show that both the voltage and the current flow are influenced by electrode polarization. The observed voltage $V(t)$ monotonically increases in the TDS time window of observation and the current $I(t)$ monotonically decays. The electrode polarization *correction* is then obtained by subtracting the function Bt^v from $V(t)$. The incident pulse $V_o(t)$ generally is an approximation to a step function with zero long-time slope, and the monotonically increasing behavior of $V(t)$, associated with the correction Bt^v, is a component of the reflected pulse $R(t)$. Since this component is subtracted in Eq. (23) from $R(t)$, it needs to be added $(+Bt^v/Z_o)$ to $I(t)$ in Eq. (24) and only after this can the correction of conductivity contribution by relation (27) be taken into account.

The experimental signal, $V(t)$, for a strong electrolyte solution of NaCl in water at 25°C (adjusted to pH 1.25 with 0.05 M HCl and with a low-frequency conductivity of 1.57 S m^{-1}) is illustrated on a log–log scale in Fig. 12 (71). The TDS multiwindow measurement (38) allow a long-time (up to 10 μs) registration of signal tails, where the signal from a dielectric with low-frequency conductivity has completely relaxed (decayed) and only the signal from the electrode polarization remains. The fractality index v was determined to be 0.785 with $B = 0.593$ by linear regression of the asymptotically linear portion. The fractality is strictly dependent on the electrode material (82), the electrode polishing (71), and the chemistry related to the interactions between aqueous electrolyte and the electrode surfaces.

The electrode polarization correction applicable for TDS measurements of conductive colloidal samples can be summarized in the following way. A refrence sample with an electrolyte composition and conductivity equal to the continuous phase is measured, and these data are subsequently used to fit the parameters v and B (as was illustrated above for the data in Fig. 12; then, as long as the conductivity and electrolyte composition of the continuous phase remain equal to that of the reference, the sample may be measured with the same electrodes. The polarization correction embodied in the v and B obtained earlier is applied by substraction of Bt^v from $V(t)$ and by adding this same function (scaled by Z_0) to $I(t)$. These corrected signals are then Fourier transformed (71) to obtain the resulting dielectric spectra, $\varepsilon'(\omega)$ and $\varepsilon''(\omega)$. In this exposition of the correction procedure we have illustrated the method, focusing upon the polarization properties of a simple two-component electrolyte solution. After correction in this case we are left with the properties of the neat solvent, water.

A comparison between the dielectric spectra of a simple electrolyte solution (pH = 1.25) with and without electrode polarization correction is presented in Fig. 13. The permittivity before and after the correction is illustrated in Fig. 13a. The uncorrected permittivity exhibits an anomalously large value at low

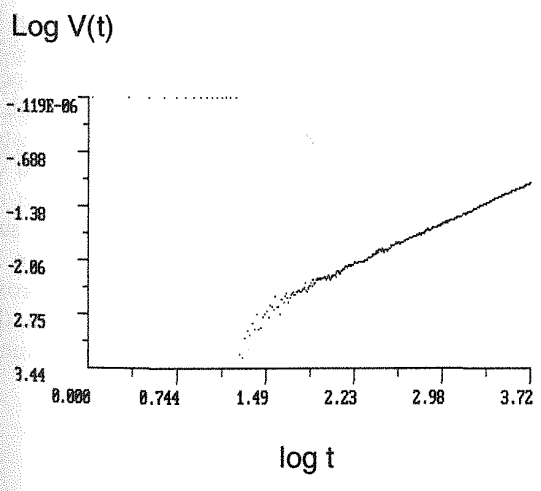

Figure 12 Voltage $V(t)$ applied to the electrolyte solution; $v = 0.785$, $V = 0.593$ (with polished stainless-steel electrodes). (From Ref. 71. With permission from American Physical Society.)

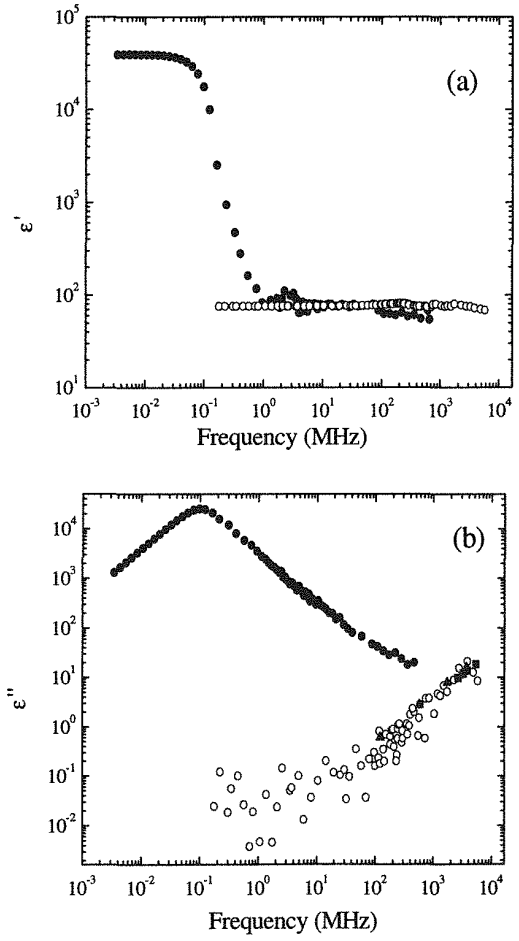

Figure 13 Fractal electrode-polarization correction for dielectric spectrum (a) ε' and (b) ε'' of simple electrolyte solution; 0.1 M NaCl at pH 1.25; ● – uncorrected; ○ – corrected; ▲ – pure water at 20°C (from Ref. 83); ■ – pure water at 25°C. (From Ref. 84.)

frequencies and seemingly undergoes some sort of dispersion process in the 100 kHz to 1 MHz region. This dispersion is highlighted as a peak (at 100 kHz) in the uncorrected dielectric loss spectrum of Fig. 13b. This dispersion essentially completely vanishes after the correction for electrode polarization has been made. The corrected permittivity in Fig. 13a is essentially independent of frequency at about 78. The dielectric loss, after correction for electrode polarization, becomes very small in the 100 kHz–100 MHz range, but shows a steady increase with increasing frequency. This increase is consistent with the well-known dielectric loss maximum of water in the region of 3 to 6 GHz, and compares well with the experimental dielectric loss values for water reported at 20°C (83) and at 25°C (84), and illustrated in Fig. 13b for comparison.

The data derived after the electrode polarization correction are in good agreement with previously published data on water. These data show unequivocally the need for electrode polarization correction at frequencies in excess of 100 MHz, and that such correction can be effected by explicitly considering the fractality of electrode polarization.

D. External Fields

The dielectric properties of a sample may be strongly influenced by its environment, and measurements of the dielectric behavior as a function of, for instance, temperature or pressure (2) are performed on a routine basis. In addition to the temperature and pressure effects, the TDS method also allows for subjecting the samples to externally applied electric or magnetic fields.

1. Electric (High-voltage Measurements)

High electric fields have been used in order to study the effect on W/O emulsions (52). In investigations on liquid crystals, external electric fields are applied in order to ensure the desired orientation of the crystals (85).

The TDS sampling heads are very vulnerable towards high voltages and electric currents. Thus, the signal applied to a sample and consequently recorded by the TDS equipment normally cannot exceed 0.2 V. In order to attain sufficiently high voltages between the electrodes to induce any changes in the sample and, at the same time and through the same line, transmit the low-voltage step pulse used in the characterization of the sample, special equipment has to be used. Thus, a broadband coaxial bias-tee is inserted into the transmission line. The bias-tee is designed so that it will let the fast rise-time pulses pass through with negligible distortion of the waveform, while the high-voltage d.c. is effectively blocked from reaching the part of the transmission line that is connected to the sampling head.

The modifications of the standard experimental set-up needed to include this method are schematically depicted in Fig. 14. A d.c. voltage supply is connected to the coaxial line via a bias-tee (Picosecond Pulse Labs, 5530A), as described above. In this way a potential difference can be applied between the cell electrodes. Owing to the short distance between the electrodes (controlled by the spacer, see Fig. 15) strong electric field result, even from moderate voltages. With a spacer thickness of 120 μm and a potential difference of 60 V, the electric field applied to the sample will be 5 kV/cm. This field strength is sufficiently strong to lead to a marked distortion of the shape of water droplets in an emulsion, and in many cases the electric field induces the coalescence of emulsion droplets. A d.c. block inserted in the line between the bias-tee and the sampling head may be applied as an additional protection of the sampling head from the high voltage; only the step pulse is allowed to travel through. The blocking of a.c. fields is more difficult to accomplish; thus, at present, this method is limited to external d.c. fields.

2. Magnetic Fields

The orientation of a sample (on a molecular or aggregate level) by the action of a magnetic field may be achieved, using a set-up as illustrated in Fig. 16 (86). The dielectric cell shown in Fig. 16a is of the open-ended coaxial sensor type, and the electrical length is found to be 0.027 mm. The magnetic field is created using rod magnets with the magnetic poles placed on either side of the dielectric cell. An alternative set-up used for measuring the sedimentation profile of suspensions containing magnetic particles is shown in Fig. 16b. In this case a magnetic field up to approximately 0.4 T is created by an electromagnet. Also, the dielectric cell is modified in order to increase the functionality of the experimental set-up (Fig. 16b).

IV. DIELECTRIC PROPERTIES OF MICROEMULSIONS

Microemulsions are thermodynamically stable, clear fluids, composed of oil, water, surfactant, and sometimes cosurfactant, that have been widely investigated

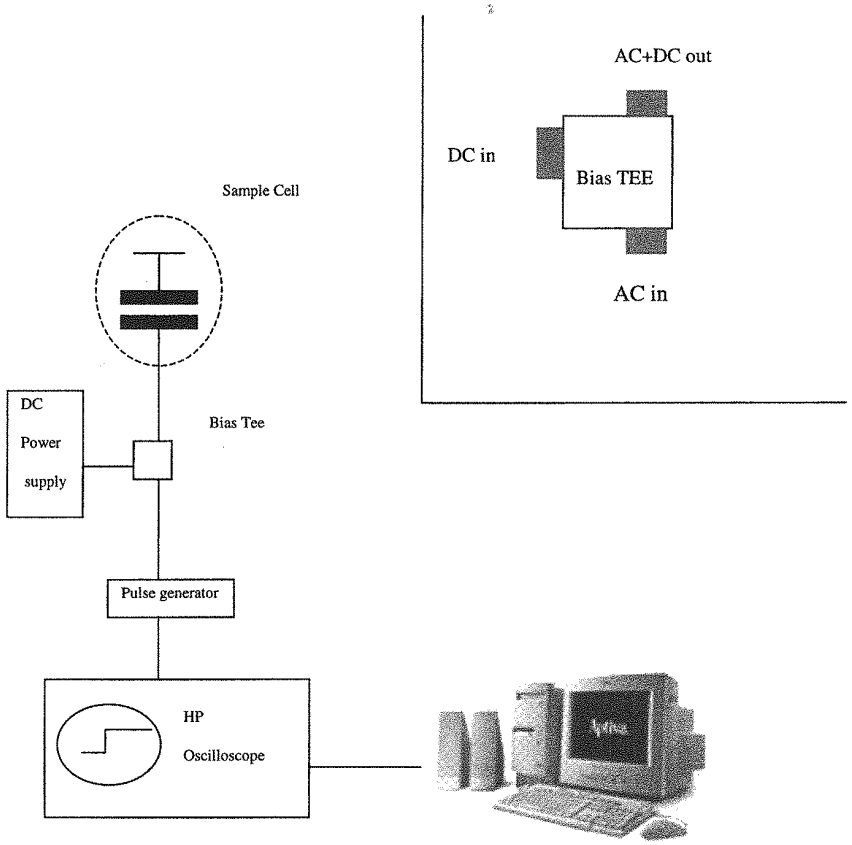

Figure 14 TDS set-up for high external electric field measurements.

during recent years because of their numerous practical applications. The chemical structure of surfactants may be of low molecular weight as well as being polymeric, with nonionic or ionic components (87–90). In the case of an oil-continuous (W/O) microemulsion, at low concentration of the dispersed phase, the structure is that of spherical water droplets surrounded by a monomolecular layer of surfactant molecules whose hydrophobic tails are oriented towards the continuous oil-phase. When the volume fractions of oil and water are both high and comparable, random, bicontinuous structures are expected to form. There are also microemulsions in which the minor component forms disks, sheets, or rods, as well as mixtures, which are microlamellar (89–92). It was found that alcohol added as cosurfactant could affect the solubilization of water in microemulsions (93, 94). The alcohol molecules can reside in both the aqueous and oil phases, and/or in the amphiphilic monolayer at the interface. A clear understanding of the role that the alcohol plays in the organization of the morphology of microemulsions has not yet been obtained and the problem of estimating the amount of alcohol participating at the interface of the microemulsion and in the bulk is not yet completely resolved.

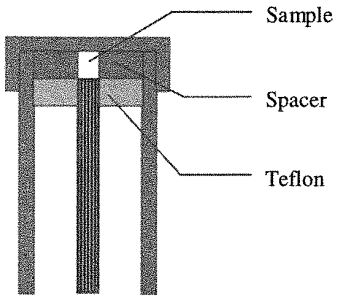

Figure 15 TDS sample cell for high-frequency for high external electric field measurements.

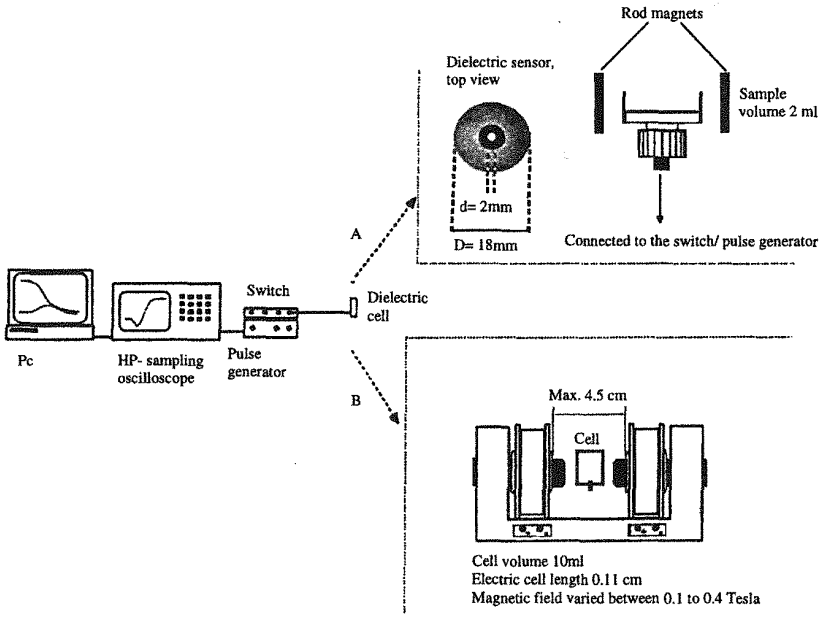

Figure 16 TDS set-up for external magnetic field measurements.

The structure of the microemulsion depends on the interaction between droplets. In the case of repulsive interaction, the collisions of the droplets are short and no overlapping occurs between their interfaces. However, if the interactions are attractive, transient droplet clusters are formed. The number of such clusters increases, when the water fraction, the temperature, the pressure, or the ratio of water to surfactant is increased, leading to a percolation in the system (95–101).

The majority of the different chemical and physical properties, as well as the morphology of microemulsions, is determined mostly by the microBrownian motions of its components. Such motions cover a very wide spectrum of relaxation times ranging from a few picoseconds to tens of seconds. Given the complexity of the chemical make up of the microemulsions, there are many various kinetic units in the system. Depending on their nature, the dynamic processes in the microemulsions can be classified into three types.

The *first type* of relaxation process reflects characteristics inherent to the dynamics of single droplet components. The collective motions of the surfactant molecule head groups at the interface with the water phase can also contribute to relaxation of this type. This type can also be related to various components of the system containing active dipole groups, such as cosurfactant, and bound and free water. The bound water is located near the interface, while "free" water, located more than a few molecule diameters away from the interface, is hardly influenced by the polar or ionic groups. In the case of ionic microemulsions, the relaxation contributions of this type are expected to be related to the various processes associated with the movement of ions and/or surfactant counterions relative to the droplets and their organized clusters and interfaces.

For percolating microemulsions, the *second* and the *third types* of relaxation processes are pertinent, characterizing the collective dynamics in the system and having a *cooperative nature*. The dynamics of the second type may be associated with the transfer of an excitation caused by the transport of electrical charges within the clusters in the percolation region. The relaxation processes of the third type are caused by rearrangements of the clusters and are associated with various types of droplet and cluster motions, such as translations, rotations, collisions, fusion, and fission.

MicroBrownian dynamics of microemulsions can be studied by various techniques including dynamic–mechanical, dielectric, ultrasonic and NMR relaxation, ESR, volume, enthalpy and specific heat relaxation, quasielastic light and neutron scattering, fluorescence-depolarization experiments, and many other methods (90, 102–107). The information thus acquired

provides an opportunity to clarify the organizational structure and the dynamic behavior of such systems.

Dielectric spectroscopy may be successful in providing unique information about the dynamics and structure of microemulsions on various spatial and temporal scales. Being sensitive to percolation, DS is expected to provide unambiguous conclusions concering the stochastic type, the long time scale cooperative dynamics, and the imposed geometric restrictions of molecular motions before, during, and after the percolation threshold in microemulsions. It also can give valuable information about fractal dimensions and sizes of the percolation clusters. On the other hand, an analysis of the dynamics on the short time scale can provide an understanding of the relaxation mechanisms in microemulsions on a geometrical scale of one microdroplet or the dynamics of surfactant or cosurfactant molecules in the interface. This is important, as it can give quantitative information about amounts of alcohol residing both in the interface and in the bulk and thus enables one to calculate the amount of bound water in the system.

The purpose of this chapter is to describe how DS can be applied to the investigation of microemulsions and how information about molecular mobility and structure can be extracted. We will show that an experimentally monitored temperature-dependent increase in ε can be explained by the temperature-dependent growth of the mean-square fluctuation dipole moment of a droplet. Analysis of the dynamic features of the known ionic and nonionic microemulsions on various time and geometrical scales will provide knowledge on both the components of the system and microdroplets as a whole. For instance, by choosing an ionic AOT/water/decane microemulsion near the percolation threshold, we can investigate the cooperative relaxation associated with charge transport in the system. By investigating a series of quaternary oil/surfactant/cosurfactant/water microemulsions prepared with the nonionic surfactants $C_{18:1}(EO)_{10}$ or $C_{12}(EO)_8$, we can calculate the amount of alcohol residing in the interface and in the bulk phases as well as the amount of bound and free water in the system. The bound water is located near the interface and is hydrogen bonded to the hydrophilic head groups of surfactant and alcohol molecules.

A. Dielectric Spectroscopy of Ionic Microemulsions Far Below Percolation

The microemulsions formed with the surfactant, sodium bis(2-ethylhexyl) sulfosuccinate (AOT), water, and oil are widely investigated systems whose dynamics, phase behavior, and structure are well known (87–90). These microemulsions reside in the L_2 phase over a wide temperature range, i.e., the microemulsions consist of nanometer-sized spherical droplets with water in the central core surrounded by a layer of surfactant molecules. In this phase, the surfactant molecules have their hydrophilic head groups facing the water and their hydrophobic tails oriented towards the continuous oil phase. Molecules of AOT can dissociate into anions containing negatively charged head groups, SO_3^-, staying at the interface and positive counterions, Na^+, distribution in the droplet interior. There is a characteristic feature for these systems, such as a small droplet radius, comparable to the thickness of the electric double layer as measured by the Debye length. The thickness of the double layer and the distribution of mobile counterions within it can be calculated from the Poisson–Boltzmann equation (108, 109).

The electrical conductivity and dielectric permittivity of the ionic water-in-oil microemulsions show quite remarkable behavior when the temperature, the water fraction, pressures, or ratio of water to surfactant is varied (95–101). In our prior research (96, 97, 107), the dielectric relaxation, electrical conductivity, and diffusion properties of the ionic microemulsions were investigated in a broad temperature region. In particular, the investigation showed that ionic microemulsions start to exhibit percolation behavior that is manifested by a rapid increase in the static dielectric permittivity ε and electrical conductivity σ when the temperature reaches the percolation onset T_{on} (Fig. 17). The appearance of the percolation reveals that in the region $T > T_{on}$ the droplets from transient clusters. When the system approaches the percolation threshold T_p, the characteristic size of such clusters increases, leading to the observed increase in σ and ε. This increase in the percolation temperature region is governed by scaling laws:

$$\sigma \sim \begin{cases} (T_p - T)^{-s} & T < T_p \\ (T - T_p)^{t} & T > T_p \end{cases} \tag{44}$$

and

$$\varepsilon \sim (T_p - T)^{-s} \qquad T < T_p \tag{45}$$

characterized by critical exponents s and t. Experimentally, the critical exponents are found to have the values $s \approx 1.2$ and $t \approx 1.9$ (96). We define the *percolation onset* as the temperature at which the microemulsion starts to display a scaling behavior for

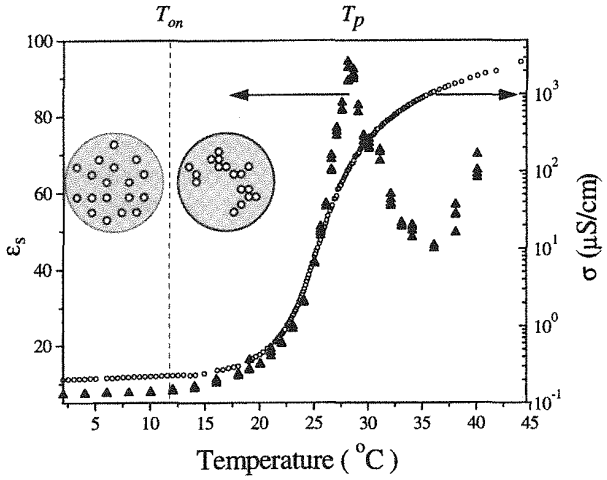

Figure 17 Schematic illustration of the structures and temperature dependence of static dielectric permittivity and conductivity for the AOT–water–decane microemulsion (17.5:21.3:61.2). (From Ref. 5. With permission from Elsevier Science B.V.)

conductivity [Eq. (44)] and for dielectric permittivity [Eq. (45)].

Below the percolation onset, both the conductivity σ and static dielectric permittivity ε of the microemulsions increase as a function of the volume fraction of droplets φ and/or temperature T(95–102). However, this increase is not significantly essential, as it is within the percolation region.

The increase of the conductivity versus temperature and volume fraction of droplets below the percolation onset can be described by the charge-fluctuation model (110, 111). In this model the conductivity is explained by the migration of charged aqueous noninteracting droplets in the electric field. The droplets acquire charges owing to the fluctuating exchange of charged surfactant heads at the droplet interface and the oppositely charged counterions in the droplet interior. The conductivity is then proportional to φ and T:

$$\sigma = \frac{\varepsilon_0 \varepsilon k_B}{2\pi\eta R_d^3} T\varphi \tag{46}$$

where η is the solvent viscosity and R_d is the droplet radius.

Unlike the mechanism of increasing conductivity below the percolation onset as a function of temperature, the temperature behavior of static dielectric permittivity has been hitherto puzzling. The static dielectric permittivity of dipolar liquids ε is proportional to the macroscopic mean-square dipole moment $\langle M^2 \rangle$ of the system unit volume and inversely proportional to the temperature T, as $\varepsilon \sim \langle M^2 \rangle / T$(1). However, the ionic microemulsions exhibit a growth of the dielectric permittivity as a function of temperature in the whole temperature interval.

Given the complexity of the chemical composition of the microemulsions, there are several sources of the dielectric polarization in the system. The contributions are expected to be related to the various processes connected with interfacial polarization, counterion polarization, and the motions of the anionic head groups of the surfactant molecules at the interface with the water phase (39, 96, 97, 112, 113). The contribution in polarization can also be related to various components of the system containing dipole groups, such as bound and free water (114).

The experimentally observed (95–101) increase in the dielectric polarization in the microemulsions in the nonpercolating region can qualitatively be imputed to two mechanisms. The first mechanism attributes the increase in ε below percolation to an aggregation of the spherical droplets with polarizability that is independent of temperature (115). However, an aggregation of droplets seems to be very unlikely at temperature far below the percolation region. An alternative mechanism is related to the temperature dependence of the fluctuation dipole moment of noninteracting and therefore nonaggregating droplets dispersed in oil. In order to provide the experimentally monitored temperature increase in the dielectric permittivity of a monodispersed system consisting of spherical droplets at a constant volume fraction, the value of the mean-square dipole moment $\langle \mu^2 \rangle$ of the droplet must grow faster than the linear function of temperature.

It has been argued that the interaction of the droplets can be modulated by changing the length of the oil chain (116). In light of this, a direct approach to elucidation of the mechanism responsible for the increase in dielectric permittivity would be to investigate the temperature dependence of ε of the microemulsions built up with various oils. An understanding of the mechanisms leading to the temperature dependence of the fluctuation dipole moment, and the development of a model for the dielectric permittivity of ionic microemulsions, is also important since it will provide insight into dielectric polarization and relaxation mechanisms of such systems.

The purpose of this part is to show how the controversy was resolved concering the main mechanism that provides the temperature dependence of the dielectric permittivity in ionic water-in-oil microemul-

sions far below the percolation region. It was shown that dielectric permittivity does not depend on the length of the oil chains and, therefore, aggregation of droplets cannot be responsible for the observed temperature dependence of ε (5, 117).

In order to explain the temperature behavior of ε far below the percolation onset a simple statistical model of polarization of nanometer-sized droplets containing negatively charged ions at the interface and positive counterions distributed in the droplet interior was developed (5, 117). In the framework of this model, when the values of the droplet size and the constant of dissociation of ionic surfactant are both small, an experimentally monitored temperature increase in ε can be explained by the temperature growth of the mean-square fluctuation dipole moment of a droplet.

1. Effect of Oil Chain Length on the Microemulsions

The dependence of static permittivity of the microemulsions as a function of temperature and volume fraction is shown in Fig. 18. This behavior over the measured temperature region can be analyzed in two separate intervals: below the onset of a percolation region T_{on} and above it. At the onset of percolation, the microemulsion starts to display a scaling behavior

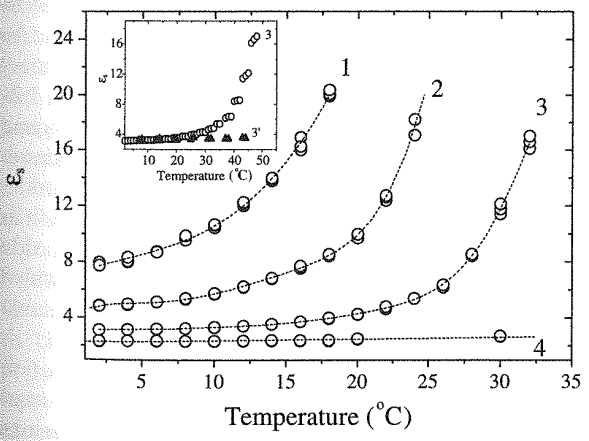

Figure 18 Static dielectric permittivity vs. temperature for the AOT–water–decane microemulsions for various volume fractions ϕ of the dispersed phase: 0.39 (1); 0.26 (2); 0.13 (3); 0.043 (4). In the inset a similar plot for the AOT–water–decane (3, ○) and AOT–water–hexane (3′, σ) microemulsions for $\phi = 0.13$. The value $W =$ [water]/[AOT] is kept constant at 26.3 for all the microemulsions. The lines are drawn as a guide for the eye. (From Ref. 5. With permission from Elsevier Science B.V.)

of conductivity and dieletric permittivity due to droplet aggregation. For the most concentrated microemulsion, $\varphi = 0.38$, a temperature of the percolation onset of $T_{on} \approx 12°C$ was determined (98); this temperature has to be significantly higher for the more diluted microemulsions ($\varphi = 0.26, 0.13$, and 0.043).

In the percolation region ($T > T_{on}$) the main origin of the steep increase in permittivity as a function of temperature (Fig. 17) is the clustering of droplets (29). We estimated (97) that at the onset of the percolation region ($T \approx T_{on}$) on the droplets have a tendency to form small dynamic, weakly bound aggregates consisting of 10 ± 5 droplets. However, far below the percolation onset the ionic microemulsion could be assumed to consist of separated noninteracting water droplets. Thus, the weak increase in ε far below the percolation onset might be explained either by the clustering of droplets or by another "unknown" mechanism. The mechanism should bring about the temperature increase in ε in the system in which the droplets are considered to be separated from one another and noninteracting. The hypothesis that the interaction between droplets increases with the oil chain length (116) can be examined by measuring the permittivity of two microemulsions of identical droplet size but made from different oils. According to the clustering mechanism, the effect of droplet aggregation should be more pronounced (at a given temperature) in a microemulsion containing decane rather than hexane, thus resulting in higher values of ε for the decane-containing microemulsion.

The dielectric measurements performed for the AOT/water/decane and AOT/water/hexane micro emulsions at the volume fraction of the dispersed phase of $\varphi = 0.13$ demonstrate the significant shift of the percolation region to the direction of high temperatures when the oil chain length decreased (Fig. 18) (118, 119). However, the values of ε for both the microemulsions are the same at low temperatures, i.e., below the percolation onset. Thus, those results do not support the hypothesis that the clustering can be responsible for the temperature behavior of the static dielectric permittivity at $T < T_{on}$, and it must be the internal processes within a droplet that determine the behavior of the dielectric polarization in the system.

2. Analysis of the Dielectric Relaxation Behavior Far Below Percolation

In order to ascertain the origins and mechanisms responsible for the observed temperature behavior of the static dielectric permittivity, let us analyze the total

dielectric relaxation behavior of ionic microemulsions. Dynamic aspects of the dielectric polarization can be taken into account by considering the macroscopic dipole correlation function (DCF) $\psi(t)$ in the time domain, or the complex dielectric permittivity $\varepsilon^*(\omega)$ in the frequency domain (38). In the microemulsions, DCF is associated with the relaxation of the entire induced macroscopic fluctuation dipole moment $\overline{M}(t)$, which is equal to the vector sum of all the dipole moments of the system (see Eq. 18).

It was shown (96) that ionic microemulsions exhibit a complex nonexponential behaviour that is strongly dependent on temperature. Far below the percolation onset ($T < T_{on}$) where the microemulsion has a structure of single spherical droplets, the main contribution in the relaxation mechanism comes from the fast relaxation processes with characteristic relaxation times distributed in the range from dozens of picoseconds to a few nanoseconds (96). These processes are inherent to the dynamics of the single droplet components and interfacial polarization. In the percolation region ($T > T_{on}$), transient clusters of droplets are formed as a result of attractive interactions between the droplets. The dielectric dispersion related to the clustering describes the collective dynamics in the system and has a *cooperative character*. The relaxation processes of this type are associated with the transfer of an excitation of a fluctuating dipole moment caused by the transport of electrical charges within the droplets and clusters as well as the rearrangement of the clusters. The characteristic time scale of these processes is within tens and hundreds of nanoseconds (96).

Let us consider the dynamics of microemulsions in the region $T < T_{on}$. The dependence of the macroscopic dipole correlation function $\psi(t)$ for the AOT/water decane microemulsion versus time at different temperatures is presented in Fig. 19. One can see that the dipole correlation function has a complex nonexponential behavior. In the first approximation it can be presented by the formal sum of N Debye relaxation processes as

$$\psi(t) = \sum_{i=1}^{N} A_i \exp(-t/\tau_c) \tag{47}$$

where τ_i are the relaxation times and A_i are the amplitudes of the processes. We note that $\sum_{i=1}^{N} A_i = 1$.

The interpolation of the experimental data was carried out by a least-squares fitting procedure of the DCF values. The most appropriate number of elementary Debye processes involved is determined by the minimum of the standard deviation χ^2. The dielectric

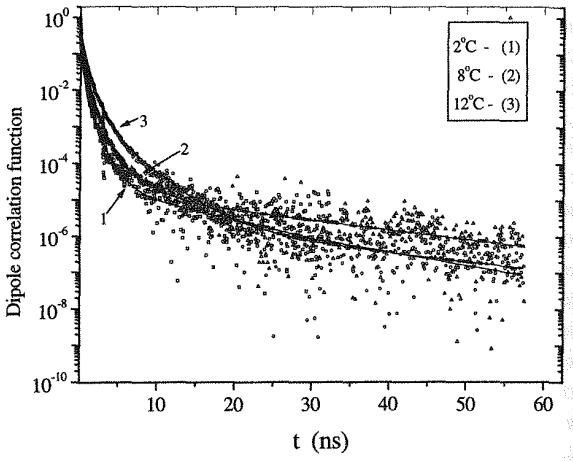

Figure 19 Time dependence of the macroscopic dipole correlation functions for AOT–water–decane microemulsion: $\phi = 0.38$ at $T = 2°C$ (1); $T = 6°C$ (2); and $T = 10°C$ (3). (From Ref. 5. With permission from Elsevier Science B.V.)

response obtained reflects some properties inherent in single particle dynamics. The best-fit curves of the experimental data are reported in Fig. 19 (solid lines) together with the experimental data. In the temperature range 2°–12°C the best fitting gave the four elementary exponential relaxation processes (5).

The longest relaxation process with the characteristic time τ_1 has a very small amplitude ($\sim 2\%$). An experimental value of τ_1 is near 10 ns. The experimental relaxation times τ_2 and τ_3 are within the ranges 1.2–1.6 and 0.2–0.3 ns, respectively. The amplitudes A_2 and A_3 of the second and third relaxation processes increase with the temperature. Since the amplitudes A_2 and A_3 have a similar temperature behavior, it is reasonable to associate them with the same relaxation mechanism. The fourth process seems to be distributed around 50 ps. Its experimental amplitude and relaxation time decrease with the temperature.

In order to understand this complex relaxation behavior of the microemulsions, it is necessary to analyze dielectric information obtained from the various sources of the polarization. For a system containing more than two different phases the interfacial polarization mechanism has to be taken into account. Since the microemulsion is ionic, the dielectric relaxation contributions are related to the movement of surfactant counterions relative to the negatively charged droplet interface. A reorientation of AOT molecules, and of free and bound water molecules, should also be mentioned in the list of polarization mechanisms. In order

to ascertain which mechanism can provide the experimental increase in dielectric permittivity, let us discuss the different contributions.

The contribution from interfacial polarization can be estimated by using one of the shell models (14, 23, 27). On the basis of the Maxwell-Wagner approach, these models describe the dielectric propreties of monodispersed suspension of coated spherical particles dispersed in a continuous medium. In all cases, the assumption that the particle radius is much larger than the Debye screening length is also made. Thus, the Laplace equation is applied in order to describe the electric potential in all three phases (core, shell, and continuous medium). If the dielectric constants and electrical conductivities of the phases are known, the shell models enable us to calculate the interfacial polarization. In particular, when the electrical conductivity of the components is negligibly small, the shell models are reduced to the dielectric mixture models (14, 27, 114, 115). The numerical calculations of the contribution of interfacial polarization to the dielectric permittivity, performed on the basis of various shell models, give similar results for all the models (96, 117). For instance, in the case of the most concentrated microemulsion, the increment of the dielectric permittivity associated with interfacial polarization, determined with the help of various shell models, ranges between 3.4 and 3.7. Note that since the polarization of both water and surfactant is inversely proportional to T, the interfacial polarization will also provide a weak temperature behavior of permittivity which is inversely proportional to T, and thus does not explain the monitored increase in permittivity.

In AOT microemulsions, where the aqueous core of the droplets also contains counterions, a considerable part of the dielectric response to the applied fields originates from the redistribution of the counterions. As mentioned in Sec. II, the counterions near th charged surface can be distributed between the Stern layer and the Gouy–Chapman diffuse double layer (28–31). The distribution of counterions is essentially determined by their concentration and the geometry of the water core. Thus, for very large droplets the diffuse double layer peters out and the polarization can be described by the Schwarz model (32). However, as already mentioned, this approach is more relevant to the dielectric behavior of emulsions than to that of microemulsions.

In the opposite case of very small droplets, AOT-hydrated micelles can be considered. The high-frequency dielectric response of very small AOT reverse micelles has been analyzed (118, 119) at a molar ratio of water to surfactant of $W < 10$. The avrage radius R_w of the water core is related to W by the semiempirical relation $R_w = (1.25\ W + 2.7)$ Å (13, 36). For almost dehydrated reverse micelles $R_w < 5$ Å, one can expect that nearly all the counterions are bound in the surfactant layer structure and immobilized. The dynamics of such a dehydrated system with a characteristic relaxation time of a few nanoseconds has been described in terms of the rotational diffusion of the whole micelle, which represents a nearly rigid structure. On increasing R_w to 15 Å ($W < 10$), an increasing number of AOT ion pairs can achieve sufficient mobility to contribute separately to the dielectric relaxation with a characteristic relaxation time of hundreds of picoseconds. The authors restricted their consideration to the case of small droplets where most of the water and counterions are considered to be bound. They associated the dynamics in the range of hundreds of picoseconds with the rotation of completely hydrated surfactant ion pairs and neglected all bulk diffusion effects of "free" counterions in the double layer. The high-frequency dynamics detected in Refs 35 and 36, with a characteristic relaxation time significantly shorter than 100 ps, were attributed to water relaxation. We note here that the dynamics associated with reorientation of water and surfactant molecules were independent of the droplet size. Therefore, we can assume that the distributed process, found from the fitting, with a characteristic relaxation time τ_4, can be associated with the described mobility of bound water and AOT.

In the intermediate case ($W > 10$), the radius of the droplet is large enough to cause the water molecules to form a pool of free water (120). The rotational diffusion of whole droplets of our microemulsions is expected to be in the range 250–300 ns (96). We did not observe any relaxation with these characteristic times, perhaps because of the very small amplitude ($< 1\%$) of this process. One can expect that in the case of systems with intermediate droplet sizes there can be two contributions to polarization caused by counterions, one stemming from bound counterions in the Ster layer and another one from concentration polarization in the diffuse part of the double layer. It was found from counterion ^{23}Na spin-relaxation measurements that, in the intermediate region of $10 < W < 70$, the diffusion motion of counterions was in fact three dimensional rather than two dimensional (121). In particular, in the case of $W = 26.3$ the magnitude of the relative Na^+ diffusion $D_S/D_0 \approx 0.2$,

where D_S is the diffusion coefficient in the surface layer of the microemulsion and D_0 is the Na^+ bulk diffusion coefficient. The orientation of the fluctuating dipole moment of the droplets caused by the applied electric field is determined by the diffusion of the counterions both along the inner surface of the droplets and along the radial direction of the double layer. The characteristic relaxation time corresponding to the surface diffusion is $\tau_s = R_W^2/2D_s$. By the same token, the characteristic relaxation time for the radical diffusion of counterions can be estimated as $\tau_0 = l_D^2/6D_0$, where l_D is the Debye length. For our microemulsions we can set l_D to be of the order of the radius of a water core $R_w = 37$ Å. Taking D_0 as in the bulk water (2×10^{-5} cm^2/s) and $D_S \approx 0.2D_0 = 0.4 \times 10^{-5}$ cm^2/s gives characteristic diffusion times of 12 and 1 ns for the surface and radial diffusion, respectively. These characteristic times agree with the observed relaxation times τ_1 and τ_2, respectively. Since the amplitude of the longest relaxation process A_1 is very small ($< 2\%$) the process associated with the diffusion along the surface is not essential in the polarization. On the other hand, the amplitudes A_2 and A_3 both increase with the temperature. Thus, we assume that the three-dimensional counterion movement in the diffuse layer is responsible for the temperature rise of static permittivity at $T < T_{on}$. Hence, this diffusion movement yields the experimentally observed second and third relaxation processes.

3. Model of Dielectric Polarization of Ionic Microemulsions

a. Static Permittivity of Ionic Microemulsions

The dielectric permittivity of an ionic microemulsion can be calculated in a general way by treating it as a monodispersed system consisting of spherical water droplets dispersed in the oil medium. In this way the system is considered as a homogeneous specimen consisting of a number of charges and/or dipoles, each of which is described in terms of its displacement from the position of its lowest energy level. The permittivity ε of the system can be derived (1, 5, 117) in terms of the dielectric polarization P and/or the total electric dipole moment M of some macroscopic volume V in the presence of the macroscopic electric field E as

$$\varepsilon - 1 = \frac{4\pi P}{E} = \frac{4\pi M}{VE} \tag{48}$$

For ionic microemulsions the total electric dipole moment M can be represented as a sum of the two contributions. One is associated with the moment, M_E, due to displacements of mobile ions in the diffuse double layer, which follow the laws of statistical mechanics, and another with the moment, M_{mix}, resulting from all other displacements in the mixture (5, 117). As was discussed above, M_{mix} is related to the contributions from various processes of polarization in the microemulsion, which is treated as a heterogeneous sytem of various components.

It was shown (5, 117) that the permittivity ε can be described by the relationship:

$$\frac{(\varepsilon - \varepsilon_{mix})(2\varepsilon + \varepsilon_{mix})(2\varepsilon + \varepsilon_w)}{\varepsilon^2} = \frac{9\varphi\langle\mu^2\rangle}{R_d^3 k_B T} \tag{49}$$

where $\langle\mu^2\rangle$ is the mean-square dipole moment of a droplet, φ is the volume fraction of the droplets, R_d is the radius of the surfactant-coated water droplet, T is the temperature, k_B is the Boltzmann constant, and ε_{mix} is the permittivity due to polarization of the heterogeneous system. Since each droplet consists of a water core surrounded by a surfactant layer in a continuous phase prepared from oil, the effect of the interfacial polarization can be accurately regarded by using a Maxwell-Wagner mixture formula [one-shell model (14)].

Equation (49) establishes a dependence of the permittivity of a microemulsion on the temperature T, volume fraction of droplets φ, and apparent dipole moment of a droplet $\mu_a = (\langle\mu^2\rangle)^{\frac{1}{2}}$.

b. Fluctuating Dipole Moment of a Droplet

For calculation of the mean-square dipole moment of a droplet, $\langle\mu^2\rangle$, the theoretical development is carried out within the framework of the following assumptions (5, 117):

1. The droplets are considered identical and the interaction between them is neglected.
2. A nanodroplet contains N_a *surfactant* molecules, N_s of which are dissociated. Due to electroneutrality the numbers of the negatively charged surfactant molecules, N^-, and the number of positively charged counterions, N^+, are equal, i.e., $N^+ = N^- = N_s$.
3. The ions are treated as point charges.
4. The average spatial distribution of counterions inside the droplets is continuous and governed by the Boltzmann distribution law.
5. All the negatively charged surfactant molecules are assumed to be located in the interface at the spherical plane of radius R_w, corresponding to the radius of the droplet water pool.

In the model a single droplet is described by the spherical coordinate system shown in Fig. 20. The dipole moment of a single droplet is given by

$$\mu = e\sum_{i=1}^{N_s}(\boldsymbol{r}_i^+ - \boldsymbol{r}_i^-) \tag{50}$$

where $\boldsymbol{r}_i^+$ and $\boldsymbol{r}_i^-$ are the radius vectors of the positively charged counterion and negatively charged surfactant head, respectively; e is the magnitude of the ion charge.

The quantity of interest is the mean-square dipole moment $\langle\mu^2\rangle$ of a droplet. It can be expressed in terms of the mean-squared fluctuations of the dipole moment μ by

$$\langle\mu^2\rangle = \langle(\Delta\mu)^2\rangle + \langle\mu\rangle^2 \tag{51}$$

where $\langle(\Delta\mu^2)\rangle = \langle(\mu - \langle\mu\rangle)^2\rangle$. As mentioned above, the mean-square dipole moment of a droplet $\langle\mu^2\rangle$ is calculated in the equilibrium state in the absence of an electric field. In this case the calculation of the electric polarization is retained in the framework of the linear theory of the electric field one can assume a spherical symmetry of the distribution of charges within a droplet. That means $\langle\mu\rangle = 0$. Hence, the apparent dipole moment in the system has a fluctuation ntaure (5), i.e.,

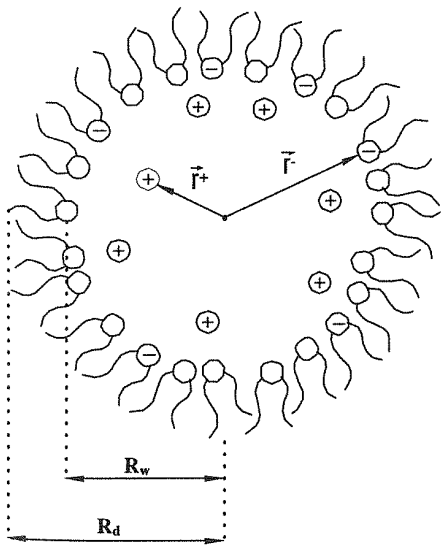

Figure 20 Schematic picture of the spherical water–surfactant droplet. The reference point is chosen at the center of the droplet. The ith ion–counterion pair is represented by radius vectors of ion and counterion, $\boldsymbol{r}_i^+$ and $\boldsymbol{r}_i^-$. (From Ref. 5. With permission from Elsevier Science B.V.)

$$\langle\mu^2\rangle \approx \langle(\Delta\mu)^2\rangle \tag{52}$$

In order to calculate the value of $\langle\mu^2\rangle$, we square the left- and right-hand sides of Eq. (50) and average the result by the ensemble of the realizations of random positions of ions. Retaining the main terms in the quadratic form, we then obtain:

$$\langle(\Delta\mu)^2 \approx e^2\sum_{i=1}^{N_s}\left[\langle(\boldsymbol{r}_i^+)^2\rangle + \langle(\boldsymbol{r}_i^-)^2\rangle\right] \tag{53}$$

A calculation of the terms $\langle(\boldsymbol{r}_i^+)^2\rangle$ and $\langle(\boldsymbol{r}_i^-)^2\rangle$ entering Eq. (53) can be performed by using the one-particle distribution functions $W_1^+(\boldsymbol{r}^+)$ and $W_1^-(\boldsymbol{r})$ that are proportional to the ion density:

$$W_1^+(\boldsymbol{r}^+) = W_1^+(|\boldsymbol{r}^+|) = \frac{1}{N_S}c(r) \tag{54}$$

$$W_1^-(\boldsymbol{r}^-) = \frac{1}{4\pi R_W^2}\delta(|\boldsymbol{r}^-| - R_W) \tag{55}$$

where R_w is the radius of the water core, $c(r)$ is the density of the counterions at the distance $r = |\boldsymbol{r}^+|$ from the center of the droplet, and N_s is the total number of the counterions in the droplet interior:

$$N_s = 4\pi\int_0^{R_W} r^2 c(r)\mathrm{d}r \tag{56}$$

By taking into account Eqs (54) and (55), Eq. (53) reads

$$\langle(\Delta\mu)^2\rangle = e^2\left\{4\pi\int_0^{R_W} r^4 c(r)\mathrm{d}r + N_S R_W^2\right\} \tag{57}$$

According to Eq. (52), relation (57) allows us to calculate the apparent dipole moment $\mu_a = (\langle(\Delta\mu)^2\rangle)^{\frac{1}{2}}$ of a droplet.

The distribution of the counterions in the droplet interior is assumed (27, 122, 123) to be governed by the Poisson–Boltzmann equation:

$$\Delta\Psi = -\frac{4\pi ec(r)}{\varepsilon_w} = -\frac{4\pi ec_0}{\varepsilon_w}\mathrm{e} - \frac{e(\Psi(r) - \Psi(0))}{k} \tag{58}$$

Where Ψ is the electrostatic potential, and ε_w is the dielectric permittivity of the water core. Here, the reference point is chosen at the center ($r = 0$) of the spherical droplet, where the counterion density is c_0 and the electric potential is $\Psi(0)$.

Equation (58) reads in the dimensionless form as

$$\psi'' + \frac{2}{x}\psi' = -e^{-\psi} \tag{59}$$

with the boundary conditions:

$$\psi(0) = 0 \tag{60}$$

and

$$\psi'(0) = 0 \tag{61}$$

where ψ and x are the dimensionless potential $\psi = e[\psi - \psi(0)]/k_B T$ with respect to the center and the dimensionless distance $x = r/l_D$, respectively. Here, the characteristic thickness of the counterion layer near the surface of the water core:

$$l_D = \left(\frac{\varepsilon_w k_B T}{4\pi e^2 c_0}\right)^{1/2} \tag{62}$$

is the Debye screening length.

The Poisson–Boltzmann equation [Eq. (58)] can be solved by numerical integration (5, 123) or by expansion of the potential ψ in the radical coordinate x (117, 122). The theoretical details of the calculations were published elsewhere (117).

It was shown (5, 117) that the total number of the counterions in the droplet interior N_s can be presented in the following way:

$$N_s = 4\pi l_D^3 c_0 \sum_{j=0}^{\infty} \frac{a_j}{2j+3} x_R^{2j+3} \tag{63}$$

where $x_R = R_w/l_D$ and a_j are coefficients of the logarithm of the power series in the Poisson–Boltzmann equation solution. Furthermore, using Eq. (62) and a result for the charge density $c(x)$, the relationship for the mean-square dipole moment $\langle\mu^2\rangle$ of a droplet can be written as follows (117):

$$\langle\mu^2\rangle = 4\varepsilon_w k_B T R_w^3 \sum_{j=0}^{\infty} \frac{a_j(j+2)}{(2j+3)(2j+5)} x_R^{2(j+1)} \tag{64}$$

In order to find the counterion density at the center of a droplet c_0 and entering Eq. (62) for the Debye length l_D, the counterion concentration $c(r)$ must be related to the dissociation of the surfactant molecules in the water core of the droplet. The dissociation of the surfactant molecules is described by the equilibrium relation (122, 123):

$$K_s(T) = c_0 e^{-\Psi\left(\frac{R_0}{D}\right)} \frac{N_s}{N_a - N_s} \tag{65}$$

where N_a is the micelle aggregation number, K_s is the equilibrium dissociation constant of the surfactant, and $\psi(x_R)$ is the dimensionless electrical potential near the surface of the water core (i.e., at $r = R_w$). Substituting $\psi(x_R)$ in Eq. (65) with the logarithm of a power series (124) $\psi(x) = -\ln\sum_{j=0}^{\infty} a_j x^{2j}$ it is possible to obtain:

$$K_S(T) = \frac{c_0 N_S}{N_a - N_S} \sum_{j=0}^{\infty} a_j x_R^{2j} \tag{66}$$

The system of coupled equations [Eqs (63), (64), and (66)], along with the recurrence formula for a_j (119) and Eq. (62) for l_D, constitute the model describing the temperature and geometry dependence of the mean-square dipole moment of the droplet $\langle\mu^2\rangle$. Furthermore, by inserting the calculated values of the mean square dipole moment into Eq. (49), we can obtain the equation:

$$\frac{(\varepsilon - \varepsilon_{mix})(2\varepsilon + \varepsilon_{mix})(2\varepsilon + \varepsilon_w)}{\varepsilon^2} = 36\varphi\varepsilon_w \left(\frac{R_w}{R_d}\right)^3 \sum_{j=0}^{\infty} \frac{a_j(j+2)}{(2j+3)(2j+5)} x_R^{2(j+1)} \tag{67}$$

This enables us to calculate the values of the dielectric permittivity ε of the system.

c. Approximate Relationships for the Fluctuation Dipole Moment of a Droplet and the Permittivity of Ionic Microemulsions

An adequate approximate relationship for the calculation of the mean-square dipole moment $\langle\mu^2\rangle$ in the case of a small droplet and/or the small dissociation of surfactant ($R_w \leq l_D$) can be obtained as a first approximation, by taking into account the first term ($j = 0$) only, in the series of expressions, Eqs (64)–(66). In this approximation, by using the relationship $x_R = R_w/l_D$, and taking into account Eq. (62), we obtain for the mean-square dipole moment:

$$\langle\mu^2\rangle \approx \frac{8\varepsilon_w k_B T R_w^5}{15 l_D} = \frac{32}{15}\pi e^2 c_0 R_w^5 \tag{68}$$

An approximate relationship for the counterion density at the droplet center c_0 can be obtained by using Eqs (63) and (65) in the first approximation, which reads:

$$c_0 \approx \left(\frac{3K_s}{R_w A_s}\right)^{1/2} \tag{69}$$

where $A_s = 4\pi R_w^2/N_a$ is the average area (cm^2/molecule) on the surface of a water core associated with one surfactant molecule. After combining Eqs (68) and (69), the mean-square fluctuation dipole moment of a droplet becomes:

$$\langle \mu^2 \rangle \approx \frac{32\sqrt{3}}{15}\pi e^2 \left(\frac{R_w^9 K_s}{A_s}\right)^{1/2} \tag{70}$$

In order to obtain a tractable relationship for the dielectric permittivity ε, we can further simplify Eq. (49) by taking into account the relative magnitudes of ε, ε_{mix}, and ε_w. For $\varepsilon_w \approx 78$ and $\varepsilon \sim \varepsilon_{mix} \ll \varepsilon_w$, we approximate in Eq. (49) the term $(2\varepsilon + \varepsilon_w)$ by ε_w and $(2\varepsilon + \varepsilon_{mix})$ by 3ε; then, by substituting Eq. (70) into Eq. (49), we obtain:

$$\varepsilon \approx \frac{\varepsilon_{mix}}{1 - X} \tag{71}$$

where

$$X = \frac{32\sqrt{3}\pi\varphi e^2}{5R_d^3 k_B T \varepsilon_w}\left(\frac{R_w^9 K_s}{A_s}\right)^{1/2} \tag{72}$$

It is easy to show that, for small droplet concentrations, $X \ll 1$; thus, an approximate relationship for ε is

$$\varepsilon \approx \varepsilon_{mix}(1 + X) \tag{73}$$

In order to explain the experimental temperature behavior of the dielectric permittivity of the system we have to consider the temperature behavior of the dissociation constant of the surfactant K_s, which has an Arrhenius behavior (108):

$$K_s(T) = K_0 \exp\left(-\frac{\Delta H}{k_B T}\right) \tag{74}$$

where ΔH is the apparent activation energy of dissociation of the surfactant in the water pool of a droplet, and K_0 is the pre-exponential factor. It is easy to show that the permittivity of microemulsions obtained from Eq. (71) or (73) for the Arrhenius behavior of the dissociation constant is the growing function of temperature in the temperature range $T < \frac{\Delta H}{2k_B}$. This is always fulfilled in the measured temperature interval for any reasonable value of the activation energy.

For numerical evaluations of the model we have to set the values of the parameters matching the studied systems. The value of the dielectric permittivity of water was assumed to be equal to that of bulk water at the corresponding temperature throughout all the calculations, i.e., $\varepsilon_w = 87.74 - 0.40008t + 9.398 \times 10^{-4}t^2 - 1.41 \times 10^{-6}t^3$ (83), where t is the temperature in degrees Celsius. The value of 2 for the dielectric permittivity of decane was adopted in the present calculations. The effective value of 8.5 was used (125) for the dielectric permittivity of AOT. The value of ε_{mix} was calculated by using the one-shell model (14). The aggregation number N_a was estimated to be 244 molecules per droplet. The value of $A_s = 65$ Å^2 was adopted for the average area on the surface of the water core associated with one AOT molecule (115).

Note that the developed model can only be applied within the special ranges of the droplet radius and ionic dissociation of the surfactant. From one side, the droplets cannot be too small. The radius of the water core must be larger than 15 Å (water-to-surfactant ratio $W > 10$) to ensure that a core of "free" water exists (118). On the other hand, the droplets cannot be too large, since the applicability range of the solution Eq. (68) is restricted by the condition $R_w < 3.27 l_D$. This condition may also be expressed in terms of the strength of the electrolyte in the droplet interior pK_s ($pK_s \equiv -\log K_s$) and/or by the degree of dissociation of surfactant $\alpha = N_s/N_a$ (5, 119). Regarding K_s of the surfactant AOT, little is known and we did not find any reliable experimental data for it in the literature. Thus, K_s can be considered as an adjustable parameter of the theory which can be calculated from the inverse problem, i.e., we can determine K_s from a knowledge of the experimentally measured permittivity of the studied microemulsions. The equilibrium dissociation constant K_s can be calculated by using Eqs (62), (66), and (67) or, in the case of small droplets and/or a low degree of surfactant dissociation, by the approximate equation (71).

Figure 21 compares the values of the experimental apparent dipole moment μ_a of the studied microemulsions, obtained from Eq. (49), together with the theoretical values obtained on the basis of Eq. (67). One can see that the apparent dipole moment $\mu_a = (\langle \mu^2 \rangle)^{1/2}$ of the microemulsions increases versus temperature. For all the microemulsions studied the magnitude of the dipole moments for various volume fractions φ of the dispersed phase does not depend on φ within a degree of accuracy better than 10%, which confirms the assumption of the model that droplets in the system can be considered as noninteracting for such concentrations of droplets.

As a final comment, let us briefly discuss the permittivity of the studied microemulsions. Figure 22 shows the temperature dependencies of the experimental permittivity and the results of the calculations on the basis of the developed model performed by using Eqs (67) and (71). The difference between the values of ε obtained from these formulas can only be observed at high φ. The calculated values of ε agree well with the experimental data in the region far below the onset

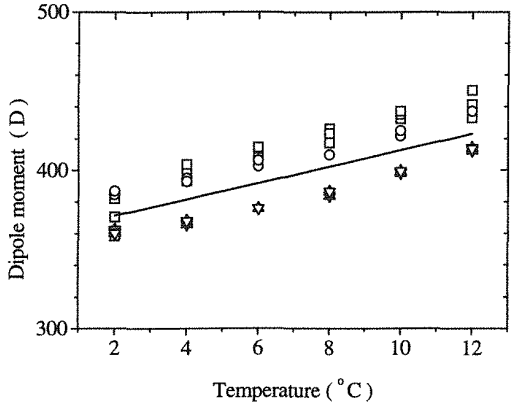

Figure 21 Temperature dependence of experimental [and calculated on the basis of Eq. (64)] macroscopic apparent dipole moments of a droplet of the AOT/water/decane microemulsions. Experimental values for the dipole moment are shown for various volume fractions ϕ of the dispersed phase: 0.043 (□ ; 0.13 (○); 0.26 (Δ); and 0.39 (▽). Calculated values are shown by the solid line. (From Ref. 5. With permission from Elsevier Science B.V.)

of percolation ($T < T_{on}$), where the assumptions of the model are fulfilled. At temperatures close to the percolation onset T_{on} and beyond it, deviations in the theoretical values from experimental data are observed. These deviations indicate the structural changes in the system that appear at percolation.

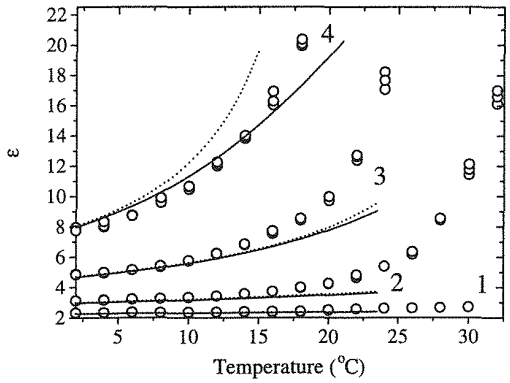

Figure 22 Experimental (○) and calculated static dielectric permittivity vs. temperature for the AOT–water–decane microemulsions for various volume fractions ϕ of the dispersed phase: 0.39 (curve 1); 0.26 (curve 2); 0.13 (curve 3); 0.043 (curve 4). The calculations were performed by using the formulas: Eqs. (67) and (71) (dashed line). (From Ref. 117. With permission from American Physical Society.)

B. Dielectric Properties of Ionic Microemulsions at Percolation

A percolation phenomenon was found in ionic microemulsion droplets when the water fraction, the temperature, the pressure, the strength of the electric field, or the ratio of water to the surfactant was varied (95–98, 101). Basically, the percolation behavior is manifested by the rapid increase in electrical conductivity σ and static dielectric permittivity ε as the system approaches the percolation threshold (Fig. 17).

The dielectric-relaxation properties in sodium bis(2-ethylhexyl) sulfosuccinate (AOT)/water/decane microemulsion near the percolation temperature threshold have been investigated in a broad temperature region (96, 97, 107). It was found that the system exhibits a complex nonexponential relaxation behavior that is strongly temperature dependent. The time–decay behavior of the dipole correlation function of the system $\Psi(t)$ was deconvoluted into normal modes and represented as a sum of a few Kohlrausch–Williams–Watts (KWW) terms, $\exp[-(t/\tau_M)^V]$, each with characteristic macroscopic relaxation times, τ_M, and stretched exponents, v, respectively (96). It was shown that, in the percolation region, transient clusters of a fractal nature are formed because of attractive interactions between droplets. An interpretation of the results was carried out in the framework of the dynamic percolation model (126). According to this model, near the percolation threshold, in addition *to the fast relaxation* related to the dynamics of droplet components, there are at least two much longer characteristic time scales. The *longest process* has characteristic relaxation times greater than a few microseconds and should be associated with the rearrangements of the typical percolation cluster. The temporal window of the intermediate process is a function of temperature. This *intermediate process* reflects the *cooperative relaxation phenomenon* associated with the transport of charge carriers along the percolation cluster (126–128).

For a description of the mechanism of cooperative relaxation, Klafter, Blumen, and Shlesinger (KBS) (129, 130) considered a transfer of the excitation of donor molecule to the acceptor molecule through many parallel channels in various condensed media. The KBS theory might be modified for describing the process of the charge transfer in colliding droplets forming a cluster and giving rise to the relaxation of the entire fluctuation dipole moment. The normalized decay function $\alpha(t)$ in the microemulsions is associated with the relaxation of the entire induced macroscopic

fluctuation dipole moment $\overline{M}(t)$ of the sample of unit volume, which is equal to the vector sum of all the fluctuation dipole moments of droplets.

The relaxation of the fluctuational dipole moment of a droplet is related to the transfer of the excessive charge (excitation) within two colliding droplets from a charged droplet (donor in the KBS model) to a neutral droplet (acceptor). The theoretical details of the model has been published elsewhere (97). This model of cooperative relaxation can be applied to fractal media such as the ionic microemulsion represented in the percolation region.

In the framework of the theory of cooperative relaxation in fractal media it is shown (97) that the macroscopic dipole correlation function $\psi(t)$ of the system is given by

$$\Psi(t) = \exp\left\{\Gamma\left[g\left(\frac{t}{\tau}\right)N, k, v\right]\left(\frac{t}{\tau}\right)^{v} + B(v)\left(\frac{t}{\tau}\right)\right\} \qquad (75)$$

where the coefficient $\Gamma[g(t/\tau), N, k, v]$ depends on the microscopic relaxation function $g(t/\tau)$ describing the elementary act of a charge transfer along the percolation cluster on the scaling parameters k, characterizing the type of the fractal similarity, and on the number of stages of self-similarity of the clusters N (Fig. 23). The τ is the microscale relaxation time describing the charge transfer between two neighboring droplets. The coefficient $B(v)$ is a correction for the KWW function at large times. The parameter v in Eq. (75) characterizes the cooperative dynamics and structure of the fractal clusters. The relationship between the exponent v and the fractal dimension D_f is given by $D_f = 3v$ (97).

As noted above, the dynamical processes in microemulsions can be classified into three types. The first type of relaxation process reflects characteristics inherent to the dynamics of the single-droplet components. The second and third types of relaxation processes characterize the collective dynamics in the system and have a cooperative nature.

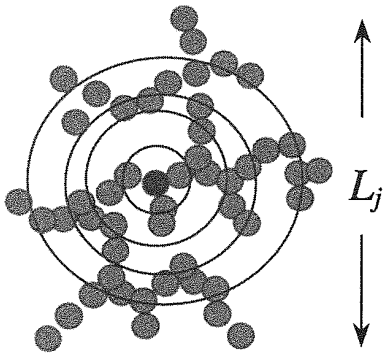

Figure 23 Schematic picture of the excitation transfer via parallel relaxation channels in the fractal cluster of droplets in the percolating microemulsions.

A detailed analysis and estimations of the relaxation-time values show (5, 96) the following hierarchy of processes on the time scale: the relaxation processes of the first type τ_1 are the fastest, with an order of hundreds of picoseconds, when compared with the time τ_c, needed to "explore" the cluster and with the rearrangement time, τ_R. The rearrangements occur on timescales of microseconds (128) and are considered the slowest process. The intermediate process ($\tau_1 < \tau_c < \tau_R$), relating to the cooperative transport of charge carriers along the clusters, has a temporal window depending on temperature. The minimal time boundary is of the order of hundreds of picoseconds, whereas the maximal time boundary has a value of tens of nanoseconds at the beginning of the percolation region and reaches 700 ns at T_p. All these contribute to a complex behavior of the dielectric correlation function. We can suppose, therefore, that near the percolation threshold the main contribution to the dynamics results from the cooperative effect related to the transfer of charge carriers along the percolation clusters, as given by Eq. (75).

The typical decay behavior of the dipole correlation function of the microemulsion in the percolation region is presented at Fig. 24. Figure 25 shows the temperature dependence of the effective relaxation time, τ_{eff}, defined within the fractal parameters, and corresponding to the macroscopic relaxation time τ_M of the KWW model. In the percolation threshold T_p, the τ_{eff} exhibits a maximum and reflects the well-known *critical slowing down* effect (131).

The stretched exponent v depends essentially on the temperature (Fig. 26). At 14°C, v has a value of 0.5. However, when the temperature approaches the percolation threshold $T_p = 27$°C, v reaches its maximum value of 0.8, with an error margin of less than 0.1. Such rapid decay of the KWW function at the percolation threshold reflects the increase of the cooperative effect of the relaxation in the system. At temperatures above the T_p, the value of the stretched exponent v decreases, and indicates that the relaxation slows down in the interval 28°–34°C. At temperatures above 34°C, the increase in v with the rise in temperature suggests that the system undergoes a structural modification. Such a change implies a transformation from an L_2 phase to lamellar or bicontinuous phases (132, 133). On the other hand, the temperature beha-

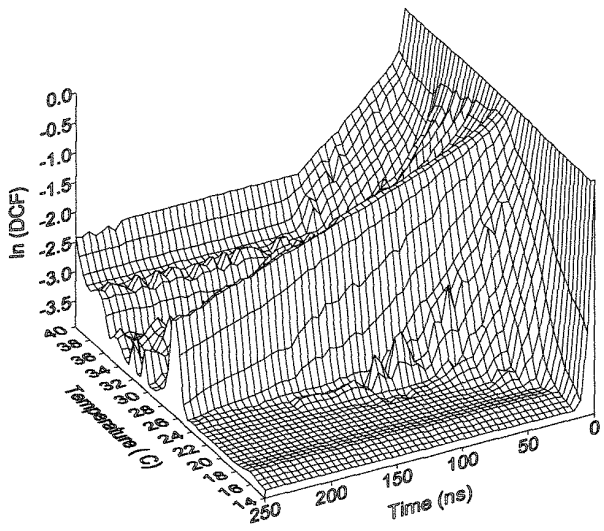

Figure 24 Three-dimensional plots of time and temperature dependence of the macroscopic dipole correlation function for the AOT–water-decane microemulsion. (From Ref. 97. With permission from American Physical Society.)

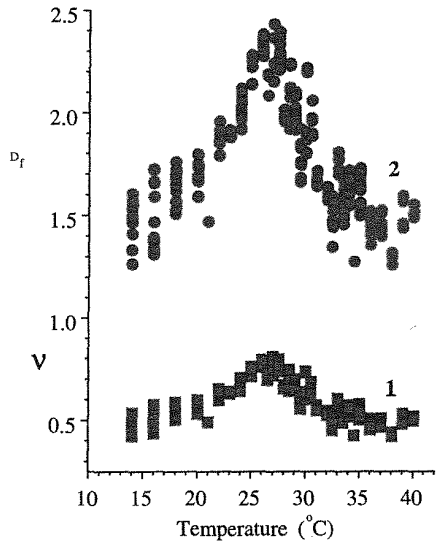

Figure 26 Temperature dependence of the stretching parameter v (□) and fractal dimension D_f (O). (From Ref. 97. With permission from American Physical Society.)

vior of the fractal dimension D_f (Fig. 26) shows that below the percolation threshold $D_f < 2$. This corresponds to a system of small clusters dispersed in space and can be described by the model of unbounded fractal sets with a D_f of less than 2 (134, 135).

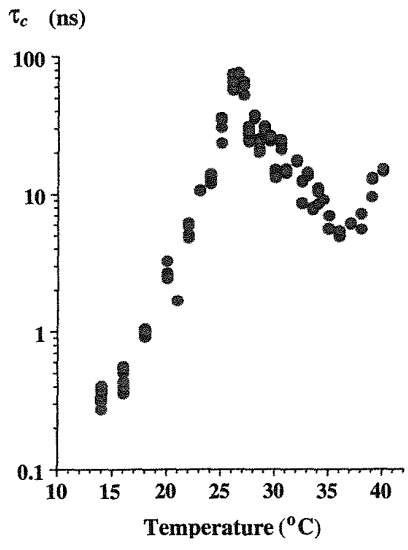

Figure 25 Temperature dependence of the macroscopic effective relaxation time τ_{eff}. (From Ref. 97. With permission from American Physical Society.)

At the percolation threshold $D_f = 2.4 \pm 0.2$, satisfactorily concurring with the literature value of 2.5 (136). Above the percolation threshold D_f decreases, which can be explained by reorganizations of the system with corresponding structural changes. A structural modification of the system at temperatures above 34°C and the appearance of more prolonged and/or ordered regions in the microemulsion leads to a new observable increase in D_f.

It was shown that the effective length of the clusters increases sharply (97, 136) and diverges in the percolation threshold in accordance with the percolation scaling law $L_N \sim (T - T_p) - v_g$ where v_g is the geometrical exponent (131). However, dispersion of the data obtained from the fitting does not enable one to estimate precisely a critical exponent v_g of this growth.

The typical number of droplets S in the aggregates may be estimated according to the relationship given by

$$S \sim (L_N/d_{drop})^{1/D_f} \tag{76}$$

where d_{drop} is the diameter of the surfactant-coated water droplet, estimated to be 100 Å. The temperature dependence of the number of droplets in the typical fractal cluster S is presented in Fig. 27.

Analysis of the temperature behavior of the calculated parameters shows that at the onset of the percolation region the droplets have a tendency to form

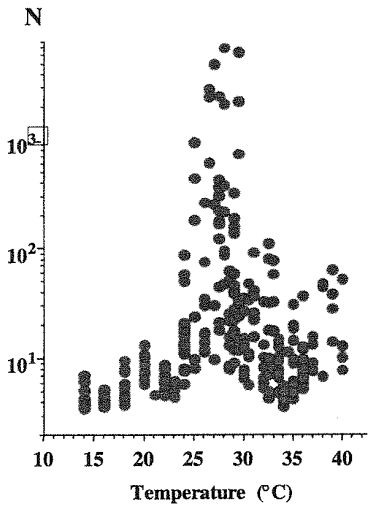

Figure 27 Temperature dependence of the number of droplets in a typical percolation cluster. (From Ref. 97. With permission from American Physical Society.)

small dynamic aggregates consisting of 10 ± 5 droplets that are weakly bound. The characteristic length of such aggregates changes in the interval $L_N \sim 600-1000$ Å. The fractal dimension at these temperatures has a value of less than 2, indicating that the aggregates are surrounded by empty spaces, i.e., separated from another. We note that each of these aggregates participates in the relaxation as independent objects with no correlation between them. At the percolation threshold, the aggregates tend to form a large percolation cluster, which participates in the cooperative relaxation as a whole object.

The fractal model described above enables us to relate the characteristics of a total cooperative macroscopic relaxation function with the parameters of the fractal medium (fractal dimension D_f and the degree of the development of fractality which is expressed by the number of self-similarity stages N). Herewith, the fractal medium has been represented by the single "effective" self-similar geometric structure. The recursive model neither describes the cluster polydispersity (cluster size distribution), nor the relaxation of the individual cluster. Therefore, it is expedient to use the complementary model in order to estimate cluster statistics and dynamics in more detail. Such a model might be developed in the framework of the general statistical description. In this description, the DCF of a complex system is represented as a result of averaging of the dynamic relaxation functions corresponding to the different random *states* of the system (99, 137):

$$\Psi(t, s_m) = \int G(t, s) W(s, s_m) ds \tag{77}$$

where $W(s, s_m)$ is the state probability density distribution function for the state variable s, depending on the effective maximal scale s_m, and $G(t, s)$ is the dynamic relaxation function in state s. The integration in Eq. (77) is performed over all possible states of the system.

For the percolation case, the function $W(s, s_m)$ was taken in the form of the "generalized exponential distribution" or "main statistical distribution" as follows (138–140):

$$W(s) \sim s^{\gamma} \exp[(s/s_m)]^{\eta} \tag{78}$$

where γ is the polydispersity index, $s_m \gg 1$ is the cut-off cluster size, and $\eta > 0$ is the cut-off rate index. The numerical values of these parameters depend on the distance from the percolation threshold. Above the percolation threshold, i.e., at $u > 0$, the function $W(s)$ describes the size distribution of all clusters except for the infinite cluster. In the continuum limit, the function $W(s)$ is the cluster size probability density distribution function. Herewith, the state variable s is just the cluster size (number of monomers in the cluster). The form of $G(t, s)$ was chosen with the help of the hypothesis of dynamical scaling as $G(t, s) = \exp[-t/\tau(s)]$, where $\tau(s) = \tau_1 \cdot s^{\alpha}$, τ_1 is the minimal time associated with the monomer relaxation, and the parameter α is the scaling index establishing a correspondence between the size of a cluster and its relaxation time. The tentative application (140) of the statistical fractal model validated the usefulness of the statistical approach. The treatment performed on the experimental data suggested that the polydispersity index, the dynamic scaling exponent, and the σ exponent are not universal quantities and that they might depend on the specific interactions in the system. Further development of that approach will give an effective tool for investigation of the polydispersity index, the dynamic scaling exponent, and other structural and dynamical parameters of microemulsions in percolation.

C. Dielectric Properties of Nonionic Microemulsions

Analysis of the dynamics on short time scales can unravel the nature of the relaxation processes and provide information about the partition of the water and alcohol between bulk and interface. It was shown

(141–143) that nonionic microemulsions usually have a very complicated dielectric behavior. From the Cole–Cole plot, for example, Fig. 28, it can be seen that the complete dielectric spectrum cannot be described by a single relaxation process. The wide nonuniform time window used (38) allows one to deconvolute the relaxation spectrum to distinguish three or four relaxation processes (dependent on water content and temperature) distributed in the interval between 10^{-11} and 10^{-9} s. Given the complexity of the chemistry of microemulsions, a precise interpretation of the dielectric relaxation mode is difficult. Dielectric relaxation contributions in such systems are expected to be related to bound and free water, alcohol molecules, and active dipole groups belonging to the surfactant molecules and associates.

1. Evaluation of the Amount of Alcohol at the Interface

Two main dielectric relaxation processes can be considered in nonionic microemulsions. The longest one, with characteristic time changes between 1 and 2 ns down to hundreds of picoseconds with increasing water content in the system, and the shorter relaxation rpocess that is characterized by time changes from 100 ps down to dozens of picoseconds. The long-term behavior has been correlated with the self-associated state of the alcohol and associated with the break-up of linear alcohol complexes. The relaxation time is related to relaxation of the alcohol in microemulsions at various water contents and can be juxtaposed with that of oil–alcohol mixtures for various concentrations of alcohol in the system.

The two relaxation processes were evaluated both for the alcohol/dodecane mixtures (Fig. 29) and for the microemulsions (Fig. 30). In order to understand the way to calculate the amount of alcohol at the interface and in the oil phase, let us first analyze the alcohol/dodecane binary mixture.

a. The Alcohol/Dodecane Binary Mixture

In such mixtures the long relaxation time τ_1 increases with increasing concentration of butanol in dodecane (Fig. 29a). In other words, diluting butanol with oil leads to a long relaxation-time reduction. The decrease in τ_1 with the oil concentration is in good agreement with the literature (144–146). On the other hand, the short relaxation time τ_2 is hardly affected by the presence of dodecane. The same behavior between the alcohol concentration and the relaxation times was detected in a pentanol/dodecane mixture (Fig. 29b).

Aliphatic alcohols are known to be strongly associated polar liquids. Alcohol molecules in the liquid

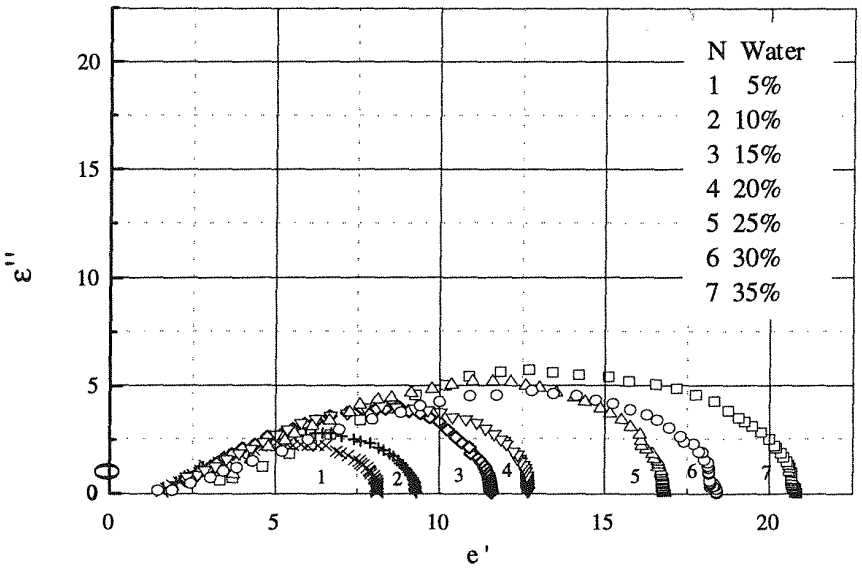

Figure 28 Cole–Cole diagram for seven mixtures of W/O dodecane/butanol/Brij 97/water microemulsions at 20°C for various water contents: 5% (1); 10% (2); 15% (3); 20% (4); 25% (5); 30% (6); 35% (7). (From Ref. 143. With permission from Elsevier Science.)

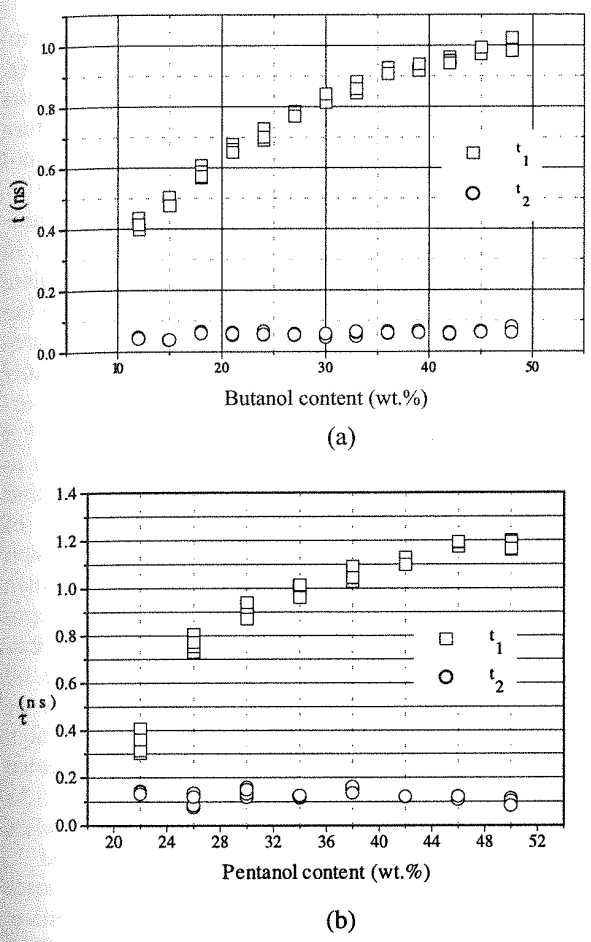

Figure 29 Dielectric relaxation times of dodecane/alcohol mixtures at 10°C for different alcohol contents (a) dodecane/butanol; (b) dodecane/pentanol. (From Ref. 141. With permission from Elsevier Science.)

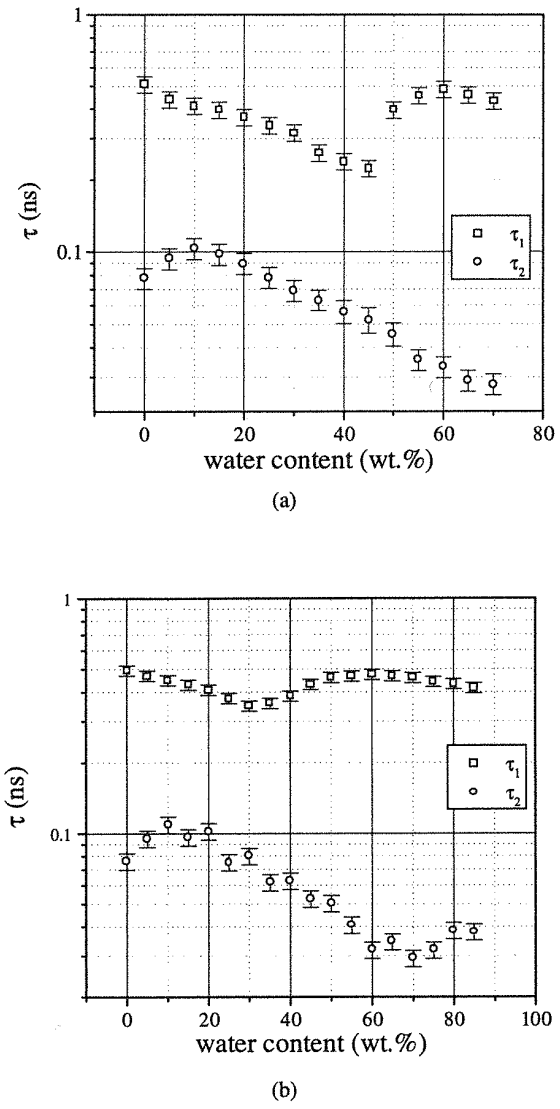

Figure 30 Dielectric relaxation times at 10°C of (a) dodecane/butanol/Brij 97/water microemulsion (system 1) and (b) dodecane/pentanol/$C_{12}(EO)_8$/water microemulsions (system 2), for different water contents. (From Ref. 141. With permission from Elsevier Science.)

phase are linked into oligomer chains by intermolecular hydrogen bonds (H-bonds) (147–149). The alcohol molecules are able to rotate around the H-bonds, resulting in the associated species existing mainly in the convoluted form. In the general case, rotation around the H-bonds is partially hindered, and the longer the hydrocarbon radical, the stronger is the hindering.

As the nonpolar dodecane is dispersed in the alcohol medium, the alcohol chains are disrupted and broken into smaller clusters. As more dodecane is introduced into the mixture, alcohol complexes become smaller until the alcohol appears as monomers, i.e., nonclustered alcohol (144–146).

The long dielectric relaxation process (presented here by τ_1) has been correlated with the self-associated state of the alcohols. It is caused by a cooperative relaxation of the average dipole moment of the whole alcohol aggregate in the pure alcohol or in the alcohol/dodecane mixture (148). Therefore, the long relaxation process will exist only in the presence of alcohol aggregates. It was shown (149) that the long relaxation time

of the alcohol is related to the average number of monomers in the alcohol cluster n, and to the relaxation time of the alcohol monomers' isotropic rotation τ' by the relation:

$$\tau = 6n\tau' \tag{79}$$

As a result of adding the hydrocarbon, smaller units of alcohol aggregate are created, and according to Eq. (79) this will lead to a decrease of the long relaxation time τ_1.

The short dielectric relaxation process (presented here by τ_2) is associated with the anisotropic motion of the monomer alcohol species in a chain cluster (149). In microemulsions, the short process is the superposition of several dielectric relaxation processes, which have similar relaxation times such as movement or rotation of the alcohol monomers, hydrate water, and surfactant polar head groups. The short relaxation time is barely affected by the alcohol concentration in the mixture since it is less sensitive to the aggregation process.

b. The Microemulsion Systems

As previously discussed, the alcohol in the studied microemulsion is located in the oil phase or in the water aggregate's interfacial film. Thus, the continuous phase of the microemulsion is actually an alcohol/dodecane binary mixture (neglecting a very small amount of water). Since the alcohol located at the interface exists as monomers, the long relaxation time observed in the microemulsion is associated with an alcohol aggregate that is only present in the continuous phase with the dodecane. In Fig. 30 it can be seen, both for Brij 97 and the C_{12} $(EO)_8$ systems, that in the range of the L_2 phase (0–50% of water), as water is added to the microemulsion, the long relaxation time τ_1 decreases. This phenomenon can be explained as follows: as more water is introduced into the system some of the alcohol (butanol or pentanol) migrates from the continuous oil phase to the interface. As mentioned above, when the alcohol concentration in the dodecane phase decreases, the alcohol clusters became smaller, reflected by a reduction of the long relaxation time. The same phenomenon of decreasing the long relaxation time with increasing water content was observed in systems containing Brij 97 with butanol as cosurfactant (Fig. 30a) and C_{12} $(EO)_8$ with pentanol as cosurfactant (Fig. 30b).

The average association number n of the alcohol molecules is determined by the alcohol concentration in the oil. The dependence of the association number n of butanol and pentanol as a function of the alcohol concentration in binary mixtures is presented in Fig. 31. The association number was calculated from the long dielectric relaxation time of the binary mixture using Eq. (77) and taking τ' as 7.1 ps for butanol and 10.4 ps for pentanol (146).

The oil phase of the microemulsion can be considered as a binary mixture of dodecane and alcohol. In this case, by using Eq. (79), it is possible to calculate the association number of the alcohol molecules in the oil phase from the long relaxation time of the microemulsion (Fig. 32). For the $C_{12}(EO)_8$/water/dodecane/pentanol microemulsions the association number varies in the range from 4 to 6 (Fig. 32a). From Fig. 31 it can be seen that these n values are in the range of 21 to 24% of pentanol in dodecane. Thus, we estimate that the pentanol concentration in the oil phase of $C_{12}(EO)_8$/water/dodecane/pentanol microemulsion decreases just slightly in the range (21–24%) when water is added. Since the total amount of each component in the microemulsion is known, it is easy to calculate the partition of the alcohol between the oil phase and the interface. From such calculations we can evaluate that, for the microemulsions with high water content (60%), 70% of the pentanol is located at the interface and 30% is dissolved in the oil. As mentioned before, this ratio changes slightly when the water content in the microemulsion is changed.

Adding water to the microemulsion can in some cases cause an inversion from the L_2 to the L_1 phase.

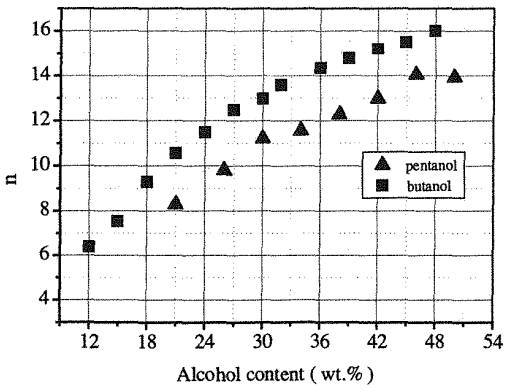

Figure 31 Association number n at 10°C, of alcohol molecules vs. its concentration in alcohol/dodecane mixtures. The association number was calculated from the long dielectric relaxation time of the binary mixture using Eq. (77). (■) Butanol/dodecane; (▲) pentanol/dodecane. (From Ref. 141. With permission from Elsevier Science.)

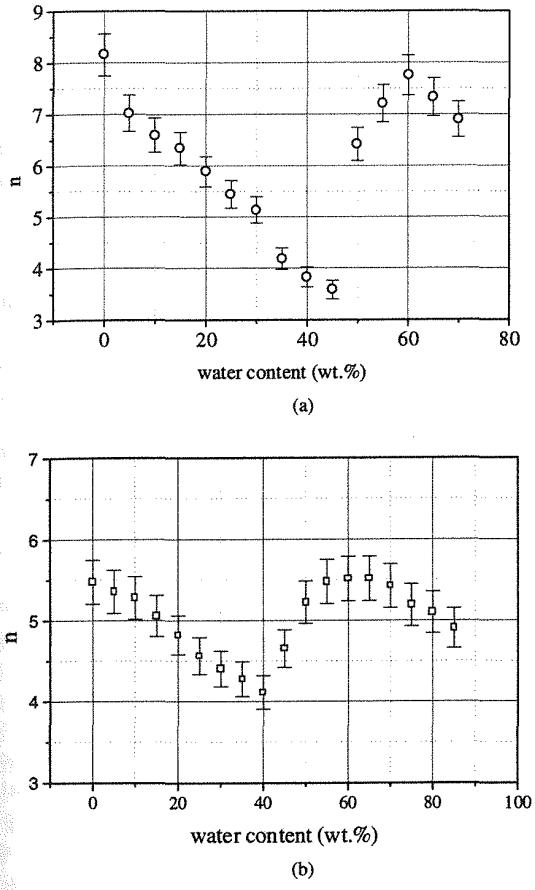

Figure 32 Association number n at 10°C, of alcohol molecules in the oil phase of the microemulsions with different water contents. The association number was calculated from the long dielectric relaxation time of microemulsions. (a) (System 1)dodecane/butanol/Brij 97/water microemulsions; (b) (system 2) dodecane/pentanol/$C_{12}(EO)_8$/water microemulsions. (From Ref. 141. With permission from Elsevier Science.)

In our system the inversion was found to be in the range 45–60 wt % water. In Fig. 32 it can be seen that the dielectric long relaxation process τ_1 and the association number n increase abruptly at 50% water concentration. This "kink" is more evident in the Brij 97–butanol system. It is reasonable to believe that this kink, which occurs in the inversion area, is due to expulsion of part of the alcohol from the interface to the oil phase. As it happens, the concentration of the alcohol in the oil phase increases and the long relaxation time increases. Hence, the inversion can be detected by the TDS method.

2. Evaluation of the Amount of Bound Water in Microemulsions

Information about the bound water fraction in some colloid systems, silica gels, and biological systems is usually inferred on the basis of the frequency- and time-domain DS measurements from the analysis of the dielectric decrements or the relaxation times (64, 150–152). However, the nonionic microemulsions are characterized by a broad relaxation spectrum as can be seen from the Cole–Cole plot (Fig. 33). Thus, these dielectric methods fail because of the difficulties of deconvoluting the relaxation processes associated with the relaxations of bound water and surfactant occurring in the same frequency window.

In microwave dielectric measurements (>30 GHz) the dielectric permittivity and dielectric losses for bound and free water show significantly different magnitudes. Thus, in measurements at high microwave frequencies the contribution from bound water in the dielectric losses will be negligibly small, and the contribution from the free water fraction can be found. In contrast to the above-mentioned procedures used for calculation of bound water from the relaxation spectrum analysis, this approach will not involve analyses of overlapping relaxation processes and can thus easily be applied to microemulsions having a complex relaxation spectrum.

It is necessary to choose a model that will adequately describe the dielectric properties of the microemulsion. Most of the existing theories (106, 153) operate with a system consisting of well-defined geometrical structures such as spherical or ellipsoidal

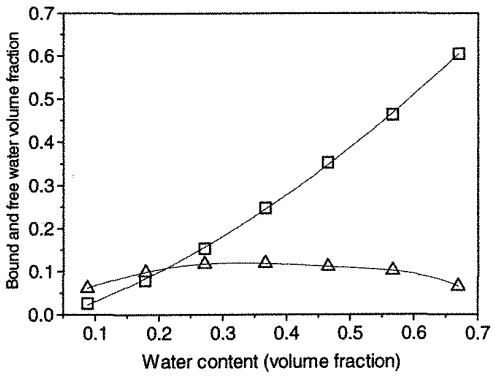

Figure 33 Relative amounts of free (□) and bound (△) water contents of the investigated microemulsion vs. total water content. (From Ref. 141. With permission from Elsevier Science.)

droplets, cylindrical or flat lamellars, etc. Since it was not known how the morphology of the microemulsion system changes with the addition of water, an approach suggested by Kraszewski and coworkers (154, 155) for the prediction of the permittivity mixture was applied. In this case, the relationship relating complex permittivity of the microemulsion with those of its components and their volume fractions may be written:

$$\sqrt{\varepsilon^*} = \varphi_m\sqrt{\varepsilon_m^*} + \varphi_f\sqrt{\varepsilon_f^*} + \varphi_b\sqrt{\varepsilon_b^*} \tag{80}$$

where φ_m denotes the volume fraction of the system occupied by the microemulsion without added water (i.e., "dry" microemulsion consisting of dodecane, butanol, and Brij 97), and φ_f and φ_b are the volume fractions of free and bound water, respectively. The volume fractions are calculated per unit volume of microemulsion. The complex permittivities of the entire system, the microemulsion with no added water, and free and bound water, are represented by ε^*, ε_m^*, ε_f^*, and ε_b^*, respectively.

Since the volume fractions of free, φ_f, and bound, φ_b, water are both unknown, it is convenient to measure the dielectric permittivity in a frequency range where the dielectric loss of bound water may be safely neglected. The relaxation spectrum of free and bound water for our systems will safely satisfy this requirement at the measurement frequency of 75 GHz. In this case, the complex permittivity of the bound water is equal to its real part, i.e., $\varepsilon_b^* = \varepsilon_b' + i0$. For the sake of simplicity, calculations of the complex dielectric constant can be written in polar coordinates, $\varepsilon^* = R\exp(i\theta)$, where $R = (\varepsilon'^2 + \varepsilon''^2)^{1/2}$ and $\tan\theta = \varepsilon''/\varepsilon'$. Now $\exp(i\theta) = \cos\theta + i\sin\theta$; therefore, substituting the corresponding terms in polar coordinates in Eq. (80) for the "dry" microemulsion, free and bound water, respectively, then rearranging and separating the imaginary parts, one can obtain the following relationship for the calculation of the bound-water fraction (156):

$$\varphi_b = \frac{\sin\left(\frac{\theta_m}{2}\right)\sqrt{R_m} - \sin\left(\frac{\theta_e}{2}\right)\sqrt{R_e} - \sin\left(\frac{\theta_w}{2}\right)\sqrt{R_w} - \varphi_m\left[\sin\left(\frac{\theta_m}{2}\right)\sqrt{R_m} - \sin\left(\frac{\theta_f}{2}\right)\sqrt{R_f}\right]}{\sin\left(\frac{\theta_f}{2}\right)\sqrt{R_f}} \tag{81}$$

Figure 33 shows the volume fraction of free, φ_f, and bound water, φ_b, in the microemulsion, calculated from Eq. (81), as a function of the total water content, φ_w. As long as there are unoccupied binding sites at the interface on the surfactant head groups and on the cosurfactant molecules, the increase in φ_w leads to an increase in φ_b. The bound-water fraction shows a maximum between 0.30 and 0.40 of the total water volume fraction, corresponding to 0.12 of bound-water volume fraction. Further addition of water dilutes the alcohol and surfactant, decreasing the number of active centers, which are able to absorb water molecules. Thus, the bound water fraction φ_b decreases after reaching the maximum.

Figure 34 plots the volume ratio between bound water and the total water amount versus water contents. The fraction of bound water decreases with increasing total water content in the system. As more water is introduced into the system, the interface approaches saturation and it is less favorable for additional water to be bound. The dilution effect described above also leads to this decrease.

Water molecules can be bound to both ethylene oxide (EO) groups of Brij 97 and to the hydroxyl (OH) groups of butanol. Unfortunately, it is not known for this system how many molecules are bound to either alcohol or surfactant. Therefore, two curves are presented in Fig. 35. The curves demonstrate the number of bound water molecules calculated per EO group and per EO + OH group versus the total water content, respectively. As the water content increases, the number of water molecules bound to EO or EO + OH groups increases and reaaches a maximum at ~ 2.5 molecules for one curve and ~ 1.5 for the other. This increase means that the water-binding

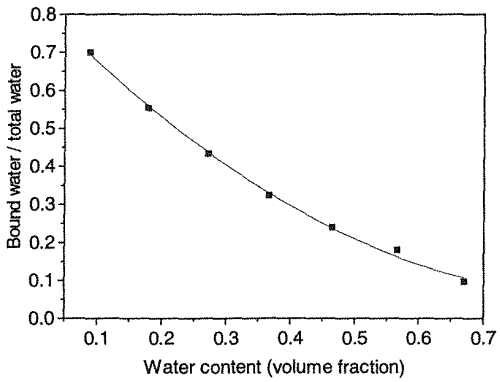

Figure 34 Ratio of bound water-to-total water content (volume of bound water divided by volume of total water) vs. water content. (From Ref. 141. With permission from Elsevier Science.)

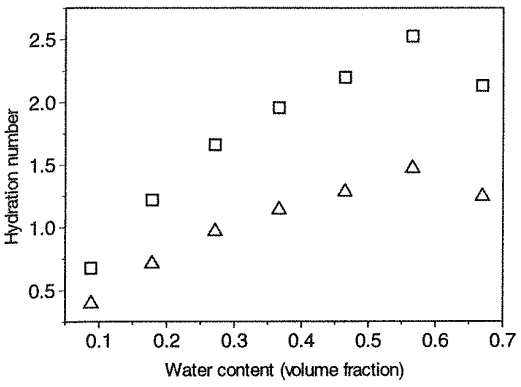

Figure 35 Number of bound water molecules for the investigated microemulsion calculated per ethylene oxide (EO) group (□) and per EO + OH group (△) vs. the total water content. (From Ref. 141. With permission from Elsevier Science.)

centers do not become saturated until ~ 0.6 of the total water volume fraction is obtained. The decrease in the number of bound water molecules per EO or EO + OH group can be due to changes in the morphology of the system above 0.6 of the water volume fraction content. The number of bound water molecules per EO group at saturation obtained from the analysis of the dielectric properties, 2.5, is in good agreement with that obtained by differential scanning calorimetry (DSC) (157), 2.8, for a similar system. However, DSC measurements may be performed only after the samples have been cooled to a very low temperature, while the microwave dielectric method can be applied at any desired temperature.

In this section we have demonstrated the potential of time-domain dielectric spectroscopy in obtaining information about both the structure and dynamics of ionic and nonionic microemulsions on different temporal scales.

V. NONEQUILIBRIUM COLLOIDAL SYSTEMS

Emulsions and suspensions of solid particles are common examples of colloidal systems that are not in the equilibrium state. As the systems destabilize and approach the equilibrium state, several processes will be involved. Typically, flocculation, sedimentation, and coalescence, etc., take place simultaneously at more or less well-defined rates, continuously changing the properties of the system.

Flocculation leads to strongly reduced interparticle distances. Also, the sedimentation process alters the particle distribution throughout the system, leading to a particle density gradient. The size distribution will change as a result of coalescence or coagulation.

There is a constant challenge for improved techniques in order to make accurate predictions on the colloidal stability of various sytems. In this section we demonstrate how dielectric spectroscopy can be applied as a technique to follow the breakdown of water-in-oil emulsions and to monitor the sedimentation of particle suspensions. Dielectric spectroscopy, combined with statistical test design and evaluation, seems to be an appropriate technique for the study of these problems. However, one should continue to seek satisfactory theoretical models for the dielectric properties of inhomogeneous systems.

A. Dielectric Properties of Emulsions

We have restricted this presentation to involve only oil-continuous emulsions. The reason for excluding water-continuous systems is that the O/W emulsions are usually stabilized by means of ionic surfactants (or surfactant mixtures) and consequently the electric double-layer effects can be very large. The electrode polarization will normally also be very strong in many O/W systems. For the TDS technique water-in-oil emulsions stabilized by means of nonionic surfactants are very good model systems.

1. Effect of Flocculation

Theoretical models for the dielectric properties of heterogeneous mixtures [for instance, Eq. (20), or extensions of this model] are commonly applied in order to explain or predict the dielectric behavior also of emulsions (106, 158). However, in the present theories a homogeneous distribution of the dispersed phase is required. This requirement is rarely fulfilled in a real emulsion system where the inherent instability makes the emulsions go through different stages on the way towards complete phase separation. Processes like sedimentation, flocculation, and coalescence continuously alter the state of the system (Fig. 36). These processes also influence the dielectric properties (159–162). Thus, the dielectric properties of one given sample may vary considerably over a period of time (160), depending on the emulsion rate.

The effect of flocculation on the dielectric properties of disperse systems is well documented, both when it comes to suspensions of solid particles and emulsions.

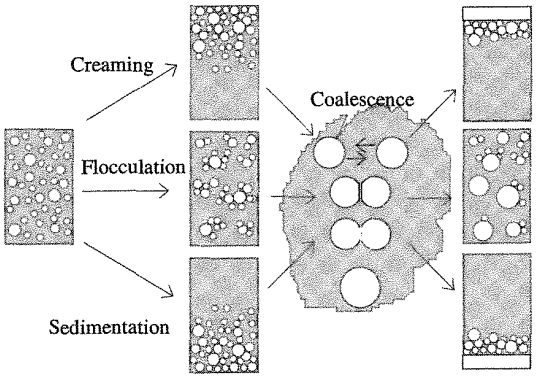

Figure 36 Schematic view of some of destabilizing processes that may take place in an emulsion, eventually leading to complete phase separation. Similar processes also take place in other types of disperse systems.

Genz *et al.* (163) found that the conductive and dielectric properties of suspensions of carbon black in mineral oil was highly dependent on shear. When a shear force was applied to the suspensions, flocculated aggregates were torn apart and a reduction in the permittivity levels was observed. When the shear stopped, the permittivity rose to previous levels. Thus, the reversibility of the shear-induced floc disintegration could be followed by means of dielectric spectroscopy.

Also, Hanai (11) exposed his systems to shear. In order to verify his theory on the dielectric properties of concentrated emulsions (161, 62), dielectric measurement on W/O emulsions were performed at rest and under influence of shear forces. At rest the static permittivities by far exceeded the values predicted from Eq. (20). However, when modestly high shear forces were applied, Hanai found good agreement between measured and predicted values. Also, in this case the reduction in permittivity upon shear was ascribed to a disintegration of flocs.

Table 1 Dielectric Parameters for a W/O Emulsion Containing 50 vol % water, Stabilized by 1% Berol 26. The Aqueous Phase Contains 5 wt% NaCl. Measurements Have Been Performed Both during Emulsification (Using Different Methods) and at Rest (Immediately after Emulsification).

Device	Rotation speed (r.p.m.)	ε_s		ε_∞	
		During mixing	At rest	During mixing	At rest
Laboratory mixer	≈ 2500	15.6	24.2	9.4	11.0
	(≈ 500)	16.9	20.9	10.4	11.3
Vortex mixer		15.4	23.9	11.0	12.9

Source: Ref. 164.

Table 1 gives the results from a simple experiment visualizing the effect of stirring on the dielectric properties of emulsified systems (164). It is seen that the difference in the static permittivity between the emulsions during stirring and at rest can be as high as 50%. In this case the volume fraction of water is constant, so the only difference between the measurements is in the state of the emulsions. Visually, no phase separation could be detected, so the difference must be due to flocculation or sedimentation, leading to a reduced droplet–droplet distance. However, the variations cannot be so large that they promote coalescence, since this was not visually observed. In a study of model W/O emulsions containing different amounts of water (Table 2) (165) it was found that dielectric models based upon spherical, noninteracting droplets could

Table 2 Dielectric Parameters Obtained Experimentally for Different Water-in-Crude Oil Emulsions, Together with Corresponding Shape Factors Found from Comparison with Theoretical Parameters (Eq. 19)

Experimental values				Oblate spheroids ($0 < A < 1/3$)			Prolate spheroids ($1/3 < A < 1/2$)		
ϕ	ε_s	ε_∞	τ (ns)	$A^{\varepsilon s}$	$A^{\varepsilon\infty}$	A^{τ}	$A^{\varepsilon s}$	$A^{\varepsilon\infty}$	A^{τ}
0.17	17.5	6.5	0.8	0.06	0.06	0.06	0.48	0.49	0.48
0.23	22.4	7.4	1.0	0.08	0.09	0.07	0.48	0.48	0.48
0.28	28.2	9.6	1.0	0.09	0.09	0.08	0.47	0.48	0.47
0.38	35.7	13.2	1.3	0.12	0.12	0.10	0.46	0.47	0.47
0.44	46.0	13.5	1.2	0.14	0.14	0.14	0.46	0.45	0.46
0.50	60.0	14.0	1.3	0.15	0.16	0.13	0.45	0.43	0.46

Source: Ref. 165.

not predict the permittivities found. In order to obtain agreement between measured values and predicted ones the traditional models on heterogeneous mixtures were modified, taking a flocculated state of the emulsions into account.

a. Linear flocs

In a first approach, it is assumed that the flocculated aggregates can be considered as spheroids, as depicted in Fig. 37. By further assuming that the volume of the floc equals the volume of the droplets, and neglecting any interactions over the thin films separating the droplets, the overall permittivity can be predicted by use of Eq. (21) or (22). The flocs are in this case characterized by one single variable, namely a shape factor, A. The easiest way to interpret A is to consider a linear flocculation (see Fig. 37) and to define an axial ratio between the major and minor axes. When doing so, corresponding axial ratios were found to be in the range from 1:3 to 1:10 (165). However, a small linear flocculation is not entirely consistent with the complex structures a flocculated system can build up. Other more complex flocculation models have also been developed.

b. Flocs as Subsystems

An alternative approach is where the aggregates, formed as a result of flocculation, are treated as subsystems of the emulsions (166). The dielectric properties of the subsystems will be decisive for the dielectric properties of the overall system.

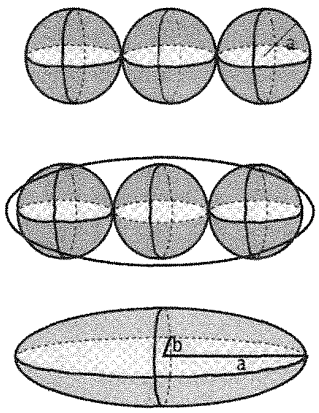

Figure 37 Linear flocs: if the droplets form small linear aggregates, the floc aggregates can be treated as spheroids and can as such be characterised by the axial ratio a/b (or consequently by the shape factor A) as introduced in Eq. (20).

In floc aggregates some of the continuous phase is entrapped between the emulsion droplets. Thus, the volume occupied by a floc will exceed the volume of the individual droplets building up the floc (Fig. 38). The volume fraction occupied by flocs, ϕ_f, can be expressed as

$$\phi_f = \frac{V_f}{V} = \frac{V_f V_d}{V_d} \Big/ V = \phi \frac{V_f}{V_d} = \frac{\phi}{\phi_{d,f}}, \quad (\phi < \phi_{d,f} < 1) \tag{82}$$

where V_f and V_d are the volumes of the flocs and droplets, respectively, V is the total volume of the system; ϕ is the volume fraction of disperse phase with regard to the total volume, whereas $\phi_{d,f}$ is the volume fraction of disperse phase with regard to the floc volume. The factor $\phi_{d,f}$ is a measure on the packing of the droplets in the flocs, i.e., a small value of $\phi_{d,f}$ means a loose structure, and a large value represents a densely packed floc.

Assuming that the droplets retain a spherical shape, the permittivity for the flocs, ε_f^*, can be calculated by using Eq. (20):

$$1 - \phi_{d,f} = \left(\frac{\varepsilon_f^* - \varepsilon_1^*}{\varepsilon_2^* - \varepsilon_1^*}\right)\left(\frac{\varepsilon_2^*}{\varepsilon_f^*}\right)^{1/3} \tag{83}$$

We can then proceed to calculate the total permittivity ε^* for the system, now treating the flocs as the disperse phase, at a concentration that equals ϕ_f :

$$1 - \phi_f = \left(\frac{\varepsilon^* - \varepsilon_f^*}{\varepsilon_2^* - \varepsilon_f^*}\right)\left(\frac{\varepsilon_2^*}{\varepsilon^*}\right)^{3d,f} \times \left(\frac{\varepsilon_2^*(1 + 3A_f) + \varepsilon_f^*(2 - 3A_f)}{\varepsilon^*(1 + 3A_f) + \varepsilon_f^*(2 - 3A_f)}\right)^{3K,f} \tag{84}$$

By use of Eq. (84) we allow for a spheroidal shape of the flocs, as expressed through the parameters A_f, 3d, f and $3K$, f. In this model the flocculated aggregates are characterized by the packing density of the droplets in the floc and a shape factor.

c. Two-component Model with a Partial Flocculation

In the approaches above (i.e., Sec. V.A.1.a and V.A.1.b) a complete flocculation, i.e., that all droplets are part of a floc, is taken for granted. This is seldom the case, and the situation sketched in Fig. 39 is more likely to occur. The system properties are then dependent both on the permittivity and volume fraction of the free droplets as well as on the floc permittivity and $\phi_{p,f}$.

The following expression, derived by Hanai and Sekine (167) gives the permittivity of a system where

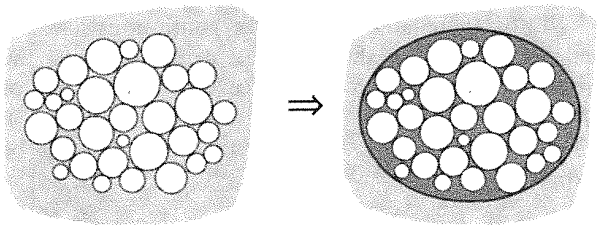

Figure 38 Flocs treated as subunits: the flocs are treated as subunits, with a volume fraction of droplets in floc (or the floc density), ϕ_{df}, that is higher than the overall volume fraction ϕ. Some of the continuous phase will be entrapped between the droplets in the floc. Thus, the volume of a floc exceeds the total volume of the droplets in it. The floc shapes are assumed to be spheroidal.

two different types of spherical particles are dispersed in the same system:

$$\ln(1-\phi) = \frac{1}{3}[\log \varepsilon_2^* - \log \varepsilon^*] + A[\log(\varepsilon^* - \alpha) - \log(\varepsilon_2^* - \alpha)] + B[\log(\varepsilon^* - \beta) - \log(\varepsilon_2^* - \beta)] \quad (85)$$

where A, B, α, and β are functions of the permittivities $\varepsilon_{1,j}$ and $\varepsilon_{1,k}$ and of the ratio ϕ_k/ϕ_j, where the subscripts j and k represent the two different kinds of particles; ε_2 is the dielectric permittivity of the continuous phase. In Eq. (85) "ln" denotes the natural logarithm of a real number whereas "log" is the principal value of the complex logarithm; ϕ is the total volume fraction particles in the system, i.e., $\phi = \phi_j + \phi_k$. [Similar expressions for multicomponent systems with randomly oriented spheroids have been derived by Boned and Peyrelasse (24).]

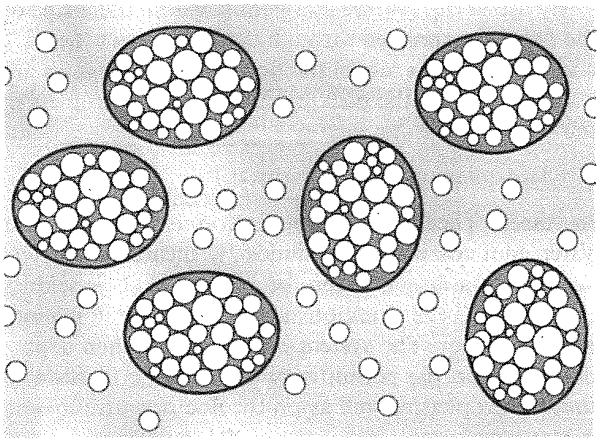

Figure 39 Model for partial flocculation.

If we treat the free water droplets as one type of particle and the flocs as the other type, Eq. (85) may be used to find the dielectric properties of a partially flocculated emulsion.

The dispersed water, present at a concentration ϕ, is distributed between two states, either as free droplets, or bound in the flocs. We can write

$$\phi = \phi_w^{\text{Free}} + \phi_w^{\text{Bound}}$$

The volume fraction of flocs in the system (ϕ_f) is related to ϕ_w^{Bound} through

$$\phi_f = \phi_w^{\text{Bound}} \phi_{d,f}$$

where $\phi_{d,f}$ is the volume fraction droplets in the flocs, as in the previous section. To apply Eq. (85) the total volume fraction occupied by the two "components" is needed and

$$\phi_{\text{Total}} = \phi_w^{\text{Free}} + \phi_f = (\phi - \phi_w^{\text{Bound}}) + \frac{\phi_w^{\text{Bound}}}{\phi_{d,f}}$$

Thus, for a given ϕ we can have a wide range of different systems, as we can freely vary ϕ_w^{Free} and $\phi_{d,f}$, within the limits $\{0 < (\phi - \phi_w^{\text{Bound}}) < \phi$ and $\theta < \theta_{d,f} < 1\}$.

Common for all models presented is that, by the right choice of parameters, one can theoretically predict static permittivities that match experimental values for W/O emulsions, and that are higher than those predicted from the models presuming a homogeneous distribution of spherical emulsion droplets. However, there are more features to the dielectric spectrum than just the static permittivity, and for the models to be deemed useful in characterizing emulsion properties they should be able to reproduce also the frequency dependence of permittivity. In other words, the complete relaxation process must be satisfactorily accounted for. When the models above have been fitted to experimental data we have experienced only a limited success in finding sets of floc parameters that yield theoretical spectra in accordance with the experimental ones (164, 165, 168, 169). Taking into account the multitude of possible configurations of the systems after flocculation, this is not unexpected, and an effort still has to be made before the dielectric properties of flocculated systems can readily be predicted.

2. Electrocoalescence

In a strong electric field the aqueous droplets in a W/O emulsion become polarized due to ion separation in the

droplets. This polarization will create an opposite field inside the water droplets. As a consequence we will have a flocculation of aqueous droplets, a so-called bridging, between the electrodes. The potential difference between droplets may be written as:

$$V_{pot} \propto Er\cos\theta \tag{86}$$

where E is the applied field, r is the droplet dimension, and θ is the angle to the applied field. With a droplet radius of 10 μm, an applied field of 0.5 kV/cm, and droplets parallel with the external field, the potential will be of the order of 0.5 to 1.0 V. Under these conditions the field over the surfactant membrane ($\approx 2l_{surfactant}$) separating two aqueous droplets is of the order of 10^6 V/cm. This is a very high local field that can create an ion transport over the surfactant film. When the ions start to cross the film a coalescence of adjacent droplets will take place. However, this transport requires a certain level, V_{crit}, before it will take place; V_{crit} can hence be taken as a measure on the emulsion stability (52). Below V_{crit} different kinds of phenomena can take place. For a single-droplet assembly one can predict a substantially increased level of flocculation, i.e., the static permittivity should increase under these conditions. If the emulsion is already in a flocculated state the applied voltage may first of all alter the droplet size distribution towards larger droplets and hence also the size of the flocs. As a consequence a drop in ε_s can be predicted. However, when the applied field is switched off the original floc size and structure will be slowly obtained and a relaxation process towards the original ε_s can be observed. The level of irreversible distortions in the droplet sizes can determine a difference in the initial ε_s and the ε_s after relaxation.

a. Percolation Phenomena in W/O Emulsions in High Electric Fields

Figure 40 shows the static permittivity of an asphaltene-stabilized model W/O emulsion versus the applied external electric field (170). The static permittivity increases with the applied electric field. This is an indication of a low degree of attraction between the aqueous droplets and, initially, a low level of flocculation. The applied electric field will induce a flocculation that consequently leads to an increase in ε_s. First to a small extent only, later more pronounced as the critical voltage is approached. However, when the critical electric field is exceeded, a steep decline in the static permittivity to a value of 5–7, is observed. This can be viewed as a percolation phenomenon according to a static model (171, 172).

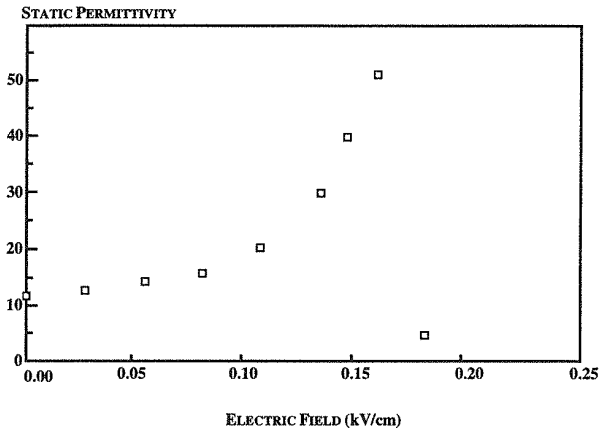

Figure 40 Static permittivity of an asphaltene-stabilized model emulsion vs. the applied external electric field. The percolation behavior is clearly seen. (From Ref. 170.)

From studies of the percolation phenomena in W/O microemulsions it has been proposed that permittivity follows a scaling law with regard to temperature (96). However, when we induce the percolation by applying a high electric field, the following scaling law may apply:

$$\varepsilon_S \sim (E_{cr-E})^{-S} \tag{87}$$

where $E < E_{cr}$. From linear regression analysis, the critical exponent s can be estimated from the slope. The data from Fig. 40 will give a slope of 0.52, which is close to the theoretical value expected from a static percolation model ($s = 0.6$) containing bicontinuous oil and water structures (172).

3. Dielectric Spectroscopy on Technical Emulsions (Gas Hydrate Formation)

Literature reports on a variety of applications of dielectric measurements in different types of technical processes. The classical application is to determine water contents in process fluids by means of capacitance measurements. This technique has also been extended to higher frequencies by Wasan and coworkers (173, 174). In the following we present a technically very important problem that combines a controlled reaction inside a W/O emulsion and dielectric spectroscopy as a process on-line instrumentation. This problem concerns the formation and transport of gas hydrates in pipelines.

Gas hydrates (clathrates) may technically be considered as an alternative form of ice that has the ability to entrap relatively large volumes of gas within cavities in the hydrate crystal matrix. The entrapped guest molecules (gas) stabilize the structure by means of van der Waals interactions, and combinations of the different unit cells give rise to structures I, II (175–177), and H (178). The most common gas to form gas hydrates is methane, but ethane, propane, butane, carbon dioxide, nitrogen, and many other types of gases may also give rise to gas hydrates.

When gas hydrates are formed in a W/O emulsion, the emulsified water is converted into clathrate structures and thus the volume fraction of free water in the emulsion droplets decreases. The formation of these new structures will alter the overall dielectric properties of the emulsion, and dielectric measurements can thus be used to follow the gas hydrate formation. In Fig. 41 this is illustrated with CCl_3F as the gas hydrate forming species in a nonionic W/O emulsion (179, 180). The decrease in the overall permittivity of the system is due to the transition of water from the liquid to the solid state (i.e., from free water to water bound in the hydrates). From the dielectric measurements we can extract information on the onset temperature for hydrate formation, induction time for the process, and so on. The permittivity level after the hydrate formation is completed is indicative of the ratio between liquid water and hydrate water, i.e., the amount of water converted into hydrate water can be readily found (179, 180).

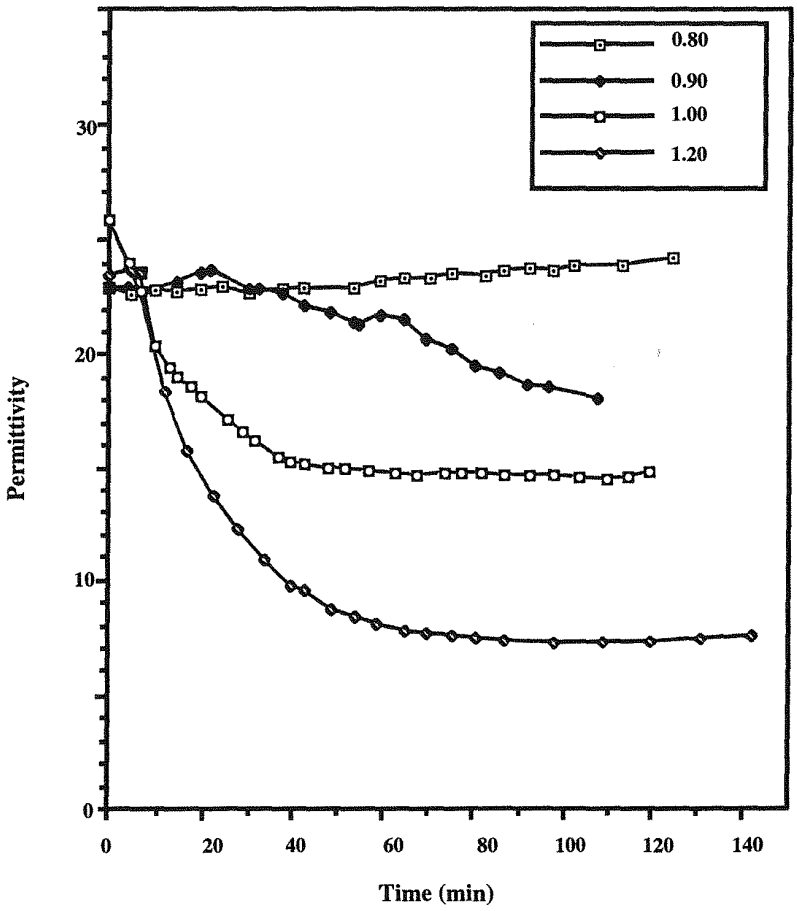

Figure 41 Static permittivity vs. time for clathrate hydrate formation in model W/O emulsions. The concentrations of CCl_3F in H_2O were 0.80, 0.90, 1.00, and 1.20, respectively, times the theoretical molar fraction 1:17 expected to be found in the hydrates. (From Ref. 179.)

If the aqueous phase contains electrolytes, a relaxation due to the Maxwell–Wagner–Sillars effect will be observed. Since the electrolyte is not incorporated in the clathrate structures, an increased electrolyte concentration in the remaining free water will result, thus changing the dielectric relaxation mode. In Fig. 42 we note that the relaxation time τ decreases from the initial 1000±100 ps to a final level of 200±20 ps during hydrate formation. The experimental value of 200 ps corresponds roughly to a 3% (w/v) NaCl solution, as compared with the initial salt concentration of 1% (w/v).

B. Suspensions

1. Sedimentation in Particle Suspensions

During sedimentation the volume fraction of suspended particles will increase near the bottom of the sample while the concentration of particles in the top layer will be correspondingly smaller. Information on the sedimentation rate and structure of the sediment layer can thus be extracted from dielectric measurements carried out at different levels of the sample.

The application of the TDS method for sedimentation studies may be illustrated with the studies carried out on two model systems, i.e., aqueous suspensions of SiO_2 and Al_2O_3, respectively. Figure 43 shows the permittivity spectra of Al_2O_3 in water as a function of the volume fraction of particulate matter. The most notable changes are in the static permittivity, which is also focused on in the following figures. Figure 44a shows the variation in static permittivity as a function of the volume fraction of SiO_2. The Hanai equation, Eq. (20), gives good estimates of the observed behavior. Figure 44b presents the corresponding data for Al_2O_3 and also in this case the Hanai model assuming spherical particles seems to describe the experimental data fairly well (181, 182).

In order to alter the sedimentation rate the surfaces of the SiO_2 and Al_2O_3 particles were modified through the adsorption of surfactants or polymers. The nonionic surfactant C_9PhEO_6 and the nonionic polymer ethyl hydroxyethyl cellulose (EHEC) were used. Figure 45 gives the influence of pH on the sedimentation of Al_2O_3 in water for pure particles (Fig. 45a) and EHEC-coated particles (Fig. 45b). At pH 8.5 (i.e., close to the isoelectric point (IEP) for alumina) the sedimentation is fast and gives rise to a porous sediment (leading to a high final level of ε). In contrast to this one can follow the slow sedimentation at pH 3.5 where we end up with a denser sediment and consequently a lower ε. For the coated particles the effect of pH is rather small (182).

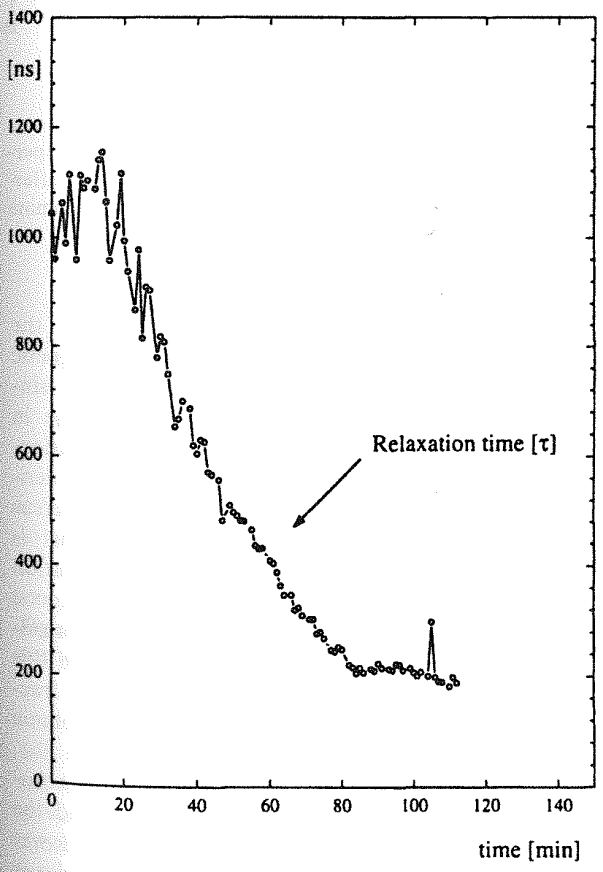

Figure 42 Relaxation time vs. time during clathrate hydrate formation. (From Ref. 179.)

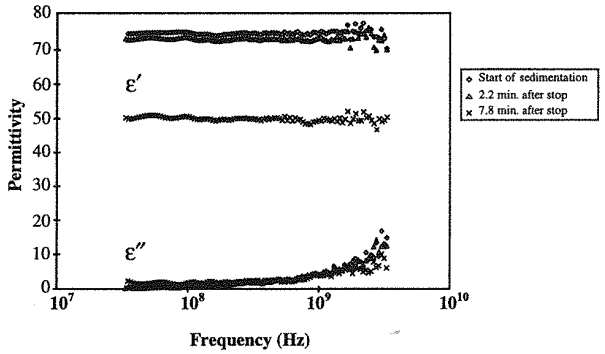

Figure 43 Dielectric spectra from an aqueous alumina particle suspension, recorded during sedimentation. (From Ref. 181.)

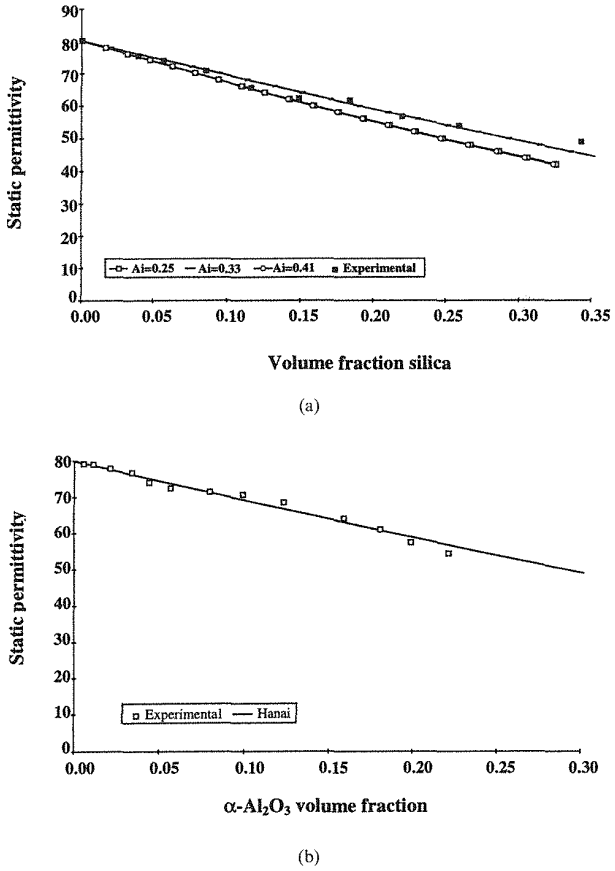

Figure 44 Static permittivity vs. volume fraction particles in aqueous suspensions: (a) silica particles, (b) alumina particles. (From Ref. 181.)

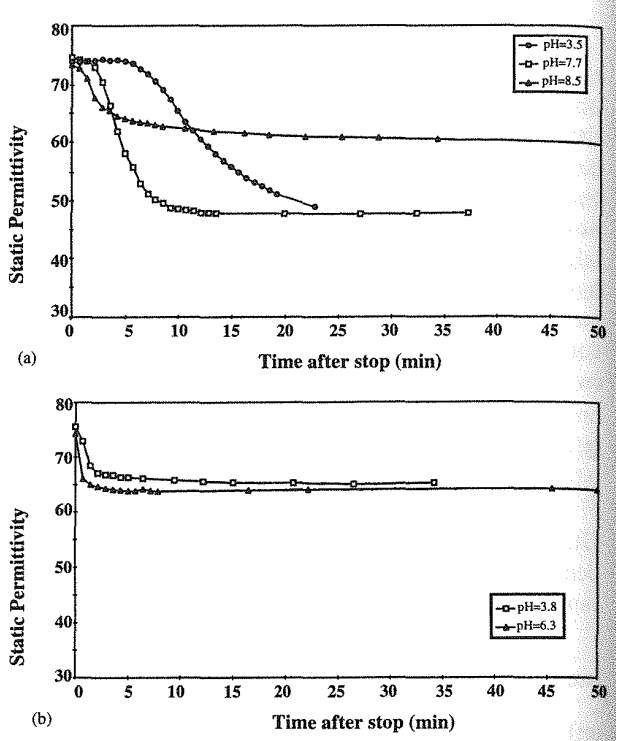

Figure 45 Static permittivity of particle suspensions vs. time, recorded during sedimentation. Measurements are performed in the bottom of the sedimentation cell, and at different pH conditions. (a) Alumina particles; (b) alumina particles coated with EHEC. (From Ref. 182.)

2. Magnetic Particles

Magnetically active monodisperse organic particles have found many technical applications especially within the separation and isolation of live cells and microorganisms. The magnetic particles are also almost perfect for sedimentation tests in applied magnetic fields, in as much as the degree of flocculation may be controlled quite accurately. In Fig. 16 an experimental design for the dielectric study of aqueous suspensions of magnetic particles is displayed (86). In this survey, monodisperse polystyrene particles (2.8–4.5 μm) containing 25% magnetic oxides have been used. When the particles are subjected to a magnetic field an induced flocculation takes place (Fig. 46). The next figure (Fig. 47) shows how the static permittivity changes with time (due to sedimentation) and with the strength of the applied magnetic field. The strength of the magnetic field will dictate the degree of flocculation. For single-particle sedimentation with a linear decrease in the static permittivity as a function of concentration, one would expect proportionality between the derivatives of volume fraction and permittivity versus time. From Fig. 47 we can observe that this is more or less always the case when the sedimentation occurs without the presence of a strong magnetic field, at least up to a period between 0 and maximally 5 min. In the presence of an external field this period is substantially shorter for low-volume fractions and substantially extended for high-volume fractions.

Two major effects will dictate the suspension behavior, i.e., the gravity-induced sedimentation and the bridging induced by the magnetic field. At lower volume fractions the distance between the particles is rather large, and the hindrance of settling is low. When a magnetic field is applied across the suspension there

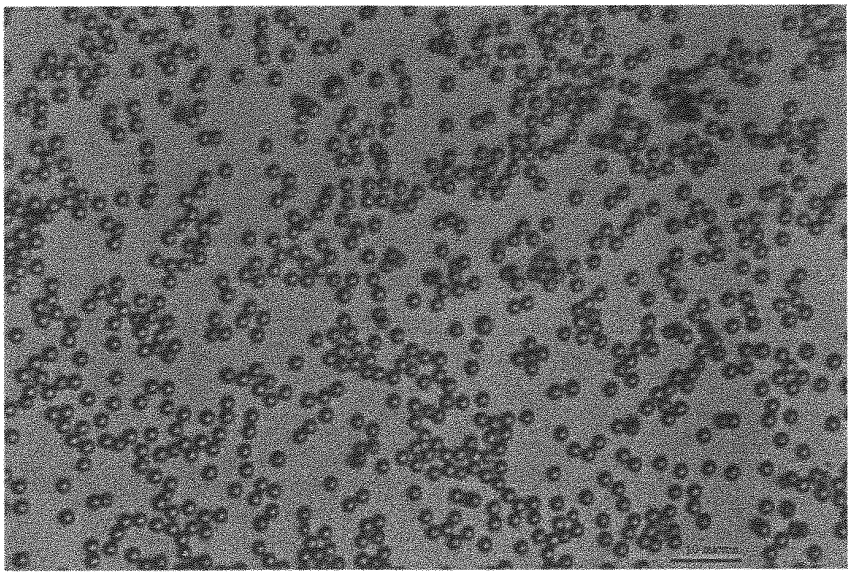

(a)

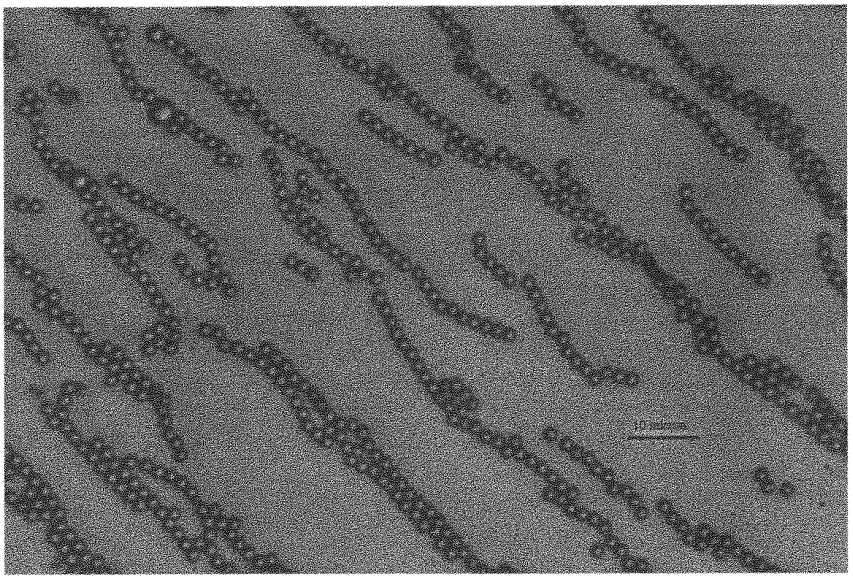

(b)

Figure 46 (a) Micrograph of polystyrene-based magnetic monodisperse particles; the particle diameter is 2.8 μm. (b) The particles are subjected to an external magnetic field. (From Ref. 86.)

will be an instantaneous sedimentation of small flocs (as seen from Fig 47 with $\phi = 0.02$ and 0.05). At higher ϕ values the initial distance between the particles is much smaller and the bridging induced by the magnetic field may lead to a network formation resulting in a hindered sedimentation. This can be observed for $\phi = 0.20$ and 0.25. For a field of 0.4 T it takes about 5 min before the sedimentation sets in while a weaker field (0.1 T) can delay the sedimentation for 3.5 min. For the highest volume fraction ($\phi = 0.25$) no significant sedimentation is observed when the magnetic field is applied.

When the external magnetic field is applied the particles will, to a greater degree, flocculate and settle as

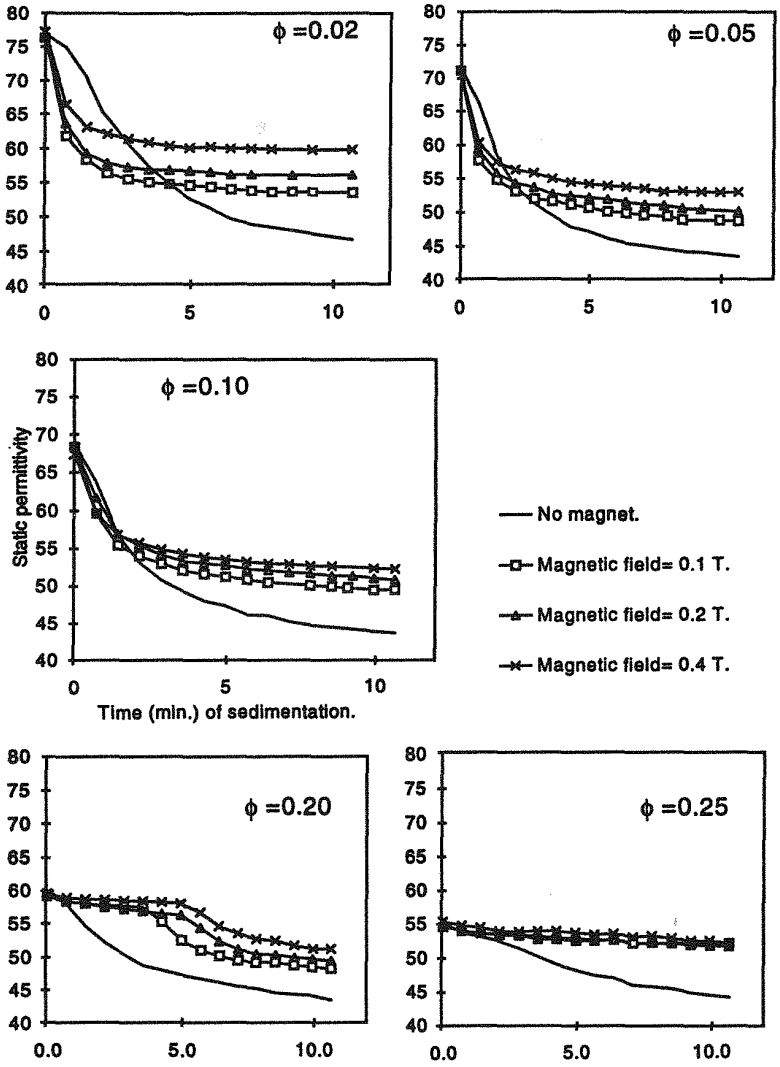

Figure 47 Static permittivity vs. time for suspensions containing the particles from Fig. (46) recorded during sedimentation. Different magnetic field strengths were applied, and the volume fraction particles were varied according to the legends. (From Ref. 86.)

flocs, giving a more porous bottom layer, as illustrated in Fig. 48. When the particles sediment individually the result is a more dense sediment. The porosity of the sediment is reflected in the level of the permittivity, a low permittivity in the sediment layer indicating a close packing of the particles.

By monitoring the dielectric properties of nonequilibrium systems a wide range of parameters describing the system may be deduced. However, more work of both a theoretical and experimental nature needs to be performed before we have a complete understanding of how the nonideal situations influence the dielectric parameters.

VI. DIELECTRIC STUDY OF HUMAN BLOOD CELLS

One of the important subjects in biophysics is the investigation of the dielectric properties of cells and the structural parts of the cells (i.e., membrane, cytoplasm, etc.). These can provide valuable knowledge

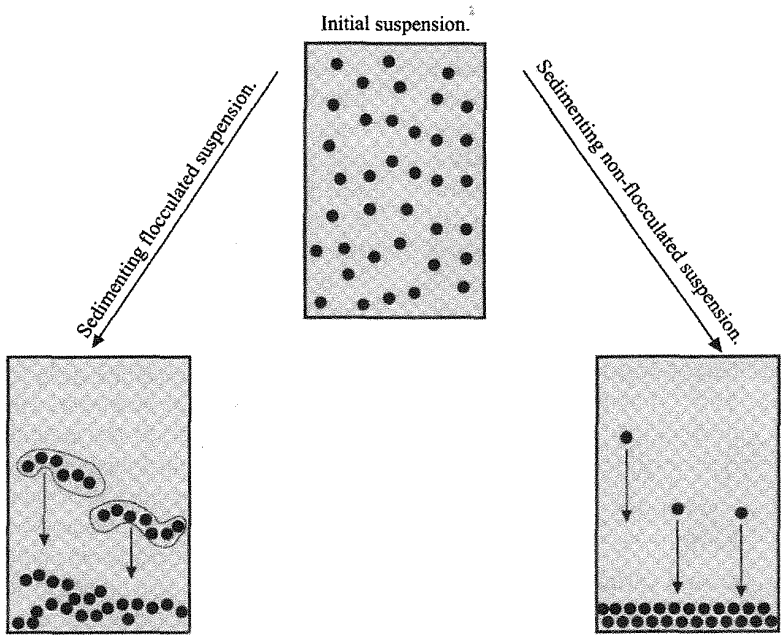

Figure 48 Schematic view on how flocculation may influence the nature of the sediments.

about different cell structures, their functions, and metabolic mechanisms.

The cell-suspension spectra are known to show a so-called β-dispersion (183), which is observed in the frequency range 100 kHz–10 MHz and can be interpreted as the interface polarization. This dispersion is usually described in the framework of different mixture formulas and shelled models of particles (14, 70, 72, 183, 184). In the example of biological cells, the interface polarization is connected to the dielectric permittivity and conductivity of the cell structural parts.

Before time-domain spectroscopy (TDS) methods were developed, investigations by frequency-domain methods were restricted by lack of techniques which allowed quick determination of the dielectric spectrum within the frequency range 10^5–10^{10} Hz (14, 64). It was quite difficult to ensure the stability of biological materials because of the long duration of the experiment. TDS allows one to obtain information on dielectric properties in a wide frequency range during a single measurement and hence to study unstable biological systems properly. This is also a much less time-consuming method, which requires very few devices to work with. Moreover, the sensitivity of the system allows one to study dilute solutions or suspensions of cells (volume fraction $< 10\%$).

A. Cell and Cell-suspension Dielectric Models

For analysis of the dielectric properties of blood-cell suspensions, several classical models are usually used (11, 14, 185–201). For small volume fractions of cells the Maxwell-Wagner model is used, while for larger ones (see Sec. II) the Hanai formula would be preferable (14, 186). It was shown (70, 72) that for dilute suspensions of human blood cells the dielectric spectra of a single cell can be successfully calculated from the Maxwell model of suspension, according to the mixture formula [Eq. (19)]:

$$\varepsilon^*_{\text{mix}} = \varepsilon^*_{\text{sup}} \frac{(2\varepsilon^*_{\text{sup}} + \varepsilon^*_{\text{c}}) - 2p(\varepsilon^*_{\text{sup}} - \varepsilon^*_{\text{c}})}{(2\varepsilon^*_{\text{sup}} + \varepsilon^*_{\text{c}}) + p(\varepsilon^*_{\text{sup}} - \varepsilon^*_{\text{c}})} \tag{88}$$

where p is the cell volume fraction, $\varepsilon^*_{\text{mix}}$ is the effective complex dielectric permittivity of the whole mixture (suspension), $\varepsilon^*_{\text{sup}}$ is the complex dielectric permittivity of the supernatant, $\varepsilon^*_{\text{sup}}(\omega) = \varepsilon_{\text{s,sup}} - i\dfrac{\sigma_{\text{sup}}}{\omega}$, σ_{sup} is its conductivity, and ε^*_{c} is the effective complex dielectric permittivity of the average cell.

1. Single-shell Model of the Erythrocytes

The dielectric properties of the spherical erythrocyte can be described by the single-shell model (14, 70,

186). In this model the cell is considered as a conducting homogeneous sphere (or ellipsoid) covered with a thin shell, much less conductive than the sphere itself (14, 186–189).

The expression for the complex dielectric permittivity [$\varepsilon_c^*(\omega)$] in the single-shell model contains five parameters: dielectric permittivity and conductivity of the cell membrane (ε_m and σ_m); dielectric permittivity and conductivity of the cell interior (cytoplasm) (ε_{cp} and σ_{cp}); and a geometrical parameter $v = (1 - d/R)^3$ where d is the thickness of the cell membrane and R is the radius of the cell. This expression is as follows (188):

$$\varepsilon_c^*(\omega) - \varepsilon_m^*(\omega)\frac{2(1-v) + (1+2v)E(\omega)}{2 + v + (1-v)E(\omega)} \tag{89}$$

where $E(\omega) = \dfrac{\varepsilon_{cp}^*(\omega)}{\varepsilon_m^*(\omega)}$, $\varepsilon_{cp}^*(\omega) = \varepsilon_{cp} - i\dfrac{\sigma_{cp}}{\varepsilon_0\omega}$, $\varepsilon_m^*(\omega) = \varepsilon_m - i\dfrac{\sigma_m}{\varepsilon_0\omega}$, and ε_0 is the vacuum permittivity.

It is possible to show that the single-shell model equation can be presented as the sum of a single Debye process and a conductivity term:

$$\varepsilon_c^* = \varepsilon_\infty + \frac{\Delta\varepsilon}{1 + i\omega\tau} + \frac{\sigma}{i\omega\varepsilon_0} \tag{90}$$

The last equation depends only on four parameters ($\Delta\varepsilon$ – dielectric strength, τ – relaxation time, ε_∞ – dielectric permittivity at high frequency, and σ – the conductivity), which are functions of the dielectric and geometrical parameters of the single-shell models. This connection between the experimental presentation [Eq. (90)] and the single-shell model [Eq. (88)] formulas allows one to conclude that only four independent parameters are required to describe the spectrum of a single cell. The fifth parameter can be expressed in terms of these four parameters. Using the high- and low-frequency limits one can derive the following relations:

$$\varepsilon_{c_0}^* \cong \varepsilon_m\left(\frac{1+2v}{1-v}\right) - j\frac{\sigma_m}{\omega\varepsilon_0}\left(\frac{1+2v}{1-v}\right)\omega \to 0 \tag{91}$$

$$\varepsilon_{c\infty}^* \cong \varepsilon_{cp} - j\frac{\sigma_{cp}}{\omega\varepsilon_0}\omega \to \infty \tag{92}$$

By fitting the single-shell model to the experimental spectrum the following four parameter combinations can be obtained:

$$\varepsilon_m\left(\frac{1+2v}{1-v}\right);\ \sigma_m\left(\frac{1+2v}{1-v}\right);\ \varepsilon_{cp} \text{ and } \sigma_{cp} \tag{93}$$

The first two terms indicate that one of the three parameters (ε_m, σ_m, or v) has to be obtained by an independent method and to be kept fixed during the fitting procedure, whereas the other two parameters can be fitted. Usually, the geometrical parameter v is fixed, since it can be calculated by using the values of the cell radius (R) and the cell membrane thickness (d), which are evaluated independently. The parameters ε_{cp} and σ_{cp} in set (93) can be calcualted directly from the fitting procedure.

It can be shown analytically that the expression for the model spectrum of a cell suspension represented by the combination of the Maxwell–Wagner formula and the single-shell model of cells can be rewritten as the sum of two Debye proceesses and a conductivity term. This is in contrast to the conclusions (190) that every interface of a shelled particle gives a single Debye-type dispersion. In the case of a one-shell particle suspension there are two interfaces. One of them is the interface between the cytoplasm and the cell membrane and the other one is the interface between the cell membrane and the suspending medium. However, Pauly and Schwan (202) have proven that for biological cells these two dispersions degenerate to only one relaxation process. Indeed, the numerical model experiment (203) has shown that the dielectric strength of the high-frequency process is about 2–3 orders of magnitude smaller than the dielectric strength of the low-frequency process and can therefore be neglected.

2. Double Shell Model of the Lymphocytes

It is well known that lymphocytes are spherical, and have a thin cell membrane and a spherical nucleus (surrounded by a thin nuclear envelope) that occupies about 60% of the cell volume (188). Therefore, the dielectric properties of lymphocytes can be described by the double-shell model (188, 190, 191) (see Fig. 49). In this model the cell is considered to be a conducting sphere covered with a thin shell, much less conductive than the sphere itself, in which a smaller sphere with a shell (i.e., the nucleus) is incorporated. In addition, one assumes that every phase has no dielectric losses and the complex dielectric permittivity can thus be written as:

$$\varepsilon_i^*(\omega) = \varepsilon_i - j\frac{\sigma_i}{\varepsilon_0\omega} \tag{94}$$

where ε_i is the static permittivity and σ_i is the conductivity of every cell phase. The subscript i can denote "m" for membrane, "cp" for cytoplasm, "ne" for nuclear envelope, or "np" for nucleoplasm.

The effective complex dielectric permittivity of the whole cell (ε_c^*) is represented as a function of the phase

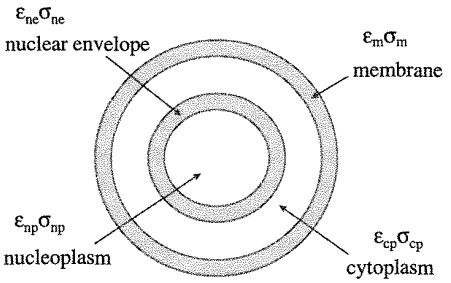

Figure 49 Schematic picture of the double-shell dielectric model of the cell. Every phase of the cell is described by the corresponding dielectric permittivity (ε) and conductivity (σ). (From Ref. 72. With permission from Elsevier B.V.)

parameters, i.e., the complex permittivities of cell membrane (ε^*_m), cytoplasm (ε^*_{cp}), nuclear envelope (ε^*_{ne}), and nucleoplasm (ε^*_{np}):

$$\varepsilon^*_c = \varepsilon^*_m \frac{1(1-v_1)+(1+2v_1)E_1}{(2+v_1)+(1-v_1)E_1} \tag{95}$$

where the geometrical parameter v_1 is given by $v_1 = (1 - d/R)^3$, where d is the thickness of plasma membrane and R is the outer cell radius. The intermediate parameter, E_1, is given by

$$E_1 = \frac{\varepsilon^*_{cp}}{\varepsilon^*_m} \frac{2(1-v_2)+(1+2v_2)E_2}{(2+v_2)+(1-v_2)E_2} \tag{96}$$

where $v_2 = [R_n/(R-d)]^3$, R_n being the outer radius of the nucleus. Finally, E_2 is given by

$$E_2 = \frac{\varepsilon^*_{ne}}{\varepsilon^*_{cp}} \frac{2(1-v_3)+(1+2v_3)E_3}{(2+v_3)+(1-v_3)E_3} \tag{97}$$

where $v_3 = (1 - d_n/R_n)^3$, $E_3 = \varepsilon^*_{np}/\varepsilon^*_{ne}$, d_n being the thickness of the nuclear envelope.

In the double-shell model every structural part of the cell (cell membrane, cytoplasm, nuclear envelope, and nucleoplasm) can be described by two parameters – permittivity and conductivity. Therefore, a cell is described by eight dielectric phase parameters, and there are three geometrical parameters that are a combination of thickness of outer and internal membranes with radii of nucleus and cell. Thus, as it seems, we could obtain all 11 parameters from the fitting of a one-cell spectrum by the double-shell equation. However, it can be demonstrated that some of the parameters are not independent in this model.

In the multishell model every shell gives rise to an additional Debye process with two extra parameters (190). Thus, in the case of the double-shell model, which contains eleven parameters, the spectrum of a suspension can be written as a sum of two Debye processes with conductivity, which includes only six parameters. This means that only six parameters from the total 11 in the double-shell model are arguments that can be fitted. The other five parameters have to be measured by independent methods and have to be fixed in the fitting process. In the fitting procedure, described elsewhere (72, 203), the radius of a cell, the thickness of both membranes, and the permittivity of cytoplasm and nucleoplasm were all fixed.

The specific capacitance of the cell membrane can be calculated directly from the cell suspension spectrum by using the following formula, derived from the Hanai–Asami–Koisumi model (192):

$$C_m = \frac{2}{3}\frac{\varepsilon_0}{R}\frac{\varepsilon_{mix(low)}}{(1-(1-p)^{3/2})} \tag{98}$$

where $\varepsilon_{mix(low)}$ is the low-frequency limiting value of the dielectric permittivity (static permittivity) of the suspension.

B. Protocol of Experiment, Fitting Details, and Statistical Analysis

The whole procedure of the human blood-cell suspension study is presented schematically in Fig. 50. The TDS measurements on the cell suspension, the volume-fraction measurement of this suspension, and measurements of cell radius are excecuted during each experiment on the sample. The electrode-polarization correction (see Sec. II) is performed at the stage of data treatment (in the time domain) and then the suspension spectrum is obtained. The single-cell spectrum is calculated by the Maxwell–Wagner mixture formula [Eq. (88)], using the measured cell radius and volume fraction. This spectrum is then fitted to the single-shell model [Eq. (89)] in the case of erythrocytes or to the double-shell model [Eqs (94)–(98)] to obtain the cell-phase parameters of lymphocytes.

In the fitting procedure for lymphocytes, the following parameters were fixed: the radius of the measured cell; the cell membrane thickness ($d = 7$ nm) (188); the nuclear envelope thickness ($d_n = 40$ nm) (188, 191); and the ratio of the nucleus radius to the cell radius ($R_n/R = (0.6)^{1/3}$). These four values represent only three geometrical parameters of the double-shell model (188, 190, 191). Two other fixed parameters were the dielectric permittivity of the cytoplasm ($\varepsilon_{cp} = 60$) (188) and the dielectric permittivity of the nucleoplasm ($\varepsilon_{np} = 120$); ε_{np} was chosen as the middle value from the range presented in other papers (188,

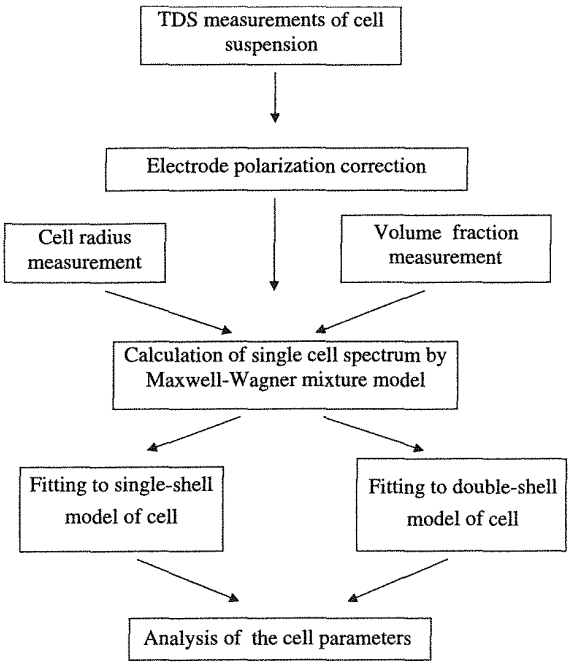

Figure 50 Flow chart of the whole protocol of human blood-cell suspension study.

191). Moreover, numerical evaluations and evidence in Refs 188 and 191 have shown that the suspension spectrum is almost insensitive to changes in the ε_{cp} and ε_{np} parameters from 30 up to 300. Students' t-test (201) was usually applied to analyze the results of the fittings.

C. Erythrocytes and Ghosts

The erythrocyte and erythrocyte ghost suspensions are very similar systems. They differ in their inner solution (in the case of erythrocytes it is an ionic hemoglobin solution; in the case of ghosts it is almost like the surrounding solution they were in while they were sealed). The cell sizes in a prepared suspension depend both on the ion concentration in the supernatant and in the cell interior (70). Thus, the dielectric spectra of erythrocytes and erythrocyte ghost suspensions have the same shape, which means that there are no additional (except Maxwell–Wagner) relaxation processes in the erythrocyte cytoplasm; thus, the single-shell model (Eq. 89) can be applied.

The frequency dependence of the effective dielectric permittivity of a single "average" erythrocyte was calculated for both samples, according to Eq. (88). The spectra obtained were almost identical, as was expected since both samples were prepared from erythrocytes of the same blood sample. The normalized dielectric permittivity spectrum of one of them (No. 1) is shown in Fig. 51 by points. The relaxation process for a single erythrocyte can be described by the Debye equation. The effective dielectric permittivity spectra of an "average" erythrocyte were fitted to the single-shell model equation [Eq. (89)] and the phase parameters of the cell were found. The fitted normalized dielectric spectrum is given in Fig. 51 by a solid line.

The membrane dielectric permittivity ε_m was evaluated from fitting with an accuracy of ± 0.05 (70). The membrane conductivity could not be estimated from the fitting as far as it was less than the accuracy limits, so it was set to zero. Insufficient accuracy of the inner phase dielectric permittivity ε_S allows only estimates of the lower and upper limits of its value. The inner phase conductivity σ_i was found with an accuracy of ± 0.01 S/m. The dimensionless parameter v was found with an accuracy of $\pm 1 \times 10^{-4}$.

As regards the ghosts, their membrane dielectric permittivity ε_m is that of the erythrocytes they were prepared from. The inner phase conductivity σ_i of

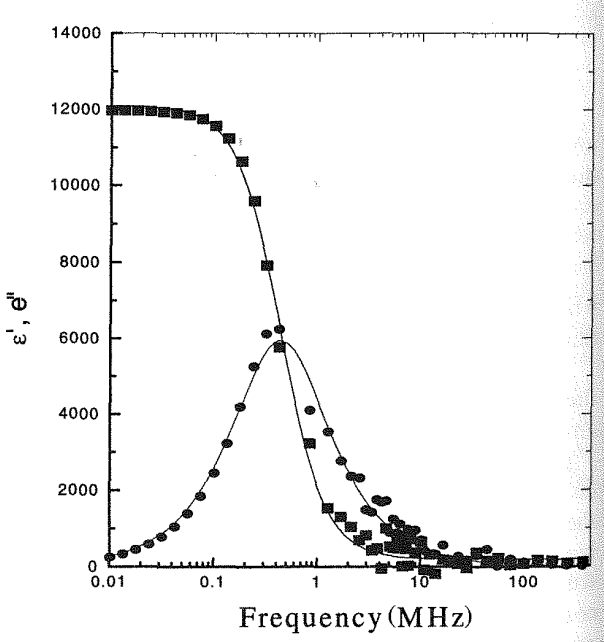

Figure 51 Dielectric permittivity spectrum of the "average" erythrocyte fitted to the single-shell model. Experimental results are figured by points, and the fitting results by a solid line. (From Ref. 70. With permission from Elsevier Science B.V.)

ghosts varied in correspondence with the conductivity of the supernatant they were placed in. The parameter v depends both on the supernatant conductivity and on the ghost preparation method.

The limits of the phase parameter variation of different erythrocytes and ghosts at room temperature are given in Table 3. The dielectric permittivities of the erythrocyte membranes are found to be distributed near 5 (Fig. 52). The erythrocyte membrane thickness was found to be 3.1 nm, assuming an average radius of 2.7 μm. This result is in good agreement with that obtained by Fricke (193, 194).

Thus, it was shown that one could apply the mixture equation [Eq. (88)] and the single-shell model [Eq. (89)] to dilute solutions of ghosts and erythrocytes. The membrane dielectric permittivity, cytoplasm conductivity, and geometric parameter v for each kind of cell were calculated. The next step was to use this approach for the dielectric property study of normal and pathological blood cells.

Table 3 Limits of Phase Parameters' Variation for Different Erythrocytes and Ghosts at Room Temperature

	ε_m	v $\left(1-\frac{d}{R}\right)^3$	d (nm) Independent measurement ($R = 2.7$ μm)
Erythrocytes	~ 5	~ 0.9967	~ 3.1
Ghosts	~ 4.8	~ 0.9967	~ 3.1

Source: Ref. 70 (with permission from Elsevier Science B.V.).

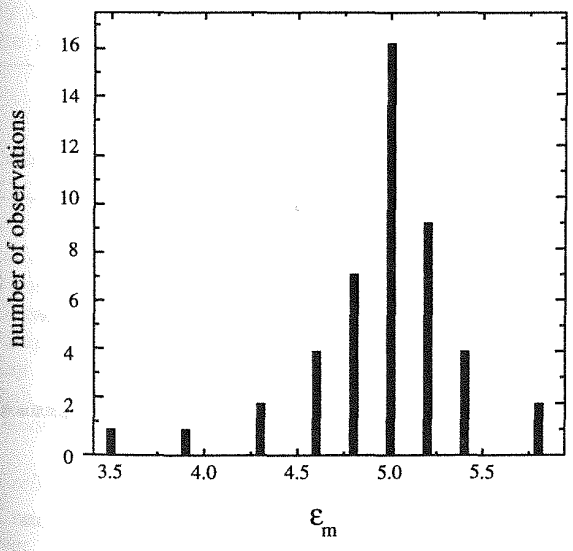

Figure 52 Distribution of the observed values of the erythrocyte membrane dielectric permittivity. (From Ref. 70. With permission from Elsevier Science B.V.)

D. Lymphocytes

1. Description of Measured Cell Samples

Nine cell populations were investigated (72): normal perpheral blood T cells, normal tonsillar B cells, peripheral blood B cells, which were transformed by infection with Epstein–Barr Virus (EBV) (Magala line), malignant B cell lines (Farage, Raji, Bjab, and Daudi) and malignant T cell lines (Peer and HDMAR). The sizes of the cells were determined by using a light microscope. The typical size distribution is shown in Fig. 53. The volume fractions were measured with a micro-centrifuge (Haematocrit) and corrected for the intercellular space, which was determined with Dextran Blue, and found to be 20.2 ± 3.2% of the volume of the pellet (204, 205). The cell populations with corresponding names of diseases, the mean value of cell radii and the volume fractions are presented in Table 4.

2. Dielectric Properties of Measured White Blood Cells

Typical examples of single cell spectra obtained for studied cell lines by the procedure described above are presented in Fig. 54. One can see that the spectra of the various cell lines are different. It should be mentioned that the transition from the suspension spectrum to a spectrum of a single average cell leads to a noise increase that is especially noticeable at high frequencies. This phenomenon is the result of the nonlinearity of Eq. (88), which was used for this calculation. In particular, the parameters for the nucleus envelope, cytoplasm, and nucleoplasm (presented in Table 5) are connected with the high frequency of the cell spectrum; therefore, these parameters were obtained with a relatively low accuracy.

The specific capacitance of a cell membrane was estimated from the value of the state permittivity of the suspension spectra by the relationship Eq. (94). This value is proportional to the ratio of the cell membrane permittivity to the membrane thickness ε_m/d, according to the formula of a plate capacitor, i.e., $C_m = \varepsilon_m \varepsilon_o / d$. Both the capacitance C_m and ratio, ε_m/d, are presented in Fig. 55. Note that in

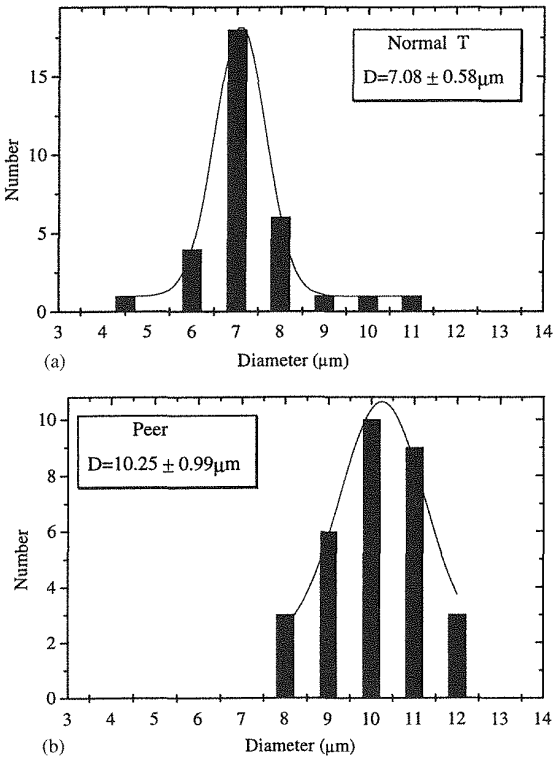

Figure 53 Typical size distributions for normal (a) and malignant (b) lymphocytes. The results of fitting by Gauss distribution function are shown by the solid line; D is the mean diameter of cells. (From Ref. 72. With permission from Elsevier Science B.V.)

this study we are not able to evaluate the permittivity and the thickness of the cell membrane independently.

One can see (Table 5; Fig. 55) that the membrane capacitance (or the similar parameter ε_m/d) has different values for the different cell populations. These parameters for B-normal cells exceed by 11% the values for the T-normal ones. Even more dramatic is the difference between the value of the membrane capacitance of the normal cells and that for all the malignant cells.

For B lymphocytes the capacitance of the normal cells is higher than that of all the malignant cells. The same parameter for the EBV-transformed line (Magala) is intermediate between the values for normal and malignant cells. According to statistical analysis by the t-test, the difference between transformed (Magala) and malignant lines is statistically significant (t-test gives the probability $0.01 < \Pr < 0.02$), whereas there is no statistically significant difference between the nondividing (B normal) and transformed (Magala) populations ($\Pr > 0.2$).

As for the T-cell population, the membrane capacitance of the malignant cells (see Fig. 55) was smaller than that of the normal T cells. However, this difference was borderline statistically significant ($0.05 < \Pr < 0.1$).

As can be seen in Fig. 56 and Table 5 the membrane conductivities of normal cells of both the B and

Table 4 List of Cell Populations Studied

Cells	Radius (μm)	Number of experiments	Volume fraction of suspension (%)	Disease
B cells				
B-normal[a]	3.3	3	1.7–3.2	–
Magala	5.3	2	5.2–7	EBV immortalized
Farage	5.2	5	4.4–8.56	Non-hodgkin's lymphoma
Raji	6.4	4	4.4–6.96	Burkitt's lymphoma
Bjab	6.3	3	2–6.4	Burkitt's lymphoma
Daudi	6.8	4	2.8–6.2	Burkitt's lymphoma
T cells				
T normal[b]	3.4	2	4	–
Peer	5.1	4	2.8–6.96	Acute lymphocytic leukemia
HDMAR	5.9	2	2.8–5.2	Hodgkin's lymphoma

[a]Tonsillar B cells.
[b]Peripheral blood T cells.
Source: Ref. 72 (with permission from Elsevier Science B.V.).

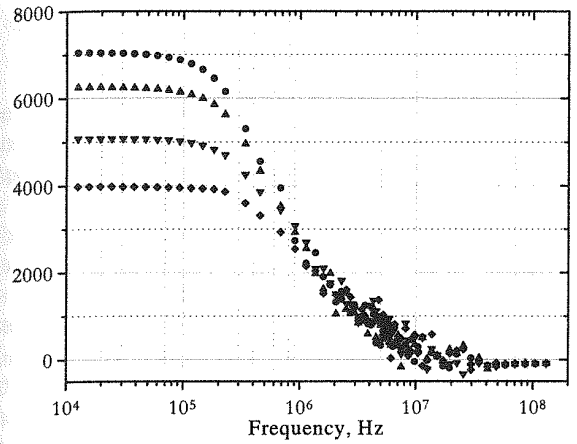

Figure 54 The real part of complex dielectric permittivity for differnt cell populations calculated from experimental suspension spectra by Maxwell–Wagner mixture model: (●) Magala; (▲) Raji; (▼) Bjab; (◆) HDMAR. (From Ref. 72. With permission from Elsevier Science B.V.)

T populations were significantly higher than for that of malignant and transformed cells. In the B-cell group, the membrane conductivity of normal cells was about six times larger than that of the average value of the malignant cell lines and the transformed cells. This difference is statistically highly significant ($Pr < 0.01$). No significant difference in the conductivity between the transformed and malignant cells in the B population were found ($Pr > 0.2$). Concerning the conductivity of T cells, the difference between normal and malignant cells was not so large as for B cells, but it was statistically significant ($0.01 < Pr < 0.02$).

The ε_{ne} value of normal B cells is about 1.3 times larger than the average value of other lines of this group (Table 5). Statistically, the difference is borderline significant ($0.05 < Pr < 0.1$).

There is a difference in the B group between normal B cells and the malignant cell lines, which is statistically high significant ($0.01 < Pr$). The normal T cells value is more than twice the average of the malignant cell lines (Table 5) and the difference is statistically significant ($0.01 < Pr < 0.02$).

The conductivity of normal B cells is larger by a factor of 1.8 than that of the average of the malignant cell lines (Table 5). This difference is statistically highly significant ($Pr < 0.01$). There is no difference in this parameter between the average of the malignant cell lines and that of the transformed cell lines. There is almost no difference between normal T cells and malignant T cells.

The normal B-cell value is larger by a factor of 1.6 or more than that of the average value of the malignant cells (Table 5), and it is statistically significant ($0.01 < Pr < 0.02$). There is a small difference between normal T cells and the average malignant cells, but this difference is statistically not significant ($0.2 < Pr$).

It is interesting to note that the conductivity of nucleoplasm is about twice that of the cytoplasm for almost all cell populations.

Table 5 Dielectric Parameters[a] of Cell Structural Parts for All Cell Populations Studied

	ε_m	σ_m ($\times 10^{-6}$S/m)	ε_{ne}	σ_{ne} ($\times 10^{-3}$S/m)	σ_{ep} (S/m)	σ_{np} (S/m)
B normal	12.8 ± 1.6	56 ± 29	106 ± 35	11.1 ± 72	1.31 ± 0.08	2.04 ± 0.29
Magala	11.4 ± 2.4	8.8 ± 0.7	72.5 ± 11.6	3.7 ± 0.9	0.55 ± 0.2	1.08 ± 0.03
Farage	9.8 ± 1.1	9.1 ± 1.4	60.3 ± 22.6	4.4 ± 2.5	0.48 ± 0.14	1.07 ± 0.43
Raji	8.8 ± 1.1	8.2 ± 0.6	79.9 ± 34.4	4.0 ± 1.6	0.58 ± 0.02	1.02 ± 0.25
Bjab	8.0 ± 0.7	11.0 ± 5.3	108 ± 35	2.1 ± 0.7	0.88 ± 0.11	1.39 ± 0.54
Daudi	7.2 ± 0.7	9.5 ± 1.4	66.1 ± 7.5	2.7 ± 0.3	0.85 ± 0.09	1.44 ± 0.35
T cells						
T normal	11.1 ± 1.4	27.4 ± 6.2	85.6 ± 16.7	8.8 ± 0.6	0.65 ± 0.13	1.26 ± 0.27
Peer	9.5 ± 0.7	12.9 ± 3.6	61.6 ± 17	2.1 ± 0.6	0.81 ± 0.09	1.42 ± 0.2
HDMAR	7.4 ± 1.2	14.5 ± 4	101.2 ± 55.3	3.0 ± 0.2	0.88 ± 0.25	1.58 ± 0.28

[a]Fitting procedure was performed by fixing the following parameters: $\varepsilon_{ep} = 60$; $\varepsilon_{np} = 120$; $d = 7$ nm; $d_n = 40$ nm, $R_n = R(0.6)^{1/3}$
Source: Ref. 72 (with permission from Elsevier Science B.V.).

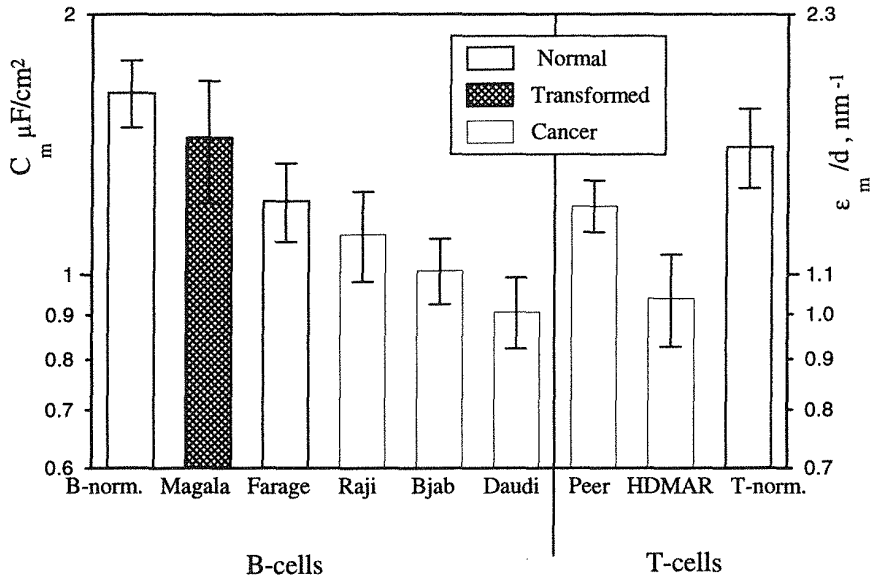

Figure 55 Capacitance of cell membrane and ratio of dielectric permittivity of the cell membrane thickness (ε_m/d) for all cell populations under investigation. Shown are the mean values of the results ±SD. (From Ref. 72. With permission from Elsevier Science B.V.)

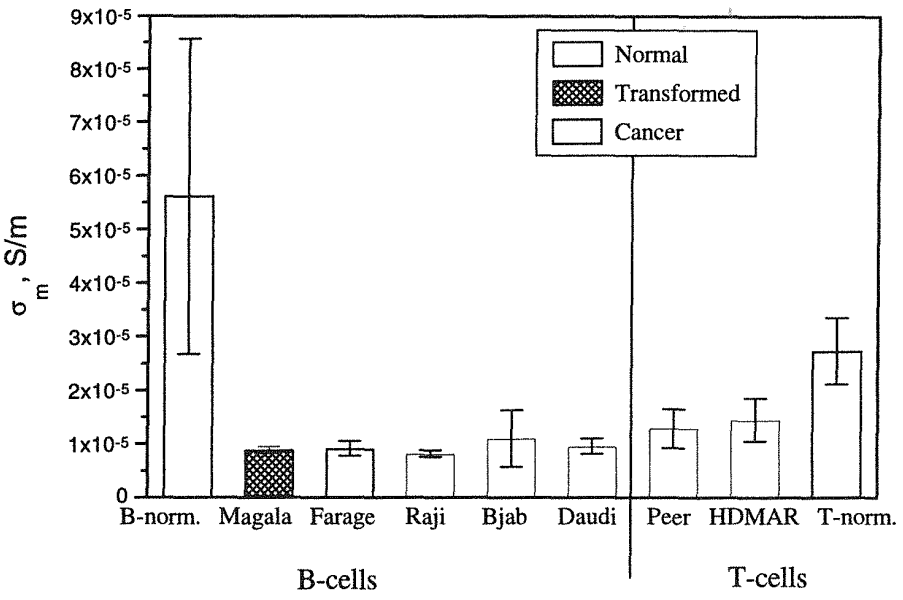

Figure 56 Conductivity of cell membrane for all populations under investigation. Shown are the mean values of the results ±SD. (From Ref. 72. With permission from Elsevier Science B.V.)

3. Main Features of Dielectric Response of Pathological Cells

The various dielectric parameters of the cell populations presented in Table 5 were obtained with cells suspended in a low-conductivity medium, in which the major components were sucrose and glucose rathr than salts. The reason for using this medium was to decrease the electrode polarization. A priori, this choice of medium raises questions about the state of the cells as compared to their native state, in which they are immersed in a solution containing salts and proteins. One can expect at least two kinds of changes when cells are transferred to a medium of low ionic strength. First, a direct change in the cell membrane integrity, and second, changes in the ionic environment within the cell due to disturbances in the cybernetic mechanism of ion regulation. Another question is whether different normal and malignant cell populations will react similarly to an alteration of the ionic strength of the environment. If changes do occur in the cells, it is important to determine their rate.

Glascoyne et al. (206) followed the change in conductivity of the medium and the leakage of K^+ after suspending various cells in low-conductivity medium. The half-time of the increase in conductivity (90% of the cation flux was of K^+ ions) was roughly 20 to 30 min, which corresponds to the value obtained by Hu et al. (200) with murine B and T lymphocytes.

In our experiments the complete measurement cycle (three repetitions) for each cell line took about 10 min and was made as soon as cells were suspended in the low-conductivity medium. Results of three successive measurements of the conductivity show very small change (noise level) of that parameter for both normal and malignant cell suspensions (72). This means that neither the ionic composition of the cells nor the cell membrane integrity changed considerably during the time required for the measurements (about 10 min) (72). This was consistent with the results of More et al. (207), Hu et al. (200), and Gascoyne et al. (206).

Furthermore, the size distribution of the cells and the microscopic morphology did not change in a noticeable way, even after an hour of suspension in the low ionic strength medium (72). It was the same as that of cells kept in their growth medium. This implies that no large changes in the intracellular ion composition occurred as a result of the suspension (208).

Our findings are consistent with the microscopic observations made by Hu et al. (200) on B and T murine lymphocytes. They also tested possible damage by the low ionic strength medium by determining the proportion of the cells that were permeable to propidium iodide. Their findings indicated that the resuspension of normal and malignant cells for not more than 10 min did not seem to effect in a considerable way the state of neither the normal nor the malignant cells.

Normal, EBV-transformed and malignant lymphocytes were recently investigated (72). Normal lymphocytes do not live for a prolonged time in culture and do not divide without addition of mitogenic stimuli. One of the methods used to immortalize lymphoid cells, so that they can live and divide under culture conditions, is to transform them with a virus such as the EBV virus. The Magala B cell line was developed in this way. Transformed cells and malignant cells share the capacity to divide in culture. Malignant cells differ from normal and transformed cells by numerous additional features. In our experiments both B- and T-cell populations could be characterized by two positive/negative properties – malignant or nonmalignant nature of the cells (cancer/noncancer), and the capacity or lack of capacity to divide (dividing/nondividing). Thus, the EBV-transformed Magala cells are noncancerous but dividing, while Farage, Raji, Bjab, Daudi, Peer, and HDMAR lines are malignant and can divide in culture. Classifying the cells in this manner and by using the *t*-test, the analysis of cell parameters was carried out,

Analysis of cell membrane capacitance (see Fig. 55) has shown that this parameter is different for various cell populations. For the B lymphocytes the capacitance of membranes of normal cells is higher than that of all malignant cells. The same parameter for the EBV-transformed line (Magala) is intermediate between the values for normal and malignant cells. This probably reflects the fact that this transformed line possesses the same dividing feature as cancer cells, but it is really noncancerous. The difference between transformed (Magala) and malignant lines is statistically significant, whereas there is no statistically significant difference between the nondividing (normal) and transformed (Magala) populations. Thus, it is reasonable to assume that in the B-cell population the decrease in specific capacitance of the cell membrane is more strongly correlated with cancer than with the dividing feature. As for the T-cell population, the membrane capacitance of the malignant cells (see Fig. 55) was smaller than that of the normal T cells. This difference was of borderline statistical significance. However, the trend of decrease in cell membrane capacitance associated with malignancy is the

same as within the B-cell group. Yet, at present, it is not possible to draw strong conclusions as in the case of the B-cell group; also, there is a lack of measurements on transformed T cells. This difficulty is true also for other parameters, even if the difference between normal T cells and the malignant ones is statistically significant.

Now let us consider the conductivity of the cell membranes (72). One can see in Fig. 56 that the membrane conductivity of normal cells of both the B and T populations was significantly higher than for that of malignant and transformed cells. There was no notable difference in the conductivity between the transformed and malignant cells in the B-cell population. Thus, in the B-cell population the decrease in cell membrane conductivity seemed to result from the dividing properties of the cells rather than from acquisition of malignant properties. Concerning the conductivity of T cells, the difference between normal and malignant cells was not so large as for B cells, but was statistically significant. Note again that no measurements for T transformed cells were performed.

For normal B cells (see Table 5) σ_{ne}, σ_{cp}, and σ_{np} are higher than for the other cell populations. Concerning the parameters of transformed cells they are in the value range of cancer cells. Thus, the dividing feature which is imminent to cancer cells as well as to transformed cells seems to be responsible for the change in these parameters in B populations.

It would be important to understand in molecular terms the mechanisms underlying the difference in the various dielectric parameters that were measured. Parameters such as conductivity and permittivity reflect the distribution of free and bound charges, in membranes, respectively, and also the polarizability of various components.

The average ionic composition of T and B human lymphocytes in the quiescent state is K^+: 130–150 mM; Na^+: 15–30 mM; Cl^-: 70–90 mM; and Ca^{2+} $\sim$ 0.1 μM. This composition has also been found in B-CLL lymphocytes (chronic lymphocytic leukemia) (209, 210). Averaging the conductivity of the cytoplasmic σ_{cp} and the nucleoplasmic σ_{np} (Table 5) of the normal B lymphocytes it was shown to have a value of 130 mM for KCl (72). Thus, as a first approximation, data on the conductivity of the inner cell solution are consistent with an assumption that the conductivities of the cytoplasm and the nucleoplasm are mainly as a result of the ionic species K^+, Cl^-, and Na^+ in aqueous media.

We want to note the fact that the conductivity of the cytoplasm is consistently lower by a factor of $\sim$ 2 than that of the nucleoplasm. This was invariably found in all B- and T-cell lines, both normal and malignant (Table 5). If the conductivity of either the cytoplasm or nucleoplasm indeed expresses mainly the transport of small ions, such as K^+, Cl^-, and Na^+ in an aqueous environment, then there must be a selective barrier between the above two phases, which is very likely the nuclear envelope (NE).

The NE of eukaryotic cells is made up of two concentric membranes, the inner and the outer envelope membrane (211). They are separated by the perinuclear space, but fuse at specific points, where they form the nuclear pore complex. The nuclear pore is composed of up to 100 different proteins, arranged in two octagonal arrays. The nuclear pores are believed to regulate the bidirectional nucleocytoplasm transport of macromolecules, such as mRNA, transcription factors, proteins, etc., which is a process that requires metabolic energy. This means that they indeed act as diffusion barriers. The open inner diameter of the pore was shown to be approximately 90 Å. The large diameter of nuclear pores has led to the conclusion that the nuclear pores are unable to regulate fluxes of ions (diameter of 3 to 4 Å) or maintain a gradient of ions across the NE. Studies, using the "patch-clamp" technique, have detected ion-channels' activity at the NE (212, 213). These findings put into focus the regulation of nuclear ions by the NE. Several classes of K^+-selective ion channels were recorded by patch-clamp techniques, with conductances of 100 to 550 pS in nuclei of different cells. Also a large, cation-selective ion channel with a maximum conductance of 800 pS in 100 mM KCl was detected. This channel is a possible candidate for the open nuclear pore, as its conductance is consistent with the geometrical dimension of the open pore. It is important to notice that this channel is open only for short times, and is mainly in the closed mode. These findings are consistent with older data (213) on microelectrode studies with in-situ nuclei, which claimed to measure a potential difference across the NE and reported low electrical conductance of that membrane complex.

The findings that the NE acts as a diffusion barrier can explain the fact that the nucleoplasm and the cytoplasm can have a different steady-state conductivity and probably also different compositions.

As shown in Table 5, the electrical conductivity of the NE is larger by two orders of magnitude than that of the cell membrane. We would then expect that the numbers of ionic channels and their nature, including their gating mechanism, would then be very different in these two types of cellular membranes.

The ability of the noninvasive TDS technique to analyze in situ the properties of the intracellular structures is very important. If indeed the two-shell model represents also the NE and the nucleoplasm, then it describes the very regions of the cell where the putative control of cell division resides, and also the region where the gene expression takes place. Electrical methods are relatively easy to apply (72, 214) and can lead the molecular biologist to decipher more rationally the control mechanism of cell growth in situ.

ACKNOWLEDGMENTS

The University of Bergen (Foundation for Senior Research Fellowship) is thanked for a grant to Professor Yuri Feldman, facilitating his contribution to this review during his stay in Bergen. The Flucha program, financed by the Norwegian Research Council (NFR) and the oil industry, is also acknowledged for financial support.

REFERENCES

1. H Fröhlich. Theory of dielectrics. Dielectric constant and Dielectric Loss. 2nd ed. Oxford: Clarendon Press, 1958.
2. CJF Böttcher. Theory of Electric Polarization, Vol 1. 2nd ed. Amsterdam: Elsevier Science B.V., 1993.
3. CJF Böttcher, P Bordewijk. Theory of Electric Polarization, Vol 2. 2nd ed. Amsterdam: Elsevier Science B.V., 1992.
4. NE Hill, WE Yaughan, AH Price, M Davis. Dielectric Properties and Molecular Behavior. London: Van Nostrand, 1969.
5. N Kozlovich, Yu Alexanadrov, A Pusenko, Yu Feldman. Colloids Surfaces A 140: 229–312, 1998.
6. S Havriliak, SJ Havriliak. Polymer 37: 4107, 1996.
7. RR Nigmatullin, YE Ryabov. Phys Solid State. 39: 87, 1997.
8. L Nivanen, R Nigmatullin, A LeMehaute. Le Temps Irreversible a Geometry Fractale. Paris: Hermez, 1998.
9. RH Cole. Dielectric Polarization and Relaxation. NATO ASI Ser., Ser. C, Vol 135. Molecular Liquids, 1984, p 59–110.
10. Yu D Feldman, VV Levin. Chem Phys Lett 85: 528, 1982.
11. T Hanai. Kolloidn Zh. 177: 57, 1960.
12. SS Dukhin, VN Shilov. Dielectric Phenomena and the Double Layer in Disperse Systems and Polyelectrolytes. trans., D Lederman. New York: Halsted Press, 1974.
13. R Pethig. Dielectric and Electronic Properties of Biological Materials. Chichester: John Wiley, 1979.
14. S Takashima. Electric Properties of Biopolymers and Membranes. Bristol: Adam Hilger, 1989.
15. B Nettelblad, GA Niklasson. J Mater Sci 32: 3783, 1997.
16. EM Trukhan. Soviet Phys – Solid State. 4: 2560, 1963.
17. TS Sørensen. J Colloid Interface Sci 168: 437, 1994.
18. JC Maxwell. A Treatise of Electricity & Magnetism, articles 310–314. New York: Dover, 1954 (originally Clarendon Press, 1891).
19. KW Wagner. Arch Electrotech 2: 371, 1914.
20. H Fricke, HJ Curtis. J Phys Chem 41: 729, 1937.
21. RW Sillars. J Inst Electr Engrs 80: 378, 1937.
22. DAG Bruggemann. Ann Phys Lpz 24: 636, 1935.
23. T Hanai. In: P Sherman, ed. Emulsion Science. New York: Academic Press, 1968.
24. C Boned, J Peyrelasse. Colloid Polymer Sci 261: 600, 1983.
25. MH Boyle. Colloid Polymer Sci 263: 51, 1985.
26. P Debye, E Hückel. Phys Z 24: 185, 1923.
27. J Sjöblom, B Jönsson, C Nylander, I Lundström. J Colloid Interface Sci 96: 504, 1983.
28. J Lyklema, SS Dukhin, VN Shilov. J Electroanal Chem 143: 1, 1983.
29. JF Rathman, JF Scamehorn. J Phys Chem 88: 5807, 1984.
30. C Grosse, KR Foster. J Phys Chem 91: 3073, 1987.
31. R Barchini, DA Saville. J Colloid Interface Sci 173: 86, 1995.
32. G Schwarz. J Phys Chem 66: 2636, 1962.
33. RH Cole, JG Berberian, S Mashimo, G Chryssik, A Burns, E Tombari. J Appl Phys 66: 793, 1989.
34. S Mashimo, T Umehara, T Ota, S Kuwabara, N Shinyashiki, S Yagihara. J Molec Liquids 36: 135, 1987.
35. D Bertolini, M Cassettari, G Salvetti, E Tombari, S Veronesi. Rev Sci Instrum 61: 450, 1990.
36. R Nozaki, TK Bose. IEEE Trans Instrum Meas 39: 945, 1990.
37. B Gestblom, E Noreland, J Sjöblom. J Phys Chem 91: 6329, 1987.
38. Yu Feldman, A Andrianov, E Polygalov, G Romanychev, I Ermolina, Yu Zuev, B Milgotin. Rev Sci Instrum 67: 3208, 1996.
39. A Schönhals, F Kremer, E Schlosser. Phys Rev Lett 67: 999, 1991.
40. U Kaatze, V Lonneckegabel, R Pottel. Z Phys Chem (Int J Res Phys) 175: 165, 1992.
41. K Folgerø, T. Friisø, J Hilland, T Tjomsland. Meas Sci Technol 6: 995, 1995.
42. JG Berberian. J Molec Liquids 56: 1, 1993
43. B Gestblom, P Gestblom. Macromolecules 24: 5823, 1991.
44. YuD Feldman, YuF Zuev, EA Polygalov, VD Fedotov. Colloid Polymer Sci 270: 768, 1992.

45. N Miura, N Shinyashiki, S Yagihara, M Shiotsubo. J Am Ceram Soc 81: 213, 1998.
46. Yu Feldman, V Levin. Chem Phys Lett 85: 528, 1982.
47. AM Bottreau, A Merzouki. IEEE Trans Instrum Meas 42: 899, 1993.
48. EK Miller, ed. Time Domain Measurements in Electromagnetics. New York: Van Nostrand Reinhold, 1986.
49. NE Hager III. Rev Sci Instrum 65: 887, 1994.
50. O Götmann, U Kaatze, P Petong. Meas Sci Technol 7: 525, 1996.
51. JG Berberian, RH Cole. Rev Sci Instrum 63: 99, 1992.
52. B Gestblom, H Førdedal, J Sjöblom. J Disp Sci Technol 15: 449, 1994.
53. T Skodvin, T Jakobsen, J Sjöblom. J Disp Sci Technol 15: 423, 1994.
54. GQ Jiang, WH Wong, EY Raskovich, WG Clark, WA Hines, J Sanny. Rev Sci Instrum 64: 1614, 1993.
55. T Jakobsen, K Folgerø. Meas Sci Technol 8: 1006, 1997.
56. YJ Lu, HM Cui, J Yu, S Mashimo. Bioelectromagnetics 17: 425, 1996.
57. S Naito, M Hoshi, S Mashimo. Rev Sci Instrum 67: 3633, 1996.
58. JZ Bao, ST Lu, WD Hurt. IEEE Trans Microwave Theory Technol 45: 1730, 1997.
59. T Skodvin, J Sjöblom. Colloid Polym Sci 274: 754, 1996.
60. MS Seyfried, MD Murdock. Soil Sci 161: 87–98, 1996.
61. JM Anderson, CL Sibbald, SS Stuchly. IEEE Trans Microwave Theory Technol 42: 199, 1994.
62. DV Blackham, RD Pollard. IEEE Trans Instrum Meas 46: 1093, 1997.
63. HP Schwan. Ann NY Acad Sci 148: 191, 1968.
64. EH Grant, RJ Sheppard, GP South. Dielectric Behavior of Biological Molecules in Solution. Oxford: Clarendon Press, 1978.
65. J Lyklema. Fundamentals of Interface and Colloid Science. Vol II. Solid–Liquid Interfaces. London: Academic Press, 1995.
66. J O'M Bockris, AKN Reddy. Modern Electrochemistry. Vol 2. New York: Plenum Press, 1977.
67. HP Schwan. Ann Biomed Eng 20: 269, 1992.
68. HP Schwan. Physical Techniques in Biological Research. Vol 6. New York: Academic Press, 1963.
69. CL Davey, GH Marks, DB Kell. Eur Biophys J 18: 255, 1990.
70. R Lisin, B Ginzburg, M Schlesinger, Yu Feldman. Biochim Biophys Acta 1280: 34, 1996.
71. Yu Feldman, R Nigmatullin, E Polygalov, J Texter. Phys Rev E 58: 2179, 1998.
72. Yu Polevaya, I Ermolina, M Schlesinger, B-Z Ginzburg, Yu Feldman. Biochim Biophys Acta 1419: 257–271, 1999.
73. I Ermolina, V Fedotov, Yu Feldman. Phisica A 249: 347, 1998.
74. RR Nigmatullin, in The Proceedings of Bordeaux Summer School–Geometrie Fractale et Hyperbolique. Derivation Fractionnaire et Fractale 3–8 July 1994. Fractals, Solutions and Chaos 11: 1994.
75. T Pajkossy, L Nyikos. Phys Rev B 42: 709, 1990.
76. T Pajkossy. J Electroanal Chem 364: 111, 1994.
77. T Pajkossy, AP Borosy, A Imre, SA Martemyanov, G Nagy, R Schiller, L Nyikos. J Electroanal Chem 366: 69, 1994.
78. SH Liu, Phys Rev Lett 55: 529–532, 1985.
79. T Kaplan, LJ Gray. Phys Rev B 32: 7360, 1985.
80. RM Hill, LA Dissado, RR Nigmatullin. J Phys Condens Matter 3: 9773, 1991.
81. K Oldham, J Spanier. The Fractional Calculus. New York: Academic Press, 1974.
82. M Stromme, A Niklasson, CG Granqvist. Phys Rev B 52: 14192, 1996.
83. JB Hasted. Aqueous Dielectrics. London: Chapman and Hall, 1973.
84. EH Grant, TJ Buchanan, HF Cook. J Chem Phys 26: 156, 1957.
85. B Gestblom, S Urban. Z Naturforsch 50a: 595, 1995.
86. B Pettersen, T Skodvin, J Sjöblom. Colloids Surfaces A 143: 323, 1998.
87. SE Friberg. Microemulsions: Structure and Dynamics. Boca Raton, FL: CRC Press, 1987.
88. B Lindman, ed. Surfactants, Adsorption, Surface Spectroscopy and Disperse Systems. Darmstadt: Steinkopff, 1985.
89. D Langevin, Annu Rev Phys Chem 43: 341, 1992.
90. J Sjöblom, R Lindberg, SE Friberg. Adv Colloid Interface Sci 95: 125, 1996.
91. U Olsson, K Shinoda, B Lindman. J Phys Chem 90: 4083, 1986.
92. PG DeGennes, C Touplin. J Phys Chem 86: 2294, 1982.
93. R Strey, MJ Jonströmer. J Phys Chem 96: 4537, 1992.
94. R Kahlweit, R Strey and G Busse. J. Phys. Chem., 95, 5344, 1991.
95. MA Dijk, G Casteleijn, JGH Joosten, YK Levine. J Chem Phys 85: 626, 1986.
96. Yu Feldman, N Kozlovich, I Nir, N Garti. Phys Rev E 51: 478, 1995.
97. Yu Feldman, N Kozlovich, Y Alexandrov, R Nigmatullin, Y Ryabov. Phys Rev E 54: 5420, 1996.
98. C Cametti, P Codastefano, P Tartaglia, S Chen, J Rouch. Phys Rev A 45: R5358, 1992.
99. F Bordi, C Cametti, J Rouch, F Sciortino, P Tartaglia. J Phys: Condens Matter A19: 8, 1996.
100. C Boned, J Peyrelasse, Z Saidi. Phys Rev E 47: 468, 1993.
101. A Ponton, TK Bose, G Delbos. J Chem Phys 94: 6879, 1991.
102. A D'Aprano, G D'Arrigo, A Paparelli. J Phys Chem 97: 3614, 1993.
103. M Wasserman. Russ Chem Rev 63: 373, 1994.

104. F Mallamace, N Micali, C Vasi, G D'Arrigo. Phys Rev A 43: 5710, 1991.
105. F Sicoli, D Langevin. J Phys Chem 99: 14819, 1995.
106. M Clausse. In: P Becher, ed. Encyclopedia of Emulsion Technology. Basic Theory. Vol 1. New York: Marcel Dekker, 1983.
107. Yu Feldman, N Kozlovich, I Nir, N Garti, V Archipov, Z Idiyatullin, Y Zuev, V Fedotov. J Phys Chem 100: 3745, 1996.
108. JA Beunen, E Ruckenstein. J Colloid Interface Sci. 96: 469, 1983.
109. E Ruckenstein, JA Beunen. Langmuir 4: 77, 1988.
110. HF Eicke, M Bercovec, B Das-Gupta. J Phys Chem 93: 314, 1989.
111. DG Hall, J Phys Chem 94: 429, 1990.
112. SI Chou, DO Shah. J Phys Chem 85: 1480, 1981.
113. C Cametti, P Codastefano, P Tartaglia. Ber Bunsenges Phys Chem 94: 1499, 1990.
114. J Peyrelasse, C Boned. J Phys Chem 89: 370, 1985.
115. MA Dijk, JGH Joosten, YK Levine, D Bedeaux. J Phys Chem 93: 2506, 1989.
116. J Lang, A Jada, A Malliaris. J Phys Chem 92: 1946, 1988.
117. N Kozlovich, A Puzenko, Yu Alexandrov, Yu Feldman. Phys Rev E 58: 2179, 1998.
118. M D'Angelo, D Fioretto, G Onori, L Palmieri, A Santucci. Phys Rev E 52: R4620, 1995.
119. M D'Angelo, D Fioretto, G Onori, L Palmieri, A Santucci. Phys Rev E 54: 993, 1996.
120. G Giammona, F Goffrede, V Turco Liveri, G Vassallo. J Colloid Interface Sci 154: 411, 1992.
121. P Huang Kenez, G Carlström, I Furo, B Halle. J Phys Chem 96: 9524, 1992.
122. M Tomic, N Kallay. J Phys Chem 96: 3874, 1992.
123. P Karpe, E Ruckenstein. J Colloid Interface Sci 137: 408, 1990.
124. M Boas. Mathematical Methods in Physical Sciences. New York: John Wiley, 1983, p 12.
125. M Belletete, M Lachapelle, G Durocher. J Phys Chem 94: 5337, 1990.
126. ALR Bug, SA Safran, GS Grest, I Webman. Phys Rev Lett 55: 1896, 1985.
127. G Grest, I Webman, S Safran, A Bug. Phys Rev A 33: 2842, 1986.
128. C Cametti, P Codastefano, A Di Biasio, P Tartaglia, S Chen. Phys Rev A 40: 1962, 1989.
129. J Klafter, A Blumen. Chem Phys Lett 119: 377, 1985.
130. J Klafter, MF Shlesinger. Proc Natl Acad Sci USA 83: 848, 1986.
131. D Stauffer, A Aharony. Introduction to Percolation Theory. Revised 2nd edn. London: Taylor & Francis, 1994.
132. D Vollmer, J Vollmer, HF Eicke. Europhys Lett 26: 389, 1994.
133. D Vollmer. Europhys Lett 27: 629, 1994.
134. BB Mandelbrot. The Fractal Geometry of Nature. New York: Freeman, 1982.
135. F Feder. Fractals. New York: Plenum Press, 1988.
136. S-H Chen, J Rouch, F Sciortino, P Tartaglia. J Phys: Condens Matter 6: 10855, 1994.
137. A Bunde, S Havlin, J Klafter, G Graff, A Shehter. Phys Rev Lett. 78: 3338, 1997.
138. LH Peebles, Jr. Molecular Weight Distributions in Polymers. New York: Wiley-Interscience, 1971.
139. RR Nigmatullin. J Appl Magn Reson 14: 601, 1998.
140. Yu Alexandrov. Dielectric Spectroscopy Investigation of Dynamic and structural properties of microemulsions. Thesis. Jerusalem, 1998.
141. Yu Feldman, N Kozlovich, I Nir, N Garti. Colloids Surfaces A 128: 47, 1997.
142. J Sjöblom, B Gestblom. J Colloid Interface Sci 115: 535–544, 1987.
143. Yu Feldman, N Kozlovich, I Nir, A Aserin, S Ezrahi, N Garti. J Non-Crystal Solids 172–174: 1109, 1994.
144. SC Mehrotra, B Gestblom, J Sjöblom. Finn Chem Lett 34: 87, 1985.
145. E Noreland, B Gestblom, J Sjöblom. J Solution Chem 18: 303, 1989.
146. MK Kreoger. J Molec Liquids 36: 101, 1987.
147. PC Brot. Ann Phys 2: 714, 1957.
148. SK Garg, CP Smyth. J Phys Chem 69: 1294, 1965.
149. VV Levin, YuD Feldman. Chem Phys Lett 87: 162, 1982.
150. M Fukuzaki, U Toshihiro, D Kurita, S Shioya, M Haida, S Mashimo. J Phys Chem 96: 1087, 1992.
151. Y Marcus. Cell Biochem Function 13: 157, 1995.
152. U Kaatze. J Solution Chem 28: 1049, 1997.
153. J Sjöblom, B Gestblom. In: SE Friberg, B Lindman, eds. Organized Solutions. Surfactants in Science and Technology. New York: Marcel Dekker, 1992, p 193.
154. A Kraszewski. J Microwave Power 12: 215, 1977.
155. A Kraszewski, S Kulinski, M Matuszewski. J Appl Phys 47: 1275, 1976.
156. N Kozlovich, I Nir, B Tsentsiper, VI Zhuravlev, A Aserin, S Ezrahi, N Garti, Yu Feldman. J Surfc Sci Technol. in press.
157. N Garti, A Aserin, S Ezrahi, I Tiunova, G Berkovic. J Colloid Interface Sci 178: 60, 1996.
158. K Asami, T Hanai. Colloid Polymer Sci 270: 78, 1992.
159. ID Chapman. J Phys Chem 75: 537, 1971.
160. B-M Sax, G Schön, S Paasch, MJ Schwuger. Progr Colloid Polymer Sci 77: 109, 1988.
161. T Hanai. Kolloidn Zh 171: 23, 1960.
162. T Hanai. Kolloidn Zh 175: 62, 1961.
163. U Genz, JA Helsen, J Mewis. J Colloid Interface Sci. 165: 212, 1994.
164. J Sjöblom, T Skodvin, T Jakobsen, SS Dukhin. J Disp Sci Technol 15: 401, 1994.
165. T Skodvin, J Sjöblom, JO Saeten, O Urdahl, B Gestblom. J Colloid Interface Sci 166: 43, 1994.

166. T Skodvin, J Sjöblom. J Colloid Interface Sci 182: 190, 1996.
167. T Hanai, K Sekine. Colloid Polymer Sci 265: 888, 1986.
168. T Skodvin, J Sjöblom, JO Saeten, T Wärnheim, B Gestblom. Colloids Surfaces A 83: 75, 1994.
169. J Sjöblom, T Skodvin, T Jakobsen. J Disp Sci Technol 15: 423, 1994.
170. H Førdedal J Sjöblom. J Colloid Interface Sci 181: 1996, 589–594.
171. G Capuzzi, P Baglioni, CMC Gambi, EY Sheu. Phys Rev E 60: 792, 1999.
172. J Peyrelasse, M Moha-Ouchane, C Boned. Phys Rev A 38: 904, 1988.
173. C Thomas, JP Perl, DT Wasan. J Colloid Interface Sci 139: 1, 1990.
174. JP perl, HW Bussey, DT Wasan. J Colloid Interface Sci 108: 528, 1985.
175. M von Stackelberg. Naturwissenschaften 11: 327, 1949.
176. M von Stackelberg, HR Müller. Z Elektrochem 58: 25, 1954.
177. M von Stackelberg, W Jahns. Z Elektrochem 58: 162, 1954.
178. JA Ripmeester, JS Tse, CI Ratcliffe, BM Powell. Nature 325: 135, 1987.
179. T Jakobsen, J Sjöblom, P Ruoff. Colloids Surfaces A 112: 73, 1996.
180. J Sjöblom, H Førdedal, T Jakobsen, T Skodvin. In: KS Birdi, ed. Handbook of Surfactants. Boca Raton, FL: CRC Press, 1997.
181. B Pettersen, J Sjöblom. Colloids Surfaces A 113: 175, 1996.
182. B Pettersen, L Bergflødt, J Sjöblom. Colloids Surfaces A 127: 175, 1997.
183. HP Schwan. Adv Biol Med Phys 5: 147, 1957.
184. F Bordi, C Cametti, A Rosi, A Calcabrini. Biochim Biophys Acta 1153: 77–88, 1993.
185. H Looyenga. Physica 31: 401, 1965.
186. T Hanai, K Asami, N Koizumi. Bull Inst Chem Res Kyoto Univ 57: 297, 1979.
187. K Asami, T Hanai, N Koizumi. Jap J Appl Phys 19: 359, 1980.
188. K Asami, Y Takahashi, S Takashima. BBA 1010: 49, 1989.
189. K Asami, A Irimajiri. Biochim Biophys Acta 778: 570, 1984.
190. A Irimajiri, T Hanai, A Inouye. J Theor Biol 78: 251, 1979.
191. A Irimajiri, Y Doida, T Hanai, A Inouye. J Mem Biol. 38: 209, 1978.
192. K Asami, Y Takahashi, S Takashima. Biophys J. 58: 143, 1990.
193. H Fricke. Nature 4381: 731, 1963.
194. H Fricke. J Phys Chem 57: 934, 1953.
195. R Pethig, DB Kell. Phys Med Biol 32: 933, 1987.
196. A Surowiec, SS Stuchly, C Izaguirre. Phys Med Biol 31: 43, 1986.
197. FF Becker, X-B Wang, Y Huang, R Pethig, J Vykoukal, PRC Gascoyne. Proc Natl Acad Sci USA 92: 860, 1995.
198. A Irimajiri, K Asami, T Ichinowatari, Y Kinoshita. Biochim Biophys Acta 869: 203, 1987.
199. A Irimajiri, K Asami, T Ichinowatari, Y Kinoshita. Biochim Biophys Acta 896: 214–223, 1987.
200. X Hu, WM Arnold, U Zimmerman. Biochim Biophys Acta 1021: 191–200, 1990.
201. GW Snedecor, WG Cochran. Statistical methods. Ames, IA: The Iowa State College Press, 1956.
202. H Pauly, P Schwan. Z Naturforsch 14b: 125, 1959.
203. I Ermolina, Yu Polevaya, Yu Feldman. Eur Biophys J Biophy 29: 141–145, 2000.
204. M Ginzburg, B-Z Ginzburg. Biochim Biophys Acta 584: 398, 1979.
205. A Zmiri, Z Ginzburg. Plant Sci Lett 30: 211, 1983.
206. PRC Gascoyne, R Pethig, JPH Burt, FF Becker. Biochim Biophys Acta 1149: 119–120, 1993.
207. R More, I Yron, S Ben-Sasson, DW Weiss. Cellular Immunol 15: 382, 1975.
208. BCK Rossier, K Geeringh, JP Kraehenbuhl. Trends Biochem Sci 12: 483, 1987.
209. GB Segal, MA Lichtman. J Cell Physiol 93: 277, 1977.
210. S Grinstein, J Dixon. Physiol Rev 69: 417, 1989.
211. C Dingwell, R Laskey. Science 258: 942, 1992.
212. AJM Matzke, AM Matzke. Bioelectrochem Bioenergetics 25: 357, 1991.
213. JO Bustamente. J Mem Biol 138: 105, 1994.
214. MT Santini, C Cametti, PL Indovina, G Morelli, G Donelli. J Biomed Mater Res 35: 165, 1997.

16

Lignosulfonates and Kraft Lignins as O/W Emulsion Stabilizers Studied by Means of Electrical Conductivity

Stig Are Gundersen
University of Bergen, Bergen, Norway

Johan Sjöblom
Statoil A/S, Trondheim, Norway

I. INTRODUCTION

A. Creaming of Emulsions

Emulsions are thermodynamically unstable systems and will, as a function of time, separate to minimize the interfacial area between the oil phase and the water phase. If a density difference exists between the dispersed and continuous phases, dispersed droplets experience a vertical force in a gravitational field. The gravitational force is opposed by the fractional drag force and the buoyancy force. The resulting creaming rate v_0 of a single droplet is given by Stokes law:

$$v_0 = \frac{2r^2(\rho_1 - \rho_2)}{9\eta} g \tag{1}$$

in which r is the hydrodynamic radius of the droplet, ρ_1 and ρ_2 are the densities of the dispersed and the continuous phases, respectively, η is the macroscopic shear viscosity of the continuous phase, and g is the gravitational constant. Stokes law has several limitations and is strictly applicable only for noninteracting spherical droplets at low concentration with a monodisperse droplet size distribution. Prediction or calculation of creaming rates in concentrated emulsions where other than hydrodynamic factors come to account is therefore complicated. Conductivity measurements have appeared to be a suitable method for determination of emulsion stability in such systems. The conductivity of emulsifons is sensitive to small changes in the volume frame of the dispersed phase, and the technique has previously been applied to predict the inversion points of emulsions (1, 2). Also, studies of sedimentation processes, creaming stability, and phase separation, utilizing this technique have been reported (3–5).

In this chapter two methods based on conductivity measurements were used to determine creaming profiles and creaming rates of water-continuous emulsions stabilized with lignosulfonates (LSs) and Kraft lignins. In the first part the influence of LS and Kraft lignin concentration on emulsion stability was studied. These emulsions had a narrow dispersion band when creaming, which made it possible to read the amount of water separated from the emulsions directly from the creaming profiles. This was achieved by designing the electrode in such a way that the conductivity was measured in a stepwise manner as the creaming progressed. In the second part the influence of electrolyte concentration on emulsion stability was studied. In this part, two pairs of electrodes were used to measure the conductivity progressively in the time interval under study, and the stability was reported in terms of initial creaming rates

and as the change in specific conductivity as a function of time. The two methods of measuring emulsion stability are discussed in Secs II and III, respectively.

B. Lignosulfonates and Kraft Lignins

Lignosulfonates and Kraft lignins are isolated from spent liquors used in the sulfite pulping and Kraft pulping process, respectively (6). Lignosulfonates are cross-linked polydisperse polyelectrolytes in which the molecules are compact spheres in aqueous solutions (7). The molecule contains sulfonate groups as well as carboyxlic, phenolic, and methoxyl groups, and the basic repeating building unit in the molecule is a phenylpropane derivative (8). The structure may be nonuniform with regard both to number and distribution of anionic groups, and also in the structure of the hydrocarbon backbone. Owing to the ionic groups in the interior of the molecule, LSs show typical polyelectrolyte expansion, where the LS molecule swells or shrinks as the concentration of the counterions varies from low to high, respectively (9, 10). The charged sulfonate groups near the surface of the molecule matrix makes LSs readily soluble in water (11). Purified LSs have found widespread practical applications because of their dispersing, stabilizing, binding, and complexing properties (12–14). Like LSs, Kraft lignins are cross-linked polydisperse polyelectrolytes, and sulfonated Kraft lignins find similar uses as LSs.

C. Lignosulfonates and Kraft Lignins as Emulsion Stabilizers

Several authors have studied the colloidal properties of particulate dispersions stabilized with Kraft lignins and LSs (15–18). From a commercial point of view the dispersing, stabilizing, binding, and complexing properties of these polyelectrolytes have made lignosulfonates useful in a range of practical applications (19–21). Several studies have also revealed that LSs are exceptional oil-in-water (O/W) (22, 23) emulsion stabilizers. Lignosulfonates have also been utilized in technical applications such as viscosity controllers in oil-well drilling fluids (24) and in improvement of the oil recovery efficacy (25–30).

Although LS does not form micelles, the molecule has both hydrophilic and lipophilic moieties. However, those two parts are not separated in a way that promotes high surface activity. The nonsolubility of LS in aliphatic and aromatic hydrocarbons, and the lack of a pronounced surface and interfacial tension-lowering properties, indicates that LS adsorbs at the oil–water interface rather than in the interface (31). A solution pressure has to be developed by the LS to force it into the interface. This means that a relatively high amount of LS must be added to give stable emulsions. The semirigid film gives rise to mechanical, steric, and electrostatic stabilization (12, 15). The solubility of LS is reduced in electrolyte-contaminated solutions, and this will force more LS to the oil–water interface. A reduction in emulsion stability, due to a reduction in the zeta potential on the oil droplets, will be compensated for by an increase in the condensed-layer adsorption. This leads to stable emulsions even in saturated salt solutions (12).

Lignosulfonates are of a highly polydisperse nature. There are indications that the low molecular weight fractions associate in solution and that high molecular weight fractions have a higher degree of molecular branching than the lower fractions (32, 33). Several investigations have shown that the LSs can function as dispersants or flocculants, depending on their molecular weight (13, 17, 18). Low molecular weight LSs act as stabilizers, while higher molecular weight LSs are of sufficient molecule length to enable them to be adsorbed on to the surface of adjacent particles. This bridging will promote flocculation and destabilize the dispersion. Other authors have reported better dispersant properties for high molecular weight LSs in concentrated kaolin suspensions (17). The influence of molecular weight on dispersant properties indicates that this molecular property will also affect the stabilities of water-continuous emulsions. Adsorption of LS on to negatively charged polystyrene latex surfaces indicates that the adsorption process is not only governed by electrostatic interactions, but also by a sort of hydrophobic interaction. It has been proposed that the hydrophobic phenlypropane ring may be of significance in this respect (17).

II. CONDUCTIVITY MEASUREMENTS AND INFLUENCE OF KRAFT LIGNIN AND LIGNOSULFONATE CONCENTRATION ON EMULSION STABILITY

A. Experimental

1. Materials and Sample Preparation

The sodium LSs (UP364, UP365, UP366, UP407, and UP411) and the Kraft lignin (Diwatex UP329) referred to in this section were delivered by Borregaard Lignotech. The properties of the lignin samples are described in a previous work (22) and here summarized in Tables 1, 2, and 3. Details of the emulsion-prepara-

Table 1 Properties of the Sodium Lignosulfonate Fractions

Sample description	UP364	UP365	UP366	UP407	UP411
pH (10% solution)	9.4	9.6	8.8		
Solids (%)	92	96.5	97.2		
Calcium (%)	0.11	0.02	0.06		
Sodium (%)	5.94	6.03	7.17		
Total S (%)	6.2	6.1	7.1	4.7	6.4
Inorg. S (%)	0.01	0.07	0.28	0.2	0.1
Org. S (%)	6.1	6.0	6.8	4.5	6.3
Methoxyl (%)	11.9	12.1	9.2	12.7	10.8
Carboyxl (%)	4.5	5.4	5.9		
Phenolic OH (%)	2.4	2.4	2.4		
Reducing Sugars (%)	0.6	0.4	4.3		
Mol. weight (HPLC)					
M_w	62,700	76,400	9300		
M_n	13,900	16,300	5100		

tion procedures are described in the same paper, although it is worth mentioning that the oil/water ratio was held constant [40/60 (w/w)], and that the LS and Kraft lignin concentrations are reported on the basis of the internal phase weight.

2. Conductivity Measurements and Electrode Design

Immediately after production, a cylindrical glass container ($d = 25$ mm; $h = 185$ mm) containing the electrode was filled with 90 ml of the emulsion. The electrode was connected to a Hewlett-Packard 4263B LCR Meter operating at a frequency of 1 kHz, and the conductivity was measured every 60 s under constant-temperature conditions (25.0° ± 0.1°C). The electrode was coated with gold to eliminate polarization effects and corrosion of the electrode material.

The electrode was made up of two 210-mm iron rods of 1 mm diameter. The lower 30 mm of the electrode was divided into insulated and noninsulated areas in the following way: 0–7, 10–17, and 20–27 mm and from 30 mm up to the connection points were insulated areas, while the areas between were noninsulated. Teflon was used as insulating material. Figure 1 demonstrates how the electrode was placed in the measuring cell.

B. Results and Discussion

1. Stepwise Conductivity Measurements

The creaming process in the emulsions studied resulted in a distinct boundary between the water-rich and oil-rich phases. A freshly prepared emulsion had a white appearance. After a few minutes a dark-brown zone containing LS and water could be seen in the lower part of the cell. Samples from the water-rich phases were studied using VEM (video-enhanced microscopy)

Table 2 Molecular Weight of Desulfonated and High Sulfonated Sodium Lignosulfonates

Molecular weight (g/mol)	UP407 (%)	UP411 (%)
> 59,000	14.9	2.8
< 59,000	85.1	97.2
< 38,000	72.2	89.2
< 16,000	47.9	70.9
< 6600	26.2	48.8
< 2755	12.2	26.0
< 1740	8.3	16.6

Table 3 Properties of the Kraft Lignin Fraction

Sample description	Diwatex UP329	Molecular weight (g/mol)	(%)
pH (10% solution)	10.6	> 12,500	30.8
Solids (%)	97.9	< 12,500	69.2
Total S (%)	5.5	< 10,000	58.7
Inorg. S (%)	0.6	< 7000	45.5
Org. S (%)	4.8	< 5000	33.1
Methoxyl (%)	10.2	< 3000	19.2
Carboxyl (%)	8.1	< 2000	10.3
Phenolic OH (%)	1.9	< 1000	1.5

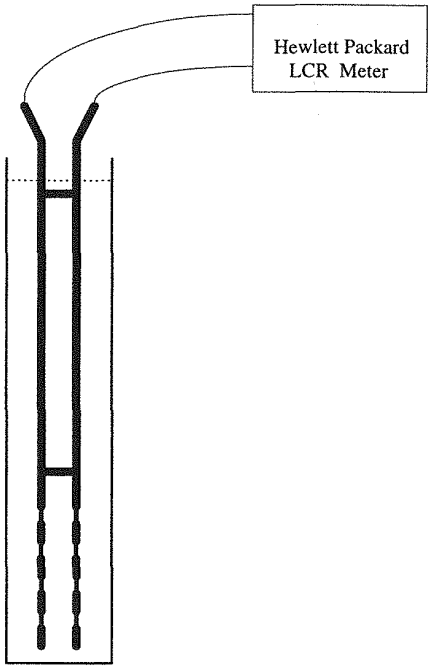

Figure 1 Schematic figure of the electrode where the isolated and nonisolated areas are shown.

(34, 35), and it was shown that the water phases contained only traces of oil. The electrode was designed to utilize the narrow extension of the zone separating the water-rich and oil-rich phases, and the dividing of the electrode into alternating insulated and noninsulated parts made it possible to follow this zone as it propagates in the measuring cell as a function of time. Figure 2 demonstrates how the conductivity in a 40/60 (w/w) oil/water emulsion stabilized with 2.0% UP366 increases as the creaming process progressed. The trend in the measured conductivity of this sample is representative for all the emulsions studied. The data are given as the normalized conductivity, G:

$$G_{nt} = \frac{(g_{nt} - g_{initial})}{(g_{end} - g_{initial})} \tag{2}$$

in which G_{nt} is the normalized conductivity at a given time t, g_{nt} is the measured conductivity at the same time t, $g_{initial}$ is the measured conductivity at time $t = 0$ and g_{end} is the last value measured. When the measurements start at time $t = 0$, it is reasonable to assume that each of these levels has an equal contribution to the total conductivity in the system. This initial situation is rapidly changed as a result of the creaming process. The first plateau in Fig. 2 reveals the frontier moving along the first insulated area on the electrode. Only small changes in the sample conductivity are measured in this area. When the frontier reaches the first noninsulated area a dramatic increase in the con-

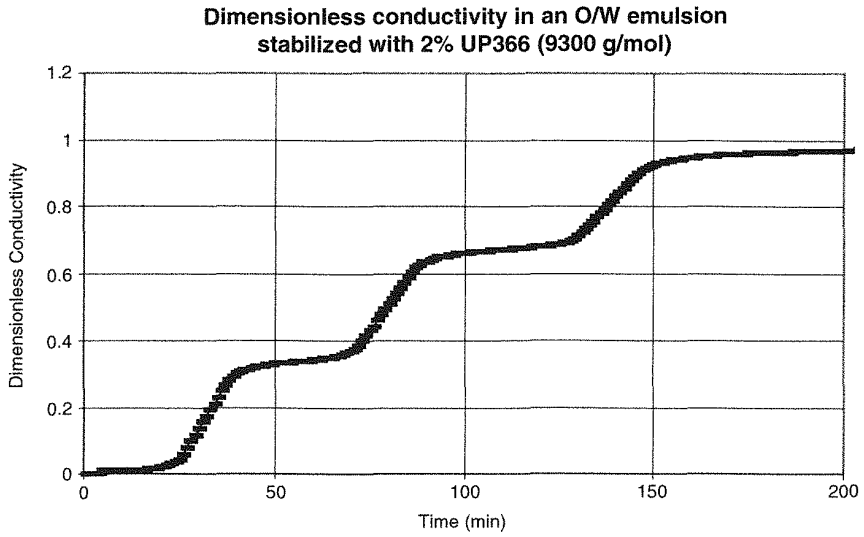

Figure 2 Dimensionless conductivity in an O/W emulsion [40/60 w/w)] stabilized with 2.0% lignosulfonate (UP366) as a function of time.

ductivity is observed. The total conductivity of the sample will at this time be dominated by the changes that occur in this area. The conductivity profile flattens out when the frontier reaches the next insulated area, and so on.

The derivatives of the conductivity plot in Fig. 2 shows how fast the conductivity changes as a function of time. Figure 3 shows that there is a fast growth and a fast reduction when the water-rich phase reaches the noninsulated and the insulated area, respectively. Highest on each top there is a horizontal plateau where the derivative shows only small alteration. The plateau represents the linear increase in the conductance that can be seen in Fig. 2, and the midpoint of each plateau represents the phase boundary located in the middle of each noninsualted level.

Generally, the conductivity is directly proportional to Φ_{water} (36); VEM revealed that Φ_{water} in the water-rich phases was very close to 100%. This makes it possible to calculate the amount of water separated from the emulsions directly from the conductivity profiles when the fixed positions of the noninsulated areas (7–10, 17–20, and 27–30 mm) are known.

Table 4 Separation of Water from O/W Emulsion Stabilized with Different Amounts of Lignosulfonate and Kraft Lignin

Sodium lignosulfonate and Kraft lignin samples	10% Separated water (min)	20% Separated water (min)	30% Separated water (min)
UP364 (0.5%)	35	75	125
UP364 (1.0%)	35	80	140
UP365 (2.0%)	50	120	190
UP365 (0.5%)	30	70	115
UP365 (1.0%)	40	95	155
UP365 (2.0%)	50	115	180
UP366 (1.0%)	40	95	150
UP366 (2.0%)	35	85	145
UP407 (0.5%)	30	65	100
UP407 (1.0%)	35	75	125
UP407 (2.0%)	50	115	195
UP411 (0.5%)	25	60	100
UP411 (1.0%)	30	70	125
UP411 (2.0%)	45	105	185
Diwatex UP329 (1.0%)	40	90	150
Diwatex UP329 (2.0%)	70	150	240

2. Effect of LS and Kraft Lignin Concentration on Creaming Stability

The amount of water separated from different LS and Kraft lignin samples was calculated at three points in time. The results are listed in Table 4 and are given in percentages of the total water-cut of the emulsions. Although all the LSs and Kraft lignins studies are efficient O/W emulsion stabilizers, the fast creaming rates observed reflect a relatively high mean droplet size as a result of the moderate homogenization energy used.

The high molecular weight (UP364 and UP365) and the desulfonated and high sulfonated LSs (UP407 and

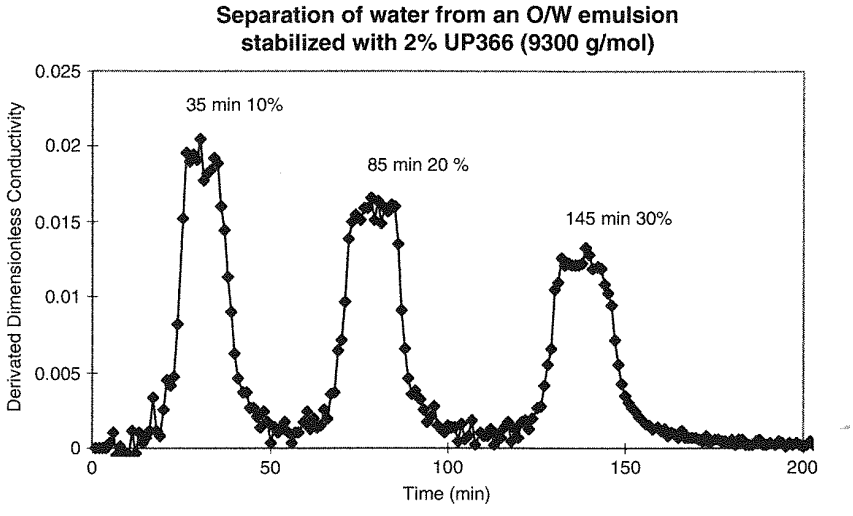

Figure 3 Derivatives of the conductance plot shown in Fig. 2.

UP411, respectively) give rise to approximately identical emulsion stabilities. The stability is significantly improved when increasing the LS concentration, which indicates an increased adsorption on to the droplet surface when the LS concentration is high. For the low molecular weight LS (UP366) the picture is somewhat different. The creaming process is slightly more rapid, and the loss in stability caused by increasing the amount of LS indicates effective adsorption on to the droplet surface at low LS concentrations. The increased emulsion stability observed using high molecular weight LS could be due to multilayer adsorption, giving both steric and electrostatic stabilization (12, 13). Also, for the Kraft lignin studied (Diwatex UP 329) the creaming rate declines when increasing the polymer concentration. The 2% sample has the slowest creaming rate of all the emulsions studied. It has been shown that the adsorption of LS on to polystyrene latex particles increases when the degree of sulfonation is low (17). The level of emulsion stability obtained, and the low degree of sulfonation of the Kraft lignin fraction indicate effective adsorption on to the oil droplets. The structural differences that are known to exist between LSs and Kraft lignins could also be important in this respect (37).

VEM was used to study diluted samples from the oil-rich phases. Figures 4 and 5 show images of O/W emulsions stabilized with low and high molecular weight LSs, respectively. The images reveal a distinct difference in the oil droplet interaction in the two samples. The high molecular weight LS gives rise to a strongly flocculated system, indicating that the molecule is of sufficient length to be adsorbed on to more than one droplet, thereby promoting flocculation (13, 18, 33). The low molecular weight LS, on the other hand, gives rise to discrete droplets with a low degree of flocculation. This is also the case for the Kraft lignin, indicating that these molecules are of insufficient length to be adsorbed on to more than one droplet. For high molecular weight LS a stretched configuration has been reported at low concentrations, and a coiled configuration at higher concentrations due to the suppression of dissociation of the ionic groups (33). The creaming rates measured indicate a reduction in the bridging ability of the LS molecules in the more concentrated emulsions.

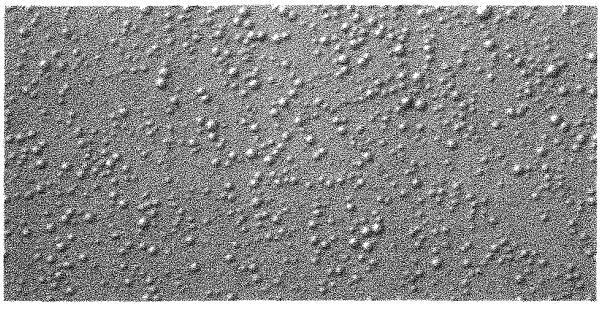

Figure 4 Oil droplets stabilized with low molecular weight lignosulfonate (UP366); 1 cm on the image correspond to a distance of 15.5 μm.

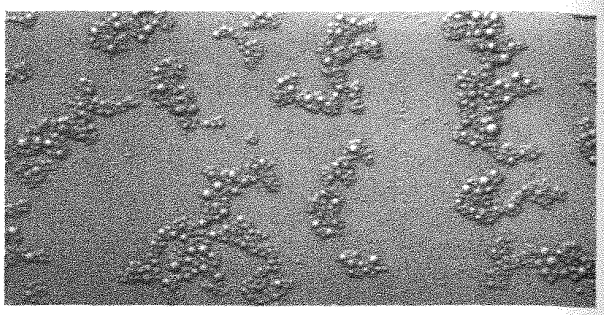

Figure 5 Oil droplets stabilized with high molecular weight lignosulfonate (UP365); 1 cm on the image correspond to a distance of 15.5 μm.

3. Accuracy of Conductivity Measurements

The validity or accuracy of the conductivity measurement technique was verified by comparing results based on conductivity data with results based on visual inspections. The creaming process was studied in emulsions stabilized with LS and LS/hexadecylpyridinum chloride (CPC) complexes. The oil/water ratio and the sample-preparation procedure are the same as outlined in Sec. II.A.1. The homogenization time was 2 min, and the high molecular weight LS (UP364) was used as polyelectrolyte. The amounts of emulsifiers used are listed in Table 5, and are given in percentages of the internal phase weight.

Figure 6 shows how the dimensionless conductivity evolves as a function of time in the emulsions studied. In Fig. 7 the creaming profile for equivalent emulsions is given on the basis of visual observations. For each system the percentage of water separated from the emulsions was calculated at different stages in the creaming process. From the values listed in Table 5 it can be seen that there is a good correlation between data found by the two techniques. This is the case both when the creaming rate is fast, as in emulsions stabilized with LS, and in emulsions stabilized with LS/CPC complexes, where the creaming rate is slower. The deivation in the results is most likely due to uncertainty in

Table 5 Separation of Water from O/W Emulsions Stabilized with Lignosulfonate (UP364) and Lignosulfonate/CPC Complexes Calculated from Conductivity Measurements and Visual Observations

Sample	Time (min)	Separated water (%): conductivity measurements	Separated water (%): visual observations
UP364	35	17	22
	110	34	34
	185	43	43
LS (1%) + CPC (0.14%)	50	9	12
	230	27	27
	445	38	42
LS (1%) + CPC (3.45%)	80	10	12
	360	25	27
	730	37	42

the visual readings. To some extent there is also uncertainty connected with reproducing the emulsions.

III. CONDUCTIVITY MEASUREMENTS AND INFLUENCE OF SALT ON EMULSION STABILITY

A. Experimental

1. Materials and Sample Preparation

In this section a further investigation of the LS fractions UP365 and UP366 described in Sec. II.A.1 was carried out. Additionally, a Kraft lignin fraction (Diwatex XP9), also delivered by Borregaard Lingotech, was studied. The properties of this fraction are summarized in Table 6. The LS and Kraft lignin concentration was 2% on the basis of the external phase weight. The polymer/salt mixture was dissolved in the aqueous phase before emulsification, and the emulsions had an internal phase weight of 30%.

2. VEM and Droplet Size Measurements

The O/W emulsions were diluted with a continuous phase to a dispersed phase concentration of about

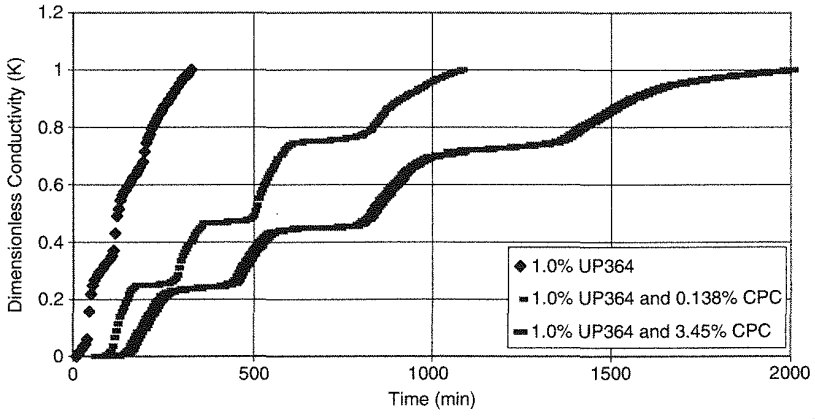

Figure 6 Dimensionless conductivity in O/W emulsions [40/60 (w/w)] stabilized with lignosulfonate (UP364) and lignosulfonate/CPC complexes as a function of time.

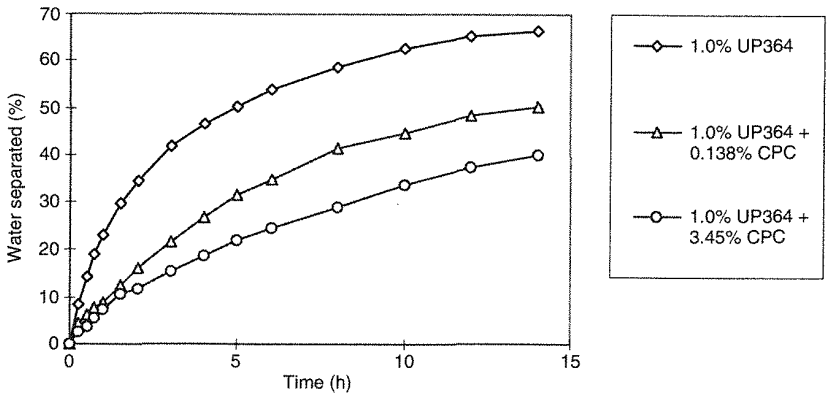

Figure 7 Water separated from O/W emulsions [40/60 (w/w)] stabilized with lignosulfonate (UP364) and lignosulfonate/CPC complexes as a function of time.

1% (v/v) to allow a microscopy study of the droplet population. The diluted emulsion was turned repeatedly to ensure homogeneous redistribution of droplets and droplet aggregates throughout the entire volume. A microslide preparative technique was chosen to allow a long-term study of the sample with minimum risk of sample distortion through evaporation or contamination. In this technique, a small volume of the diluted emulsion was introduced into a flat, open-ended glass capillary of rectangular cross-section. When the ends were sealed, the prepared sample was protected and could be studied over an extended period, in this case with a Nikon Optiphot-2 microscope. For determination of droplet size, images of the dilute emulsion were digitized with a black/white CCD camera (Hitachi KP-160) and a framegrabber captureboard (Integral Technologies Flashpoint PCI) into a computer for image analysis. Due to the complexity of the images, featuring in some instances severe three-dimensional flocculation and reduced transparency as well as broad size distributions (prohibiting full automation of measurement), the analysis required an investment of manual labor.

Table 6 Properties of the Kraft Lignin Fraction

Sample description	Diwatex XP9	Molecular weight (g/mol)	Molecular weight (%)
pH (10% solution)	10.6	> 12,500	43.5
Solids (%)	91.7	< 12,500	56.5
Total S (%)	4.8	< 10,000	46.1
Inorg. S (%)	1.3	< 7000	35.1
Org. S (%)	3.5	< 5000	26.9
Methoxyl (%)	8.4	< 3000	16.8
Carboxyl (%)	9.5	< 2000	9.6
Phenolic OH (%)	2.1	< 1000	1.7

3. Conductivity Measurements and Electrode Design

The conductivity measurements were performed using the same instrumentation as described in Sec. II.A.2. Figure 8 shows how the electrodes were placed in the sample cell containing the emulsion. The two electrode pairs were designed to measure the conductivity in the lower and the upper part of the emulsion, respectively. This was achieved by insulating parts of the electrodes with Teflon tubes. By using this design the conductivity was measured in the lower 35 mm and the upper 35 mm of the sample container.

B. Results and Discussion

1. Progressive Conductivity Measurements

Initially, in a freshly prepared emulsion, the oil droplets were homogeneously distributed in the entire sample volume. This situation was rapidly changed as a result of the creaming process. As the creaming process progressed, the conductivity in the lower part of the emulsion increased because of the decreased volume fraction of oil in this region. At the same time the conductivity in the upper part declined. The difference in the measured conductivities was cal-

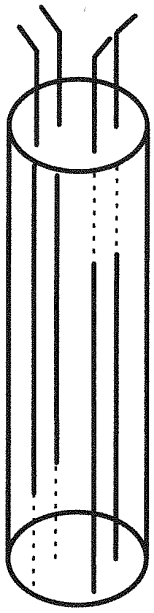

Figure 8 Schematic views of the electrodes immersed in the measuring cell containing the emulsion.

culated, in terms of percentage, from the following equation:

$$\Delta C = (C_{\text{lower}} - C_{\text{upper}})/C_{\text{lower}} \times 100 \qquad (3)$$

The creaming profiles are presented as the deviation in specific conductivity as a function of time. Creaming rates were quantitatively determined by calculating the slope of the first linear part of the creaming profiles.

The validity and accuracy of the conductivity-measurement method were verified by comparing the signals from the electrodes at the initial stage. At this point an homogeneous emulsion should give equivalent conductivity readings in the whole sample volume. However, as a general trend, the initial conductivity was slightly higher in the upper part of the measuring cell. This could be due to formation of air bubbles when pouring the emulsion into the measuring cell. The measured values leveled after a few minutes and then ΔC progressively increased. Experimental data used for calculation of creaming rates and creaming profiles were therefore obtained after an initial stabilization period of 10 min. The reproducibility of the method was evaluated, and it was found, as shown in Fig. 9, that the deviation between creaming profiles of equivalent emulsions was negligible.

2. Salt Effect on Creaming Stability

Kraft lignin- and LS-stabilized emulsions were studied, using different electrolytes at different concentrations: no salt, 10^{-2} M NaCl, and 10^{-4} and 10^{-2} M $AlCl_3$, $FeCl_3$, and $Cr(NO_3)_3$. Figure 10 shows the typical creaming profiles obtained, and illustrates how these electrolyte affect the emulsion stability. Tables 7 and 8

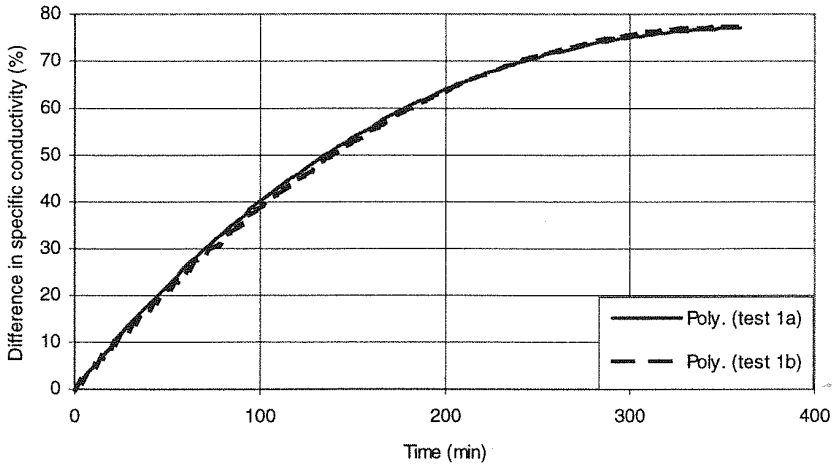

Figure 9 Reproducibility of the conductivity measurements of lignosulfonate-stabilized emulsions measured at 25°C.

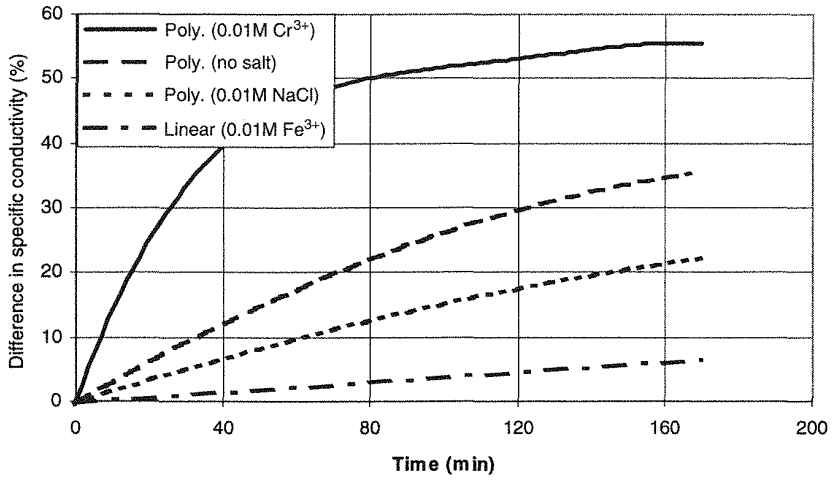

Figure 10 Creaming profiles of emulsions stabilized with low molecular weight lignosulfonate (UP366) measured at 25°C.

summarize initial creaming rates and differences in specific conductivities (ΔC) at two points in time for the LS- and the Kraft lignin-stabilized emulsions, respectively.

The creaming rates presented in Table 7 show that in the emulsions with no added salt, the low molecular weight LS fraction gives rise to creaming rates slower than those of the high molecular weight fraction. This observation reflects the better flocculating properties of UP365. Adding NaCl to the UP365 emulsion increased further the flocculation due to shielding of the electrostatic repulsion between the droplets. VEM showed single droplets and high numbers of dimers and trimers in the emulsion without salt, while flocs containing less than five droplets were negligible in the NaCl sample. VEM showed flocculation also in the UP366 samples but to a lower extent. Most likely this is because of a high fraction of molecules with insufficient molecular length to be adsorbed on to more than one droplet. It has been shown that both the size of the LS molecules and the adsorbed layer thickness decrease in electrolyte

Table 8 Initial Creaming Rates and Changes in Specific Conductivities in Kraft Lignin-Stabilized Emulsions

Concentration of electrolyte	Kraft lignin (XP9)	
	Slope	ΔC (160 min)
No salt	0.002	0.4%
10^{-2} M NaCl	0.007	1.2%
10^{-2} M Al^{3+}	0.01	1.7%
10^{-2} M Fe^{3+}	0.01	1.6%
10^{-2} M Cr^{3+}	0.005	0.8%

Table 7 Initial Creaming Rates and Changes in Specific Conductivities in Low and High Molecular Weight-Stabilized Emulsions

Concentration of electrolyte	Low MW lignosulfonate (UP366)			High MW lignosulfonate (UP365)		
	Slope	ΔC (80 min)	ΔC (160 min)	Slope	ΔC (80 min)	ΔC (160 min)
No salt	0.34	23%	35%	0.63	34%	43%
10^{-2} M NaCl	0.19	13%	22%	0.80	44%	55%
10^{-2} M Al^{3+}	2.90	55%	65%	0.02	1.5%	3%
10^{-2} M Fe^{3+}	0.04	3%	6%	0.02	2%	4%
10^{-2} M Cr^{3+}	1.63	50%	56%	0.01	1%	2%
10^{-4} M Al^{3+}	0.36	23%	36%	0.37	24%	43%
10^{-4} M Fe^{3+}	0.33	25%	38%	0.74	34%	45%
10^{-4} M Cr^{3+}	0.39	21%	34%	0.74	34%	43%

solutions (10, 17). The increased creaming stability observed when adding NaCl to the UP366 emulsion could be due to the formation of a condensed surface layer with a further reduction of the already moderate bridging ability of UP366.

Regarding coalescence, the two LS fractions also gave different stabilities. The high molecular weight LS gave stable emulsions both with and without NaCl added. while the separation of clear oil using the low molecular weight fraction was significant. The addition of salt increased the separation process considerably, and the amount of clear oil phase after 4 weeks was 60 and 10% (of the total oil cut) in the emulsions with and without NaCl, respectively. In the very dense top layer of the creamed emulsions the maintenance of the droplet stability requires an effective mechanical barrier to suppress coalescence. The instability of the emulsions using UP366 shows that the mechanical strength of the adsorbed LS layer is weak and that the electrostatic contribution to the stabilization is crucial to prevent coalescence. It is well known that adsorption preference occurs with respect to the molecular weight and that, at equilibrium, high molecular weight polymers adsorb preferentially over lower molecular weight ones (38, 39). The stability differences observed could imply that the 2% LS concentration is sufficient to give multilayer adsorption in the UP365 emulsions but not in the UP366 emulsions. The coalescence rate could also be affected by molecular diffusion: the Ostwald ripening effect (40–45). Ostwald ripening is observed when the oil from the emulsion droplets exhibits minimal solubility in the continuous phase. The chemical potential of the oil in the larger droplets is lower than in the smaller droplets, which leads to a diffusion transport of oil from the smaller toward the larger droplets. The importance of Ostwald ripening in the systems studied is not clear, but most likely it is of minor importance because of the very low solubility of Exxol D80 in the water phase. The diffusion across the interface may also be sterically impeded by the adsorbed LS layer (46). If the separation of clear oil was significantly affected by Ostwald ripening one would expect to observed an increase in the population of large droplets, reducing the fraction of the smaller droplets. However, measured droplet size distributions of the emulsion containing no salt revealed identical droplet populations in the freshly prepared and the 4-week samples, with droplet diameters of less than 2.5 μm. Droplets of diameter greater than 4,5 μm were not observed in the fresh emulsion, while approximately 10% of the dispersed volume was found in droplets of diameters greater than 4.5 μm in the aged emulsion. These results strongly indicate that the coalescence observed in the UP366 samples is governed by gravitation.

Metal salts at high concentrations had a pronounced effect on the creaming rates of the high molecular weight LS samples. As can be seen from Table 7, the ΔC(160 min) values fall from about 44% in the emulsion containing no salt to about 2–4% in the samples containing metal salt. The initial creaming rates were also very efficiently reduced. When adding metal salt to the aqueous phases the pH may be lowered due to hydrolysis of the $[M(H_2O)_6]^{3+}$ ions to hydroxy species (47). The pH values of the aqueous phases are listed in Table 9. As the pH is lowered from about 9 in the pure LS solutions to about 3–5 in the solutions containing 10^{-2} M salt, the ionization of the carboxyl and sulfonate groups will be suppressed, although the sulfonate group will be appreciably dissociated also at low pH ($pK_a \approx 2$) (15). The suppression of dissociated groups increases the tendency of hydrogen-bond formation between LS molecules, and reduces the swelling of the molecules (15). The effect of pH variations on the emulsion stability was studied by adjusting the water phase containing UP365 to pH 4 with hydrochloloric acid, and it was found that the creaming stability at this pH was very close to that of the sample at pH 9.5. Also, the fact that the pH ranges from 3 to 5 in the LS/metal salt samples and that these emulsions gave rise to approximately identical creaming rates indicates that the LS-electrolyte interaction directs the emulsion stability. How this interaction alters the properties of the LS and the LS adsorption at the oil/water interface is of vital importance in this respect.

The increased emulsion stability indicates that the addition of metal ions modifies the high molecular weight LS fraction so that the flocculating properties are reduced. This was confirmed by studying VEM images. While the UP 365 sample without electrolyte

Table 9 pH of the Aqueous Phase of the Lignosulfonate- and Kraft Lignin-Stabilized Emulsions

Concentration of electrolyte	LS (UP 366): pH	LS (UP365): pH	KL (XP9): pH
No salt	8.5	9.5	9.9
10^{-2} M NaCl	9.0	9.7	9.8
10^{-2} M Al^{3+}	4.1	4.3	5.5
10^{-2} M Fe^{3+}	2.7	3.3	5.0
10^{-2} M Cr^{3+}	4.4	4.9	5.9

added was characterized by flocs existing of three to more than 50 droplets, the aluminum and chromium samples were characterized by discrete droplets. The iron sample was also much less flocculated than the pure LS emulsion, but flocks containing up to 10 droplets were observed. Also, a displacement of the DSDs (droplet size distributions) to smaller droplet diameters in the metal salt-containing emulsions would reduce the creaming rates. According to Stokes law the creaming rate of a single emulsion droplet is proportional to the square root of the droplet radius. Normalized DSDs, however, revealed very similar distributions for all the emulsions under study, with the main droplet population in the region 0.5–3.0 μm. Figure 11 shows the DSD of UP365-stabilized emulsions containing NaCl and different metal salts. The DSDs were based on approximately 1000 measured droplets for each sample. According to work done by Orr this brings the error to well below 5% at the 95% confidence level (48).

VEM was also used to study the colloidal stability of LS in the different solutions. Particulate LS was not observed in the samples containing 10^{-2} M electrolyte, although it was shown that coagulation occurred with further addition of metal salt and that UP365 was more sensitive than UP366 to coagulation. At a concentration of 2×10^{-2} M Al the UP365 sample became turbid, and a rigid macroscopic network of coagulated LS was observed in the microscope. The iron and chromium concentrations had to be 6×10^{-2} M to obtain the same effect. In comparison UP366 was not coagulated even at metal salt concentrations of 8×10^{-2} M. This is in agreement with the findings of Nyman and Rose, showing that high molecular weight LS fractions are more sensitive to coagulation than are fractions at lower molecular weights (37). The strong coagulation quality of Al^{3+} indicates that the UP365 emulsion may be stabilized by particulate aluminum/LS complexes. Although particles were not observed at the emulsification concentration, the principles described by Chamot (49) limit the lower resolving power of light microscopy to approximately 0.2 μm, which implies that particles of lower dimensions would not be observed. The critical coagulation concentrations of LS, on the other hand, are reported to be sharp and well defined (37). This, together with almost identical creaming rates obtained when using high salt concentrations, indicates that Al, Fe, and Cr modify UP365 in the same manner. The most important effect on the emulsion characteristic seems to be the reduced flocculation properties. At lower concentrations small differences in the effects of the salts were observed. The initial creaming rate of the aluminum sample was only half of what was found in the chromium and the iron sample. Compared to the pure LS sample 10^{-4} M Al had a stabilizing effect while the effect of chromium and iron was slightly destabilizing. The strong interction between aluminum and UP365 indicates that the flocculating properties of the LS are partially reduced also at low concentrations. The iron and chromium concentrations seem to be too low to alter the LS properties, but sufficient to reduce the electrostatic repulsion between the oil droplets. The

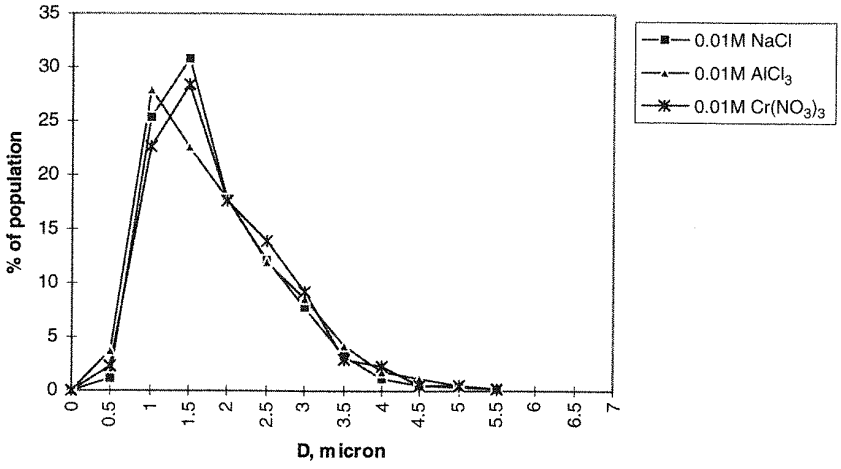

Figure 11 Droplet size distributions of UP365-stabilized emulsions containing electrolyte.

slightly increased creaming rates indicate that a small growth in droplet flocculation takes place. The pH in the 10^{-4} M LS–electrolyte solutions was only slightly less than in the pure LS solutions.

Metal salts strongly affected the creaming rates also in the low molecular weight LS-stabilized emulsions. The 10^{-2} M Fe sample became stable and had a initial creaming rate and ΔC values close to what was found in the corresponding UP365 sample. The aluminum and chromium, on the other hand, had a very destablizing effect, being most pronounced for aluminum. Obviously the effects of the salts depend on the molecular weight of the LS. Figure 12 shows the droplet size distributions of UP365 and UP366 stabilized emulsions containing 10^{-2} M Al. The distributions are similar and do not reflect the very different creaming rates. VEM pictures showed that aluminum effectively reduced the droplet flocculation in both emulsions. The differences in the creaming rates then have to be addressed to differences in the electrostatic interaction of the droplets. Aluminum obviously reduces the charge of UP366 more effectively than of UP365. This is because of the smaller molecules in the UP366 fraction. The reduced electrostatic repulsion between the emulsion droplets implies that aluminum acts as a destabilizer in the UP366 emulsion. This is in agreement with findings by Askvik (50), which have shown that the charge of LS/aluminum complexes, in addition to the pH and concentration ratio, vary with the molecular weight of the LS. The less-pronounced increase in the creaming rate of the chromium sample indicates a more moderate decrease in the charge of the droplets. The sample was also more flocculated than the aluminum sample. Iron strongly reduced the creaming rates independently of the molecular weight of the LS. It has been shown that both high and low molecular weight LSs contain their negative charge under the prevailing conditions in this work (50). This is due to hydrolysis of the aquo ions of iron(III) yielding $Fe(H_2O)_4(OH)_2^{2+}$ which does not reduce the LS charge as effectively as does $Al(H_2O)_6^{3+}$ (51). This, together with the reduction of the flocculation properties of both LS fractions, leads to Fe acting as an emulsion stabilizer in both samples. The emulsions containing 10^{-2} M metal salt all became stable against coalescence. These factors indicate formation of a condensed surface layer of enhanced mechanical strength on the droplets. Metal salts at lower concentrations had little effect on the emulsion characteristic.

The creaming rates of the Kraft lignin-stabilized emulsions were all very low with a slightly destabilizing effect observed when adding electrolytes. Kraft lignins in electrolyte solutions, and the coagulating effects of hydrolzyed metal ions on Kraft lignin sols have been reported by Lindström (52, 53). The critical coagulation concentrations (CCCs) of trivalent metal ions were reported to be sharp and well defined. It has also been shown that Kraft lignins are very resistant to coagulation by NaCl although critical coagulation concentrations have been reported at high concentrations. In this work coagulated Kraft lignin was observed in the samples containing 10^{-2} M metal

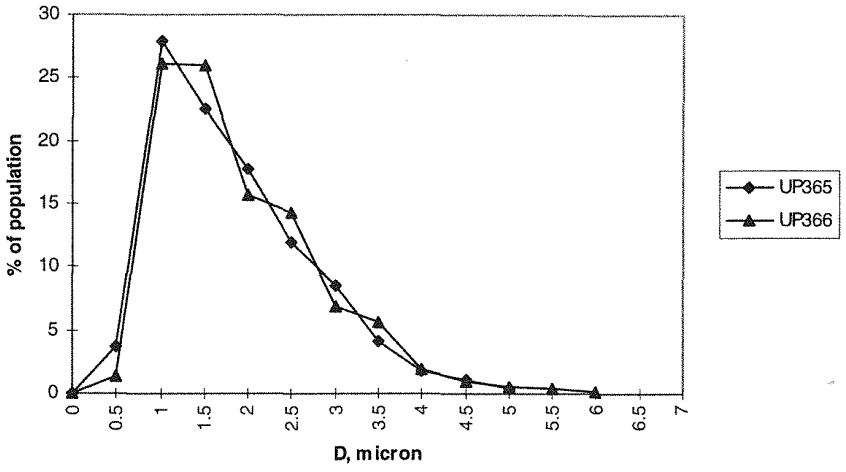

Figure 12 Droplet size distributions of UP365- and UP366-stabilized emulsions containing 10^{-2} M Al.

salts, but not in the NaCl sample, which is in agreement with earlier findings that state that Kraft lignins are more easily coagulated than lignosulfonates (37). As a consequence the metal salt-containing emulsions were stabilized by particles, while the pure Kraft lignin XP9 and the NaCl-containing emulsions were characteized by polymer stabilization. In the latter case, flocculation was observed, while the metal salt-containing samples consisted of discrete nonflocculated droplets. Figure 13 shows DSDs of Kraft lignin- and LS-stabilized emulsions. As can be seen from the figure the DSDs are almost identical. When adding metal salts to the Kraft lignin samples a small dislocation of the droplet distribution towards higher diameters was observed. This, and a possible lower net charge of the emulsion droplets, may explain the increased creaming rates of these emulsions despite the fact that they are nonflocculated.

The creaming rate of the Kraft lignin-stabilized emulsion without added metal salts was low compared to that of the corresponding LS samples. Although both Kraft lignins and LSs are viewed as spherical polyelectrolytic microgels, the polyelectrolytic behavior is reported to be less marked for the Kraft lignins (52). Kraft lignins have also been reported to be less hydrophilic than LSs (37). It is probable that this, and the type and amount of anionic groups in the lignin derivates, will influence their behavior as dispersants (18). The much higher amount of carboxyl groups in the Kraft lignin fraction compared to that in the LS fraction could be of importance in this respect. The low creaming rate observed indicates an adsorbed layer of high charge density on the emulsion droplets. Most likely this and the moderate flocculation properties of the Kraft lignin fraction give rise to the high stability. All the Kraft lignin-stabilized emulsions were also stable against coalescence.

ACKNOWLEDGMENTS

Financial support from Borregaard Lignotech, the Norwegian Research Council, and the technology program Flucha is gratefully acknowledged. Doctor Scient Øystein Sæther is thanked for assistance with the microscopy images.

REFERENCES

1. KH Lim, DH Smith. J Disp Sci Technol 11: 529–545, 1990.
2. BP Brinks, J Dong. Colloids Surfaces A: Physicochemical Eng Aspects 132: 289–301, 1998.
3. M Bury, J Gerhards, W Erni. Int J Pharm 76: 207–216, 1991.
4. M Bury, J Gerhards, W Erni, A Stamm. Int J Pharm 124: 183–194, 1995.
5. F Kiekens, A Vermeire, N Samyn, J Demeester, JP Remon. Int J Pharm 146: 239–245, 1997.
6. E Sjöström. Wood Chemistry, Fundamentals and Applications. 2nd ed. New York: Academic Press 1993, pp 114–164.

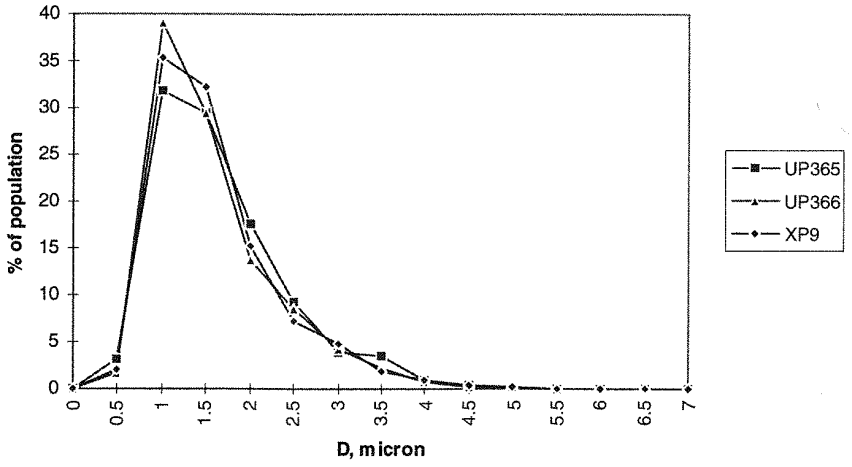

Figure 13 Droplet size distributions of Kraft lignin- and lignosulfonate-stabilized emulsions.

7. AK Kontturi, K Kontturi. J Colloid Interface Sci 120: 256–262, 1987.
8. K Forss, KE Fremer. Papper och Trä 8: 443–454, 1965.
9. AK Konturri. J Chem Soc Faraday Trans I 84: 4033–4041, 1988.
10. PR Gupta, JL McCarthy. Macromolecules 1: 236–244, 1968.
11. A Rezanowich, DAI Goring. J Colloid Sci 15: 452–471, 1960.
12. WC Browning. Appl Polym Symp 28: 109–124, 1975.
13. SLH Chan, CGJ Baker, JM Beeckmans. Powder Technol 13: 223–230, 1976.
14. JM Hachey, VT Bui. J Appl Polym Sci; Appl Plym Symp 51: 171–182, 1992.
15. JC Le Bell. The Influence of Lingnosulphonate on the Colloidal Stability of Particulate Dispersions. PhD dissertation, Åbo Akademi, ÅBo, 1983.
16. CA Herb, S Ross. Colloids Surfaces 1: 57–77, 1980.
17. TF Tadros. Colloid Polym Sci 258: 439–446, 1980.
18. A Rezanowich, FJ Jaworzyn, DAI Goring. Pulp Paper Mag Can 62: 172–181, 1961.
19. JR Salvesen, WC Browning. Rts Com Chem Ind Week 61: 232–234, 1947.
20. T Lindström, C Södermark, L Westman. J Appl Polym Sci 21: 2873–2876, 1980.
21. GG Allan, DD Halabisky. Pulp Paper Mag Can 17: 64–70, 1970.
22. SA Gundersen, J Sjöblom. Colloid Polym Sci 277: 462–468, 1999.
23. WC Browning. J Petrol Technol 7: 9–15, 1955.
24. RV Lauzon, JS Short. The colloidal interaction of ferrochrome lignosulfonate with montmorillonite in drilling fluid applications. The 54th Annual Fall Technical Conference and Exhibition of the Petroleum Engineers of AIME, Las Vegas, NV, 1979, SPE 8225.
25. CI Chiwetelu, V Hornof, GH Neale, AE George. Can J Chem Eng 72: 534–540, 1994.
26. V Hornof, R Hombek. J Appl Polym Sci 41: 2391–2398, 1990.
27. V Hornof. Cellulose Chem Technol 24: 407–415, 1990.
28. C Chiwetelu, V Hornof, GH Neale. Trans IChemE 60: 177–182, 1982.
29. JE Son, GH Neale, V Hornof. J Can Petrol Technol (July–Aug.): 42–48, 1982.
30. C Chiwetelu, G Neale, V Hornof. J Can Petrol Technol (July–Sept): 91–99, 1980.
31. WC Browning. Surface Active Properties of Lignosulfonates. Proceedings IV International Congress on Surface Active Substances. Vol 1, Sect A, Brussels, 1964, pp 141–155.
32. PG Shotton, PC Hewlett, AN James. Tappi 55: 407–415, 1972.
33. JL Gardon, SG Mason. Can J Chem 33: 1491–1501, 1955.
34. B Kachar, DF Evans, BW Ninham. J Colloid Interface Sci 99: 593–596, 1984.
35. B Kachar, DF Evans, BW Ninham. J Colloid Interface Sci 100: 287–301, 1984.
36. DAG Bruggerman. Ann Phys 24: 636–664, 1935.
37. V Nyman, G Rose. Colloids Surfaces 21: 125–147, 1986.
38. JM Kolthoff, RG Gutmacher. J Phys Chem 56: 740–745, 1952.
39. RE Felter, LN Ray. J Colloid Interface Sci 32: 349–460, 1970.
40. C Wagner. Z Elektrochem 65: 581–591, 1961.
41. M Kalhweit. Adv Colloid Interface Sci 5: 1–35, 1975.
42. M Kalhweit. Faraday Discuss Chem Soc 61: 48–52, 1976.
43. K Parbhakar, J Lewandowski, LH Dao. J Colloid Interface Sci 174: 142–147.
44. AS Kabalnov, AV Pertzov, ED Shchukin. Colloids Surf 24: 19–32, 1987.
45. AS Kabalnov, ED Shchukin. Adv Colloid Interface Sci 38: 69–97, 1992.
46. B Vincent. In: TF Tadros, ed. Surfactants. London: Academic Press, 1984, pp 183–184.
47. TL Brown, HE LeMay Jr, BE Bursten. Chemistry: The Central Science. 5th ed. London: Prentice Hall, 1991, pp 894.
48. C Orr. Determination of particle size. In: P Becher, ed. Encyclopedia of Emulsion Technology, Basic Theory, Measurement Applications. New York: Marcel Dekker, 1988, pp 137–169.
49. EM Chamot. Elementary Chemical Microscopy. 1st Ed. New York: John Wiley, 1915, pp. 15.
50. KM Askvik, J Sjöblom, P Stenius. Colloids Polymer Sci, submitted.
51. JW Akitt. Progr NMR Spectrosc 21: 1–149, 1989.
52. T Lindström. Colloid Polym Sci 257: 277–285, 1979.
53. T Lindström. Colloid Polym Sci 258: 168–173, 1980.

24

Chemical Demulsification of Stable Crude Oil and Bitumen Emulsions in Petroleum Recovery—A Review

Chandra W. Angle
Natural Resources Canada, Devon, Alberta, Canada

I. INTRODUCTION

The presence of emulsions in petroleum recovery operations is generally undesirable. Dehydration of the oil is demanded for various reasons. Among the foremost reasons are the high costs associated with transportation, corrosion, and heat demands, in addition to the problems caused by the presence of water/solids in the refining of crudes or in the upgrading of heavy oils and bitumen. This chapter reviews the chemical dehydration of crudes, heavy oils, and bitumen. First, we present a brief introduction on the extraction processes and the emulsions involved, followed by an outline of the scope of this review.

Emulsions formed in crude oil and bitumen during extraction operations are usually water-in-oil (W/O) macroemulsions (>0.1 to 100 μm in diameter). Macroemulsions are kinetically stable, unlike microemulsions, which are thermodynamically stable. In conventional oil recovery (high-energy process), the crude is often in contact with formation water or injection water, as in secondary recovery. In tertiary or enhanced oil recovery, surfactants are used purposely in water floods to make microemulsions for enhancing the flowability of the crude. Crude-oil macroemulsions are produced when two immiscible liquid phases such as oil and water are mixed via the input of mechanical or thermal energy into the processes. Conventional crudes held under high pressures and temperatures amidst porous rocks are recovered by drilling. Emulsions in these oils form mainly through contact with formation water. As crude oil is pumped through various pipes, valves, chokes, etc., under high pressure and/or high temperature, fine water droplets are formed, producing macroemulsions.

The recovery of heavy oil requires stimulation for flow. Flow is often achieved by reducing the viscosity of the oil by heating, as in steam-assisted gravity drainage (SAGD) and fire floods, or by the addition of viscosity-reducing agents. The recovery of water-wet bitumen from oil sands begins with a low-energy process of mining followed by conditioning with process water to release the bitumen. After release, the oil is separated in a series of process stages. Flotation of the bitumenous froth from the middlings and tailings is followed by removal of solids and excess water by dilution, demulsification, and centrifugation. The froth invariably contains 30–60% water before dropout. After dropout, the bitumen product contains 2–3% water which must be dehydrated. Bitumen production from a hot-or cold-water extraction process invariably entails a high degree of emulsification of water and air in the oil. The froth (oil-rich phase) must be treated to remove water, solids, and entrapped air.

Generally, in all recovery processes, if saline water is in contact with the oil, then the salts present in the W/O emulsion droplets must be removed. A washing process is used to remove the salts from the oil after

pumping from the reservoir and before transportation. In all these processes W/O emulsion formation is prevalent.

Spills of crude oil on the sea quickly form a W/O emulsion known as "chocolate mousse" which contains approximately 80–90% water. Wave action supplies the mixing energy. These must be demulsified (1) as well.

The crude-oil market demands that water in crudes from all these processes must be removed to a level of less than 0.5% BS&W (bottoms, solids, and water) (2, 3). In order to remain competitive, emulsions must be resolved economically. The available treatment options are mechanical, thermal, via electrotreators (electrocoalescers), chemical, or a combination of physical and chemical methods. Chemical demulsification is one of the most economical means of dehydrating oil.

A. Scope

The following review presents the chemical demulsification of W/O emulsions by first introducing crudes and bitumens in terms of the diagenetic diversity and chemistries of their components. Based on the premise that a full appreciation of demulsification must be preceded by an understanding of the basics of the field and laboratory emulsions, we have reviewed demulsification and some of the characteristics of light crude, heavy oil, and bitumen emulsions researched globally. Thus, in this work the composition and behavior of the natural emulsifiers present in the crudes and some factors responsible for emulsification in the field and laboratory are addressed first.

The second approach is understanding how the emulsions' natural stabilizers and their environment can be modified to augment destabilization. This is addressed by a description of the interfacial architecture of the emulsions in terms of how the structure may be first understood and then destabilized by probing the pseudostatic film behavior. This is followed by a description of dynamic properties of the interdroplet lamella, and thin-film behavior with and without demulsifiers. In all these systems the modification of the chemistries of the indigenous surfactants at the interfaces together with the dispersed water chemistry are suggested as tools that may be used toward destabilization. The effects of temperature and heat are addressed briefly.

Thirdly, a fourth section discusses chemical demulsification processes. Flocculation, creaming/sedimentation, and coalescence and the lamella drainage model are covered. The fifth section discusses the expected performance demanded of demulsifiers for various systems and processes.

This is followed by a description of the chemicals used as demulsifiers in practice and in research. The agricultural and petroleum sources of the basic chemical building blocks are indicated. The typical responses for selected types of chemicals are discussed, in terms of published research findings to date.

Lastly, the impact of demulsifier choices and chemistries on petroleum recovery operations are discussed. We conclude with identification of the need for cooperation between research providers, petroleum operations, and chemical suppliers geared towards an effort for full scientific understanding of demulsification. Examples of crude-oil properties and demulsification are drawn from over three decades of published results of researchers worldwide. Examples of demulsification of bitumen W/O emulsions are excerpted from work performed in the author's own laboratory at CANMET.

II. PROPERTIES OF CRUDES, BITUMEN, AND WATER

A. General Properties of Crudes and Bitumen

The world's fossil fuel resources consists of natural gas, liquids (oil sand bitumen and petroleum), and solids such as coal and oil shale. Petroleum represents associated gas, crude oil, and heavy oil (4). The appearance of crude oil ranges from watery white to black liquid. The thin nearly colorless liquid is mobile and flows easily, and the almost black liquid is viscous and thick. Light oils have a low boiling point and heavy oils a high boiling point. Petroleums are fairly balanced systems in terms of the interactions of their components in forming a smooth "solution" while occurring "in situ". Crude oil and bitumen are mixtures of organic compounds normally separated by fractionation through boiling-point differences in the components. Bitumens have a higher proportion of higher-boiling-point constituents than conventional crude oil.

Unlike coal, which is solid and whose surface properties and characteristics are reflections of a Cretaceous (5, 6) or Carboniferous (7, 8) geologic period corresponding with depth of burial, etc., crude oil does not bear such a clear correlation. The fluidity of crude oil made it highly mobile during diagenesis and maturation. The crude moved from its source fossil

biomass location. In oil sands the heavy bitumens were integrated in loosely held fine rocks consisting of clays and silica. Crude-oil properties are more closely linked to the rocks through which they moved (9, 10). Thus, the composition of the oil varies, depending on the precursors, i.e., the nature of the biomass sediment, the underground environment, the temperatures and pressures experienced under the maturation conditions, and the naturally occurring migrations or separation processes involving inorganic catalysts (11).

Experience has shown that crudes from adjacent wells can be different in composition. The surface, physical, and chemical properties of associated emulsions can be expected to be as diverse and complex as the source crudes and water. The variances in the elemental C, H, and N composition of components such as asphaltenes of crudes from various geologic origins as compiled (10, 12) show no apparent pattern emerging from the data as was the case with coal (5, 7). Sharma et al. (13) have shown the use of bitumen asphaltenes as thermal maturation indicators.

B. Chemistries of Crude Oils and Bitumen

1. Chemical Characteristics

In a series of published works (4, 9), Speight has shown the distribution of various organic structures in conventional crudes relative to heavy oil and bitumen. Heavy oils and bitumens have the largest proportions of polynuclear aromatics and polycycloparaffins, and the lowest proportions of normal and branched-chain paraffins and monocycloparaffins. Heavy oils and bitumens have boiling points higher than those of conventional crudes. The high degree of isomerization in organic chemicals found in all crudes and bitumens accounts for some of the complexity and variability of crudes of similar elemental analytical C, H, N, O, and S composition.

Crude oils have the same elemental make up globally. The carbon content of crude oils is relatively constant, but the varying quantities of hydrogen and heteroatoms are responsible for the major differences between the petroleums. The elemental composition ranges are carbon (83–87%), hydrogen (10–14%), nitrogen (0.1–2%), oxygen (0.05–1.5%), and sulfur (0.05–6.0%). Metals such as vanadium, nickel, and iron occur as metalloporphyrins, which add polar character to the oils. In petroleum refining the metals also poison catalysts. In refining, the nitrogen decreases the yield, and the presence of sulfur not only demands extra processing, but also indicates a lower quality product. These elements constitute a mixture of organic molecules classified as saturates, aromatics, resins, and asphaltenes (SARA), and waxes. The classification is empirically based on distillation fractions and solubility in alkanes (9).

Data published on crude-oil composition are often based on SARA components. This is illustrated in Table 1. Variations arise from the sources and the methods of extraction. Although the major components of crude oil are the same throughout the geologic

Table 1 Properties of Crude Oils and Bitumen

Crude oil property	Athabasca bitumen[a]	Heavy oil – Boscan[b]	California[b]	Ninian North sea[b]	Alberta light[b]	Kuwait[b]	Arabian light[b]	West Texas intermediate[b]	Udang[b]
API°gravity	8.2–9.1	10.9	13.2	NA	36.8	31.1	31.8	36.4	14.3
Viscosity at 0°	640,000	8,826,000	31,000	NA	18	90	31	140	81,890
and 15°C (cP)	to > 72,000 at 39°C	485,500	6400		6	22	14	49	10,700
Hydrocarbon content (wt %)									
Saturates	16.9	25	19	61	78	28.5	51	60	32
Aromatics	18.3	35	35	30	18	56.2	39	26	41
Resins	44.8	22	23	8	3	15.3	6	6	24
Asphaltenes	17.2	18	22	2	1	2.7	3	1	3
Waxes		4	3	6	7	6	4	4	1

[a] *Source*: Ref. 36.
[b] *Source*: Ref. 35.

origin, the proportions of the SARA components and their chemistries differ from source to source. Figure 1 shows a schematic of petroleum as represented by Pfeiffer and Saal (14).

Saturates describe paraffinics and cycloparaffinics or napthenics which are alkyl (methyl, ethyl, isopropyl) substituted cyclopentanes and cyclohexanes. The normal or branched alkanes and cyclic structures consist of one to five rings and various degrees of alkylation. According to Mackay (15), cyclic structures dominate in degraded oils. The saturates are the solvents for the higher-molecular-weight components.

If an oil is described as highly paraffinic and waxes are identified, these are usually "paraffinic waxes" which have basically straight- and branched-chained hydrocarbons ($C_{18}H_{38}$ to $C_{40}H_{82}$). Wax contents up to 50% (Altamount Utah) and as low as 1% in Louisiana can be found (16). Wax solubility in the crude oil is dependent on the chemical composition of the crude, as well as the pressure and the temperature the waxes experience (17, 18). Wax crystallizes out as an equilibrium temperature and pressure is reached around the cloud point of approximately 77°C. Leontaritis (19) describes the wax deposition envelope as the thermodynamic point in the pressure, temperature, phase composition diagram where crystallization occurs. Wax crystals are partially responsible for increased crude-oil viscosity and some of the changes in flow behavior from Newtonian to nonNewtonian. As temperature decreases crude becomes very viscous (pour-point range 16.5°–51.5°C). Thus, the viscosity of the waxy crude will depend on both the oil viscosity and the aggregation of wax crystals, whose sizes depend on the rates of cooling. Methane prevents wax crystal agglomeration, while butane decreases it by dilution (20). Wax is completely hydrophobic and is not surface active. However, the waxes are believed to attach themselves to the nonpolar ends of polar surface-active components of crudes (21). In this form they contribute to emulsion stability by participating in the interfacial film architecture. Their contribution to increased oil phase bulk viscosity assists in preventing coalescence by decreasing the mobility of the droplets (22, 23).

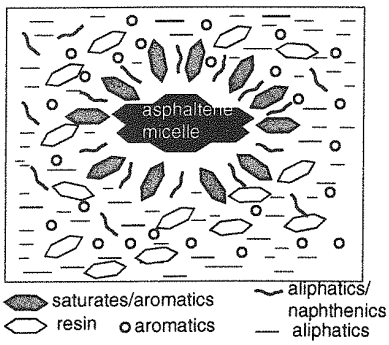

Figure 1 Schematic of petroleums. (From Ref. 14.)

Aromatics in crude, on the other hand, are similar in structure to saturates, but contain many condensed aromatic rings instead. Low concentrations of oxygen and nitrogen are found in some polycyclic aromatics. Increased amounts of condensed rings of napthenics are attached to the aromatic rings. Molecular weight increases with increased condensation (4).

The polars describe mainly the resins, asphaltenes, and the poryphyrins, as well as the trace nitrogen found in bases, the nonbasic poryphyrins, the oxygen in the phenols, the napthenic acids and esters, and the sulfur in sulfide and disulfide bonds. The polars and the metalloporphyrins are indicated as emulsifier species involved in stabilizing the emulsions (24, 25). Resins, which will be discussed later with asphaltenes, contain O, N, and S in the form of carbazoles, fluorenones, fluorenols, carboxylic acids, and sulfoxides. These are attracted to water interfaces.

2. Crude Oil Acidity

The relative acidity of the crude is an indicator of the presence of polar acidic species such as phenols, napthenics, heterogeneous organic species, and anionic surfactants in the sample (26).

The acid numbers (mg KOH/g crude needed for neutralization) are indicative of the corrosivity of the crude and so suggest a value detrimental to crude (27). Jennings studied 164 crudes from 78 fields to determine an overall view of acidity (28). Worldwide crude oil acid numbers vary from less than 0.01 to as high as 3 (29). Relative to this, values for Canadian heavy oil (0.3–2.8) and bitumen (3.7) appear on the high side, closer to 3 (30, 31). There have been attempts at correlating acid numbers with the stability of emulsions, and using this as an empirical means of selecting demulsifiers for treating Venezuelan crudes (32). However, the correlations have not been tested on other crudes.

A polarity indicator was developed by Bruning, using inverse gas chromatography for 98 Brazilian and 5 foreign (Far East and Russia) crudes (33). The API° gravities [crude oils are classified by the American Petroleum Index (API°) gravity, which is a number derived empirically (141.5 divided by specific

gravity at 15°C minus 131.5)] were correlated with these numbers. Low API° corresponded to high polarity. Crudes of extra high polarity (above 500) appeared to be highly degraded or to have high heteroatomic content and a propensity to form very stable emulsions that would require demulsification for more economic processing. However, according to Bruning, high numbers do not necessarily indicate degraded crude (34). Tests must be done to confirm such degradation or oxidation. In most cases the number reflected high asphaltenes and resin contents. Crudes with polarities between 300 and 400 have emulsion separation problems, while low-polarity crudes (from 200 to 300) appear to have no treatment difficulties. These characteristics of crude oils are indicative of the possibility of the formation of tight (very stable) or loose (not very stable) emulsions that require demulsification treatments. Demulsifiers are often selected on this basis as well.

3. Physical Characteristics

a. Specific Gravities and Viscosities

The specific gravities of crudes and bitumen vary from 0.75 (57 API°) to 0.95 (17 API°). API° gravity indicates the relative categorization of the crude as light (>30), medium (15–30), and heavy (<15). A high API° indicates lighter products that are saleable. Bitumen and heavy oil are of low API° with densities closer to water. This presents difficulty in gravity separation techniques. However, viscosity differences are large between crudes and water. Table 1 describes some physical and chemical properties of bitumen and crudes from various sources (35, 36).

The increase in API° has been correlated with increased reservoir depth (synonymous with increased temperature), which results in an increased fraction of compounds with less than 12 carbons (more paraffinic) in the crudes (9). High API° is normally associated with low asphaltene content and high sulfur content (9). The major physical differences between bitumens, heavy oils, and conventional oils reside in the specific gravity and the viscosity. These are very high in bitumen and heavy oils due to a preponderance of high-molecular-weight aromatic components such as resins and asphaltenes. Bitumen has the highest viscosity, followed by heavy oils, and then conventional crudes, at all temperatures. In a comparison of viscosity with increasing temperature for conventional crudes, heavy oils, and bitumen, there is an almost parallel asymptotic decrease in viscosity as temperature is increased. The highest viscosity values at each temperature were attributed to bitumen, followed by heavy oils and conventional crudes [4] (see Fig. 2).

Waxy crude oils, such as those found in the North Sea (20), would not produce a smooth decline in viscosity with increases in temperature. Wax as fine particles would contribute to a high viscosity and when heated between 50°C and 65°C would melt or solubilize in low-molecular-weight components, producing a more homogeneous fluid (17, 18). The properties of crude oils and bitumen are listed in Table 1.

b. Molecular Weights and Micellar Sizes

As determined by vapor-pressure osmometry (VPO), the average molecular weights (MWts) of Canada's heavy oil from Norman Wells, Countess, and Cold Lake were reported to be 197, 334, and 585 g/mol, respectively (37). Relative to other feedstocks the range appears as given in Table 2.

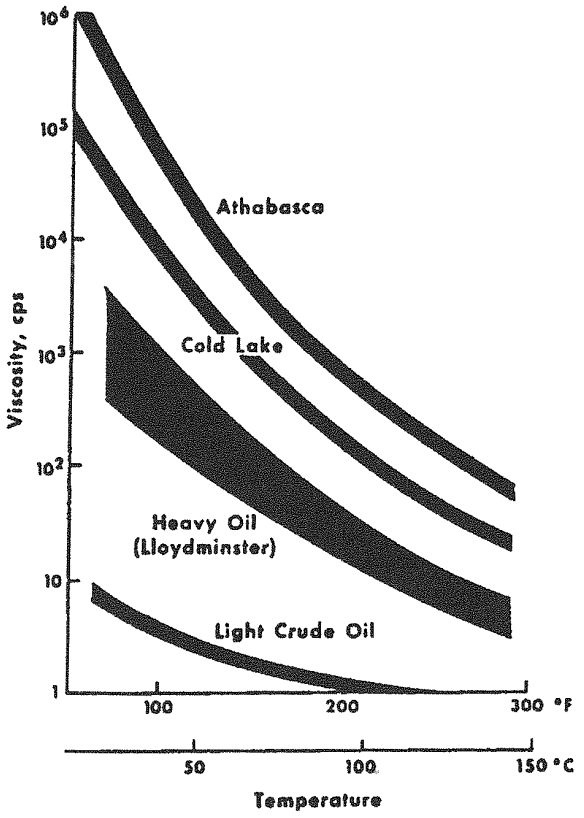

Figure 2 Viscosity decreases with increasing temperature for conventional crudes compared with heavy oils and bitumens. (From Ref. 4.)

Table 2 Range of Molecular Weights for Petroleum Feedstocks

Property	Coal	Vacuum residue	Heavy oil bitumen	Crude oil	Gasoline
H/C atomic ratio	0.5–0.8	1.3–1.35	1.4–1.5	1.6	2.0
Molecular weight	10,000	1000	500	300	100

Source: Ref. 4.

For additional data on crude oils with MWt around 300 g/mol the reader is referred to Speight (4). High asphaltene content is synonymous with higher MWt in oils. In VPO determinations all asphaltenes in heavy oil tend to have higher MWt than their resin counterparts (4, 38). The resins are generally of lower MWt than the asphaltenes. Ferworn et al. (39) have published data on the average MWt (300–500) of some of Alberta's crude oils and their properties and their distributions in various solvents (37). The agglomeration (40) of the asphaltene components and the bitumen behavior with paraffinic solvents are also discussed by Funk (41).

Extensive data on the chemical and physical properties of asphaltenes have been published in several texts. The MWt of asphaltenes in various solvents and at various temperatures are reported by Speight (42). The MWts range from 2000 to 7000 g/mol based on geologic period (Cretaceous, Carboniferous, Devonian) and depending on the methods of precipitation. For the pentane-precipitated asphaltenes, when solubilized in benzene, the MWt reported was 5120 g/mol; when solubilized in pyridine the MWt was 13,390 g/mol. Asphaltenes extracted by 3-pentanone showed higher MWts of 18,000 g/mol. For the heptane-precipitated asphaltenes, when dissolved in benzene, the reported value for MWt was 8500 g/mol, and when dissolved in nitrobenzene, the MWt was 2880 g/mol. The reported MWt of asphaltenes appeared to decrease with polarity of the solvent and increase with concentration in the solvent, suggesting that the association structures or micellar sizes are influenced by thermodynamic solubility-parameter differences between the asphaltenes and the solvent. Resins appear to have a MWt close to 700 for pentane solubles and 1050 for heptane solubles. The MWts of resin are less affected by solvents and are generally significantly lower than those of the corresponding asphaltenes (4).

Thus, asphaltenes (43) are high MWt pentane- or heptane-insoluble fractions of crudes and are readily peptized by resins which are the alkane-soluble fraction. Figure 3a–c illustrates a few of the various chemical models developed for asphaltenes from structural and chemical analysis. Resins make up the outer protective coating of asphaltene micelles or clusters (43–45). The resins are dissolved in the oil, are also surface active and polydisperse with a range of polarities and aromaticities. Figure 4 illustrates the chemistry for a typical resin molecule (46). Resins sometimes from reversible micelles. The resins are less polar and of lower MWt than asphaltenes and appear as dark sticky semisolid liquids in n-alkanes. Manek (23) characterized the asphaltenes and resins of three Canadian heavy oils, one Texas heavy oil, and one California heavy oil to show the relative surfactant-enhanced dispersibility of asphaltenes in resins.

The insolubility of asphaltenes causes deposits in pipes, wells, and valves, and in the formations. Dubbed as the colloids of crudes (47, 48), the asphaltene chemistry has received considerable attention. Asphaltenes are considered as major polar species with high aromaticity and are known as the major building blocks of the mechanical barriers or interfacial films formed at the W/O interface. Increased MWts is consistent with high aromaticity and greater numbers of incorporated heterocyclic structures containing the heteroatoms. Their structures have received considerable attention of late.

Even in dilute solutions they associate (49, 50). Published sizes of the micelles vary from 2 to 4 nm. Sophisticated analytical techniques such as small-angle X-ray diffraction (SAXS), small-angle neutron scattering (SANS), and NMR were used to study the asphaltene particle or "micelle" sizes (51). MacKay (15) reported that a MWt of 10,000 g/mol would correspond to a 2 to 4-nm cluster. This is very much smaller than a 1-μm water droplet, and considered to be 1/100 to 1/1000 the droplet diameter. This topic is worthy of a review on its own. However, the colloidal properties

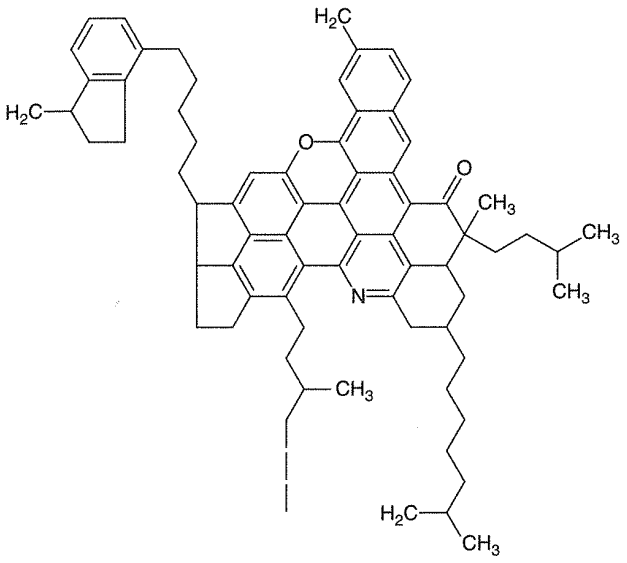

(a)

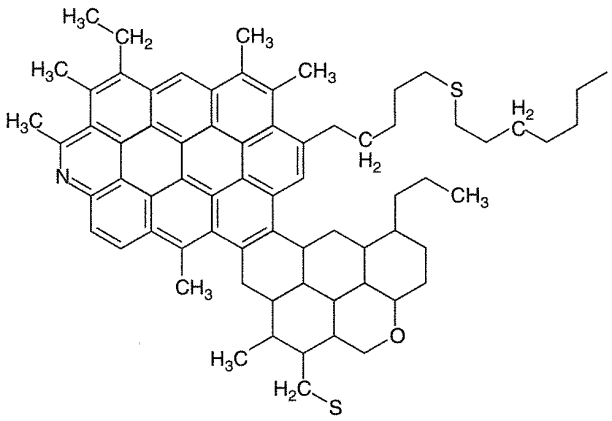

(c)

Figure 3 Models of asphaltene chemical structures: (a) California; (b) Venezuela; (c) Athabasca. (From Refs 4,42, and 43.)

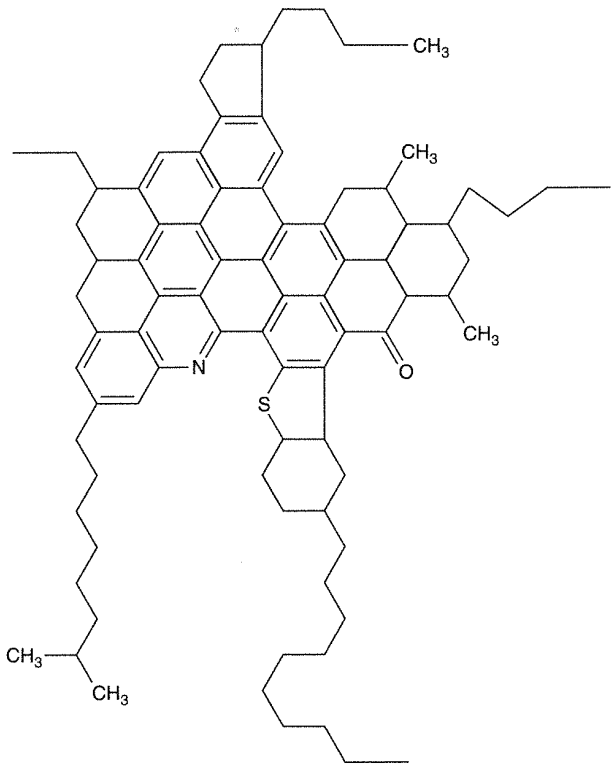

(b)

of asphaltenes, micelles, and solvent effects are compiled and reported by several authors (52, 53).

From data obtained by SANS analysis, Sheu and Storm (48) reported that the sizes of asphaltene micelles in a good solvent such as toluene/pyridine fall in the range 3.0–3.2 nm.

Although asphaltenes have been extensively studied in terms of colloidal (47, 54–56) and fractal properties (37, 57) they are not yet fully understood in terms of their interactions with other components of crudes, solubilities in various solvents and crudes, precipitation, and micellization (58). Asphaltenes appear to be the key component, together with resins, in forming a mechanical skin often described as structurally rigid, viscoelastic, or a deformable interfacial film – and the barrier to coalescence. Much of emulsion stability research which focussed on the film stability described the films in terms of mechanical or rheological behavior with varied characteristics of the system. Figure 5 shows a schematic of these fractions arranged about the interface of a water droplet. The natural surfactants are illustrated with the head group in the water phase and tails in the oil phase. As time progresses the organization of the surface-active species changes in the interfacial region. The changes, which lead to more concentration of species at the interface over time, will be discussed later in this chapter. Figure 6 describes

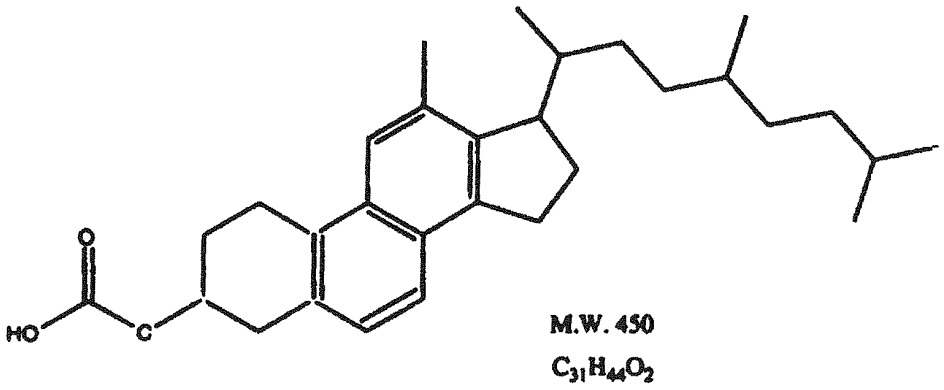

Figure 4 A model of resin chemical structure. (From Ref. 46.)

other components that may be present inside and outside the droplets.

C. Water

In the petroleum industry, not all W/O emulsions are the same. The nature of emulsions formed in crude oil often depends on many factors: the geologic source and the engineering processes utilized in the crude oil recovery, the chemical and physical characteristics of the crudes and their thermal history, the type of mixing and energy introduced, and, most importantly, the formation and process water chemistry and composition. All these determine the stability and the sizes of the emulsion droplets.

All formation or extraction water differs in ionic composition and pH. Generally, formation water for the North Sea crudes is far more saline than that for the heavy oils and bitumen. Table 3 compares typical water compositions found in emulsions (59–61).

Thus, the W/O emulsions reflect the complexity of the above factors. Since the natural chemistries of crude oils or petroleum contain the stabilizers of the W/O emulsions, the chemical destabilization or demulsification requires knowledge of not only the emulsion interfaces, but also the physicochemical characteristics of the oil and water.

Parts of this complexity are addressed in published information on chemical destabilization of crude W/O emulsions. Examples include studies on California (62), Salem (63), Texas (64), Louisiana (65), North

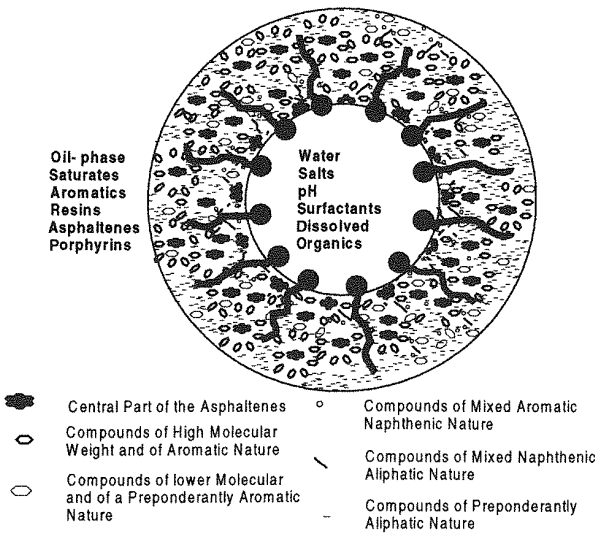

Figure 5 Schematic of droplet of W/O emulsion with petroleum fractions arranged in the interfacial layer or skin around the droplet at early stage of formation. Solids and waxes are not indicated.

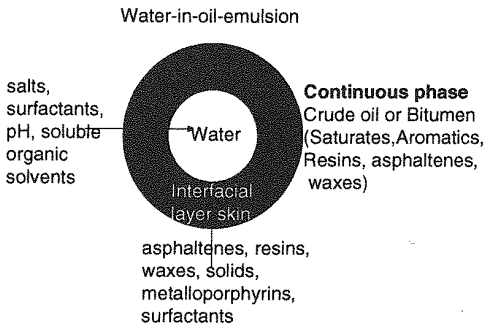

Figure 6 Schematic of components of crude oils and bitumen to be considered in an emulsion droplet and the interfacial layer.

Table 3 Water Composition – North Sea and Alberta Oil Sands Pond Water

Ions	Forties[a] formation (ppm)	Ninian[a] formation (ppm)	Magnus[a] formation (ppm)	North sea water[a] (ppm)	Athabasca Pond 2 water[b] (ppm)
Na^+	33,000	8300	6000	12,000	350
Cl^-	58,500	12,500	9000	19,600	40
Ca^{2+}	3950	12,500	80	400	6.3
Mg^{2+}	500	190	15	1325	3.8
HCO^-_3	450	30	1700	140	932
SO^{2-}_4	< 10	15	70	2750	9.9
Ba^{2+}	210	–	100	–	0.16
Fe^{2+}	170	–	–	–	0.4
pH	5.8	7.8	7.4-	7.8	8.5
Dissolved solids	99,500	22,600	17,000	38,140	n/a

[a] *Source*: Ref. 59.
[b] *Source*: Refs 60 and 61.

Sea (66, 67), Kuwait (68), Assam (69), Indian (70, 71), Boscan and other Venezuelan (72, 73), Velden (74, 75), Bavarian (76), Hungarian (22), Egyptian (77, 78), Norwegian (79–81), and Canadian (82–88) heavy oils and bitumen. The crudes, heavy oils, and bitumens differ geographically, and hence in their diagenetic histories. Their physical and chemical properties reflect their diversity not only in the W/O emulsions formed in them, but also in the response of their emulsions to demulsifiers. Because of the water and electrolytes, petroleum W/O emulsions translate into high processing heat requirements, corrosion problems, and increased transportation costs. Demulsification is a necessity.

III. FORMATION AND STABILITY OF CRUDE OIL AND BITUMEN EMULSIONS

A. Production Emulsions and Stability

In the process of crude oil extraction and transportation the formation of emulsions is inevitable. As the immiscible fluid mixtures pass through piping valves, porous rocks, etc., and experience turbulence, especially at high pressure and/or high temperature, breakup and deformation occur. If the ionic composition or pH of the water is favorable, and surface-active agents are present, emulsion formation is enhanced (89–92). The degree of emulsification depends on several factors: the energy of the process, the amounts of surface-active components in the crude oil, the physicochemical properties of crudes, water, and surfactants, and the residence time, as emulsions age. Aged crude-oil interfacial films become more resilient over time (74, 93) and are therefore more difficult to demulsify (94, 95). Finer and more stable emulsions occur with prolonged high-energy input in these systems.

In a destabilization scheme, one first assesses the degree of stability of the emulsion. There is a need to know how much time and energy are crucial for the process, the phase compositions, and the emulsifier(s) chemistry. For the experienced engineer, this information then allows some deductions on the configuration of emulsifiers around the droplets, and the rheological properties of both the interfacial film on the droplet and the interphase lamella between droplets. The viscosities of the emulsions and continuous oil phase are also important for decisions on destabilization (96).

In production the quantities of water in emulsions vary from 30% W/O formed in oil sands extraction processes to 80 or 90% in the form of "chocolate mousse" during an oil spill at sea (97, 98). Real systems are more complex and heterogeneous than the ideal systems. The W/O droplets are fine, well dispersed, and very stable. Asphaltene content is around 17% in bitumenous emulsions and around 2% for North Sea crudes. Figure 7 shows a confocal photomicrograph of a bitumen froth emulsion freshly extracted at CANMET. The solids present are shown as white specks; the dark spots are emulsion droplets in a bitumen continuous phase. The composition is 41% bitumen, 44% water, and 15% solids.

Some emulsions exist for a few minutes; others can stay in suspension for years. The life/death cycles are dependent on the stability and the destabilizers. The sizes of the droplets and the rigidity of the surface film barrier determine the lifetime of the emulsion droplets. For convenience in treatment, the terms for definition of stable emulsions are determined by their

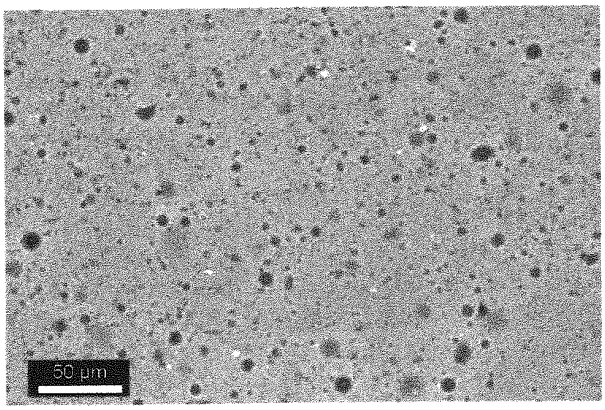

Figure 7 Confocal photomicrograph of freshly extracted bitumen froth – Dark spots are water droplets, white specks are solids particles. Composition by weight is 41% bitumen, 44% water, 15% solids.

persistence in the process time scale, and thus are categorized kinetically only in operational terms. Planned studies on emulsions should consider operational conditions in the experimental design.

It has been found that the finer the emulsions the more stable they are in terms of resistance to coalescence, as the fine emulsions behave as hard nondeformable spheres (99). The increased ratios of the dispersed water phase to continuous oil phase determine the packing factor. Most often a packing density of 0.74 tends to be critical for destabilization (100) for ideal monodisperse spheres in a hexagonal arrangement in the systems (101). This packing factor increases considerably for polydisperse systems such as crude oil emulsions. With creaming there is increased packing and some deformation occurs in the more elastic systems; the emulsions may appear as foams, with phase ratios between 0.8 and 0.9. Any increase in the critical packing factor can cause instability of the emulsions. Thus, valuable information on stability or instability (102) can also be obtained by varying the volume fraction of the dispersed phase under flow conditions. Here, the emulsion bulk rheological responses are a function of imposed external stresses and constraints and can be signatures to the system stability in a process.

The period of time in which the droplets do not coalesce without mechanical, electrical, or chemical aids has become the kinetic guideline for stable emulsions. In the extraction of oil in the petroleum industry very stable emulsions are undesirable. The exceptions are "orimulsion" fuels (103), made in Venezuela, and/or emulsions especially tailored in formulation for transportation in pipelines (104, 105). These must be destabilized on delivery (106, 107).

Much of the early literature published on chemical demulsification involved emulsions of crudes from offshore operations and other conventional land-extracted light oils. Thus, much of the knowledge acquired about crude-oil emulsion stability was based on paraffinic crudes of low asphaltene content. It is essential to be aware that results for crudes of the North Sea operations were based on a high wax content, and low asphaltenes and resins content (108) (see Table 1), when compared with results for highly aromatic and asphaltenic heavy oils and bitumen, which are low in wax, and higher in resins. The latter emulsions would be those of Canadian (Alberta) bitumen, heavy oils from Boscan (Venezuela), and Canada and California crudes, which are all highly aromatic and asphaltenic. These W/O emulsions are known to be very stable or "tight" (23).

Generally, oilfield emulsions are most often W/O with the surface-active emulsifiers residing in the crude-oil continuous phase. According to the Bancroft rule (109) the phase for which the emulsifiers are most soluble is the continuous phase. The emulsifiers possess some degree of polarity which attracts them to the water phase. Solid emulsifiers would be very fine particles in a state of incipient flocculation (110). The emulsifiers may be one or more of the following: solids which are partially hydrophobic with contact angle ($\theta \geq 90°$), polar asphaltenes and resins with some partial insolubility induced by solvents which dilute the crude oils, or metalloporphyrins integrated within the asphaltenes (24, 25).

A knowledge of solvents and solubilities is crucial for understanding the (in)stability. The solvent power is a function of the molecular structures. Aromatics have the greater dispersion forces and higher solution energies and thus superior solvent power. For Athabasca bitumen (111) the solvencies are as follows: paraffins < olefins < napthenes < cyclo-olefins < condensed napthenes < aromatics < condensed aromatics. This is also true for other crude and heavy oils (50) to various degrees. Thus, the choice of solvent can determine the degree of emulsion stability.

The structures of asphaltenes, as first deduced by Pfeiffer and Saal (112), showed them as fine aggregated particles solubilized in resins (14). Later, the solvent effects on their colloidal natures and their roles in the resiliency of the interfacial film formed at the boundary between the water droplet and the oil phase became important in the destabilization models (113, 114).

The role of waxes in emulsion stability has been studied in great detail for paraffinic crudes, especially for crudes that were spilt in the sea (115, 116). Waxes are believed to interact hydrophobically with the asphaltene and resin micelles present in the crude oils (18, 20, 21) and become part of the emulsion film. Waxes were hypothesized to adhere to the asphaltenes and resins, since waxes are oil soluble and not surface active. With such emulsions, the temperature prehistory and cooling rates have a greater impact on the emulsion stability. The rate of cooling influences the wax crystal sizes (17, 18). Thus, the type and history of emulsions must be considered before a demulsification treatment is selected.

Generally, the less soluble, surface-active materials tend to accumulate at the water/oil interface building the film structure. The thickness and concentration of these materials around the droplet periphery build over time until the layer becomes a structural barrier against coalescence with other droplets.

B. Emulsions on a Bench Scale

Emulsification and demulsification of bench emulsions have been reviewed extensively in the past (89–92). The reader is referred to these publications for a more detailed fundamental background on theories and developments in laboratory measuring techniques for stable emulsions (117). To determine a destabilization program for emulsions it is often advisable to seek to understand first the interfacial properties in the emulsions (118). Most of this understanding is derived from bench studies.

Often, in bench studies aimed at understanding emulsion-stabilization mechanisms, a hypothesis is devised. Most often the components of crudes are first separated, and a model emulsion is prepared from various combinations of the components in a model oil and in water of quality similar to that of formation or process water. The stability or instability is traced either by water resolution or by observing the interfacial film properties under some form of externally applied stress over time. The stress may include temperature increases or solvent changes. The system may then be modified by the demulsifier and the changes in behavior are compared to that without the demulsifier. Deductions are then made about the film mechanics of the system in response to the variables.

When actual crude oil is studied, comparisons of the responses of the components in crude are usually made with those of the whole crude oil under similar conditions. Often the actual field system is used to test conclusions arrived at on model systems. In many cases the behaviors of several crude oils are compared under similar conditions for rigor. It is therefore important that representative crude oil samples from a process be obtained.

In the following discussions the published experimental findings are presented interrelatedly first in terms of internal oil chemistry at the interface and instabilities based on its composition, secondly in terms of effects of water chemistry, and thirdly in terms of demulsifier interaction. We include the activity of interfacial components involved in the structure of the protective skin, the behavior(s) of this structure with changes to water chemistry or solvency, or the effects of changes in film structure itself due to modification of relative proportions of interfacially active components. In some examples, developments in interfacial rheology, which is both a tool for understanding stable films and a means of rationalizing the effects of demulsifiers in demulsification, are discussed interrelatedly. Films may be sensitive to crude oil type, gas content, aqueous pH, salt content, temperature, age, and the presence of demulsifiers. Demulsifier performance is also influenced by many of these variables.

We distinguish first between the adsorbed skin at the W/O interface and the gap or lamella between approaching drops, which may be described as: W/I-interface/O/I-interface/W. Here, "I" is the boundary layer of the interface on the droplet surface, and O is crude oil or dilute bitumen between two water droplets, interfaces. Figure 8 is a photomicroph of two bitumen-stabilized water/oil droplets showing the interfacial skin and the interdroplet lamella. Figure 9 is a photomicrograph of several water droplets show-

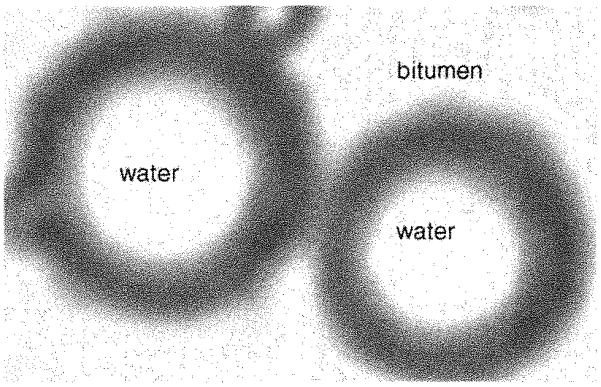

Figure 8 Photomicrograph of two water droplets showing the interfacial skin and the interdroplet lamella.

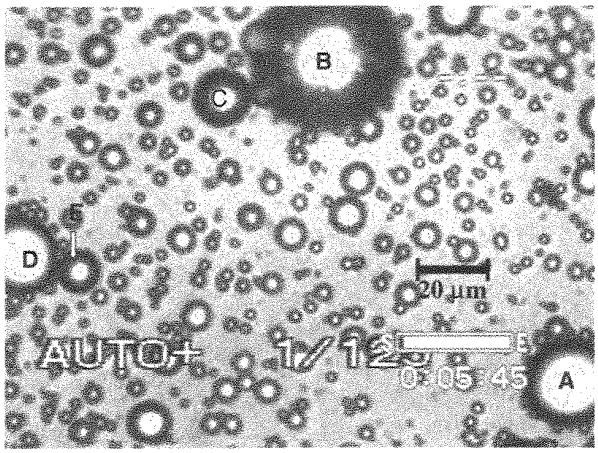

Figure 9 Photomicrograph of water in bitumen emulsion distribution with interfacial layer shown as the dark ring around the white droplet.

ing thick bitumen interfacial skins as dark circles around the bright water droplet. The continuous phase is the diluted bitumen.

Emulsion formation mechanisms are not the reverse of demulsification mechanisms. Crude-oil emulsion formation may involve one or more mechanisms based on the process of immiscible phases interacting, in time, with energy. To date, the detailed mechanisms are not yet understood completely, especially for petroleum emulsions.

In the laboratory, very reproducible W/O emulsions of monodispersed size distributions can be prepared when all the variables for emulsification are controlled. The variables for a bench laboratory study are: emulsifier type and concentration, energy of mixing, time of mixing, method of mixing, volume fractions of oil and water phases, type and viscosity of oil, quality of water, and temperature. The mixture is blended in specific vessels, usually with rest intervals to control the rigidity of the film. The conditions are reproduced from batch to batch. In real production this is not often the case. The immiscible phases are subject to variable high shear for 2–8 min in offshore production and 40–50 min in the oil sands extraction process. Emulsion size distributions therefore vary with different systems.

Several bench-scale model emulsions were prepared from bitumen in toluene, by varying only the water quality to observe the basic differences in the emulsions.

Figure 10 (a,c,e) shows a series of photomicrographs of model bitumen emulsions freshly prepared with deionized, 1 mM NaCl and synthetic pond water. Figure 10 (b,d,f) shows that emulsions become larger with age, supporting the kinetic instability. After 24 h there are differences in the final appearance of the emulsion for each sample of water used. The growth of droplets is due to Oswald ripening. It is expected that the interfacial film would differ in strength. Note the increasingly finer emulsions initially formed as the water changed from deionized to NaCl to synthetic pond water under identical experimental conditions. After 24 h the same trend is still observed.

C. Emulsions' Interfacial Film Structure and Instabilities

Undertaking first to achieve an understanding of the building blocks of the mechanical film could lead to the detection of surface weaknesses at which a demulsifier can be targeted. We illustrate this with examples from the literature.

In a review on formation and stability, Mackay (15) has suggested that the most stable emulsions have water particles in the 1 to 5 μm range, with a film thickness of 1/100 the diameter of the droplet. For bitumen W/O emulsions we have found in our laboratory that these are typical average droplet sizes (see Figs 7, 9 and 10). If we deduce the film structure from the components of crudes, then droplets are much larger than the components in the film. Mackay and Mason (119) have reported that asphaltene clusters can be about 2–4 nm in diameter and Neumann and Paczynka-Lahme (120) reported that asphaltenes were retained on filters of pores of 35 to 10 nm, while resins were retained on pores of 5 nm. Speight (4) reported that the asphaltene sheets are 10–15 Å by 6–15 Å. Bhardwaj and Hartland (74) reported that on an emulsion droplet the average cross-sectional interfacial area occupied by surface-active species from crude oil was experimentally shown to be 366 Å^2, while that for the asphaltenes in toluene was 253 Å^2. Larger water droplets (>10 μm), which will cream faster, tend to have a thinner film of between 1/100 and 1/1000 of the droplet diameter, on crude oil emulsions according to MacKay (15).

1. Observations of Destabilization of the Pseudostatic Film

The thick protective interfacial skins are considered as largely responsible for the stability of crude oil emul-

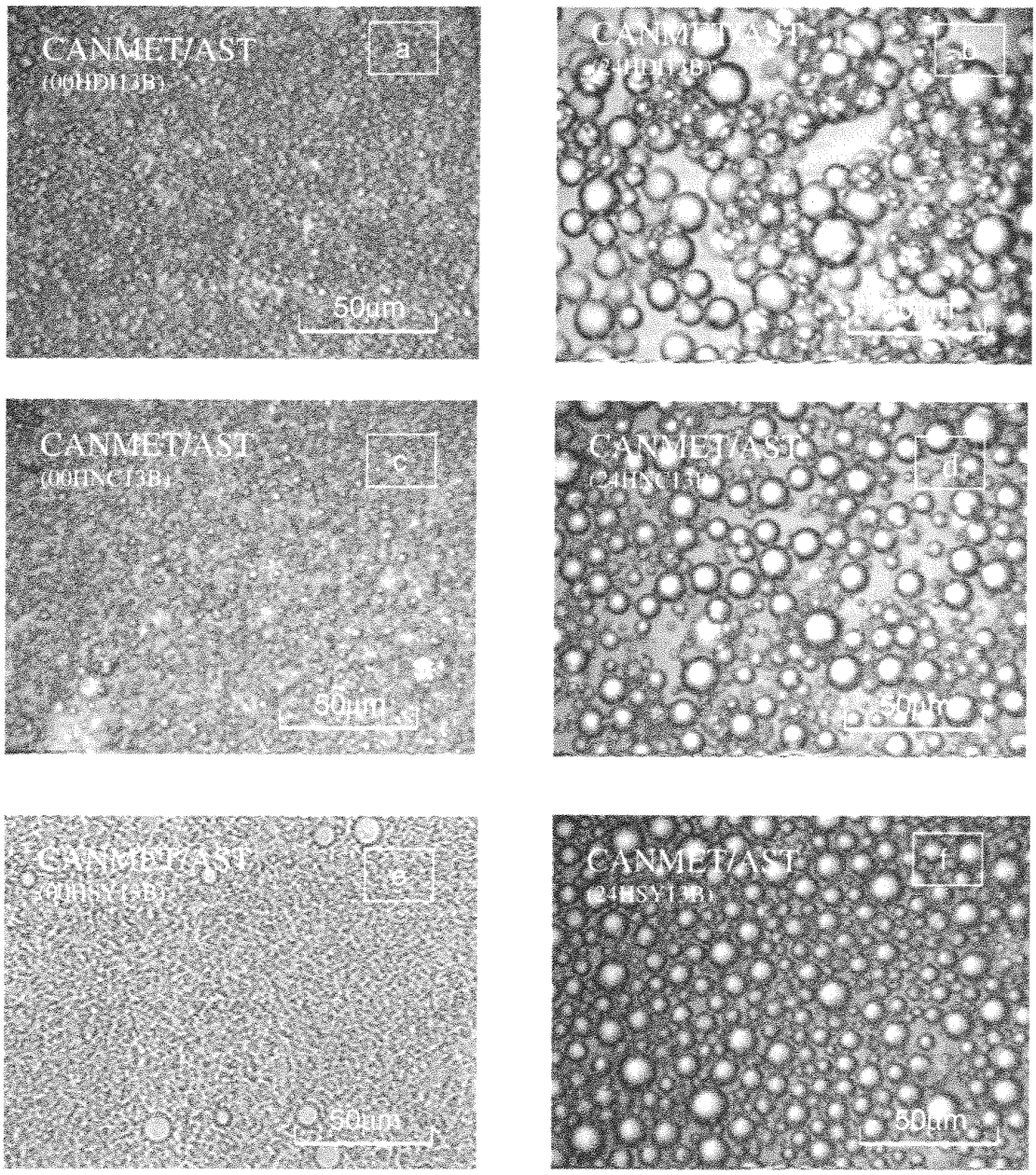

Figure 10 Photomicrographs of model bitumen W/O emulsion made with 13% synthetic pond water in a 30% bitumen-in-toluene solution. Left – droplets immediately after preparation; right – droplets after 24 h of aging. Deionized water (a,b); 0.001M NaCl (c,d); synthetic water (e,f). (Courtesy of C.W. Angle, in house research, CANMET.)

sions. This has been established in the past half a century in early studies (121). Hunter (122) offered a description of various types of interfaces where he considered two bulk phases separated by a planar phase or skin containing a structure of adsorbed materials and a liquid-like film phase. Based on the complexity of composition and curvatures he categorized them as A,B,C, and D. The differences are based on the mass of adsorbed materials, the sizes of head groups, and the charged ions present. Crude oils mostly match category C which has no coulombic contributions. By using the retraction of sessile drops of water/oil/

water, Roberts, as early as 1932 (123), made the observation of a thick film of oil at the crude oil/water interface.

In 1948, Lawrence and Killner (124) indicated that both good and poor solvents affected the surface viscosity of the film. Poor solvents such as the aliphatics showed higher surface viscosity, while a good solvent such as toluene containing 1% asphaltene in hexane had lower surface viscosity with a plastic film behavior.

In 1954, Blakey and Lawrence indicated that asphaltic components were responsible for the stability of sea water in admiralty fuel oil (125). In 1956, Reisberg and Doscher (126) showed that crude oil films existed at temperatures close to 90°C, indicating the importance of the rigid oil/water interfacial films in stabilizing emulsions.

In 1960, Blair (94) published findings obtained on an elastic membrane, which when compressed, developed wrinkles and thick striations about the point of disturbance for several crude oil/water interfaces. He found that in time the striations disappeared by an annealing process, and the interface then finally assumed a more uniform appearance. After using a surface film balance to measure the spreading forces (from 16 to 31 dyne/cm) for several crude oils on water with and without demulsifiers, he concluded that stability arises from the formation of a condensed and viscous interfacial film of adsorbed soluble material from the petroleum phase. Specific demulsifiers have spreading pressures sufficient to displace the petroleum film, leaving a thin film with little resistance to coalescence.

Since then, many studies were undertaken to understand the nature, strength, and weaknesses of the mechanical barrier or surface film on a droplet relative to emulsion resolution. Often these studies used a combination of microscopic observation of droplets formed and resolved, and interfacial rheological studies.

Thus, the discussions that follow include several important factors. These are that: (1) the activity of interfacial components is involved in the structure of the protective skin; (2) the behavior of this structure changes with water chemistry or solvency due to mass transfer and interfacial dissipation effects; (3) the changes in structure may be due to modification of the relative proportions of components; and (4) for understanding stable films and as a means of measuring demulsification, one may adapt the new developments in interfacial rheology as tools. These are all factors considered in past studies and which are described in the following sections.

2. Measuring Instability of the Film by Pendant-drop Retraction

Pendant-drop retraction experiments on 10 crudes were conducted by Strassner (113, 127). A pendant drop is illustrated in the schematic of Fig. 11. Strassner studied asphaltene and resin films as the interfacial area of the drop was varied. He described the films as either mobile and/or as transition films. The mobile film was a semisolid skin which, under compression, momentarily distorted. The transition films showed no distortion under drop contraction. Pendant-drop retraction experiments were conducted on medium to light crude oils of varied asphaltene-to-resin ratios for which he categorized film rigidities. Since heavy Venezuelan crude oil of high viscosity could not be measured by this technique, he extracted the resin and asphaltenes from this crude. He then varied the asphaltene-to-resin ratio in both the emulsions and in the films. He showed that the resins contributed to mobile films and the asphaltenes to more rigid incompressible films. He concluded that asphaltene and resin interactions were mainly responsible for the film properties of crude oil. The rigid films had high interfacial viscosity and the mobile films low interfacial viscosity.

Further examination of the films by changes in pH of the brine phase led to the conclusions that the rigid films formed by asphaltenes were stronger in acidic pH, became intermediate at neutral pH, and were mobile at basic pH. This behavior was characteristic of the asphaltenes' amphotericity. In addition, stronger oil wetting of silica occurred at acidic pH. The mobile

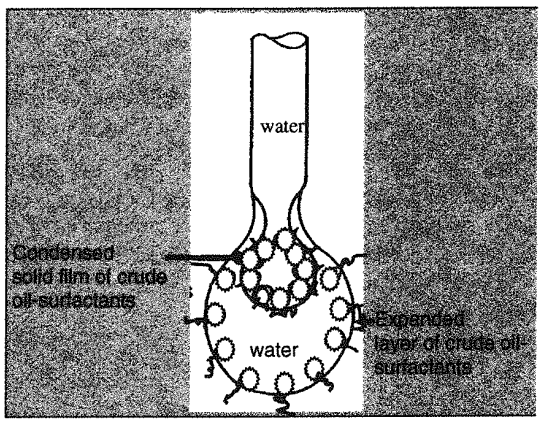

Figure 11 Schematic of a pendant drop with a condensed film of surface-active material on retraction, and expanded film during expansion. (From Ref. 74.)

resin films were stronger in basic pH, and weaker in acidic pH. This was also an indication of the resins weakly acidic nature.

Strassner (127) examined a third component, "waxes". He showed that resin and waxes do not oil-wet silica. Waxes had no significant effect. He concluded that the waxes only contribute to increased viscosity of the oil phase. At low salt concentrations asphaltenes plus resins will oil-wet silica at acidic pH, but will water-wet silica at basic pH. He examined Venezuelan crude oil and distilled water, and found the most breakout of water occurred at pH 10. In this case there was a transition to a mobile weak film, and interfacial tension was still high. However, when the water was changed to a bicarbonate solution, this transition occurred at pH 6, where maximum water breakout was observed at the high interfacial tension. The role of interfacial tension is discussed later in this text.

MacLean and Kilpatrick (21) recently confirmed that the integrity of the films was sensitive to solvency parameters such as aromaticity and asphaltene-to-resin ratios, as well as polar functional groups. They confirmed Strassner's findings, using North Sea crudes (113). They suggested that modifying the state of dissolution of asphaltenes should decrease the ability to stabilize the emulsions, and that asphaltenes are solubilized with resins and can only stabilize in a state of incipient flocculation. They inferred that as a molecular solution asphaltenes do not stabilize emulsions. The state of dispersion of asphaltenes (molecular versus colloidal) is critical to the strength or rigidity of the interfacial films and hence the stability of petroleum emulsions (48, 52). The balance of acidic to basic groups in its structure, and with that of resins, determines the degree of association for film formation. Earlier, Fordedahl et al. (128) in studies of crude oil emulsions in high electric fields by dielectric spectroscopy showed the influence of interaction between indigenous surfactants. They claimed that resins alone are not stabilizers, and that asphaltenes are the stabilizers even though resins have high interfacial activity. A mixture of 1% asphaltenes and 1% resins gave the critical ratios required to give the necessary film rigidity for a stable emulsion. However, these emulsions were still less stable than the original crude from which the fractions of asphaltenes and resins were derived (129).

Cottingham et al. (130) destabilized and restabilized shale oil emulsions by adding proportions of pentane solubles (resins) to shale oil emulsions, thus quickly separating the phases. They stabilized the emulsions indefinitely by adding both solubles and insolubles to the emulsions. These factors among others can be considered in demulsification.

Recently, Puskas et al. (131), using FTIR, Raman, VPO, X-Ray, rheology, SAXS, and UV techniques, conducted an extensive characterization study of fractions that were deemed to be structural components of Hungarian paraffinic-based crude-oil emulsions. They attributed stability of the interfacial emulsion film to a solid hydrophobic paraffin derivative or organocolloid of lamellar structure containing polar end groups. Together with asphaltenes, resins and oleophilized solids as components of the film structure, they deduced the formation of a cohesive three-dimensional film structure. The interfacial film had mechanical stability and flexibility. The increased viscosity of the crude oil also increased the coherent structure of the paraffin particles or waxes. They found that toluene softened the structure containing the paraffin particles and caused an increase in viscosity.

Mackay and coworkers (15, 132) performed emulsification studies, using wax and asphaltene mixtures as stabilizers. They showed that waxes are not stabilizers on their own but, together with asphaltenes at a high ratio and proper blending, form stable emulsions. They tried to quantify stability by indexing it to the proportion of mass ratios of each crude oil component to total oil mass. The number was indicative of a strong or weak mechanical film barrier. They claimed that asphaltenes alone form a strong interfacial film, resins make the asphaltene barrier less rigid and more easily deformed, and wax aids in film rigidity. All these findings suggest that the internal chemistries of the crude oil components or solvents may be a few of the control parameters useful for selection of demulsifiers.

Bridie et al. (1) found that asphaltenes are two to five times more effective than waxes as stabilizing agents. In a stable emulsion containing 6.6% asphaltenes and 9.8% wax, the emulsion was still stable if 90% of asphaltenes were removed. Waxes as crude oil stabilizers for North Sea crudes have been investigated by Thompson et al. (133, 134) who showed that waxes melt as the temperature increases, and separation efficiency increases at 60°C, which is above the wax melt temperature.

The roles of interfacially active fractions of crude in emulsion stability were confirmed by Felian et al. (135) and Sjöblom et al. (136). According to Sjöblom et al., when discussing the impact of chemical destabilization, there must be a strong basis for understanding the stability mechanism. The interactions between the destabilizer and the active components of crude oil

will dictate the sequence for destabilization in the system. They studied 10 Norwegian crudes of various SARA and wax contents. Some had high ratios of resins to asphaltenes. They found palmitic acid as an active stabilizer. When compared with heavy oil standards, asphaltene contents in North Sea crudes are extremely low, which suggests that other factors must enter into forming the stable interfacial films. Sjöblom et al. (136) indicated that palmitic acids, which they identified in their crudes, would adsorb very readily at the W/O interface and, because of their nonbulky nature, may tend to pack efficiently depending on the concentration. On the other hand, Acevedo et al. (52) attributed surface activity of the interfacial film partially to carboxylic acids, which they were able to extract from asphaltenes of Venezuelan heavy crudes. They concluded that carboxylic acids were integrated within the asphaltene micelles at the W/O interface. Other studies (137), conducted on Russian crudes, show the influence of the components on emulsion film strength (138, 139).

3. Surface Pressures Used as Measure of Film Instabilities with Demulsifiers

A Langmuir balance was adapted for studying the interfacial films of crude oil/water by Kimbler et al. (140). They plotted the surface pressures, Π, versus area as the film was compressed and observed the normal pattern of phase transitions such as gaseous (flat slightly rising), expanded (rise), and condensed liquid (change in slope of rise) phases. Figure 12 shows a schematic of the typical surface pressure/area isotherm for a simple surfactant, a monolayer of myristic acid measured in a Langmuir apparatus (141). Variations in the shapes of the curve indicate the state of the film. Collapsed films were identified by observation of the changes in the shapes of the isotherm.

Kimbler et al. (140) studied the addition of a destabilizer such as Triton X-100, which produced only expanded crude-oil films. It was noted that a drop in film pressure at a constant compressed area might be indicative of film dissolution or reorientation of structural elements. Changes in temperatures may change the adsorption rate and the buildup of interfacial film, and decrease the bulk viscosity. Temperature may change the rate of the relaxation process at constant compressed area (fall in film pressure), or change the rate of buildup of resistance to film compression (142).

Jones et al. (59) used a similar Langmuir-like trough for studying crude oil/water interfaces. They examined crudes such as Kuwait, Iranian, Ninian, Forties, and

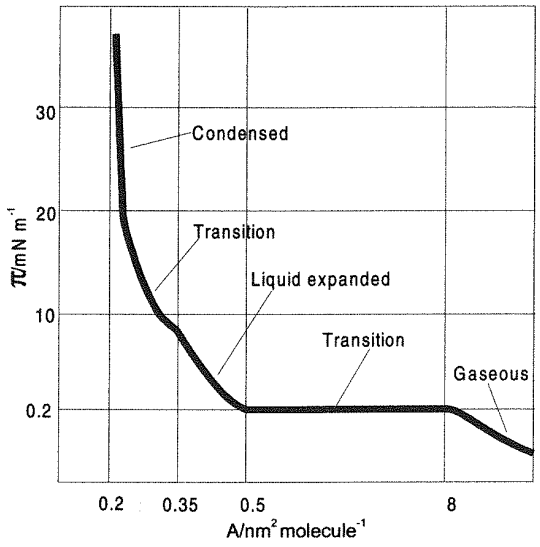

Figure 12 Schematic showing transitions of a typical surface pressure/area(Π/A) isotherm for a compressed monolayer of surfactant myristic acid spread on 0.1M HCl in a Langmuir-trough apparatus. (From Ref. 141.)

Magnus. Using the changes in the shapes of the Π–area curves and the fall in pressures (relaxing), they distinguished three types of film behavior: incompressible nonrelaxing (Iranian heavy and Ninian), incompressible relaxing (Forties and Kuwait), and compressible relaxing (Forties freshly added to water). On heating, the temperature increase caused the incompressible relaxing film to become a compressible relaxing film. The Magnus crude made a weak compressible film which became rigid and nonrelaxing and insensitive to temperature increases even in low bulk phase, when the light ends were evaporated. They suggested that high interfacial viscosities can be obtained by compressing the interfacial film, showing how the rate of thinning of these films can be greatly reduced based on their responses to compression. The kinetics of the relaxation process would determine the extent of the dynamic barrier to coalescence. Demulsifiers would change this.

By observing the responses of the films to two demulsifiers, they found that the ethoxylated phenol was a film displacer and inhibitor for aged films and that the carboxylic acids containing alkoxylated ester were film inhibiting if added to crude oil before contact with the water. They also found that Ca^{2+} ions rendered the film incompressible and this resulted in a more stable emulsion. They also suggested that pendant-drop retraction could not be used to distinguish

between relaxing compressible films and incompressible relaxing films. They suggested that viscous buildup should be shown; otherwise, interpretations based on the pendant-drop experiments can be misleading.

The Langmuir-balance technique was adapted for the study of Indian crudes by Singh and Pandey (69). They separated the crudes into anionic, cationic, and nonionic fractions and studied the effects of electrolytes and pH on their film properties. Maximum film pressure was observed for films made with the anionic fraction and minimum film pressure for the cationic fractions. Increased electrolyte concentrations caused increased viscosity and less resolution of emulsions. Film pressures were maximum at pH 12 and more stable emulsions resulted. The electrolyte also had an adverse effect on the demulsifier.

Singh (143) followed up this study to understand the performance of unidentified demulsifiers with a change in solvent properties. By noting the relative decrease in surface pressures resulting from added demulsifiers in various solvents, he found that benzene was the best in that it helped the demulsifier to lower the surface film pressures. The lowering of interfacial tension was measured at the same time and the results suggested that rapid adsorption occurred. It was concluded that structure, orientation, and film pressures were the most important factors in demulsifier performance.

Mohammed et al. (144, 145), in a series of studies, examined several aspects of emulsion films with and without demulsifiers as well as their chemistries. Using the Langmuir balance for studying the air/crude/water interface, they examined the surface pressure Π–area isotherm for monolayers of Buchan crude's asphaltenes and resins and their mixtures, spread on distilled water at pH 6.2 and 25°C. They found that the asphaltenes upon compression formed solid films, that could withstand pressures up to 45 mN m^{-1} in contrast to the resin films at 7 mN m^{-1} which thereafter collapsed. The asphaltenes formed highly stable emulsions in contrast to the resins alone, which formed the least stable emulsions. They found that film compressibility and emulsion stability decreased as resin content increased. Temperature increases caused no significant effects on asphaltene monolayer compressibility as was observed earlier by Reisberg and Doscher (126) for natural crude oil films.

Nordli et al. (146), using the Langmuir-balance technique, studied the monolayer properties of the interfacially active fractions extracted from six North Sea crude oils over a subphase of distilled water and simulated formation water. The pH and salinity were varied. They compared additives such as butanol, benzyl alcohol, and octylamine, added to the subphase, to note changes in film compressibilities. A typical phase-change pattern for Langmuir curves of surface pressure versus area was observed for all cases. The smallest specific area attributed to the liquid expanded states was reached by the lowest-molecular-weight species. Films, in this case, were more condensed as the temperature increased. At constant pressure, the changes in the surface pressure were monitored over time for each film. The time for relaxation was 60 min for the low-molecular-weight fraction, and 320 min for the high-molecular-weight fraction. Distilled water in the subphase showed decreased specific area for the same film, and a pH of 2.6 caused a shift to higher specific area. Salt had no significant effects.

According to Taylor and Mingins (142) a drop in film pressure at constant compressed area may be indicative of film dissolution or reorientation of structural elements. If there is no resistance to compression, an unstable emulsion results. Changes in temperature may change the adsorption rate and the buildup of the interfacial film. A decrease in the bulk viscosity may change the rate of the relaxation process (fall in film pressure) at constant compressed area and change the rate of buildup of resistance to film compression.

D. Destabilization and Interfacial Film Rheology

Developments in measurement techniques for monitoring interfacial changes occurred for the purpose of understanding emulsion stability. However, the techniques were equally useful in measuring destabilization induced by changes to the internal natural chemistries of the system or with addition of chemical demulsifiers. The adaptation of the Langmuir film balance was only one tool for a pseudostatic system. However, as the fluid dynamics in the films and interphase (or lamella) of two approaching droplets or in a highly concentrated emulsion dispersion was discovered to be more complex and bore similarity to the polyhedral structures of foams, the need to study the emulsion interfacial films under stresses became apparent. Much was learned from foam studies.

A detailed treatise on the fundamentals and applications of thin films, i.e., lamella plus surface film, is found in Ivanov (147). The two major forces involved in the lamella behavior are thermodynamic (disjoining forces) and hydrodynamic. Further in-depth studies on the thermodynamics are presented in de Feijter (148) and Hirasaki (149) and on the hydrodynamics in Maldarelli and Jain (150). Because of the complexity

of this topic, which is not within the scope of this chapter, the following discussions will be limited to the understanding that this research brought about concerning the nature of the films and the process of film thinning by chemical demulsification.

The interfacial rheology of films has been extensively discussed by Edwards et al. (151) and briefly by Tadros (152), and reviewed in relation to emulsions and foams by Malhotra and Wasan (153). A two-dimensional fluid interface can only be treated as an independent body when it is highly viscous or highly elastic. It cannot be treated separately from the bulk fluid which may provide viscous drag and influence the direction of flow. Simply, interfacial rheology describes the flow behaviour in the interfacial region between two immiscible fluid phases. The adsorbed surface-active components at the crude oil/water interface alter the hydrodynamic resistance to interfacial flow. As the molecular weight of the adsorbed species increases, the interface exhibits viscoelastic behavior. This is most likely in the case of bitumen W/O emulsions. The chemical demulsifier interaction alters not only the physical/chemical properties but the rheological behavior. Figure 13 is a schematic of the physicochemical and dynamic factors involved in droplet interactions.

1. Crude Oil Interfacial Rheology – Background

There are four rheological parameters which describe the response to imposed interfacial stresses or deformation. For a Newtonian interface, the significant rheological properties that determine interfacial motion are the interfacial shear viscosity, η_s, the interfacial dilational viscosity, η_d, and the interfacial tension gradient. The interfacial shear elasticity, ε_s and viscosity, η_s, describe the resistance of the interface to changes in shape of the interface element. Here, the area is kept constant and the resistance is measured. On the other hand, the interfacial dilational elasticity, ε_d, and viscosity, η_d, describe surface resistance to changes in interfacial area. The interface is expanded without shear and the resistance is measured. Figure 14 shows schematically the shear and dilational forces on an interface in determining shear and dilational viscosity.

The need for the dilational data arose due to the manifestation of Gibbs–Marangoni effects or surface-tension gradients occurring during film thinning. The surface-tension gradients and hence the elastic behavior are influenced by changes in temperature, concentration of surface-active agents, and/or compression and expansion of the interface.

Detailed theoretical treatments of the dilational properties of liquid films can be found in several studies. Kristov et al. (154) performed a parametric study determining the compositional surface elasticity of model systems. Loglio et al. (155) reported on the dilational viscoelasticity of fluid interfaces modeled for transient processes, Edwards and Wasan (156) discussed foam dilational viscosity, and Lucassen-Reynders and Van den Temple (157) reported on the surface dilational modulus caused by variation of surface tension from a small-amplitude sinusoidal area variation. Recently, Yeung et al. (158) modeled the expanding pendant drop in their explanation of interfacial mass-dissipation effects.

2. Measuring Destabilization by Dynamic Interfacial Shear Viscometry

Dynamic shear measurements may be conducted by using several interfacial rheological instruments. A detailed reference list on these is found in a treatise by Malhotra and Wasan (153). Among those specially

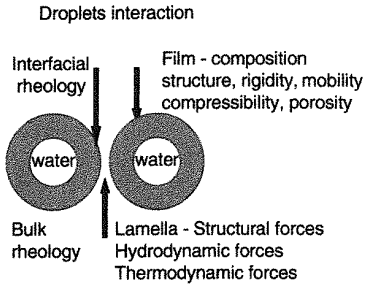

Figure 13 Schematic on the physicochemical and dynamic factors involved in the droplet interaction.

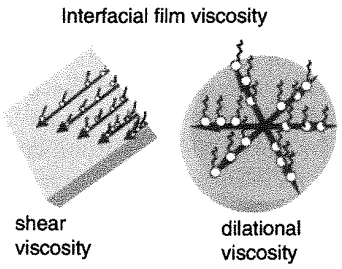

Figure 14 Schematic of shear and dilational forces involved in measuring the corresponding viscosities at a W/O interface.

used for interfacial shear viscometry are a ring viscometer, a disk viscometer, a knife-edge viscometer, a deep-channel surface viscometer, and various modifications to these as described by Edwards et al. (151) and Boyd and Sherman (159). The majority of these are for interfacial shear measurements.

Cairns et al. (160) gave a detailed description of interfacial shear viscometry of crude oil/aqueous 1% NaCl systems. Kuwait crude had a low η_s and produced unstable emulsions, while Iranian heavy had a high η_s and stable emulsions. They showed that η_s decreased with increases in pH and NaCl, and η_s increased with aging. The aging effect invariably is a result of interfacial material build up over time, recently described by Neumann and Paczynska-Lahme (120) for crude W/O emulsions. Cairns et al. (160) concluded that the stability of emulsions was favorable when there was a rapid adsorption of surface-active agents (detected by a fall in interfacial tension), followed by a rapid rise in η_s, and that maximum emulsion stability occurred when pH and η_s were highest. When comparing Zakum and Murban (0.08% asphaltenes) with Tia Juana (3.05% asphaltenes) in the pH range 2–11 a high asphaltene content did not correspond with high η_s. With Ca^{2+}, η_s was high and interfacial tension fell rapidly, leading to intermediate emulsion stability; yet with Na^+, η_s was low, interfacial tension fell slowly, and emulsions were unstable.

Grist et al. (161) provided a detailed critique of the biconical bob tension pendulum viscometer in interfacial shear viscosity measurements of Forties water/crude oil systems. They reported that a highly viscous interface reduces oil film drainage and is responsible for the high water content of "chocolate mousse" in oil spills as well as increased emulsion stability. Graham et al. (162) showed reduced η_s with demulsifier and methanol, and that overdosing led to both increased η_s and emulsion stability. Wasan et al. (163) in their study of Salem crude/brine, measured the η_s responses with a deep-channel interfacial viscometer with and without a petroleum sulfonate demulsifier. The demulsifier activity was enhanced with a cosurfactant such as hexanol. They reported that as η_s increased coalescence decreased. Later Pasquarelli and Wasan (164), using a viscous traction shear viscometer, showed that, with Salem crude and demulsifier TRS 10–80, the emulsion became more stable at high η_s. On examination of the η_s of the fractionated crude (one high-asphaltenes fraction and one high-resin fraction) against brine and alkaline water, they found that η_s was highest in the high-asphaltene fraction film against first brine and then water, giving 7.1 and 6.7 surface poise, respectively. Under similar conditions, against brine and water phase, respectively, the resins' η_s showed 0.004 and 0.00074 surface poise, while the η_s of the source crude oil were 0.25 and 0.00043 surface poise, respectively. Taylor (165) also indicated that the aging of the Romashkino, Ninian, and Kuwait crudes with an external added surfactant can retard the buildup of η_s. Neustadter et al. (166) used the conical bob torsion pendulum rheometer to study the interfacial rheology of Iranian heavy, Kuwait, and Forties crude oil–water films. They showed the same η_s for all crudes, and suggested that one cannot use only interfacial shear viscosity to predict emulsion behaviour and that the compressibilities and elasticities are not reflected in this viscosity.

3. Destabilization and Dynamic Interfacial Viscoelasticity

To achieve both shear viscous and shear elastic properties, oscillatory measurements can be performed where one movable component of the rheometer is oscillated at given amplitudes and frequencies, and a sinusoidal wave is propagated. The complex modulus, ε^*, is then related to the elastic and viscous vector components, which are the real and imaginary coefficients of the frequency function.

Mukerjee and Kushnick (167) suggested that the interfacial dilational modulus can be obtained by a Fourier-transformed pulsed-drop technique similar to the method used by Clint et al. (168) in which the Langmuir trough was used in studying the interfacial tension (γ) variation with periodic variation in interfacial area. The frequency-dependent complex modulus, $\varepsilon^*(f)$, is equated to a real elastic modulus, $\varepsilon'(f)$ (dilational elastic modulus), plus an imaginary modulus $i\varepsilon''(f)$ (dilational viscosity modulus), and set equal to $(d\gamma/dA/A)$. The dilational elastic modulus is the interfacial tension gradient which is in phase with the area, A, change. The dilational viscosity modulus is 90° out of phase with the area change.

Mukerjee and Kushnick (167) showed that at low frequency the demulsifier behaves as a soluble monolayer, and at high frequency as an insoluble monolayer. Variation in interfacial tension from a local change in area is virtually instantaneous. This gradient is short circuited when the demulsifier molecule moves to and from the surface to bulk or is sufficiently soluble in the bulk phase.

Mukherjee and Kushnick's definitions were as follows: the interfacial tension increment, $d\gamma$, per unit

fractional area change, dA/A, is eq'uated to the complex modulus, $\varepsilon^*(f)$;

$$\varepsilon^*(f) = \varepsilon'(f) + i\varepsilon''(f) = d\gamma / d A/A \quad (1)$$

$$= d_\gamma / d \ln A \quad (2)$$

Where $\varepsilon'(f)$ and $\varepsilon''(f)$ are the real and imaginary components at a frequency f.

For an air/liquid system a measure of the surface-tension variation resulting from the imposed periodic area variation in the Langmuir trough is performed. If both dilational viscous $\eta_d = \varepsilon''(f)$ and dilational elastic $\varepsilon_d = \varepsilon'(f)$ data are needed, and if a Langmuir-type trough is used, then one barrier can be oscillated and another barrier can be used to adjust the extent of the interfacial area. The calculation of the complex modulus, ε^*, requires complete scans at different frequencies.

There are many difficulties associated with this technique when applied to crude oil systems according to Mukherjee and Kushnick (167). They by-passed these difficulties by using the method developed by Neustadter and coworkers (168, 169) for crude oil systems by following the dynamic interfacial tension with step changes in interfacial area. A complete frequency spectrum is obtained by Fourier transform (FT) of the dynamic interfacial tension data:

$$\varepsilon^*(f) = 2\pi i f / \Delta \ln A \int_0^\infty \Delta\gamma(f) e^{-2\pi i f t} dt \quad (3)$$

$$\varepsilon'(f) = 2\pi i f / \Delta \ln A \,[\text{Real FT } (\Delta\gamma)] \quad (4)$$

This is the dilational elastic modulus or the interfacial tension gradient which is in phase with the area change.

At low frequency they found that the demulsifier behaved as soluble monolayers and the tension was governed by the bulk concentration and did not change with change in area. At high frequency the demulsifiers behaved as insoluble monolayers and the change in interfacial tension resulting from area change was instantaneous:

$$\varepsilon''(f) = 2\pi i f / \Delta \ln A \,[\text{Imaginary FT } (\Delta\gamma)] \quad (5)$$

This is the dilational viscosity modulus which occurs when the demulsifier is soluble in the bulk liquid. Area compression and expansion produce a tension gradient, which is diminished by the periodic transfer of demulsifier to the bulk from the surface and vice versa. The viscosity component amplitude is 90° out of phase with the area change.

This technique was used to show that demulsification effectiveness can be correlated with a low dynamic interfacial tension gradient, especially at low interfacial shear viscosity and this is evidenced by a sharp rise in interfacial tension at low frequencies for ineffective demulsifiers.

Alternatively, interfacial tension can also be measured continuously with area changes, with an expanding or contracting pendant-drop instrument adapted to oscillatory measurements as described by Bhardwaj and Hartland (74). Dilational data are obtained without introducing shear as the interface is expanded and contracted. This is also often achieved with an expanding drop volume or bubble-pressure tensiometer (65). Nikolov et al. (170) have recently developed this technique and an instrument to study oil/water systems.

Tambe et al. (171) used model systems of colloidal-laden interfaces of emulsions made up of 2 wt% graphite, 20 ml deionized water, and 30 ml decane. They modeled the system to understand factors that control the colloid-stabilized emulsions as was studied previously by Wasan and Menon (172, 173). They showed that, for viscoelastic films of finite dilational elasticity, interfacial rheology plays a dominant role in film-drainage rates. They suggested that the characteristic relaxation times are related to the ability of a demulsifier molecule to diffuse to the interface in response to a concentration gradient while minimizing the Marangoni flows, which retard film drainage. They suggested that the film-drainage rate is sensitive to the dilational elasticity of the interfaces. For viscous interfaces (zero dilational elasticity) the drainage rate is independent of interfacial dilational viscosity.

Neustadter et al. (166) earlier measured interfacial dilation elasticities, ε_d, and viscosity, η_d, for Iranian crude oil/water and deduced that the extent of the relaxation process was not a function of time due to the lack of change in viscosity, η_d, at fixed frequency. However, as frequency changed, η_d decreased, indicating that the relaxation involved the interchange of bulk material to and from the interface. The increased elasticy, ε_d, with time suggested that there was irreversible adsorption of high-molecular-weight species.

Nordli et al. (146) later found larger relaxation time for the films with the higher-molecular-weight surface-active species derived from North Sea crude. For crude W/O emulsions, Neumann and Paczynska-Lahme (120) concurred that the emulsions are stabilized by thick films with Gibbs elasticity, and the more the interfacial activities of the components differ from each other the higher the elasticity modulus of the multicomponent films.

During compression and expansion, a molecular relaxation process occurs for that time scale. It is expected that there will be characteristic relaxation rates (times). It is expected that the molecular relaxation process will include: (1) increased packing by surface diffusion of low-molecular-weight species; (2) molecular conformational changes of irreversibly adsorbed high-molecular-weight species; (3) desorption; and (4) readsorption of low-molecular-weight reversibly adsorbed molecules. These may occur during the compression and expansion stages. The response can also be interpreted as solvent losses from the molecular films.

Neustadter et al. (166) indicated that, if the frequency of the longitudinal wave is varied, the bulk-to-interface interchange occurs during compression/expansion of the film. There may be a short-circuiting of the interfacial tension gradient, and then information on the relaxation rates and dilational properties may be obtained. In this interchange one may observe a low apparent compression modulus. A phase shift between the imposed strain (change in area) and resultant stress (change in interfacial tension) would occur. Different interfacial tensions with compression/expansion would be produced with molecular reorientation of irreversibly adsorbed species. With the increase in frequency of oscillation there is less bulk to interface interchange. Only for species of greater solubilities and shorter chain length would diffusional interchange be important. For the long-chain irreversibly bound components, which are almost insoluble, slower reorientation will occur. Neustadter et al. (166) emphasized that relaxation plays an important role in the behavior of the crude oil/water interface. With age, low dilation elasticities increase and no change in dilation viscosities occur.

E. Further Studies on Shear and Dilational Viscosity of Crudes

In 1987, Eley et al. (72) used the pendant-drop retraction method in the study of film compressibilities of crude oil/water interfaces for three crudes. These varied in asphaltene content. Libya (Brega) had 0.46 g/L, Kuwait 3.7 g/L, and Tia Juana (Venezuela) 5.94 g/L. They added a dispersant containing a nonionic oil-soluble surfactant, and observed increased film compressibilities. The concentration of effective dispersant correlated with the asphaltene content. At the same time the decreased interfacial tension corresponded with increased film compressibilities and this was explained as a displacement of asphaltenes from the interface by the dispersant.

They adapted an interfacial shear rheometer (plate/rod) to measure the shear viscoelasticity of the system with and without dispersant. At an applied shear stress, creep curves for the system were monitored. There were no instantaneous elasticity and viscosity for the Kuwait and Tia Juana crudes with and without dispersant. They attributed this to a network structure of flocculated asphaltenes in the films. They found that there was some dilatancy in their crude oil films, described as a "stick/slip" flow in their flow curves. However, this flow was attributed to thick films of asphaltene particles building up at the interface. Using creep measurements, they examined a model system of asphaltenes/n-heptane/toluene. They found a retarded elastic deformation, which was different from the response of the crude oils. This suggested to them that there was a different type of interfacial structure formed with the model oil, and this may be attributed to the solvency of the medium and not to the lower asphaltenes content in the model system.

Further details of interfacial rheology of crude-oil emulsion films are discussed extensively by Menon et al. (174), Neustadter et al. (166), Mohammed et al. (175), Tambe et al. (176), and Mukherjee and Kushnick (167). They discussed the effects of demulsifiers on the interfacial properties governing the crude-oil demulsification.

Neustadter et al. (166) first discussed the crude-oil interfacial film in terms of pseudostatic film compressibility when the Langmuir balance was used for studying the liquid/liquid interface. This technique showed less variation in adsorption and showed that all but the most surface-active species were squeezed out during compression. The whole interphase region was then probed using a biconical bob torsion pendulum device suitable for high interfacial shear measurements. It responded to small changes in adsorption in the interphase region.

Highly viscous interfacial films retarded the rate of film drainage during coalescence of water droplets. They found that a highly viscous film at pH 6 led to maximum stability. They also suggested that to increase the interfacial viscosity of a low interfacial viscosity film, one should compress it. Interfacial shear viscosities were investigated with all three crudes, Iranian heavy, Kuwait, and Forties, which had similar interfacial shear viscosities.

Interfacial rheology should be used with care as a predictive tool for emulsion stability/instability. Graham et al. (162) showed that there was reduction

in interfacial shear viscosity of Forties crude oil/water interface with demulsifier added in methanol. Cairns et al. (177) revealed for Zakum, Murban, and Tia Juana crudes/water systems, that interfacial shear viscosity, η_s, decreased with increased pH, and η_s decreased with increase in electrolyte NaCl. Also, η_s increased over time. This did not correlate with the asphaltenes content.

Wasan et al. (163) used a deep-channel viscometer in studying the interfacial shear viscosity of Salem crudes/water with and without the addition of petroleum sulfonate and salts, as well as Illinois crude/brine with pentadecyl benzenesulfonate. They showed a decreased coalescence time with decreased shear viscosity. A viscous traction shear viscometer was used for fractionated crude oil/brine by Pasquarelli and Wasan (164), who showed that increased interfacial shear viscosity is correlated with decreased coalescence. Later, Wasan correlated interfacial shear viscosity with film-drainage time to determine effective demulsifiers (178).

Taylor (165) observed that surfactants used as destabilizers retard the build up of material at the oil/water interface for aging Ninian, Romaskino, and Kuwait crudes. Mohammed et al. (144) studied the rheological behavior of the North Sea Buchan crude oil/double-distilled water interface by oscillatory interfacial shear rheometry, using the biconical bob rheometer in the oscillation and creep modes. They used creep measurements to obtain relaxation data. This crude is known to produce very stable emulsions, yet its heptane-precipitated asphaltenes were only 0.058 g/mL. They attributed Newtonian viscosity to the adsorption of low-molecular-weight components of crude, and the build up of the interfacial films to high-molecular-weight components forming a network structure with viscoelastic properties. They investigated the effects of temperature and of demulsifiers Unidem 120 and BJ18 in xylene on the film viscoelasticity. They found that at 45°C the interfacial film viscoelasticity became more liquid-like. The increased viscosity with increase in temperature was a result of loss of light ends. The Unidem 120 caused a change in the aged film character from solid-like to liquid-like, and BJ18 prevented the film buildup. They traced these effects through the relaxation time from creep curves with and without demulsifiers, as well as observing a decreased viscous component in the oscillatory measurements.

Chen et al. (179) used optical microscopy to study the same crude-oil emulsions in an electric field. They modeled the system with a computer simulation based on a hard-sphere model describing the droplets as stabilized by a rigid asphaltene film. They identified two different types of coalescence. The mobile interfacial films led to low emulsion conductivities owing to immediate droplet/droplet coalescence, and the incompressible interfacial film led to low emulsion conductivities due to droplet-chain formation and bridging between the electrodes.

Malhotra (180), in a parametric study, showed that interfacial mobility and the rate of film drainage depend on the interfacial shear viscosity when the viscosity is in the range 10^{-5} to 10^{-3} Pa.ms. Outside this range the interfacial viscosity had no effect. Interfacial viscosity as low as $< 10^{-5}$ Pa.ms can lead to stable emulsions (181).

The reported information on film rigidity, compressibility, and other aspects of interfacial rheology indicates that the highly viscous and elastic films are stable. In most of the compressibility studies on crude oil films, the films were made with the various surface-active components of crude oil and/or the crude oil itself. The drop-retraction, Langmuir-type trough, and pendant drops pulsed at various frequencies of expansions and contractions were tools for studying the mechanics and fluid dynamics of the dilating interfacial films. In addition, sophisticated shear rheometers, including oscillatory and creep measurements, were used to obtain shear viscosity, elasticity, and film relaxation data. Typically, these measurements were made with and without demulsifiers, with changes in water quality, pH, or solvent properties when demulsifiication was investigated.

Wasan and coworkers (63, 65, 174) extended techniques for studying film rheology of the foam lamella to studies of crude-oil emulsion lamella. Using a capillary balance technique and light interferometry, the film thinning of foams was studied with and without chemical demulsifiers, with solvent properties changed, etc. (182). They confirmed that there were two contributions to emulsion stability – a structural component that originates from the nature of the bulk phase, and an adsorbed-layer contribution to film stability (170). This will be covered in another chapter in this series.

F. Destabilization and Interfacial Tensions

The equilibrium interfacial tension between water and oil is a measure of the adsorption of surface-active components to the interface and can be related to surface excess by the Gibbs equation (183). However, in crude oil systems the activity/concentrations of the surface-active components are not easily determined. Indirect measures are applied. In most process condi-

tions with short resident times, it is the dynamic interfacial tension gradient that is important. Interfacial tension also tells whether or not the demulsifier is surface active, and as will be shown later, this is important for demulsification. The interfacial tension gradient is the important factor for rendering the interface immobile. The interfacial tension gradient is used in a measure of Gibbs surface elasticity, E, or as an indication of changes in free energy. When the interface is expanded or contracted, then $E = -d\gamma/d\ln\Gamma$, where γ is the measured interfacial tension, and Γ is the interfacial concentration or Gibbs surface excess. This elasticity is an indication of the ability of the interface to adjust the interfacial tension when stressed.

The interfacial tension, γ, in the Gibbs adsorption equation is used for equilibrium conditions as bitumen components are adsorbed. Measurement techniques available are extensive. Some of these methods are: duNouy ring, maximum bubble pressure, drop volume, Wilmhelmy plate, sessile drop, spinning drop, pendant drop, capillary rise, oscillating jet, and capillary ripples. These and many others are referenced extensively by Malhotra and Wasan (153). These authors also showed that there is no correlation between emulsion stability and interfacial tension. The nature of the film dominates stability. Some relationships between interfacial tensions and crude oil properties follow.

The interfacial tension values of crude oil/water or asphaltenes–resins/water are strongly dependent on pH and salt content of the aqueous phase. With toluene as the solvent, bell-shaped γ–pH curves were observed for heavy Venezuelan crude/brine systems (125), distilled-water washings of diluted bitumen/air (11), and light crudes (126). Luthy et al. (184) showed similar results for heavy southern Californian, light Arabian, and waste petroleum oil/brine systems. Figure 15 illustrates the interfacial tension pH effect of crude oil/water systems (184). A bell-shaped γ–pH curve with a maximum at pH 6 was observed for all crudes. Similar findings were observed for Zakum, Murban, and Tia Juana medium crude oil/water interfaces, with pH changes showing a maximum interfacial tension at pH 6 by Cairns et al. (185). They suggested that increased emulsion stability is expected to occur at very high and low pH only because of adsorption of surface-active components at these pH values. The interfacial tension in these cases reflects only the adsorption of interfacially active components at the interface. Acevedo et al. (186) found similar results for Venezuelan crudes and explained that, at low pH (< 7), the adsorption of basic groups is dominant. At

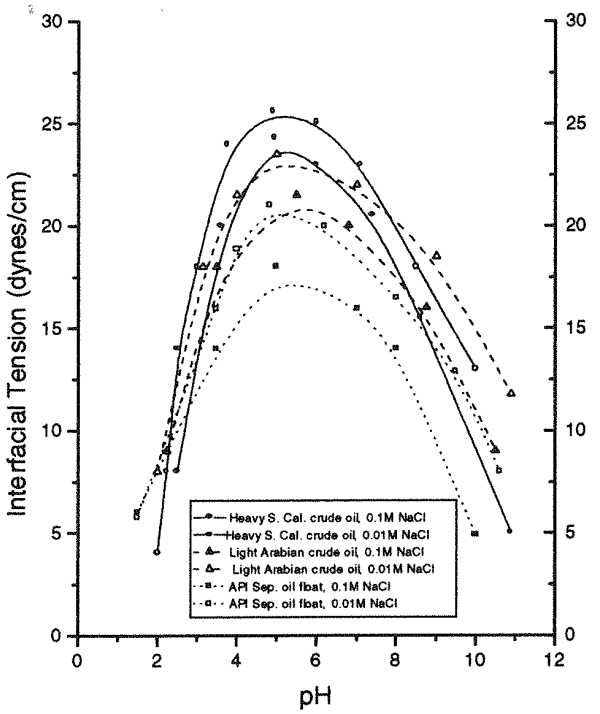

Figure 15 Interfacial tension changes with pH, showing the maximum for various crudes. (From Ref. 184.)

high pH (> 8), ionized carboxylic acids integrated in the adsorbed asphaltenes micelles are dominant, and an acid–base pair is adsorbed in the neutral region (pH 6–8). Xu (187) showed that the dynamic interfacial tension of the bitumen/water interface decreased with increased caustic concentrations as the interface aged. Similar decreases were noted as the bitumen concentration increased, indicating that adsorption of natural surfactants after saponification is time dependent. Similar observations were made for Ratawi asphaltenes (188). Through interfacial tension measurements the critical micelle concentrations of light and heavy fractions of Ratawi asphaltenes and desorption kinetics in organic solvents (189) were studied.

In all cases adsorption at the W/O interface is very slow and time dependent. The rate is lower for acidic and neutral pH. At basic pH, adsorption is much faster. These are often reported as aging effects, especially as changes at the interfaces go on for days or weeks. Malhotra (180) discussed detailed adsorption models and related this to film-drainage rates.

One can thus offer the conjecture that demulsification may be enhanced when films are weaker, which may or may not correspond with a high interfacial tension, since the film properties/architecture are

dependent on many factors that in turn depend on both the crude oil and the water. Eley et al. (72) and others discussed earlier have shown that, at acidic and neutral pH, the films are solid-like and highly viscous. Large increases in interfacial viscosity and elasticity were observed for crude oil/water with a change in pH from neutral to alkaline (73).

The times for development of an adsorbed layer or the conditions by which adsorption is minimized are factors which can be used to improve chemical demulsification. There is no correlation between decrease in interfacial tension and increased coalescence rates (190), notwithstanding the data showing decreased shear viscosity and increased coalescence rates (163).

Low interfacial tension is important for decreased energy requirements in the emulsion formation stage, but it does not appear to play such a role in demulsification. At an interfacial tension of 5 dyne/cm, in order to overcome LaPlace pressure and break up of a drop of 10 μm, one requires an external pressure gradient of 100 psi/cm, and for a 0.1-μm drop, a gradient of 10^6 psi/cm. The increase in interfacial energy for changing 10 ml water into droplets of 10 μm at interfacial tensions of 5 dyne/cm is 3×10^4 dyne/cm. If we compare this energy with that required to raise the temperature of the same water by 1°C at an energy cost of 4.2×10^8 dyne/cm, then the emulsification process of producing droplets from a bulk uses significantly less energy than the energy needed for temperature change or the energy for breakup of an already formed emulsion droplet. The smaller droplets behave as hard spheres. Thus, an easier means of destabilization would be by chemical demulsification augmented by changes in internal natural surfactant composition.

G. Effects of Temperature and Heat on Destabilization

Heat has its own advantages and disadvantages in the demulsification process (135, 191). Heat may also contribute to the disruption of emulsion film material by the differential expansion of the water inside the droplets, perhaps creating higher burst pressures. With increasing temperature the viscosity and density differences between water and heavy crude oils begin to diverge. The density of the oil is reduced faster than the density of the water as temperature increases, showing a larger divergence below 150°C. Since heat increases the density differences between bulk oil and water droplets it leaves a greater chance of accelerated settling, between 50°C and 125°C.

Also, as heating reduces the bulk viscosity of the oil, it also reduces the fluid resistance (106). The settling of water droplets is faster in less viscous oils. Because heating puts increased energy into a system there is a higher frequency of droplet collisions.

The increased temperature of the system may lower the interfacial shear viscosity, which may lead to an improved rate of film drainage between adjacent drops. Menon and Wasan (62) demonstrated the decrease in interfacial viscosity of shale oil/water at increased temperatures and showed analogous behavior at increased demulsifier concentration. Thompson et al. (133) reported that, at increased temperatures, some incompressible nonrelaxing films tend to relax and the rate of buildup of the resistance to film compression increases. Demulsifiers then reduce the kinetic barrier to coalescence.

Sometimes heat will deactivate the demulsifier if its solution chemistry is sensitive to heat. The cloud points of the nonionics occur at specific temperatures based on the chemical structure and oil-phase chemistry. In aromatic oils the phase-inversion temperature (PIT) is lower than the cloud point; in n-paraffins and cycloparaffins the PIT is higher than the cloud point. Phase inversion may result in some cases (192, 193) as the temperature approaches the cloud point.

Heating may augment destabilization of stable crude emulsions in which waxes play a large role. This is more likely with highly paraffinic crudes found in the North Sea (20) and paraffin wax crystals melted by heat. With asphaltenic or highly aromatic crudes, heating has less effect on the stability of the emulsions unless the viscosity and density of the interfacial barrier and continuous phase are reduced considerably. Stockwell et al. showed that the heating prehistory affected the emulsion stability of North Sea crudes but not the Canadian asphaltenic crudes (17). This was related to the crystallization sizes of the waxes in the North Sea crudes and the absence of wax crystals in the asphaltenic Canadian crudes. Neumann and Paczynka-Lahme (120, 194) held that, at increased temperatures, the interfacial films with asphaltenes remain intact but with the resins, stability increases. At high temperatures, resins form liquid-crystalline lyotropic mesophases for several crudes tested at 90°C. Stable films are suggested to have considerable viscoelasticity (195). Breaking emulsions with high resin contents is not easy because of the formation of either hexagonal or lamella liquid crystals at the interface at high temperatures.

Sometimes heating enhances the transport of the demulsifier chemicals to the interface as well. A com-

bination of heating and demulsifiers was found to be synergistic in breaking stable emulsions formed with Alaskan North Slope, Bonny Light, and BCF-17 crudes in a simulated spills study conducted by Stroem-Kristainsen et al. (196). This synergism with heat was also observed for breaking other North Sea (197) crudes' W/O emulsions (66, 198) and Nigerian (199) crude oil emulsions, when heat alone was ineffective. Nonionic surfactants performed better as demulsifiers at elevated temperatures for Hungarian (135) Algyo crude oil emulsions. If heat solubilizes the stabilizing surfactants into either the oil or water phase, the interfacial film will be weakened, leading to destabilization of the emulsion.

IV. CHEMICAL DEMULSIFICATION PROCESS

Emulsification and demulsification are both complex processes. However, as noted earlier, demulsification is by no means the opposite of emulsification (200, 201). This is especially the case in the petroleum industry. In order to demulsify a crude W/O emulsion efficiently, it has been emphasized that it is advantageous to understand first the characteristics of the emulsions, the nature of interfacial films, and hence the causes of stability. Accordingly, in choosing a demulsification protocol, one would first identify key factors responsible for the stability, find the target properties to modify toward destabilization, introduce sufficient energy to promote coalescence, and find the best conditions to allow phase separation.

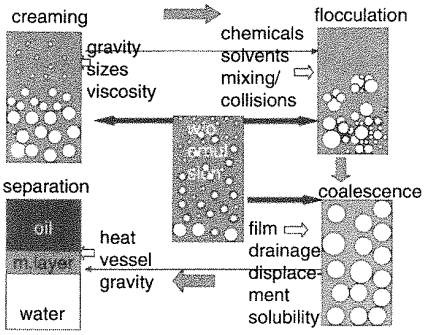

Figure 16 Schematic illustrating the various stages of demulsification process.

Demulsification of emulsions can be summarized by four phenomena occurring either sequentially or simultaneously. These are flocculation and/or aggregation, creaming or sedimentation, coalescence, and phase separation. The efficiency depends upon the matching of the demulsifier with the process residence time, the concentration and stability of the emulsion, the temperature, the process vessel, and the mixing, all of which affect the aggregates before coalescence occurs. These various stages are illustrated in Figure 16. The figure shows a schematic describing four stages of demulsification. It summarizes the changes as the emulsion is influenced by chemicals, solvents, mixing conditions, size distributions of the droplets, heat, and the vessel used for separation.

Figure 17 is a photomicrograph of flocculation and coalescence of a bitumen-stabilized W/O emulsion after treatment with an oil-soluble demulsifier. The

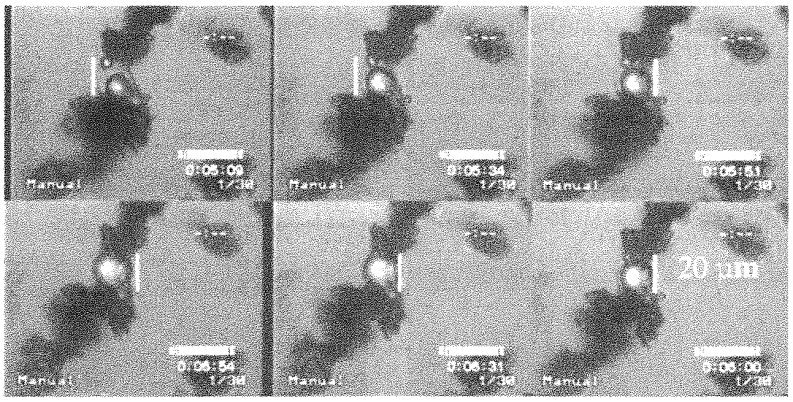

Figure 17 Photomicrograph of flocculation and coalescence of a bitumen-stabilized W/O emulsion after treatment with an oil-soluble demulsifier. (From Ref. 82.)

large droplet approaches the smaller droplet and they eventually coalesce. In this case, coalescence is the rate-determining step. Figure 18 shows bitumen W/O emulsions droplets before and after treatment with a demulsifier in the oil phase. The aggregates of larger droplets, after treatment, indicate that coalescence occurs during or before flocculation. Note the change in the distribution of finer droplets from 10 s to 24 h after treatment.

In industry, if crude oil emulsions do not coalesce and/or phase separate in a given time frame, and persist throughout the process, the emulsion is deemed stable or tight. Demulsification can be monitored by bulk phase separation over time and/or by a more fundamental approach of examining the interfacial dynamics which provides some understanding of the demulsification mechanisms. The first is used in the field and/or as part of a laboratory study. Here, efficiency is defined as the rate of coalescence and water resolution, by tracing the fraction of water resolved over time and using an initial slope of the curve as an efficiency factor (202). The second approach is more complex and is most often used in research. It includes flocculation, coalescence, and film-drainage phenomena. In the second approach, monitoring the growth of droplets over time or the disappearance of droplets into the bulk phase provides data that have been used in the development of many models on coalescence kinetics (203–205). However, obtaining experimental data to test these models relies on techniques such as microscopy and image analysis, light scattering, or turbidimetry (62, 76, 206, 207). Many theories (208, 209) have been developed for the droplet growth or disappearance over time as a measure of emulsion stability (90, 210) and instability (211). Droplet growth through water attraction by holes developed in the interface, or by Oswald ripening mechanisms, are a few of the reasons behind coalescence. The lamella drainage approach involves the interplay of both surface/interfacial forces and hydro-

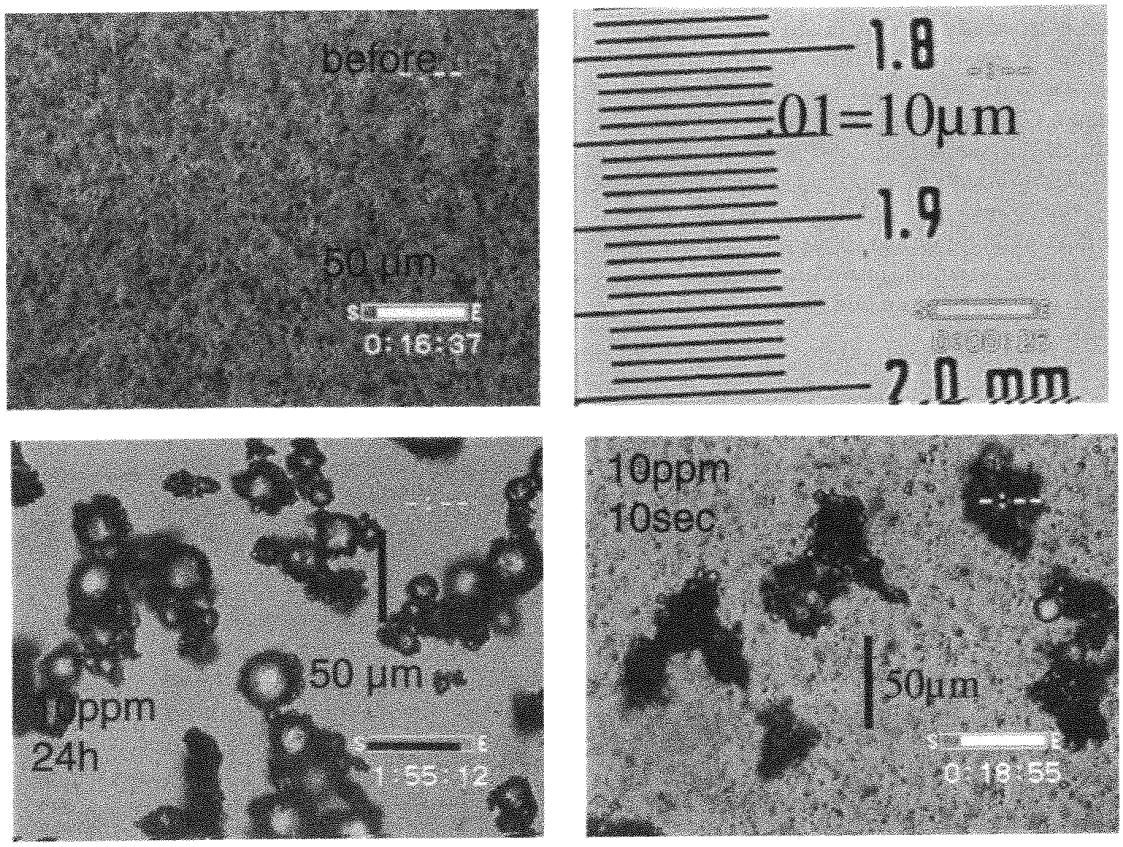

Figure 18 Photomicrograph of bitumen W/O emulsion before and after treatment (after 10 s and 24 h clockwise) with a demulsifier showing the aggregates of larger droplets with smaller droplets attached. (From Ref. 82.)

dynamic forces (212). Interfacial rheology is important in the latter.

A. Creaming and Coalescence

For a simple two-phase system consisting of an upper organic phase and a lower oil/water emulsion phase, Ostrovsky and Good (213) distinguished between the kinetic and aggregative instability of macroemulsions. The kinetic instability was identified as sedimentation or creaming, which was distinguished from aggregative instability. They developed a model in which the system coalescence occurred under agitation, and then traced coalescence and sedimentation times. The latter arose out of their studies on drop size versus agitation relationships, the former through low interfacial tension (range 0.024–0.33 dyne/cm) and coalescence–time correlations.

However, according to Vold and Vold (214), creaming is the separation of an emulsion into a concentrated and a dilute fraction through centrifugation or gravitational settling. The concentrated part is rich in the dispersed phase and the remaining dilute phase has finer droplets. The rate of creaming of noninteracting particles depends on density differences and the square of the droplet radius. If particles are interacting and held in a confined space, the rate of creaming involves complex hydrodynamics, wall effects, and hindrances. If the particles are aggregated the creaming rates are higher than the rate with the primary particles owing to the larger aggregate radius and the relative porosity (tightness or loose nature) of the aggregate. Flocculation may help to accelerate creaming, as particle concentration increases. The floc which is sedimenting more rapidly also sweeps or intercepts smaller droplets during the mass movement. Visually, creaming appears as a moving boundary of highly turbid material away from a lesser turbid material. This boundary is used to trace separation rates.

If coalescence or rupture of the interdroplet films common to two contacting droplets occurs during or before creaming, the destabilization rates are measured by tracing the changes in droplet size distributions with time, or by counting the number of droplets of specific diameters over the same time. In the case where a droplet merges with the bulk, the times of both approach and merge are measured.

One of the first theoretical interpretations of the coagulation process for hydrophobic sols was developed by Smoluchowski (215). This was later extended to flocculation and coalescence kinetics (216). Becher (89, 100, 117, 211) describes these theories in some depth. He stated that demulsification is the most important and the most complete example of emulsion stability. There is a distinction between a dilute emulsion system and a concentrated system. In the dilute system it is expected that the rate of flocculation is much lower than the rate of coalescence. As the droplets increase in number (or volume fraction), there is a much faster increase in the rate of flocculation and a slower increase in the rate of coalescence. In highly concentrated emulsions, coalescence can be rate determining. Over a certain range of concentrations the two processes can be the same order of magnitude.

One can thus add chemicals in a dilute system such that the rate of flocculation is unaffected but coalescence is inhibited. In some cases, creaming can be ruled out if the densities of the two phases are adjusted closely as in bitumen emulsions. Becher has noted that tracing the number of particles as a function of time is more sensitive than the specific interface method, as a 10% decrease in interfacial area is accompanied by a 27% decrease in the number of particles for a fixed size distribution.

Smoluchowski (215) modeled the decrease in particle numbers over time. In the model there was no distinction between single droplets, primary particles, and aggregates. The number of particles diffusing through a sphere surrounding a given particle in a unit time is equal to the number of particles adhering to a single particle. Therefore, for fast, irreversible flocculation alone in a dilute dispersion Smoluchowski's expression is:

$$N = N_0/(1 + a N_0 t) \tag{6}$$

where N_0 = the number of particles at time zero, N = the number of particles at time t, a = rate-determining constant = $8\pi Dr$, D = diffusion coefficient = $kT/6\pi\eta r$, r = droplet diameter, k = Boltzmann constant, T = temperature, η = the viscosity, and the half-life of an emulsion becomes $1/aN_0$. A plot of $1/N$ versus t gives the rate constant a, which approximates to $a = 10^{-11}\text{cm}^3\text{s}^{-1}$.

In a flocculating concentrated emulsion, $aN_0 \gg K$, and the contribution of unreacted primary particles is negligible. A rapid flocculation rate relative to the rate of coalescence is given by Van den Tempel (216):

$$N = N_0\,[1 - \exp(-Kt)]/KT \tag{7}$$

Here, K = coalescence rate constant, and T = absolute temperature. When the rates are equal for both coalescence and flocculation, $a = 10^{-12}$ to 30×10^{-11} cm^3s^{-1}. When coalescence is slow the collision frequency and the duration of collisions are more